ISOSPIN MIXING AND THE ^{30}P$(p,\gamma)^{31}$S REACTION RATE

By

Michael Bennett

A DISSERTATION

Submitted to
Michigan State University
in partial fulfillment of the requirements
for the degree of

Physics – Doctor of Philosophy.

2016

ABSTRACT

ISOSPIN MIXING AND THE ^{30}P$(p,\gamma)^{31}$S REACTION RATE

By

Michael Bennett

The ^{30}P$(p,\gamma)^{31}$S reaction rate is critical for modeling the final elemental and isotopic abundance of ONe nova nucleosynthesis, the calibration of proposed nova thermometers, and the identification of presolar nova candidate grains. Unfortunately, the rate is essentially unconstrained experimentally, despite numerous studies using a variety of experimental techniques, largely due to uncertainties in the spins and parities of the narrow, isolated ^{31}S proton capture resonance states that likely govern the proton capture reaction rate.

The beta decay of ^{31}Cl, which preferentially populates important $l = 0$ ^{30}P proton capture resonances in ^{31}S, is a useful tool for studying the properties of these states. Using an accelerated beam of ^{31}Cl, we have observed the beta-delayed gamma decay of a number of ^{31}S states up to excitation energy $E_x = 7200$, including states within the ^{30}P$(p,\gamma)^{31}$S Gamow window for peak nova temperatures. Herein we report the results of this study, including: the production of a ^{31}Cl beta decay scheme with over twice as many ^{31}S gamma transitions as the most recent literature scheme; the observation of isospin mixing of a resonance with isospin $T = 1/2$ at $E_x = 6390.2(7)$ keV with the nearby $T = 3/2$ ^{31}S isobaric analog state (IAS), giving it an unambiguous spin and parity of $3/2^+$; and the clear identification of the second $T = 3/2$ ^{31}S state and the results of several tests of the isobaric multiplet mass equation for both the lowest and second-lowest $A = 31, T = 3/2$ quartets.

Of making many books there is no end,
and much study is a weariness of the flesh.

Eccl. 12:12

This dissertation is dedicated to H. Michael Sommermann
and Warren F. Rogers, the first people to teach me that being
a good physicist is more than the making of many books.

ACKNOWLEDGMENTS

Of course, none of this could have been possible without the work of my advisor, Dr. Chris Wrede. Chris has a tremendous ability to seek out important problems in nuclear astrophysics and conceive of new ways to answer those questions, and I am very grateful for the opportunity to have been involved in multiple important projects as his graduate student. Chris was patient with me as I made basically every mistake it is possible to make as a grad student, and continuously encouraged me to become the best researcher I could. I am truly indebted to him for helping me develop as much as I did during my time at Michigan State.

I also have to thank my incredible thesis committee: B. Alex Brown, Laura Chomiuk, Carl Schmidt, Hendrik Schatz, and Ulrike Hager. Their insights throughout the process of planning, executing, and analyzing the results of my thesis experiment helped to make me a better and more thoughtful scientist. Ulrike especially deserves special thanks for exhibiting superhuman flexibility and stepping in at the last moment to witness my dissertation defense when a committee member was unavailable.

In addition to my advisor Chris, I am indebted to the other members of the Wrede group for their support, especially David Pérez Loureiro. Without David's coding expertise, the analysis of my thesis experiment would have been tremendously inefficient. David not only helped me with the sort of the experiment data, but helped me develop my own insight into how the analysis software could be used. Sarah Schwartz, Brent Glassman, and Cathleen Fry all provided assistance and support before, during, and after the experiment, and I am grateful to have not been an academic "only child." I can only hope I provided them as much support in their own growth.

The experiment itself would have been a spectacular failure if I had been left to my own devices to prepare for and execute it. Our wonderful collaborators all deserve thanks in this area, but I am greatly indebted to Sean Liddick and his Beta Group, especially Chris Prokop, Nicki Larson, and Scott Suchyta, for their help with simulations, detector setup and maintenance, calibration, data acquisition, and many other things. Other NSCL faculty and staff played important roles in the experiment as well, from Craig Snow and the design group, to Tom Ginter and the A1900 group, to Jim Vincent, Kurt Kranz, and the other electrical engineers, to the cyclotron operators who worked tirelessly to save the experiment when the accelerator failed within ten minutes of the start of data taking. The NSCL community contributed many seemingly-small but vitally-important things to the experiment, and I cannot thank the workers here enough.

Graduate school is rarely a pleasant and simple endeavor, and at a number of times throughout my tenure as a student at MSU, I despaired of succeeding at the challenge. I am lucky to have had so many incredible friends, from my *Dungeons & Dragons* group (thanks for three years of incredible storytelling – but it's spelled *"T-H-I-N-N-U-S"*) to my die-hard board game friends who didn't shy away from fourteen-hour space opera games ("MAUOOOOB!") to my brothers at House Chaos Dunk (there are too many inside jokes to choose just one here), to those willing to drop everything and meet to discuss philosophy at Peanut Barrel at one in the morning, to Alanna Pawlak, who has stood by me through thick and thin for the past two years. Academia can be a lonely, nervous place, and it has been a life-saver to have calming, supportive relationships with people who have always made me feel like I belong.

My family deserves praise for their constant support and patience during the five years it took me to complete my Ph.D. They never wavered in believing I could achieve this milestone,

and I cannot thank them enough for their lifelong support of my academic progression.

TABLE OF CONTENTS

LIST OF TABLES

LIST OF FIGURES

Chapter 1

Introduction

1.1 Overview of Pertinent Physics

1.1.1 An Introduction to Nuclear Physics

The periodic table of elements is organized according to the increasing number Z of protons in an atom of each element, but for each element, multiple isotopes exist with identical Z but differing numbers N of neutrons. These isotopes are commonly organized according to the so-called *chart of nuclides* (Fig. 1.1), with the number of protons in the nucleus increasing along the vertical axis and the number of neutrons in the nucleus increasing along the horizontal axis. As shown in Fig. 1.1, isotopes of an element are arranged in horizontal rows and, because they share the proton number Z, have identical chemistry while possessing different nuclear properties. Nuclei with identical neutron number N are called isotones, and nuclei with the same total number of nucleons (so-called "mass number" $A = Z + N$) are called isobars.

Only a small fraction of all known nuclei are stable; these are represented in the chart of nuclides (Fig. 1.1) by the black squares. The remaining nuclei are radioactive and undergo some form of *nuclear decay*, transforming sequentially into stable nuclei. The two primary forms of decay for light nuclei are *particle emission* and *beta decay* (commonly abbreviated with the Greek symbol β). For example, neutron-deficient nuclei to the left of stability on
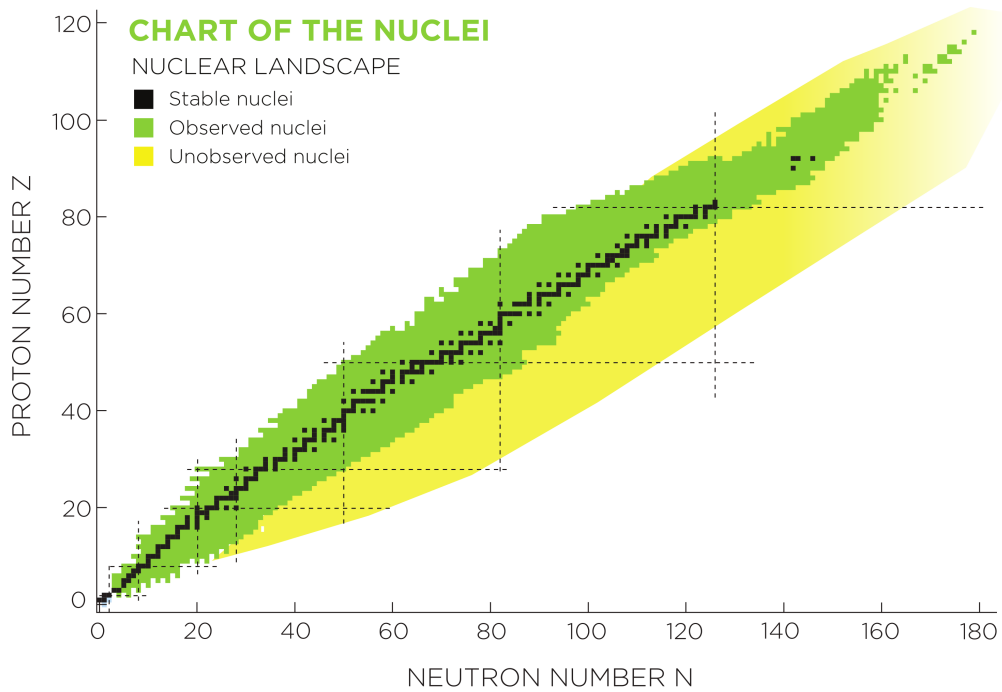
Figure 1.1: The chart of nuclides. The vertical axis represents the number of protons Z in a given nucleus and the horizontal axis represents the number of neutrons N in the nucleus. All isotopes of a given Z possess identical chemical properties, but the nuclear physics properties of a given element are different from one isotope to the next. The black squares along the center of the distribution are the stable nuclei; the green region represents unstable nuclei that have been observed, while the yellow region represents nuclei expected to exist but as of yet unobserved.

the N axis of the chart of nuclides decay either via proton or alpha-particle emission, or by undergoing beta-plus decay. Beta-plus decay, in which the nucleus transforms a proton into a neutron and emits a positron (a beta-plus particle, β^+) and electron neutrino, occurs via the weak interaction. A nucleus, like an atom, may exist in one of a number of quantized energy states; particle emission such as proton decay requires the *parent* nucleus (that is, the nucleus that is undergoing decay) to be in a state with mass greater than that of the *daughter* nucleus (that is, the nucleus into which the parent decays) plus the particle. This is true for all nuclei including those beyond the edge of the chart of nuclides, the "drip line," investigation of which is an active field in nuclear science and is beyond the scope of this work. If the energy of this state is higher than the ground state, it may be attained, for example, by the absorption of a gamma-ray γ that adds its energy to that of the parent nucleus. For proton emission of, for example, ^{16}O, this process would be notated: $^{16}\text{O}(\gamma, p)^{15}\text{N}$.

In principle, in an environment with an abundance of protons, the reverse also happens: such *proton capture* is notated in a very similar fashion: $^{15}\text{N}(p, \gamma)^{16}\text{O}$ represents the combination of a ^{15}N nucleus and a proton to form ^{16}O; the resulting photon carries away energy given off in the capture reaction (more details in Section 3.2). On the neutron-rich side of the chart of nuclides, neutron emission and beta-minus decay occur to mirror the decay of unstable nuclei on the neutron-deficient side. And, in some circumstances, a nucleus may emit an alpha particle (α), a ^{4}He nucleus. In each of the above cases of decay, the nucleus changes in Z, N, and/or A. A heavier nucleus ($A > 56$) may also *fission*, breaking into constituent daughter products such that the binding energy per nucleon in each daughter nucleus is higher.

These various decay processes all move the nucleus toward stability. Since beta-decay preserves mass number A, a lighter nucleus could conceivably be transformed to a heavier

one via a series of particle captures and beta decays. However, since most unstable nuclei are extremely short-lived, it has historically been difficult to study their properties. The field of nuclear astrophysics originated through attempts to answer this and other large-scale questions: What is the origin of the elements? How do stars generate their energy? And how do the energetic stellar events observed throughout the galaxy such as supernovae, neutron star mergers, and other cataclysmic events contribute to the observed distribution of isotopes throughout the galaxy?

1.1.2 Nuclear Astrophysics and the Lives of Stars

The modern field of nuclear astrophysics was born from work culminating in the late 1950s with the publication of the treatise *Synthesis of the Elements in Stars* [1] and the independent formation of the lecture series *Stellar Evolution, Nuclear Astrophysics, and Nucleogenesis* [2]. In these works, both the origin of the elements and the energy generation of stars were proposed as the consequences of nucleosynthesis: the building up of protons and neutrons into light elements, and the subsequent building of heavy elements from those lighter pieces. Various galactic sources were proposed as sites for nucleosynthesis. The Big Bang produced hydrogen (protons), neutrons, and, through nucleosynthesis of these two building blocks, the additional light nuclei ^{3}He, ^{4}He, and ^{7}Li [3]. With few exceptions originating from processes like cosmic ray interactions, all elements besides hydrogen, helium, and lithium are produced in stars.

Stars are categorized according to their composition. "Population I" stars like our Sun have compositions affected by the materials ejected in the death throes of older "Population II" stars. But even these ancient stars exhibit some metallicity – in fact, every star that has ever been observed has some metals in it. A proposed first generation of stars, the

4

$$p + p \rightarrow {}^{2}\text{H} + e^{+} + \nu_{e}$$

$${}^{2}\text{H} + p \rightarrow {}^{3}\text{He} + \gamma$$

$${}^{3}\text{He} + {}^{3}\text{He} \rightarrow {}^{4}\text{He} + 2p$$

$${}^{2}\text{H} + p \rightarrow {}^{3}\text{He} + \gamma$$

$$p + p \rightarrow {}^{2}\text{H} + e^{+} + \nu_{e}$$

1 billion years   1 second   1 million years
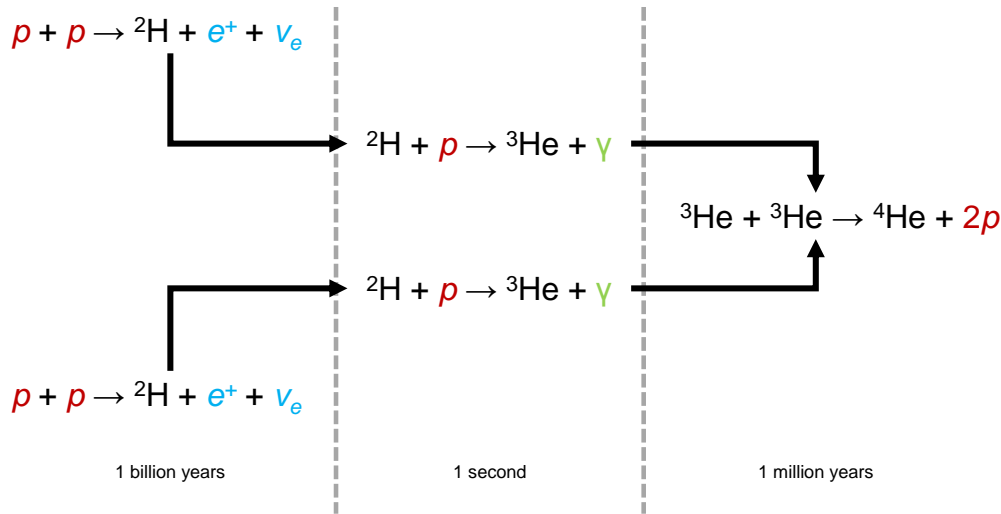
Figure 1.2: The *pp*-I chain, which produces ^{4}He from fusion of four protons (^{1}H). The arrows indicate the order of processes, while the times noted at the bottom of each section (demarcated by the dashed gray lines) denote the time for the reaction to occur in a stellar environment like that of the Sun. The extremely long timescale of the first reaction, $p + p \rightarrow {}^{2}H + e^{+} + \nu$, is due to the repulsive Coulomb barrier between the two protons. This long timescale is offset by the colossal number of protons in the Sun, $\sim 10^{57}$. The *pp* chain dominates energy production in stars as massive as the Sun.

"Population III" stars, was formed out of hydrogen and helium within about 10^{9} years after the Big Bang [4].

Stellar nucleosynthesis is the process of fusing the nuclei that make up the initial composition of a star into progressively heavier nuclei. Stars spend the majority of their life burning hydrogen into helium because this fusion yields more energy than subsequent reactions. Through nucleosynthetic processes such as the *pp* chain (Fig. 1.2) and the *CNO* cycle (Fig. 1.3), ^{1}H is fused into ^{4}He, proceeding through the nuclei ^{2}H and ^{3}He in the process. Beyond these elements, stars produce heavier elements via nucleosynthetic processes such as the triple-α process, which combines three ^{4}He nuclei into ^{12}C, and the ^{12}C(α, γ) reaction, which produces ^{16}O. These reactions release energy, causing the star to expand and cool, and keeping it in so-called *hydrostatic equilibrium* against gravitational collapse.

In principle, a star may generate energy by fusing successively heavier elements in its
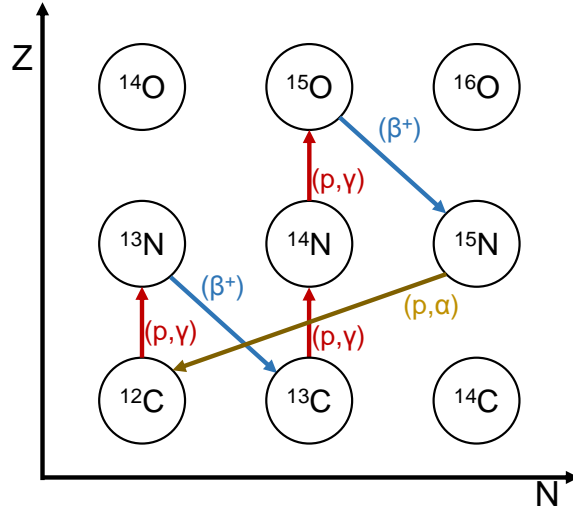
Figure 1.3: The CNO-I cycle, which, similar to the *pp* chain (Fig. 1.2), produces a ^{4}He nucleus from the fusion of four protons. Unlike the *pp*-chain, however, the CNO cycle is catalytic, consuming the four protons necesary for ^{4}He production but not the ^{12}C nucleus through which the ^{4}He is created. The CNO cycle dominates energy production in stars of greater than about 1.5 $M_\odot$.

core until it produces ^{56}Fe and ^{56}Ni, after which the energy released from nuclear fusion is less than the release from fission of heavier nuclei into lighter constituent pieces. A star's nucleosynthetic endpoint is determined primarily by its mass; less massive stars, on the order of the mass of the sun ($M_\odot$), do not reach sufficient internal temperatures for fusion beyond oxygen, while stars less than about 0.3 $M_\odot$ will not even fuse to carbon. Stars of mass about 8-10 $M_\odot$ will produce neon. Despite the variance in nucleosynthetic endpoint, however, these stars all have the same fate: they will run out of fuel, shed their outer layers, and collapse into a compact star known as a white dwarf. Stars with mass greater than about 10 $M_\odot$, however, produce elements up to $A = 56$ via fusion of neon, oxygen, and silicon and will eventually end their lives as a neutron star or black hole.

Elements heavier than $A = 56$ are produced either via the "slow neutron-capture process" which is believed to occur mostly in giant stars, or in cataclysmic events such as mergers

of neutron stars or the death of stars much more massive than the Sun. In the latter case, the core of the massive star can no longer produce additional thermal energy through nucleosynthesis and is consequently unable to fight off gravity. It therefore collapses, releasing gravitational potential energy that powers an explosion known as a *supernova*, during which nucleosynthesis of heavy elements can occur in the ejected material. The core simultaneously collapses into a neutron star or black hole, depending upon the mass of the progenitor star. The ejected material, including a mix of heavier elements, is jettisoned off into space in a core-collapse supernova; the material may then eventually become part of a gas cloud where new stars may form. In this way, stellar material is recycled for use as fuel in future generations of these nuclear furnaces.

1.2 Classical Novae

As mentioned above, stars with masses on the order of one solar mass $M_\odot$ do not fuse elements heavier than neon, or possibly magnesium [5]. As such a star finishes the main sequence of its life and runs out of hydrogen in its core, it expands to become a red giant. During this time, the star's core contracts until it becomes hot enough to fuse helium into carbon and oxygen, while hydrogen burning continues in a shell surrounding the core. When the star runs out of helium in its core, the core, which depending upon the mass of the star is now composed predominantly of either carbon and oxygen (for less massive stars) or of oxygen and neon (for more massive stars), contracts yet again. At this point, the star jettisons its outer layers into a cloud known as a planetary nebula. The hot core of the star becomes a *white dwarf,* a small star of mass up to 1.4 $M_\odot$ with a composition dependent upon the composition of the core of the progenitor, again either carbon-oxygen

(a ""CO" white dwarf) or oxygen-neon (an "ONe" white dwarf). Lighter stars than the Sun will produce white dwarfs composed of helium, while stars with mass 8-10 M$_\odot$ will produce white dwarfs composed of oxygen and neon. No fusion occurs in the white dwarf; instead, further collapse is prevented by electron degeneracy pressure. White dwarfs radiate their stored thermal energy, becoming less hot and less visible over time.

For isolated stars, this represents the end of nucleosynthesis. However, it has been estimated that up to a third of stars exist as binaries – systems where two stars orbit a gravitational center [6]. In these cases, the stars may gravitationally interact and can have profound effects on each other's evolution. In a system where a white dwarf star co-orbits a less-massive main sequence star, the hydrogen-rich star may overflow its own *Roche lobe,* the region of space, bound by a gravitational equipotential surface, within which the star's gravity attracts nearby material. The hydrogen-rich material may then flow into the Roche lobe of the white dwarf via a process known as *accretion*, slowly spiraling onto the surface of the white dwarf in a disk orbiting the star. This accretion slowly builds up an envelope of hydrogen-rich material on the surface of the white dwarf [7].

Because the white dwarf surface is so much more dense than the hydrogen, the incoming material does not fully mix with the material that forms the white dwarf. While some mixing does occur in the bottom-most layer of the hydrogen *envelope* [8], the majority of the envelope remains hydrogen-rich and becomes increasingly hotter as it is compressed. This continues until the hydrogen-rich material becomes electron degenerate itself. At some point after this, the material becomes hot enough that hydrogen burning occurs, but because the material is degenerate, it cannot expand to cool itself off and maintain equilibrium [9]. Consequently, the envelope becomes hotter and hotter in a so-called *thermonuclear runaway,* which continues unabated until the degeneracy is lifted. In the process, the material accreted
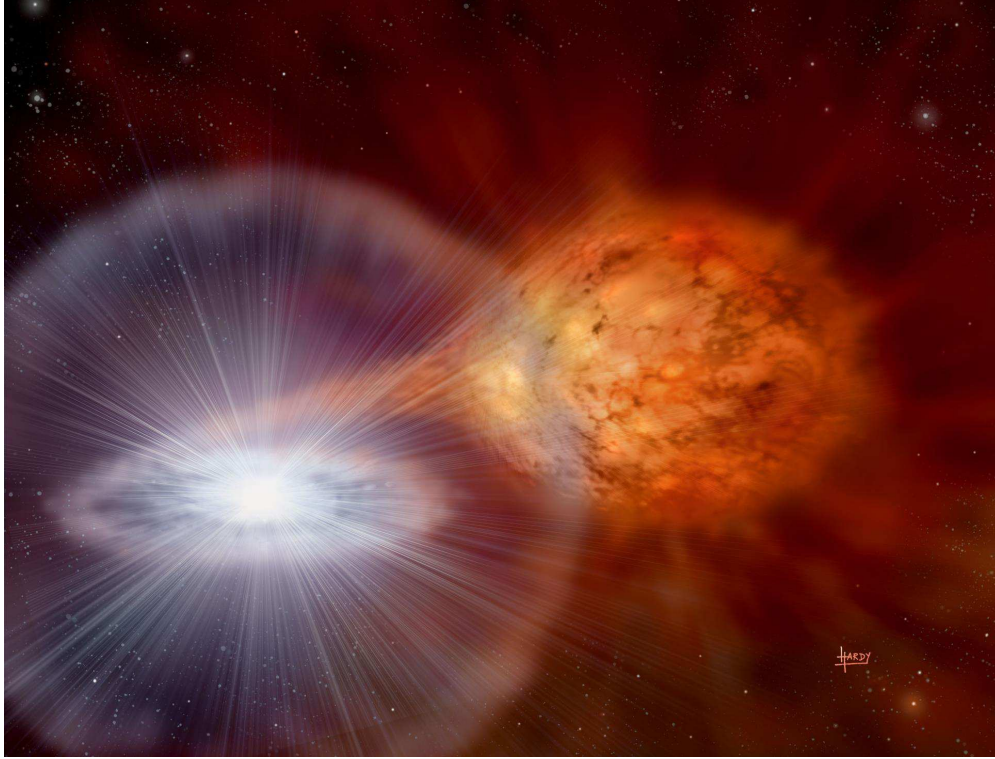
Figure 1.4: An artist's depiction of a classical nova in a binary system. The accretion disk, consisting of hydrogen-rich material flowing from the main sequence companion star (right), is shown at the equator of the white dwarf (left). Image copyright David A. Hardy, www.astroart.org

onto the white dwarf blows off in an explosion known as a *classical nova* [10]. Novae are categorized according to the type of white dwarf on which they occur: *CO novae* occur on the less massive white dwarfs composed primarily of carbon and oxygen, while *ONe novae* occur on the heaviest white dwarves, composed of oxygen and neon. An artist's depiction of a nova in a binary system is shown in Fig. 1.4.

Novae are powerful explosions, releasing $\sim 10^{45}$ ergs of energy [11] and causing the white dwarf to increase in brightness by factors anywhere from 1,600 to 10^7, with peak luminosities between 10^4 and 10^5 L$_\odot$ [12]. Unlike the more powerful supernovae, however, classical novae do not destroy the star on which they occur, meaning that they can be recurrent, with a period equal to the amount of time before accreted matter onto the white dwarf explodes

9

again. They occur far more frequently than supernovae in our galaxy, with an expected occurrence rate of 30 ± 10 per year [13], compared with an expected supernova rate of one every 40 ± 10 years [14].

Approximately 10 novae are observed in our galaxy per year (the difference between expected and observed number is due to interstellar dust in the galactic plane, which obscures the light emitted from the nova, as well as the lack of systematic survey techniques), allowing for observational study using both ground and space-based telescopes. Light curves, which measure the brightness of a nova as a function of time, have been recorded for novae in radio, infrared, optical, ultraviolet, X-ray, and gamma-ray regions of the electromagnetic spectrum. These different measurements of novae have helped to determine various properties of these stellar explosions: the rate and duration of the energy output, the nova's distance from Earth, and the density and temperature of the ejected material throughout the explosion. Spectroscopy has also been used to partially determine the elemental composition of the nova ejecta.

Similar to supernovae, material from the explosion is jettisoned out into space; novae however are less energetic than supernovae and release a smaller amount of matter, between 10^{-7} and 10^{-3} $M_\odot$ [15, 10], compared to between 1 and 10 $M_\odot$ for supernovae. As this material expands outward from the white dwarf, it cools, forming dust grains that preserve the specific composition of the nova material at the time it condenses. These grains, carrying a record of the nova conditions, travel throughout the galaxy and may in time be caught up in the formation of a new star or planetary system. Thus, these cataclysmic explosions may leave a distinct – and measurable – imprint on nascent stars and their attendant systems.

Chapter 2

Nuclear Astrophysics: Motivation for Study of $^{30}\mathbf{P}(p,\gamma)^{31}\mathbf{S}$

2.1 Elemental and Isotopic Abundances

As discussed in Chapter 1, the distribution of elements is the result of nucleosynthesis at various sites throughout the Universe's lifetime. It is possible to quantify this distribution both observationally and theoretically. For example, temperature and density models of the early Universe have been used to explain the currently-observed distribution of roughly 75% hydrogen and 25% helium by mass as a result of the relative numbers of protons and neutrons produced in the Big Bang. [4]. The distribution of the remaining elements is mainly due to stellar nucleosynthesis; however, because stars of different ages contain different amounts of heavy elements to begin with, the relative distribution of elements may differ between any two given stars or planetary systems in the galaxy, or even between two galaxies [16].

An important concept in nuclear astrophysics is the idea of *abundance*, the relative measure of the amount of a given element found in a specific location. The abundances of elements in a given system play an important role in its construction. Because our own solar system formed around an Nth-generation star, for example, it contained heavy elements such as iron, and was able to form terrestrial planets. Figure 2.1 depicts the elemental abundances
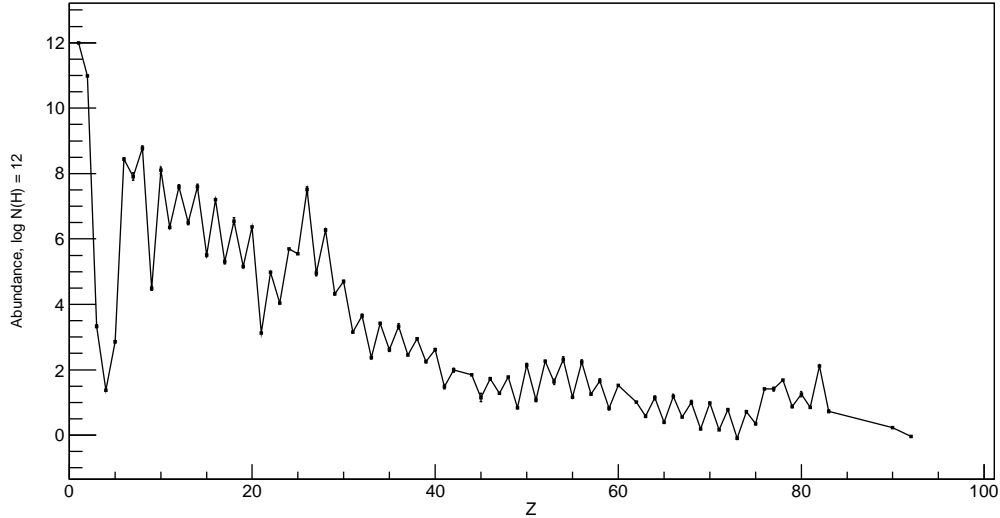
Figure 2.1: Solar system elemental abundances 4.56 billion years ago as a function of elemental number Z, plotted from data in Ref. [16]. The vertical axis has been normalized so that the hydrogen abundance value is set at 10^{12}. The other elemental abundances are relative to that number.

present in our solar system at the time of its formation. Of interest to nuclear astrophysics is the related concept of *isotopic* abundance; measuring the relative amounts of carbon-12 to carbon-14, for example, allows for radioactive carbon dating of ancient organic compounds on Earth's surface.

In principle, solar system abundances may be determined in several ways. Solar absorption and emission spectra (Fig. 2.2) may be used to determine the elemental makeup of the Sun, which is presumed to have undergone very little elemental change from the formation of the Sun out of the presolar nebula. Unfortunately, these spectra are based on atomic transitions and do not yield information about isotopic solar system abundances. Terrestrial materials, on the other hand, are readily accessible and may be studied in depth, allowing for the direct determination of precise isotopic abundances. However, because of the high temperatures and pressures present during the formation of Earth, chemical fractionation of terrestrial materials means that abundances determined from terrestrial sources do not
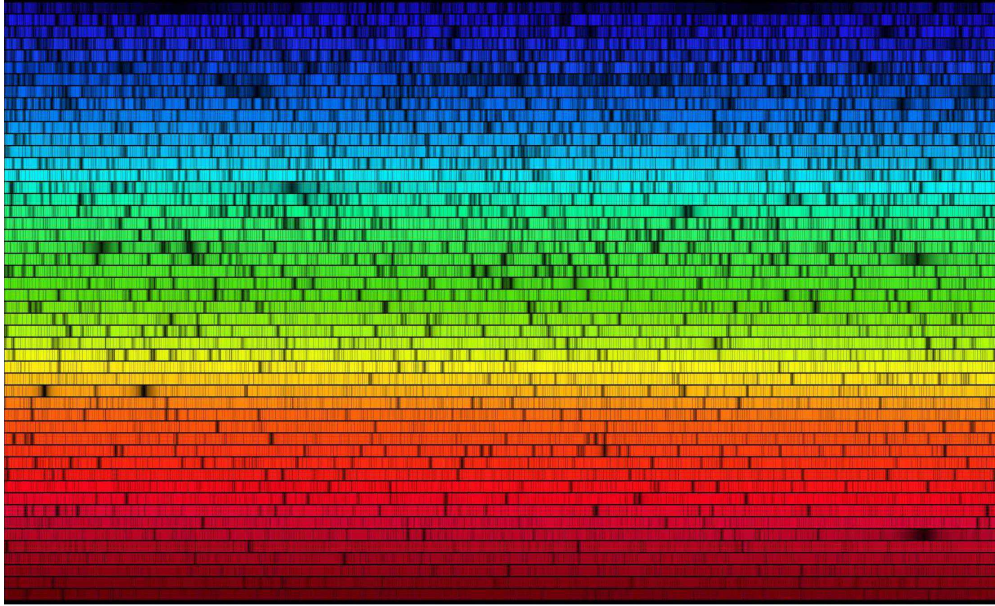
Figure 2.2: A solar photosphere absorption spectrum taken in the visible region of the electromagnetic spectrum between 392 nm (blue) and 692 nm (red). The dark lines at particular wavelengths throughout the spectrum are due to atomic absorption of photons of that wavelength, corresponding to a transition to an excited atomic state of that atom. Since each atomic element possesses its own energy scale, the pattern of absorption lines in the solar spectrum may be used to infer the elemental makeup of the photosphere.

typically match the composition of the solar system at large. A promising method to determine isotopic abundances is thus direct study of material formed in the presolar nebula that was unexposed to the high temperatures and pressures that resulted in the formation of the planets. Such material exists in the form of ancient meteorites, comets, and asteroids.

2.1.1 Meteorites and Their Analysis

Over 50 thousand meteorites have been discovered on Earth. Of these, the vast majority originated in primordial asteroids formed in the nascent solar system. Thus, meteorites comprise a promising path to data on the composition of the solar system as it was 4.6 billion years ago, as well as the processes that occurred as it formed.

Meteorites are classified into three categories based on their compositions: iron, stony-

iron, and stony. Both the iron and stony-iron meteorites, which together comprise only approximately 6% of meteorite falls, have undergone significant melting, making them unsuitable for abundance determination. Stony meteorites, which contain the highest amount of organic compounds, are themselves split into two broad categories, *chondrites* and *achondrites*, based on the presence or absence of small, round grains comprised mostly of silicate material called *chondrules*. Achondrites, like stony-iron and iron meteorites, have also been subject to igneous processes; however, these comprise only 8% of meteorite falls. The remaining 86% of meteorites are chondrites [17]. Examples of each of these meteorite types are shown in Fig. 2.3.

Chondrites are thought to have originated in primordial asteroids which formed in the protostellar disk but never grew large enough to heat up and undergo the chemical differentiation present in planetary bodies. As such, the chondrules present in them are thought to have remained largely unchanged from the formation of the solar system as well. Chondrites themselves are classified into three groups; of these, the carbonaceous chondrites are of greater importance to studies of abundances than the enstatite and ordinary chondrites [16] because a subset of the group, the *Ivuna*-type carbonaceous chondrites (CI chondrites), were never heated above 323 K [18]. CI chondrites exhibit the closest agreement overall with solar abundances, with the exception of H, C, N, O [19], and the noble gases[16]. These meteorites can thus be used to obtain not only primordial elemental abundances but isotopic abundances as well, giving a window onto the composition of the solar system in its infancy.

2.1.2 Isotopic Abundances in Classical Novae

Like stellar nucleosynthesis of the Sun and most other stars, the thermonuclear runaway of a classical nova is powered primarily by hydrogen burning. The initial burning is spurred by

Figure 2.3: Iron (top left), stony-iron (top-right), achondrite (bottom-left), and chondrite (bottom-right) meteorites. All of the meteorites with the exception of the chondrite have undergone varying degrees of chemical differentiation as a result of heating. Photo Credits: Ji-Elle, Doug Bowman, Captmondo, and H. Raab
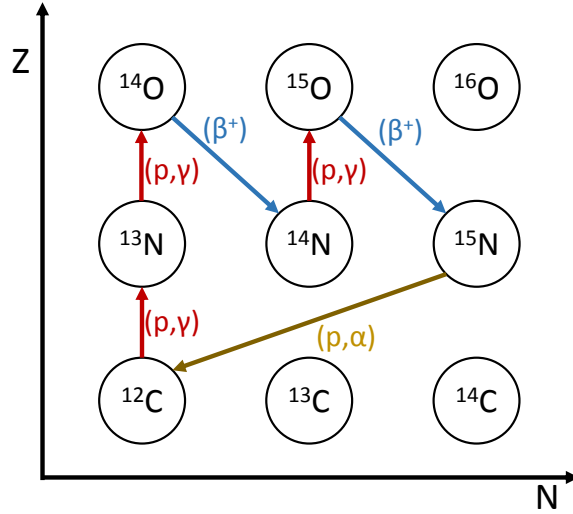
Figure 2.4: An excerpt of the chart of nuclides showing the "hot" CNO cycle. As illustrated here, the hot CNO cycle breaks out from the "cold" cycle when ^{13}N captures a proton instead of undergoing beta decay; this is due to the increased temperature in the stellar environment, making the relative time for proton capture shorter than the ^{13}N beta-decay half-life of 10 minutes.

the pp chain, but the explosive burning that occurs as the nova reaches its peak temperatures is powered by the hot CNO-cycle (Fig. 2.4). In this environment, nucleosynthesis on "seed nuclei" such as ^{17}O can occur, fusing heavier elements up to $A \approx 40$ via a series of (p, γ) and (p, α) reactions and β^+ decays. This process is known as *nova nucleosynthesis* (Fig. 2.5).

As with any nuclear process, nova nucleosynthesis yields a distribution of isotopes produced by the burning. These final abundances characterize the nova and are themselves dependent upon environmental factors in the nova: for instance, maximum temperature achieved. As with the Sun, the presence of specific lines in nova spectra are clues to the final elemental abundances [20]. However, the same problem exists as with solar spectra: only elemental abundances may be inferred. For novae, a comprehensive investigation of isotopic abundances is even more difficult, since it is not possible to sample the system in which the nova occurs from across the galaxy beyond spectral lines (carbon and oxygen isotopic ratios
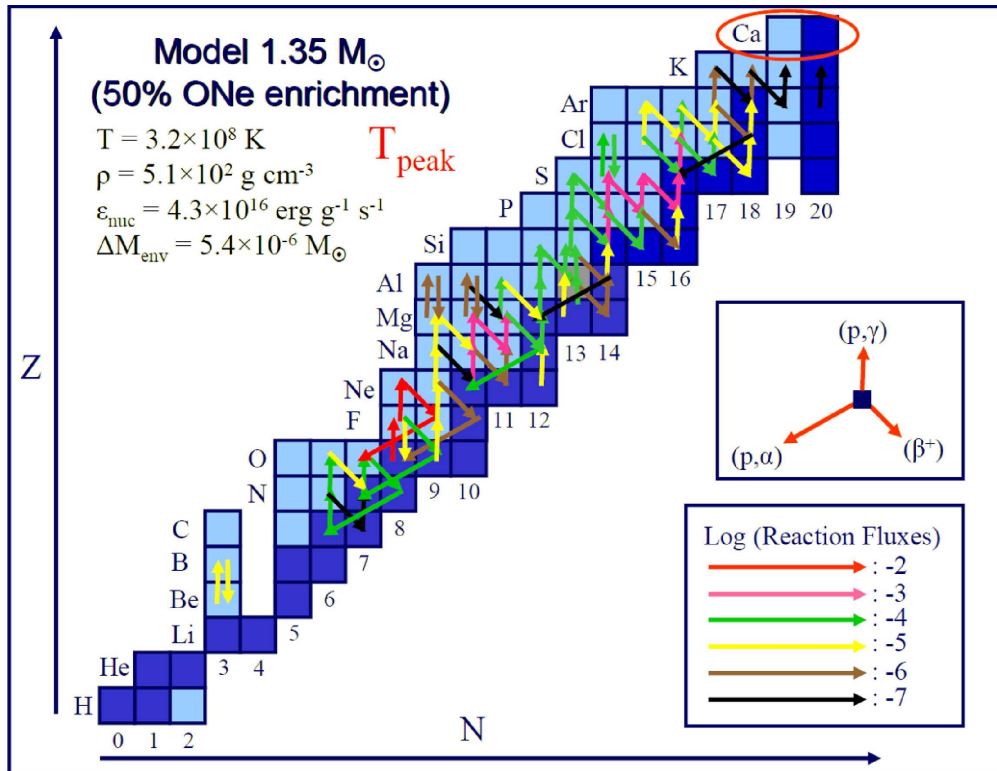
Figure 2.5: A section of the chart of nuclides showing the extent of classical nova nucleosynthesis. The dark blue boxes represent stable isotopes, and each arrow represents either a proton capture, beta decay, or (p, α) reaction. The red circle near the top of the figure denotes the endpoint of nova nucleosynthesis, around calcium. Figure credit: Ref. [20].

can be inferred from molecular lines from CO novae).

Typically, theoretical models are used by astrophysicists to estimate nova isotopic abundances. Such models may, for example, use a one-dimensional hydrodynamic code to simulate the evolution of the nova environment integrated with a nuclear reaction network to simulate the nucleosynthesis [21]. These nuclear reaction networks take input abundances of seed nuclei and, given tabulated rates as a function of temperature of each reaction involved in nucleosynthesis, produce theoretical isotopic abundances for the nova. Because only a few hundred nuclear reactions are involved, and those reactions lie close to the line of stability, it is possible to use mostly experimentally-determined reaction rates in the models [10]. Thanks to experimental work to measure and characterize the various reactions involved in nucleosynthesis, most reactions of importance to nova yields have been experimentally measured and characterized sufficiently. Until recently, only three reactions stood out as challenges to constraining nova abundances: $^{25}\text{Al}(p,\gamma)^{26}\text{Si}$, $^{18}\text{F}(p,\alpha)^{15}\text{O}$, and $^{30}\text{P}(p,\gamma)^{31}\text{S}$, and a 2013 study provided an experimentally determined $^{25}\text{Al}(p,\gamma)^{26}\text{Si}$ reaction rate [22, 23]. However, experimentally constraining at least the $^{30}\text{P}(p,\gamma)^{31}\text{S}$ reaction rate has been challenging. In fact, a recent evaluation of reaction rate uncertainties [24] concluded that attempting to calculate a meaningful $^{30}\text{P}(p,\gamma)^{31}\text{S}$ reaction rate from the available experimental information was futile because the nuclear physics was so poorly understood.

2.1.3   More Nucleosynthesis: Nova Thermometers

In addition to affecting the final isotopic abundances of nova nucleosynthesis of the isotopes in the mass range $30 \leq A \leq 40$, the $^{30}\text{P}(p,\gamma)^{31}\text{S}$ reaction rate also affects the calibration of so-called *nova thermometers*. A recent study [25] proposed the use of relationships between simulated abundance ratios of various elements and peak nova temperatures as a means to
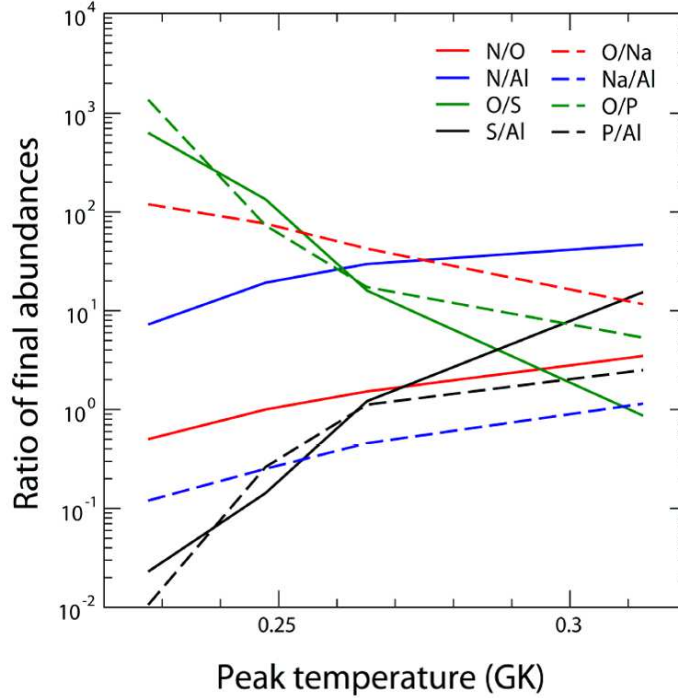
Figure 2.6: The eight nova thermometers proposed as the most useful for constraining peak nova temperatures in Ref. [25]. Each line represents the ratio of the notated elemental abundances as a function of temperature. The four most steeply-varying lines all involve either phosphorus or sulfur abundances, making precise determination of these elemental abundances a high priority. Figure credit: Ref. [25].

constrain the highest temperature a nova could achieve. This study used a nuclear reaction network with an updated library of reaction rates [26] and hydrodynamic nova models over a range of progenitor white dwarf masses from $1.15-1.35$ M$_\odot$ to simulate ONe nova explosions and subsequent nucleosynthesis. It recorded the final elemental abundances and peak temperatures reached by the novae during the simulations and plotted the relationships (Fig. 2.6).

The study found that, of the eight proposed elemental abundance ratios which varied most strongly with peak temperature, the two most strongly temperature-dependent ratios were O/S and S/Al, with the ratios O/P and P/Al following closely behind. However, the study concluded that the applicability of these thermometers was limited, partly due to

limitations in the observation and spectral analysis of ONe nova ejecta, but also due heavily to the lack of available experimental information on the $^{30}\text{P}(p,\gamma)^{31}\text{S}$ reaction rate. In fact, as in Ref. [24], the study was not even able to use experimental data to produce a reaction rate, instead opting for the purely theoretical Hauser-Feshbach statistical model [27] (see Section 3.3.1). The study called for new laboratory measurements of the rate in order to ascertain the validity of the nova thermometers O/S, S/Al, O/P, and P/Al.

In principle, isotopic abundances are not only useful for a theoretical understanding of nova nucleosynthesis or a computational study of their peak temperatures. In the situation described in Chapter 1, a grain of dust may condense from a nova outflow and travel to a young planetary system in the process of formation. If the material into which this grain embeds itself never draws close enough to its parent to cause chemical changes through heating, the grain may retain a distinct record of the isotopic abundances of its parent nova. In the event that such a grain, having entered our solar system during its formation, then makes its way to Earth, analysis may be carried out in the same manner as for a solar system grain and the nova grain's isotopic composition may be determined experimentally and compared to nova models. Such a grain, created before the birth of the solar system, can thus allow for in-laboratory study of an astrophysical process that occurred somewhere in the galaxy over 4.5 billion years ago.

2.2 Presolar Grains

Despite the knowledge that a number of diverse nuclear processes created the mixture of elements that formed the solar nebula [1], it was originally thought that the the formation process had homogenized the presolar materials which would form the solar system, resulting

in uniform solar system isotopic abundances. The first indications of anomalous isotopic composition in meteoritic grains occurred in 1954 and 1964 with the observation of divergent amounts of hydrogen [28] and xenon [29]. Further evidence in 1973 in the form of a meteoritic excess of ^{16}O opened the door to the idea that not all material present at the formation of the solar system had been homogenized, and the search for signatures of presolar material continued with observation of isotopic divergences in a number of other elements [30].

Isotopically anomalous meteoritic grains may have one of a number of origins [30]. They may be the result of decay processes of long-lived radioactive isotopes such as ^{26}Al, which is formed throughout the galaxy in giant stars and at other sites, with a half-life of $\sim 1 \cdot 10^6$ years; this radioactive ^{26}Al is caught up in the formation of the solar system and lends its signature to these samples in the form of its beta-decay daughter nucleus, ^{26}Mg. They may be so-called *calcium-aluminum-rich inclusions*, which may be formed from crystallization or melting of condensed liquid in the early solar system [31]. They may also simply be the result of local inhomogeneities in the solar nebula. In each of these cases, the sample may be the result of incomplete mixing in the solar nebula, but while it retains some of the characteristics of its site of origin, it does not exhibit isotopic ratios divergent enough to preclude creation in the young solar system. Those meteoritic grains whose isotopic abundances are different enough from solar system abundances to preclude a solar origin are known as *presolar grains*.

Presolar grains may originate from any stellar process which produces dust influenced by nucleosynthesis. Each grain carries a unique record of the process that spawned it, and as a result presolar grains from different sources exhibit isotopic abundances that are distinct from one another, even as they are distinct from solar abundances. These diverse grains also exhibit diverse compositions: for example, a majority of supernova grains are made of carbon in the form of diamond, while a majority of grains formed in *asymptotic giant branch*

21

(AGB) stars are *silicon carbide* (SiC) grains. Supernova or other processes may also produce SiC grains with their own unique isotopic abundances; thus, even grains of similar large-scale composition may reveal diverse origins upon examination.

2.2.1   Presolar Nova Grains

SiC grains are the most extensively studied of the presolar grains because they are both comparatively larger than other types of grains and because they are more numerous and easily found in meteorites such as CI chondrites. Because these grains are large enough to study individually as opposed to in bulk, techniques such as secondary ion mass spectroscopy (SIMS) [32] may even allow for measurements of elements with small chemical presences in the grain. Laser ablation and resonance ionization mass spectroscopy (RIMS) [33] have also proven useful for measurements of heavier elements such as strontium, zirconium, and molybdenum [34]. SiC grains have anomalous isotopic abundances of not only silicon and carbon, but of a sizeable list of other elements: N, Mg, Ca, Ti, noble gases, and refractory elements such as Sr, Zr, Mo, Ba, Nd, and Sm. [30]. A scanning electron microscope image of a SiC grain is shown in Fig. 2.7.

In quantifying the precise isotopic abundances of key species in particular grains, several different populations of SiC grains have been identified. In order to easily differentiate between these populations and their prospective origin processes, it is possible to plot characteristic isotopic abundance ratios as shown in Figs. 2.8 and 2.9. In each of these cases, different populations of grains are shown to have distinct ratios of isotopic species of key elements. Mainstream grains and types A and B grains are thought to be produced in various types of carbon stars in which the CNO cycle, helium burning, and the slow neutron capture process (*s*-process) occur. Types Y and Z grains are most likely produced in low-mass
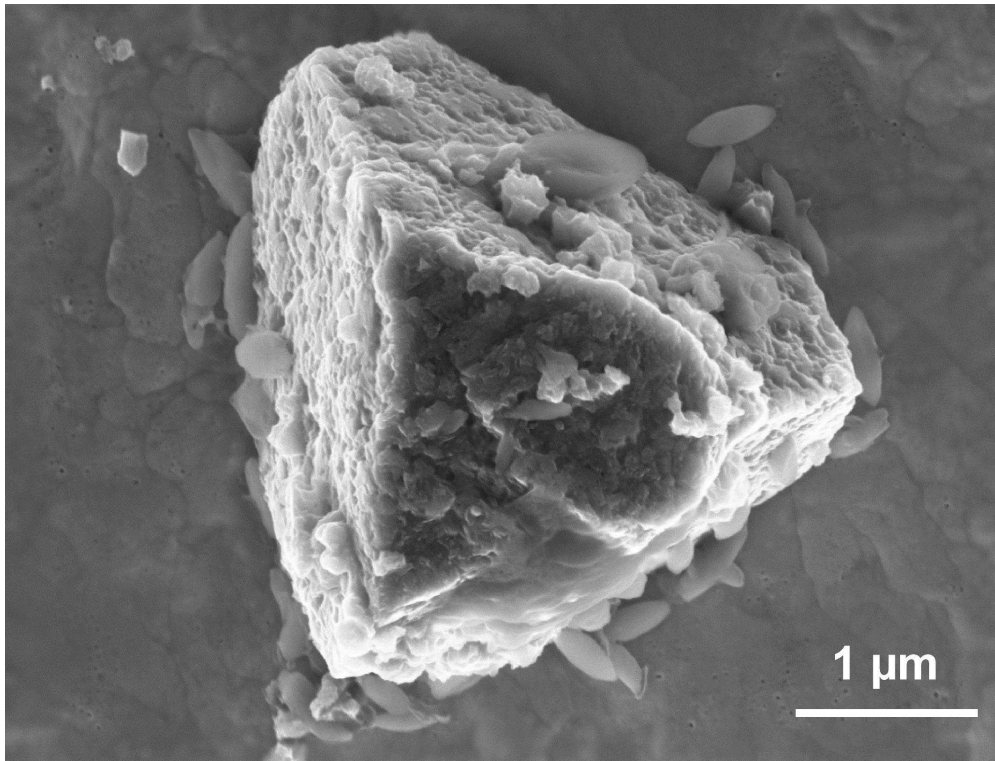
Figure 2.7: A SEM image of a silicon-carbide (SiC) grain, taken from the Murchison meteorite, a carbonaceous chondrite. Note the grain's large (several microns) size. Isotopic analysis has revealed that this grain is indeed a presolar grain, with an origin before the solar system. Photo credit: Max-Planck-Institut Für Chemie
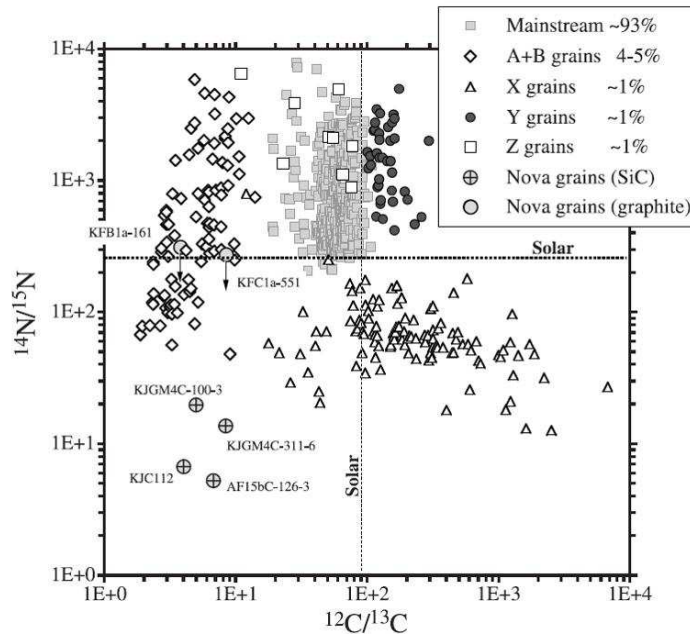
Figure 2.8: A plot of the ratios of carbon and nitrogen isotopic abundances as determined for a number of SiC presolar grains and some graphite grains. The dotted cross in the center of the plot denotes solar system abundances, and the various populations of grains, denoted with different symbols, are shown to be distinct based on the combination of the two ratios. As an example, the so-called nova grains are shown here to be deficient by nearly an order of magnitude in both ^{12}C relative to ^{13}C and in ^{14}N relative to ^{15}N, when compared with solar abundances. Figure credit: Ref. [35].

AGB stars with relatively small amounts of metal in which mixing between layers occurred. X-type grains have been proposed to originate in supernovae. For a thorough discussion of the natures of different presolar grain populations, see Ref. [30].

The so-called "nova grains" exhibit characteristically high ^{30}Si/^{28}Si ratios along with characteristically low ^{12}C/^{13}C and ^{14}N/^{15}N ratios. Nova models broadly predict that as the mass of the white dwarf on which the nova occurs increases, the relative amount of Si increases as well, as the temperatures reached during nucleosynthesis increase enough to produce silicon isotopes. Thus, oxygen-neon (ONe) novae, which occur on the most massive white dwarfs, are a possible origin process for these candidate nova grains [36].

24
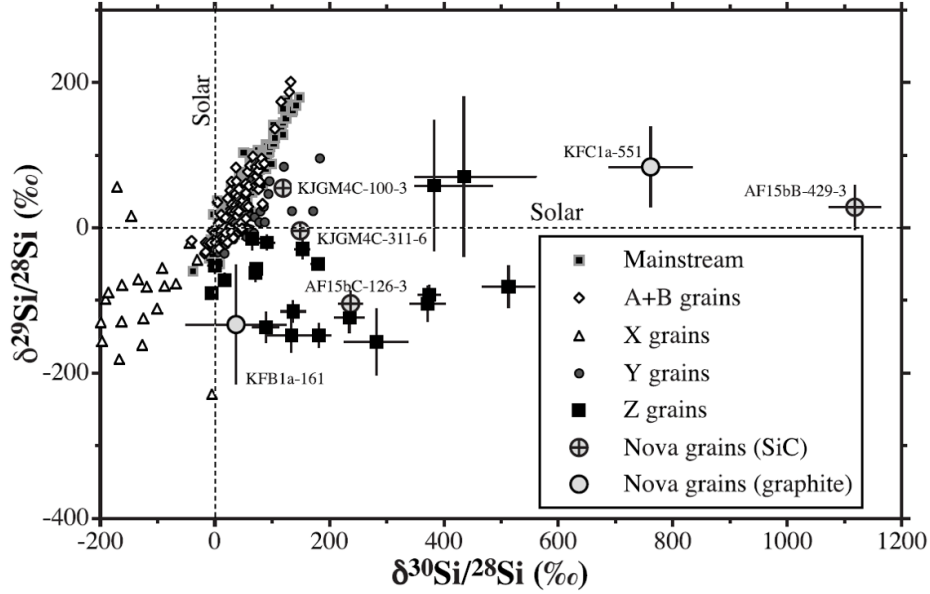
Figure 2.9: A plot of the ratios of the abundances of the stable silicon isotopes. The dotted cross centered at the origin denotes solar system abundances. The notation used here is "permil:" $\delta^{29,30}\mathrm{Si}/^{28}\mathrm{Si} = [(^{29,30}\mathrm{Si}/\,^{28}\mathrm{Si})/\,(^{29,30}\mathrm{Si}/^{28}\mathrm{Si})_\odot - 1] \times 1000$, such that a placement of 100 along the axis represent a 10% higher ratio than solar, and a placement of 1100 represents a 110% higher ratio. Figure credit: Ref. [35].

2.2.2 Comparison with Nova Models

As mentioned in Section 2.1.2, the output isotopic abundances of nova models may be compared with the observed isotopic abundance ratios of candidate nova grains. In principle, because there are so few nuclear reactions whose rates have not been constrained by experiment, it should be straightforward to assess whether or not candidate nova grains truly do originate in classical novae. Indeed, the comparison of isotopic ratios of carbon and nitrogen isotopes in nova models to those in analyzed grains reveals a generally good agreement [35]: both the models and the grains themselves exhibit deficits of both ^{12}C and ^{14}N when compared to ^{13}C and ^{15}N respectively. However, these agreements are overshadowed by the uncertainties in the model abundances of the silicon isotopes, which are so large as to completely preclude a definite assessment. These uncertainties are the result of uncertainty

in one single reaction: $^{30}P(p,\gamma)^{31}S$ proton capture.

^{30}Si is produced via the beta decay of ^{30}P, $^{30}P(\beta^+)^{30}Si$. The alternate path for destruction of ^{30}P in novae is via proton capture, $^{30}P(p,\gamma)^{31}S$. These processes compete to determine the total amount of ^{30}Si produced in novae: if the $^{30}P(p,\gamma)^{31}S$ rate is comparatively fast, more ^{30}P is destroyed via proton capture and less ^{30}Si is produced. Conversely, a slow rate yields more ^{30}Si. The half-life for ^{30}P beta decay is well-known to be 2.498(4) min, but the proton capture reaction is, comparatively, essentially unconstrained [24]. In fact, if the lower and upper limits of the rate are adopted instead of the central rate, the amount of ^{30}Si relative to ^{28}Si produced in the nova models becomes an excess of a factor of ∼6 or a *deficit*, respectively [35]. Better constraints for the $^{30}P(p,\gamma)^{31}S$ reaction rate are thus critical to answering the question of whether candidate nova grains truly do originate in classical novae.

2.3   The $^{30}P(p,\gamma)^{31}S$ Reaction Rate: Purpose of This Work

As discussed above, the rate of the $^{30}P(p,\gamma)^{31}S$ reaction plays an integral part in answering a number of important questions for classical nova studies due to its influence on nova observables. What is the final isotopic abundance distribution of novae in the mass region above ^{30}P? How high a temperature can novae actually reach? And do presolar nova grains truly come from novae? The first two questions are intertwined, as the maximum temperatures of novae are relevant to the question of *CNO cycle breakout*, a process by which novae could produce dramatically different isotopic abundances. The answers to *all* of these questions, however, involve constraining the $^{30}P(p,\gamma)^{31}S$ rate. Unfortunately, as will be dis-

cussed in more detail in Chapter 4, studying $^{30}\text{P}(p,\gamma)^{31}\text{S}$ is no trivial task, and the rate still remains largely unconstrained experimentally, despite numerous studies. Understanding the $^{30}\text{P}(p,\gamma)^{31}\text{S}$ reaction rate involves addressing a number of considerations: the environment in which the reaction takes place, the energies of the particles involved in the reaction, and even the specific nature of the capture reaction itself. All of these are factored into the derivation of the *thermonuclear reaction rate*, the rate of the reaction in the astrophysical environment.

The present work constitutes an experimental study using the beta decay of ^{31}Cl to populate a number of ^{31}S energy states important to $^{30}\text{P}(p,\gamma)^{31}\text{S}$ and measuring their properties via their gamma-decay. The experiment itself will be discussed in Chapter 4, while results and conclusions will be discussed in Chapters 5 and 6. Before discussing the experiment, however, it is useful to engage in a brief discussion of the nuclear structure concepts and formalism used to derive and interpret results in the experiment – this is the focus of the following Chapter 3.

Chapter 3

Formalism and Theoretical

Considerations

The term "reaction rate" in reference to $^{30}\text{P}(p,\gamma)^{31}\text{S}$ is somewhat loaded. There are in principle a number of ways to quantify the combination of a proton and a ^{30}P nucleus into ^{31}S: the *cross section*, a factor with geometric units describing the likelihood of combination of the two bodies; the *reaction rate*, which factors in the relative speeds of the particles; the *thermonuclear reaction rate per particle pair*, which normalizes over the distributions of energies of the particles in an astrophysical environment. In practice, when discussing or tabulating the "reaction rate" of a given reaction, astrophysicists are concerned with this last quantity. The term *thermonuclear reaction rate* reflects the fact that the energies of particles in astrophysical environments like novae are due to their thermal motion.

In the present section, we begin with a short derivation of the thermonuclear reaction rate equation and a discussion of the nature of particle capture in astrophysical environments, including *direct* and *resonant* capture reactions. Following that, we discuss ways to calculate the reaction rate when not every parameter involved in the calculation can be constrained experimentally, including the *Hauser-Feshbach* statistical model. Lastly, although they are not strictly related to astrophysics, we discuss two concepts important to nuclear structure and to the derivation and interpretation of results in the present work, the *nuclear shell*

model and the *isospin model.*

3.1 Derivation of the Thermonuclear Reaction Rate

In general, to calculate a particle capture reaction rate between a *projectile* (say, a proton) and a *target* (say, a nucleus in a stellar environment), several factors must be taken into account. These include: a geometrical factor $\pi\lambda^2$, where $\lambda = \frac{2\pi\hbar}{\sqrt{2mE}}$ is the deBroglie wavelength of the projectile; the interaction between the projectile and target, which can be represented by a matrix element $|\mathcal{M}|^2$; and a factor called the *penetrability*, essentially the probability that the projectile will approach near enough to the target to interact. This penetrability factor $P_l(E)$ accounts, for example, for the relative angular momentum of the projectile with respect to the target – radial motion of the projectile with respect to the center of the target results in an effective energy barrier which the projectile must overcome to interact. Combining these factors yields the following proportionality for the cross section for capture:

$$\sigma \propto \frac{1}{E} \cdot |\mathcal{M}|^2 \cdot P_l(E) \tag{3.1}$$

where E is the energy of the projectile.

Charged particle reactions such as proton capture require consideration of additional factors: because both the projectile (proton) and target (nucleus) of the reaction are charged, the penetrability must account for the *Coulomb barrier*, the repulsive potential between the nucleus and the proton. The penetrability $P_l(E)$ factor of the s-wave (that is, $l = 0$) proton capture can be shown using the expansion of the transmission coefficient $\hat{T}$ to be dependent

upon the Sommerfeld parameter η:

$$P_l(E) \propto e^{-2\pi\eta}, \quad \eta \equiv \sqrt{\frac{\mu}{2E}} \frac{Z_1 Z_2 e^2}{\hbar} \tag{3.2}$$

where Z_1 and Z_2 are the proton number of the projectile and target, respectively, μ is the reduced mass of the projectile-target system ($\mu = \frac{M_1 M_2}{M_1 + M_2}$), e is the fundamental charge, and E is again the projectile energy. As expected, this penetrability increases as the center-of-mass energy of the reactants increases.

From an astrophysical standpoint, the proton capture rate is also dependent upon a number of environmental factors including the relative densities of projectile protons and target nuclei and temperature, the latter of which affects the energy of the projectiles. It is possible to derive an expression for the rate of a nuclear reaction in a way that illustrates this fact. For the reaction $X + Y \rightarrow Z + W$, where X and Y, are, for example, a proton and a nucleus, the rate may be written:

$$r_{XY} = N_X N_Y v \sigma(v) \tag{3.3}$$

where r_{XY} is the *reaction rate* per unit volume and time, N_X and N_Y are, for X and Y respectively, the number per unit volume, v is the relative velocity of the projectile-target system, and $\sigma(v)$ is the reaction cross section in terms of that velocity. Since the velocities of projectiles and targets in the astrophysical environment are not constant, it is possible to use a generalized distribution for the range of possible velocities and write:

$$r_{XY} = N_X N_Y \int_0^\infty v f(v) \sigma(v) dv \tag{3.4}$$

where we can additionally define $\langle \sigma v \rangle_{XY} \equiv \int_0^\infty v f(v) \sigma(v) dv$ as the *reaction rate per particle pair*. As mentioned above, it is typically this value that is tabulated in place of the reaction rate r_{XY}, normalized by the Avogadro number N_A: $N_A \langle \sigma v \rangle_{XY}$. This *thermonuclear reaction rate* is in units of $\mathrm{cm}^3 \mathrm{mol}^{-1} \mathrm{s}^{-1}$, and reflects, as mentioned, the fact that the kinetic energy of the nonrelativistic projectile and target is their thermal motion, dependent upon the temperature of the stellar plasma [3].

In fact, because the particles involved in the reaction are nonrelativistic and nondegenerate and are in thermal equilibrium with one another, the relative velocity distribution of the projectile-target system can be described using a Maxwell-Boltzmann distribution, $f(v)$:

$$f(v) = \left(\frac{\mu}{2\pi kT} \right)^{3/2} e^{-\mu v^2/(2kT)} 4\pi v^2 dv \tag{3.5}$$

where μ and v are again respectively the reduced mass and center-of-mass velocity of the projectile-target system, T is the temperature of the stellar environment, and k is the Boltzmann constant. Using this as the distribution in the equation for the reaction rate per particle pair, and converting from a velocity distribution to an energy distribution using $v = \sqrt{2E/\mu}$ and $dE/dv = \mu v$, the following result is reached:

$$\begin{aligned} \langle \sigma v \rangle_{AB} &= \int_0^\infty v f(v) \sigma(v) dv = \int_0^\infty v f(E) \sigma(E) dE \\ &= \sqrt{\frac{8}{\pi\mu}} \frac{1}{(kT)^{3/2}} \int_0^\infty E \sigma(E) e^{-E/kT} dE \end{aligned} \tag{3.6}$$

where the reaction rate depends upon the temperature T, center-of-mass energy E, reduced mass μ, and the cross section $\sigma(E)$, which itself differs between different reactions and is dependent upon the factors above.

For proton capture in a stellar environment, the reaction rate as noted here depends
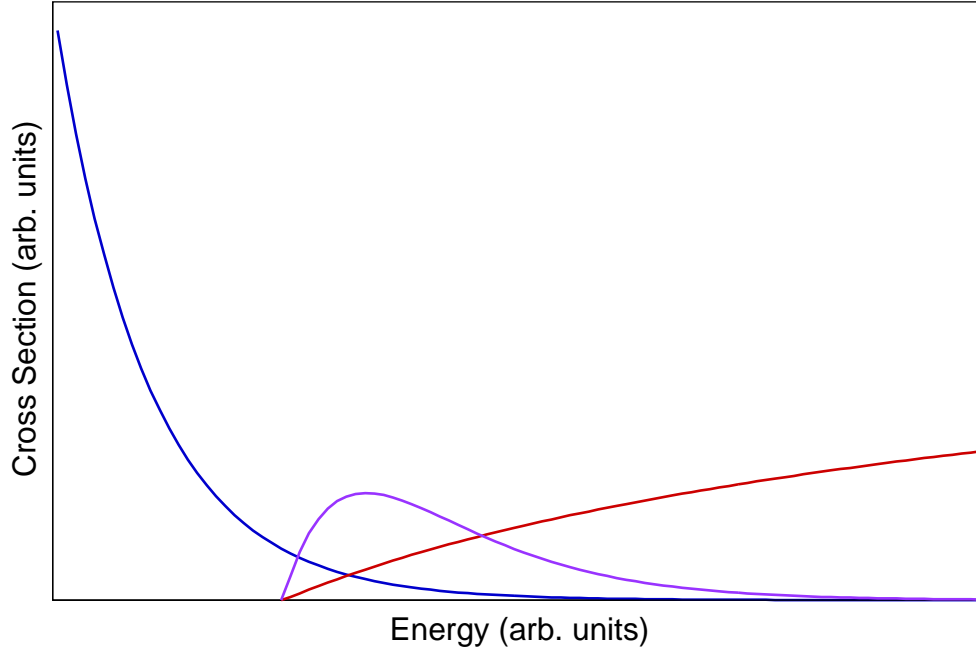
Figure 3.1: An abstract figure denoting the Gamow window and the Gamow peak for proton capture in a stellar environment. The blue line shows the Maxwell-Boltzmann energy distribution of the particle in the environment; that is, it shows the decreasing probability of finding a particle at a given energy as the energy increases. The red line shows the energy dependence of the penetrability; that is, it shows that the higher-energy the proton is, the more likely it is to approach near enough to the nucleus to interact. The purple line shows the combination of these two factors to create a region of increased reaction probability, the Gamow window. The purple line has been multiplied by a factor of 100 in this plot to illustrate the effect.

not only upon the Maxwell-Boltzmann exponential factor $e^{-E/kT}$ but, as above, the proton capture penetrability factor ($P_l(E) \propto e^{-1/\sqrt{E}}$, Equation 3.2). These two factors combined yield a distribution with a well-defined maximum (Fig. 3.1); this maximum is named the *Gamow peak*. The narrow area of increased reaction probability surrounding the Gamow peak is known as the *Gamow window*, and physically reflects both the fact that an increasingly energetic proton is increasingly more likely to penetrate the Coulomb barrier and the rapidly diminishing probability of the stellar environment producing such a proton as energy increases.

Thus, for experimenters wishing to measure the reaction rate directly, Equation 3.6 sug-

gests that it is necessary to measure the cross-section $\sigma(E)$ at energies ranging throughout the Gamow window in order to determine the thermonuclear rate. This can be difficult experimentally, but for certain reactions there is another consideration: the presence of *resonances*.

3.2 Direct and Resonant Capture Reactions

Equation 3.6 is a generalized reaction rate for particle capture as described in Chapter 1, effective for determining the *direct capture* reaction rate over the relevant energy region. For charged particle captures, this region is the Gamow window. Physically, a direct capture results when a nucleus ^{A}Z captures a proton into a bound state, simultaneously emitting a photon which carries away the energy difference between the initial state of the target nucleus ^{A}Z plus the proton and the bound state of the product nucleus $^{A+1}(Z+1)$ (Fig. 3.2).

However, in the event that the product nucleus has an excited state in the Gamow window, there will be a so-called *resonant capture* contribution to the reaction rate as well as the direct capture rate. In this case, the target nucleus and projectile proton have a center-of-mass energy E_r such that when they combine, they form the product nucleus in its excited state (Fig. 3.2). If this *resonance state* then undergoes gamma decay, the energy of the resulting photon reflects only the differences in energies between the resonance state and the state in the product nucleus to which the resonance decays. Because this state is unbound (i.e. it is above the *proton emission threshold*, the binding energy for the nucleus plus the proton), it may also re-emit the proton into the ground state of the target nucleus or one of its excited states. The relative probabilities for decay through various channels
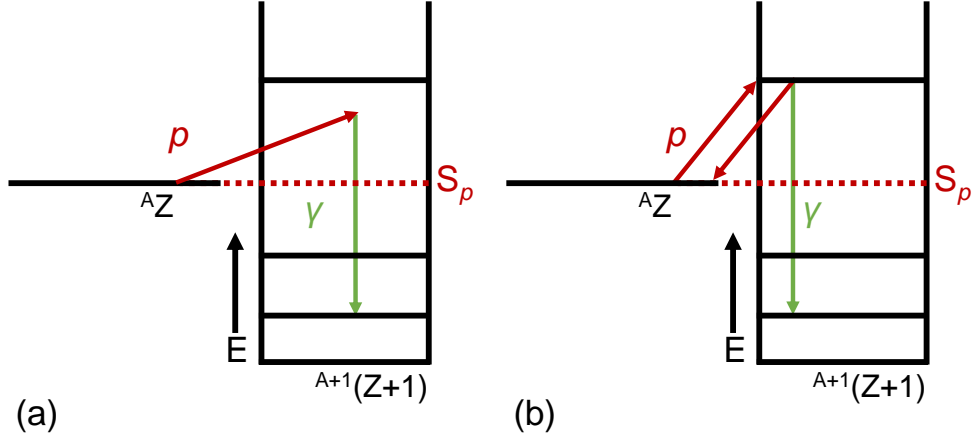
Figure 3.2: A simple figure showing (a) direct proton capture into a nucleus and (b) resonant capture into the same nucleus. In direct capture, the initial nucleus combines with a proton, then emits a gamma-ray into a lower bound state of the compound nucleus. The energy of the gamma-ray is only a function of the initial nucleus energy, the proton energy, and the final state energy. In resonant capture, the initial nucleus captures a proton into a higher, unbound state in the compound nucleus. That state may either re-emit the proton or emit a gamma-ray, deexciting into a lower state of the compound nucleus. In this case the energy of the gamma-ray is the energy difference between the resonance state and the lower state.

such as proton emission or gamma decay are given by the *partial widths* Γ_p, Γ_γ, or, for the general decay channel i, Γ_i.

Resonant capture is characterized by an extremely enhanced cross-section in a region peaking around the *resonance energy* E_r (the energy above the proton threshold) of the resonance state. This peak is described in part by its full width at half-maximum, Γ, the *total width* of the resonance. This total width Γ is equal to the sum of partial widths of all decay channels: $\Gamma = \Sigma_i \Gamma_i$. Depending upon the value of Γ, a resonance may be categorized as *broad* or *narrow*. The present discussion is limited, for the purposes of this work, to narrow resonances, where Γ is much less than few keV and the resonance width is such that the decay partial widths Γ_i do not vary with energy.

Because of the sharp peak in cross-section around the resonance energy, the formula for direct capture does not completely describe the energy dependence of the cross-section. The

resonant-capture cross-section for an isolated resonance involving two decay channels (e.g. proton emission and gamma decay) is described by the one-level Breit-Wigner formula:

$$\sigma(E) = \frac{\lambda}{4\pi} \frac{(2J+1)}{(2J_A+1)(2J_B+1)} \frac{\Gamma_1 \Gamma_2}{(E_r - E)^2 + \Gamma^2/4} \tag{3.7}$$

where J and E_r are the total spin and resonance energy of the resonance state, J_A and J_B are the spins of the projectile proton and target nucleus, and Γ_1, Γ_2, and Γ are the partial widths and total width, respectively. Deriving this Breit-Wigner description of narrow resonances is beyond the scope of this work, but an excellent review may be found in Ref. [3]. Using this cross section in the reaction rate calculation (Equation 3.6), the following result is obtained:

$$N_A \langle \sigma v \rangle = N_A \frac{\sqrt{2\pi} \hbar^2}{(\mu k T)^{3/2}} \omega \int_0^\infty \frac{\Gamma_1 \Gamma_2}{(E_r - E)^2 + \Gamma^2/4} e^{-E/kT} dE \tag{3.8}$$

where $\omega \equiv (2J+1)/[(2J_A+1)(2J_B+1)]$. As above, for a narrow resonance the partial widths Γ_i are constant over the total width of the resonance. In addition, the Maxwell-Boltzmann factor $e^{-E/kT}$ can be approximated as a constant, evaluated at E_r, allowing all three to be pulled out of the integral. The integral is then easily analytically calculated:

$$\begin{aligned}
N_A \langle \sigma v \rangle &= N_A \frac{\sqrt{2\pi} \hbar^2}{(\mu k T)^{3/2}} \omega \frac{\Gamma_1 \Gamma_2}{\Gamma/2} e^{-E_r/kT} \int_0^\infty \frac{\Gamma/2}{(E_r - E)^2 + \Gamma^2/4} dE \\
&= N_A \frac{\sqrt{2\pi} \hbar^2}{(\mu k T)^{3/2}} \omega \frac{\Gamma_1 \Gamma_2}{\Gamma/2} e^{-E_r/kT} \pi \\
&= N_A (\frac{2\pi}{\mu k T})^{3/2} \hbar^2 \omega \gamma e^{-E_r/kT}
\end{aligned} \tag{3.9}$$

where $\gamma \equiv \Gamma_1 \Gamma_2 / \Gamma$. The quantity $\omega \gamma$ is known as the *resonance strength*, and in practice the reaction rate for a narrow resonance depends *only* on this quantity and on the resonance

energy. This means that, unlike for the direct capture case where the cross section must be measured at a number of energies in order to determine its energy dependence, the reaction rate through a given resonance may be calculated from the measurement of only a few parameters: the spins of the projectile, target nucleus, and resonance state of the compound nucleus, and the partial widths of decay for each channel from the resonance state. In the case where one of the partial widths is much smaller than the other, $\Gamma_i \ll \Gamma_j$, $\gamma = \frac{\Gamma_i \Gamma_j}{\Gamma_i + \Gamma_j} \approx \Gamma_i$. When a number of narrow, isolated resonances contribute to the reaction cross-section, their contributions are simply summed:

$$N_A \langle \sigma v \rangle = N_A (\frac{2\pi}{\mu kT})^{3/2} \hbar^2 \sum_i (\omega\gamma)_i e^{-E_{ri}/kT} \tag{3.10}$$

Thus, for capture reactions where excited states of the product nucleus lie within the Gamow window, the resonant capture reaction rate dominates over the direct capture rate and determination of the various nuclear parameters involved in the resonance states becomes paramount to accurately describing the rate. Because these parameters are intrinsic to the states and not a function of temperature or external energy, they may be measured through a number of different techniques. In fact, because $^{30}\text{P}(p, \gamma)^{31}\text{S}$ is thought to be dominated by narrow, isolated resonances, study of these states offers a potentially fruitful means of constraining the rate. Some of the techniques that have been used to study the $^{30}\text{P}(p, \gamma)^{31}\text{S}$ reaction will be discussed in Chapter 4.

3.3   Reaction Rate: Theoretical Considerations

In the event that one or more of the parameters involved in a resonant capture reaction are unknown experimentally, theoretical estimations may be used to supplement existing

information. For proton capture reactions, Γ_γ may be estimated using, for example, the nuclear shell model, and Γ_p may be estimated using the following formula:

$$\Gamma_p = \frac{2\hbar}{R_n}\left(\frac{2E_r}{\mu}\right)^{1/2} P_l(E_r, R_n) C^2 S \theta_{\text{s.p.}}^2 \qquad (3.11)$$

where E_r is again the resonance energy, $R_n = 1.25(A_A^{1/3} + A_B^{1/3})$ fm is the interaction radius, $P_l(E_r, R_n)$ is the penetrability which itself can be calculated numerically by computing the regular and irregular Coulomb wave functions F_l and G_l respectively ($P_l = 1/[F_l^2 + G_l^2]$) [37], C is a Clebsh-Gordan coefficient, S is the single-particle spectroscopic factor, and $\theta_{\text{s.p.}}^2$ is the single-particle reduced width. The factor $\theta_{\text{s.p.}}^2$ contains information regarding the nuclear structure of the compound level and depends upon the interaction radius R_n, orbital angular momentum l, and number of nodes n in the single-particle radial wave function $\phi_l(R_n)$:

$$\theta_{\text{s.p.}}^2 = \frac{R_n}{2}\phi_l^2(R_n) \qquad (3.12)$$

This estimation of Γ_p may be used in place of an experimentally-measured partial width, particularly at energies close to the proton emission threshold where the energy of the incoming proton is low and the proton partial width is thus much lower than the gamma-decay partial width, $\Gamma_p \ll \Gamma_\gamma$. In this case the total width Γ may also be approximated $\Gamma \approx \Gamma_p$, as above.

3.3.1 The Hauser-Feshbach Statistical Model

Unsurprisingly, only a small subset of the vast number of nuclear reactions relevant to the numerous stellar burning processes have been measured experimentally. In cases where no

experimental parameters have been measured, it is possible to estimate the reaction rate using the *Hauser-Feshbach* statistical model [27]. Derivation of the model formalism is beyond the scope of this work, but briefly, the model assumes there is a high level density in the compound nucleus and that consequently there is a large number of resonance states through which the reaction can proceed. It then calculates a cross-section through each of these resonances using the level density and other input parameters such as the transmission coeffecient and averages over the energy region, providing a statistical estimate of the reaction cross section in the region of interest. Hauser-Feshbach calculations for proton capture reactions are typically reliable within a factor of $\approx 2-3$ – but only if the level density of the compound nucleus is large enough in the region of interest [3]. In cases where the level density is relatively low, Hauser-Feshbach may provide an unreliable estimate of the cross-section and thus the reaction rate. $^{30}\text{P}(p,\gamma)^{31}\text{S}$ is expected to to be at the edge of applicability for the Hauser-Feshbach rate because the density of states in the Gamow window is relatively low.

3.4 The Nuclear Shell Model

Analogous to the model for electrons in atomic orbitals, it is possible to model the energy states of a given nucleus by taking into account the fact that protons and neutrons are both fermions which obey the Pauli exclusion principle. The shell model treats the nuclear potential according to the *Woods-Saxon potential* (Figure 3.3) with an additional interaction coupling the nucleon spin to its orbital angular momentum. Protons and neutrons independently fill orbitals, with certain "magic numbers" of nucleons corresponding to increased stability according to the closure of "shells" of nuclear orbitals with quantum numbers n (the
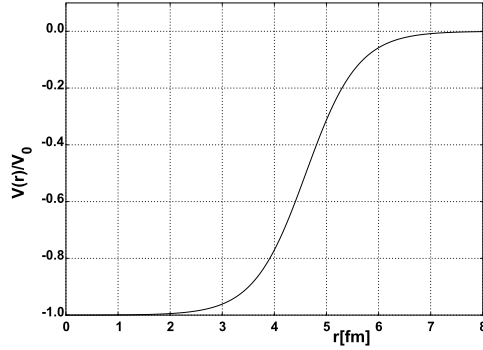
Figure 3.3: The Woods-Saxon potential commonly used to model the nuclear force. The form of the potential is: $V(r) = -V_o/[1 + \exp(r - R/a)]$ where V_o is the potential depth, $R = 1.25A^{1/3}$fm (A the mass number), and a represents the "surface thickness" of the nucleus.

number of nodes in the wave function), l (the orbital angular momentum), and j (the total angular momentum), typically using the notation nl_j to denote the combination of quantum numbers that defines the state. The $1s$ orbital has $l = 0$, for example, and can thus hold only **two** nucleons (spin-up and spin-down; that is, total $j = 1/2$ and $j_z = \pm 1/2$), the $1p$ orbital with $l = 1$ can hold **six** nucleons, two in the $1p_{1/2}$ orbital ($j = 1/2, j_z = \pm 1/2$) and four in $1p_{3/2}$ ($j = 3/2, j_z = \pm 3/2, \pm 1/2$).

The "magic numbers" can thus be derived from the total number of nucleons contained at the shell closures: 2 ($1s$, closing the s-shell), 8 ($1s+1p$, closing the p-shell), 20 ($1s+1p+1d+2s$ closing the sd-shell), etc. Unlike the atomic shell model, the nuclear shells do not strictly correspond to a particular quantum number and instead represent only places where the binding energy of the nucleus has large gaps between orbitals, hence examples such as the sd-shell, which includes the $1d_{5/2}, 2s$, and $1d_{3/2}$ orbitals. A graphical representation of the shell model and its comparison to the harmonic oscillator is shown in Figure 3.4.

By accounting for these considerations, the shell model can be used to predict the spin and parity of the ground state of a given nucleus. For example, ^{30}P, with 15 protons and 15 neutrons, fills the $1s$, $1p$, and $1d$ orbitals for both protons and neutrons, with one proton
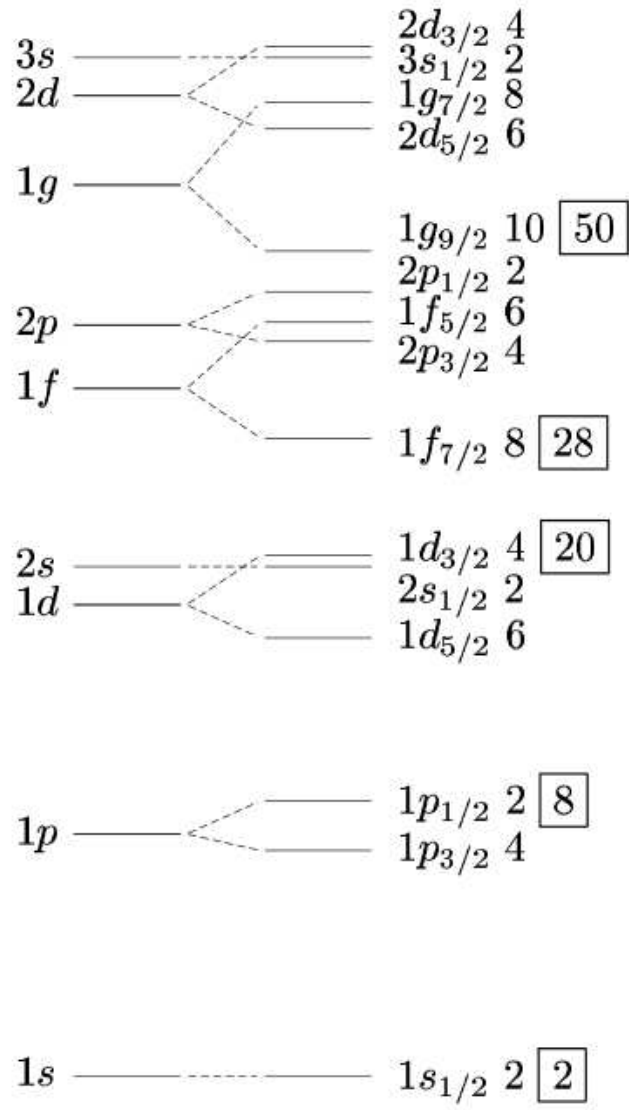
Figure 3.4: Comparison of the energy levels of the nucleus using the simple harmonic oscillator potential (left) and using the full shell model (right). As shown, the spin-orbit interaction splits the harmonic oscillator levels, and the large gaps in binding energy that cause the shells do not necessarily correspond to the gaps between harmonic oscillator levels. Figure credit: Bakken (GPL).

and one neutron each in their respective $2s$ orbital. The nucleus can here be thought of as an inert *core* of 14 protons and 14 neutrons (that is, an inert ^{28}Si core) with total angular momentum $j = 0$, because it completes the $1d_{5/2}$ orbital, and two extra *valence* nucleons, each with $j = 1/2$. The two extra nucleons sum to a total $j = 1$. Because the two nucleons are in an orbital with $l = 0$, the parity is positive and the shell model correctly predicts a spin and parity of the ^{30}P ground state of $J^\pi = 1^+$.

In principle, the shell model can also be used to predict the energies, spins, and parities of excited states in the nucleus. However, although the ground state spin and parity can be inferred from the spins and parities of individual nucleons, this is not necessarily true for excited states. This is due to the *collectivity* of the nucleus, or the tendency of many nucleons to be simultaneously involved in nuclear excitations. As with the calculation for the ^{30}P ground state, it is customary for shell model calculations to treat a given nucleus as an inert core with one or more valence nucleons, limiting the *valence space* of the calculation to a few orbitals above the closed core to reduce calculation costs. Because the calculation for the nucleus's structure is arbitrarily truncated at some point, the calculation must use a so-called *effective interaction,* which accounts for the truncation in the Hamiltonian used for the calculation.

One very commonly-used Hamiltonian is the "Universal sd-shell" (USD) interaction [38]. The USD models USDA and USDB produce two-body effective Hamiltonian matrix elements meant to treat the interaction between nucleons in the sd-shell space. These matrix elements are in part derived from a fit of experimentally-known energy levels on nuclei in the mass region from ^{17}O to ^{39}K, and can be used in calculations to not only predict the energies, spins, and parities of nuclear states in a given sd-shell nucleus, but probabilities for electromagnetic transitions between states (e.g. $B(E_n)$, where n is the order of the electric transition) as

well as transition probabilities for beta decay (a more thorough discussion about beta-decay strengths follows in Section 3.5.1).

For the calculation of astrophysical reaction rates, in the case when energy levels for a given nucleus, gamma-decay branches for those levels, and beta-decay probabilities to those levels from a parent nucleus can be calculated, measurements may be compared to theory in order to constrain the spin and parity of observed states. In cases where parameters such as Γ_p are needed to calculate a resonance strength of the level, quasi-theoretical Γ_p values based on observed energies and calculated nuclear structure components may be used to give a meaningful estimate of the resonance strength and, hence, the reaction rate, with reduced theoretical uncertainties when compared with the Hauser-Feshbach statistical model.

3.5   Mirror Nuclei and the Concept of Isospin

Another tool useful for determining the spin and parity of nuclear states is the existence of *mirror nuclei*, nuclei with identical mass number A but conjugate proton number Z and neutron number N. In principle, the nuclear structure of mirror nuclei should match closely: as shown in Figure 3.5, for example, the energies of excited states in ^{13}C and ^{13}N are very similar, and the spins and parities of the states are identical. Thus, if parameters such as spin and parity are know precisely in a given nucleus, that information can be used to help constrain matching states in the mirror nucleus – assuming that the states' mirror assignment can be made accurately.

The usefulness of mirror nuclei is a consequence of the *isospin* model, a concept introduced by Werner Heisenberg in 1932 [39]. Because the nuclear force is charge-independent and the masses of the proton and neutron are nearly the same, it is possible to treat them not as
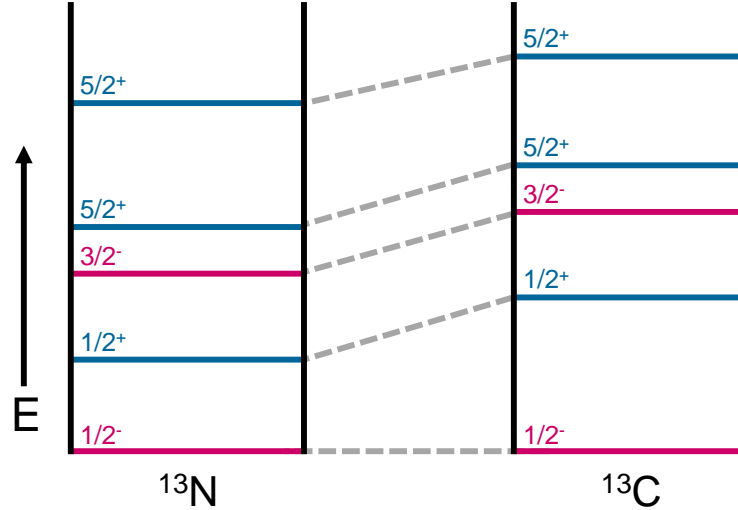
Figure 3.5: Comparison of the first five energy levels of ^{13}N and ^{13}C. The ground-state energies of the two levels have been adjusted to be equal, and the relative heights of the states in each nucleus represent the relative excitation energies of those states. The spins and parities of the states are also shown, and color is given to denote positive or negative parity states. The relative spacing of levels in a given nucleus is not to scale as this figure's purpose is simply to show the mirror symmetry between these two nuclei.

individual particles, but as projections in a so-called *isospin doublet* of a single particle, the nucleon. This particle has both spin $j = 1/2$ and *isospin* $T = 1/2$, with projections $T_z = +1/2$ for neutrons and $T_z = -1/2$ for protons. In this way, a given nucleus can be seen to have total isospin projection $T_z = (N - Z)/2$ [1]. However, each state of a given nucleus, although sharing the same projection, does not necessarily carry the same total isospin T.

The mathematical formalism for isospin is very similar to that for standard angular momentum. For example, a state with a given total isospin T can have any of the $2T + 1$ projections $-T < Tz < T$. In the case of ^{13}C and ^{13}N as shown in Figure 3.5, the similarities between the level schemes can thus be interpreted as the observation of isospin states with the same isospin across nuclei but with different isospin projections. In the most basic example of this case, the ground states of the two nuclei can be interpreted as the $T_z = +1/2$ (^{13}C)

[1]This is the convention for nuclear physics. The convention differs from the original conception of the proton as a $T_z = +1/2$ particle and the modern convention in particle physics. This convention was chosen so that the more numerous neutron-rich nuclei have positive isospin projection
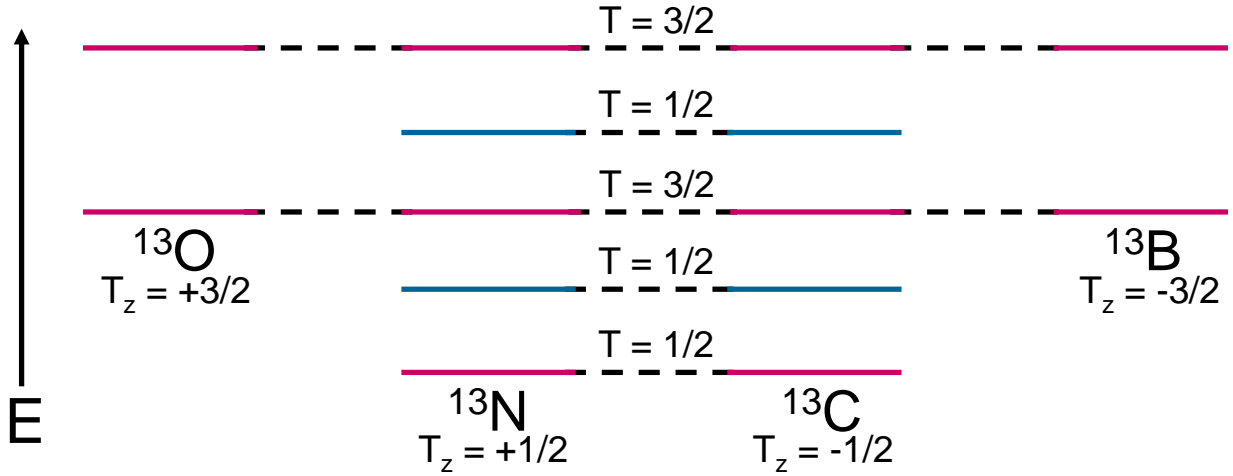
Figure 3.6: A simple graphical depiction of $T = 1/2$ isobaric doublets in ^{13}C and ^{13}N and $T = 3/2$ isobaric quartets in ^{13}B, ^{13}C, ^{13}N, and ^{13}O. Here the energy levels have been equalized to demonstrate the manifestation of perfect isospin symmetry more clearly. As shown, the ground states and multiple excited states in ^{13}N and ^{13}C make up the $T_z = +1/2$ and $T_z = -1/2$ members of the first two $T = 1/2$ doublets, and certain excited states of ^{13}N and ^{13}C comprise the $T_z = +1/2$ and $T_z = -1/2$ members of the $T = 3/2$ quartets completed by analogous $T_z = +3/2$ and $T_z = -3/2$ states in ^{13}O and ^{13}B, respectively. The spacing between levels is arbitrary and is meant only to show the symmetry of the isobaric analog states.

and $T_z = -1/2$ (^{13}N) members of a $T = 1/2$ doublet. In general, states in these nuclei will share the isospin of the ground state. However, certain higher energy states, such as those analogous to the ground states of ^{13}B ($T_z = +3/2$) and ^{13}O ($T_z = -3/2$), will have isospin corresponding to their own multiplet (e.g., members of a $T = 3/2$ quartet). These states can be seen as members of an isospin multiplet, as shown in Figure 3.6. Generally, states with similar wave functions that share an isospin value across nuclei are known as *isobaric analog states* (IAS) of one another; these states share the same spin and parity as well, allowing for the mirror symmetry described above.

3.5.1   Isospin and Beta Decay

Since both the proton and neutron carry their isospin and unique isospin projection, any process that affects the number of nucleons in a nucleus, for example beta decay, changes at the very least the projection T_z, and usually the isospin T as well. In the case of beta decay, the nucleon numbers N and Z change but the total mass A remains constant. This changes the isospin projection $\Delta T_z = \pm 1$; that is, a nucleon flips its isospin projection. Beta decay proceeds through two couplings of the weak interaction, the vector (V) and axial-vector (A) components, with decay rate from initial nuclear state to final nuclear state given by the equation:

$$W_{i,f} = (f/K_o)[g_V^2 B_{i,f}(F_\pm) + g_A^2 B_{i,f}(GT_\pm)] \tag{3.13}$$

where f is a dimensionless constant that depends on the Q-value of the decay, $K_o = 1.8844 \cdot 10^{-94}$ erg^2 cm^6 s, g_V and g_A are the coupling constants for the vector and axial-vector decays, and $B(F)$ and $B(GT)$ are the transition strengths for the vector channel ("Fermi Decay") and axial-vector channel ("Gamow-Teller Decay"), with $\pm$ denoting β^+ and β^- decay. The operators of the Fermi and Gamow-Teller transitions are $\mathcal{O}(F_\pm) = \Sigma_i t_{\pm i}$ and $\mathcal{O}(GT\pm) = \Sigma_i \sigma_i t_{\pm i}$, where i is the summing index over all nucleons in the nucleus, $t_\pm$ is the raising/lowering ladder operator that changes the isospin projection T_z by one, and σ is the nucleon spin operator. In the case of the Fermi operator it can be seen that the eigenvalue of the operator acting on a state is given by:

$$t_\pm \left|T, T_z\right\rangle = \sqrt{T(T+1) - T_z(T_z+1)} \left|T, T_z \pm 1\right\rangle ; \tag{3.14}$$

the Fermi strength B(F) is simply given by:

$$B(F) = | \langle T_f, T_{zf} | t_{\pm} | T_i, T_{zi} \rangle |^2 = (T(T+1) - T_{zf}(T_{zf}+1)) \delta_{T_f T_i} \delta_{T_{zf} T_{zi} \pm 1}, \qquad (3.15)$$

allowing for quick calculation of the expected Fermi strength of a given beta decay transition based on the isospin and isospin projection of the initial state.

3.5.2 Selection Rules

From these operators it can be seen that the Fermi transition moves only between spin projections T_z of isospin multiplet members without changing the total isospin T. This results in a beta decay selection rule: Fermi transitions are those exclusively between a ground state and its isobaric analog state: $\Delta T_z = 1, \Delta T = 0, \Delta J = 0$. Because of the addition of the spin operator, the selection rules for Gamow-Teller transitions are less stringent: $\Delta T_z = 1, \Delta T = 0, \pm 1, \Delta J = 0, \pm 1 (J = 0 \nrightarrow J = 0)$. The Fermi transition can be thought of as proceeding between two states within the same isospin multiplet, while the Gamow-Teller transition can be thought of as proceeding between two states from different multiplets (which may or may not share the same isospin).

Because the strength of the Fermi transition is concentrated into a single state (the IAS), Fermi transitions generally proceed at an increased rate compared to Gamow-Teller transitions. The Gamow-Teller transition strength, by comparison, is usually fragmented between many final states. Fermi and Gamow-Teller transitions are labeled "allowed" transitions ($J = 0 \rightarrow J = 0$ decays with $\Delta T = 0$ are *pure* Fermi transitions and are labeled "superallowed"). Transitions not allowed by these selection rules (e.g., $\Delta J = 2$) are labeled as "forbidden" – that is, the matrix element of the transition is zero and they are theoretically

prohibited from happening. In reality these transitions do proceed, but at a greatly reduced rate.

As shown here, both spin and isospin selection rules play a part in constraining which final states are populated in a nuclear process. For example, in proton capture onto ^{30}P, the $T = 1/2$ proton couples to the $T = 0$ ^{30}P ground state. This means that only ^{31}S states with $T = 1/2$ are populated. Conversely, for the beta decay of the $T = 3/2$ ^{31}Cl ground state to ^{31}S, there is a strong transition to the $T = 3/2$ IAS. Unfortunately, even though this state is populated via the Fermi transition, making its spin and parity precisely known $(J^\pi = 3/2^+)$ it is not expected to be populated at all in the ^{30}P$(p, \gamma)^{31}$S proton capture, if isospin is a good quantum number.

3.5.3 The Isobaric Multiplet Mass Equation

So far, we have discussed isospin as though it were a perfect symmetry, and the nucleons as though their charges were irrelevant. If this were truly the case, isobaric analog states between nuclei would all share the same mass excess Δ [2], as shown in Fig. 3.6. The fact that they do not (as shown in Figure 3.5, for example) is due to the charge of the proton. Because the Coulomb force acts only on protons, the energy value of multiplet member states is perturbed systematically across the multiplet according to the proton number Z. This shift can be treated with first-order perturbation theory: the *isobaric multiplet mass equation* (IMME), first proposed by Wigner [40, 41], predicts that isobaric analog states within a multiplet of given T have mass excesses related to one another according to their

---

[2]Mass excess is the difference between the mass of a nucleus and the mass of its constituent nucleons, $M(Z, A) - A \cdot m_u$. For an excited state, the mass excess is this (negative) value plus the (positive) excitation energy E_x of the state.

isospin projection:

$$\Delta(T_z) = a + bT_z + cT_z^2 \qquad (3.16)$$

where a, b, and c are coefficients that can be calculated from the theory or obtained by fitting the measured mass excesses of the multiplet member states with a quadratic function. If the mass excesses of enough multiplet members are known (for example, for three members of an isospin quartet), the IMME can be used to predict the mass excesses of the unobserved member states. If the ground state mass excess of the nucleus of such a state is known precisely, a predicted excitation energy E_x can be calculated as well. The IMME has historically been very successful, only failing in a few known cases [42, 43, 44, 45]. Reasons for the breakdown of the IMME could include: the presence of many-body charge-dependent forces [46]; a failure on the part of the perturbation theory, indicating a need for higher-order terms; inaccurate measurements; or *isospin mixing* of the multiplet member with a nearby state of a different isospin [47].

3.5.4   Isospin Mixing

The perturbative effects of the Coulomb force can be thought of as the result of two factors: the relative range difference between the nuclear force and the Coulomb force (i.e., the former only acts between closely neighboring nucleons while the latter acts over the whole nucleus) and the relative strengths of the interactions as mass increases (i.e., the former increases, to first order, linearly with nucleon number, while the latter increases $\sim Z^2$) [48]. Thus, for increasingly heavy nuclei, the Coulomb interaction may have a greater effect on the viability of isospin as a good quantum number.

Along with the perturbation of isobaric analog state mass excesses described above, the Coulomb interaction can result to some degree in the *mixing* of states with differing isospins. In this case, the Hamiltonian matrix for the interactions involving these states contains off-diagonal elements corresponding to an isospin interaction between them. For a simple two-level model with states $|1\rangle = |J_1T_1\rangle$ and $|2\rangle = |J_2T_2\rangle$,

$$H = \begin{pmatrix} H_{11} & H_{12} \\ H_{21} & H_{22} \end{pmatrix}$$

where H_{11} and H_{22} include the contributions to the Hamiltonian from nuclear interactions and the off-diagonal elements H_{12} and H_{21} contain the isospin-mixing terms. Because the Coulomb force is rotationally and time-reversal invariant, the matrix is real and symmetric, with $H_{12} = H_{21} = V\delta_{J_1J_2}$, where V is the mixing strength and the $\delta_{J_1J_2}$ denotes the fact that only isospin-mixing terms affect the off-diagonal elements due to the rotational invariance. Now, instead of $|J_1T_1\rangle$ and $|J_2T_2\rangle$ being isospin eigenstates of the Hamiltonian, they form the basis for new eigenstates (with $J_1 = J_2 = J$):

$$|\psi_1\rangle = \cos\theta|JT_1\rangle + \sin\theta|JT_2\rangle \tag{3.17}$$

$$|\psi_2\rangle = -\sin\theta|JT_1\rangle + \cos\theta|JT_2\rangle \tag{3.18}$$

where the *mixing angle* θ is given by $\tan 2\theta = \dfrac{2V}{D}$, where D is the energy difference between the original states. From this expression, it can be seen that only states whose energies are near each other (that is, D is small) will mix non-negligibly. This two-state mixing system follows the standard two-state mixing formalism for quantum mechanics: the

levels are perturbed in energy according to their unperturbed spacing D and the mixing matrix element V according to the equations

$$E = \sqrt{D^2 + 4V^2} \tag{3.19}$$

$$E = D + 2\delta \tag{3.20}$$

where E is the observed (perturbed) energy difference between the states, D is again the unperturbed energy, V is the mixing matrix element, and δ is the perturbation.

In the case when one of the mixed states is an isobaric analog state populated by a Fermi transition, the mixing angle can be calculated experimentally from the determination of the observed Fermi strengths to the two mixed states:

$$R = \tan\theta = \sqrt{\frac{B_2}{B_1}} \tag{3.21}$$

where B_2 and B_1 are the strengths of the transitions to the second and first state listed in Equations 3.17 and 3.18, respectively. The unperturbed mixing matrix element V and unperturbed energy spacing D may then be calculated purely from quantities based on observables:

$$D = E\frac{1 - R^2}{1 + R^2} \tag{3.22}$$

$$V = E\frac{R}{1 + R^2}. \tag{3.23}$$

In this case (mixing between an IAS and a nearby state), the Fermi transition constrains the spin and parity of the IAS, which in turn constrains the spin and parity of the mixed state. Thus, observation of isospin mixing between an IAS and a nearby nuclear state in an energy region where the spins and parities of states are poorly constrained could provide a constraint on the spin and parity – properties of that state relevant for calculating the resonance strength of a reaction.

Chapter 4

Experimental Considerations and NSCL Experiment 12028

As mentioned in Section 2.1.2, the $^{30}\mathrm{P}(p,\gamma)^{31}\mathrm{S}$ reaction is critical to answering a number of astrophysical questions, but its rate is so poorly experimentally constrained that until 2007 the adopted rate was based on the statistical Hauser-Feshbach calculation. However, the Hauser-Feshbach model calculates the rate based on an assumed high density of states, which is typically only valid at mass numbers and/or energies higher than the Gamow window for this reaction. In addition, the model does not take into account individual low-energy resonances, which as previously discussed are likely to dominate the rate at nova temperatures. Thus, experimental measurement of the resonance states in the energy region directly above the proton threshold is of key importance for moving toward an accurate calculation of the rate.

Ideally, the properties of the resonances involved in this reaction would be measured directly. In principle, proton capture reactions may be measured in nuclear physics facilities either by accelerating a hydrogen beam and impinging it upon a heavy target ("regular kinematics") or the reverse, accelerating a beam of the target nucleus and impinging it upon a hydrogen target ("inverse kinematics"). Since $^{30}\mathrm{P}$ has a half-life of just 2.5 minutes, maintaining a target long enough to perform a direct measurement using a hydrogen beam

with sufficient statistics is unfeasible, leaving the reverse-kinematics method the only feasible means of studying the reaction directly.

There are two major currently-used methods of producing a radioactive beams for direct study of the ^{30}P$(p, \gamma)^{31}$S reaction by inverse kinematics. *Fragmentation* involves producing a beam of a readily-available stable isotope, accelerating it to high energies (the exact energy depends upon the accelerator used and the charge-to-mass ratio of the nucleus in question – for example, the coupled cyclotron facility at the National Superconducting Cyclotron laboratory typically accelerates stable ions to between 80 MeV/u [1] and 170 MeV/u), and impinging it upon a thin, light target. This so-called *primary beam* is fragmented to produce a number of lighter constituent pieces, including the desired short-lived nucleus. The resulting "cocktail" beam of various isotope species can then be filtered using magnetic fields to produce a purer *secondary beam* of the desired isotope for study. The fragmentation technique can allow for relatively high rates of production, but because the beam is accelerated to very high energies *before* production of the desired isotope, it is difficult to study low-lying resonances directly without slowing the beam down to stellar energies.

The "Isotope Separation On-Line" (ISOL) technique involves the acceleration of a beam of light, stable nuclei, which bombards a target to produce radioactive isotopes. The choice of both stable beam and production target affects which type of isotopes are produced, and the desired isotopes must also be extracted from the target; these low-energy isotopes are then ionized at a source and separated by mass to produce a pure beam of low energy ions. These ions are accelerated and delivered to the experimental setup. Unlike fragmentation, these ions can be accelerated to a variable desired energy and at a much better purity, allowing for more straightforward direct study of capture reactions such as ^{30}P$(p, \gamma)^{31}$S. The

---

[1]that is, MeV per nucleon

ISOL technique is notable in that it can produce relatively pure beams when compared to fragmentation, since the mass separation occurs before acceleration. However, the intensity of the beam is dependent upon a number of chemistry-related factors that may make it difficult for certain species of interest to leave the target, meaning that not every isotope that is desired for study is practical to produce via this technique.

Unfortunately, both of these methods are inefficient at producing ^{30}P for direct study of ^{30}P$(p,\gamma)^{31}$S. ISOL does not produce a sufficiently intense beam because phosphorus is a "refractory" element, and even using techniques such as gas stopping of beams and reacceleration, fragmentation facilities are currently unable to produce a beam with high enough intensity and low enough energy to populate the relevant resonance states. Because of this, a number of *indirect methods* have been employed to populate these important states and measure their properties. Because the properties (spin, parity, resonance energy, total and partial widths) of the nuclear states involved in the reaction are independent of the reaction mechanism, and because for resonant capture the cross-section is entirely dependent upon these parameters, populating them indirectly and measuring their decay [2] can provide constraints on the parameters that constrain the reaction rate.

Indeed, a number of indirect methods have provided a considerable amount of information on the states potentially involved in the ^{30}P$(p,\gamma)^{31}$S reaction. Both the diverse and ingenuitive techniques used to study ^{31}S as well as the experiments performed themselves are worth discussing briefly.

---

[2]This method of measuring these states is contingent upon the so-called *Bohr independence hypothesis*, or *amnesia assumption*, the assumption that the mode of decay of a compound nucleus is independent of its mode of formation. This hypothesis is based on the notion that the lifetime of the compound system is much longer than the timescale for formation and decay (that is, at least several times the time it takes for a nucleon to traverse the nucleus), and that the compound nucleus therefore "forgets" all "memories" except those pertaining to conservation laws. For higher energies, where resonances overlap, this assumption has been shown to be invalid. See Refs. [49, 50, 51, 52] for discussion and relevant experiments.

4.1 Techniques for Indirect Study of $^{30}\mathbf{P}(p, \gamma)^{31}\mathbf{S}$

4.1.1 Single-Nucleon Transfer Reactions

Single-nucleon transfer studies of $^{30}\mathrm{P}(p,\gamma)^{31}\mathrm{S}$ involve populating excited states of $^{31}\mathrm{S}$ by impinging a fast, light projectile such as p, d or $^3\mathrm{He}$ onto a heavy transmission target of a stable nucleus with a mass number one less than or one greater than 31. The light projectile gains one nucleon from or loses one nucleon to the target, gaining or losing energy as well in the process. The transformed projectile (ejectile) then continues on its way and can be analyzed either using silicon detectors that record its energy or by using a spectrograph, where its kinetic energy is measured in terms of its rigidity in a magnetic field. The resulting spectrum will show peaks at various energies, which correlate to the energy transferred between the reactants to create the compound nucleus and, hence, the excitation energies of the levels populated.

In principle, this measurement may be made at a number of azimuthal angles and the relative intensities of the peaks of any excited state may be compared to determine the orbital angular momentum l of the projectile and consequently the populated state, but in order to confidently determine the total spin and parity J^{π} of the state, it is usually necessary to calculate a theoretical angular distribution for the ejectile, assuming the allowed J^{π} values for the state based on the triangle rule for angular momentum, and compare to experiment. Because the initial spin of the target and projectile are both known, it is also possible to compare results to shell model calculations of excitation energies and J^{π} values and infer the spins and parities of the resonance states.

4.1.2   In-Beam Gamma-Ray Spectroscopy

By definition, "gamma-ray spectroscopy" refers to any experimental procedure that involves the accumulation and analysis of an energy histogram of gamma-rays. In-beam gamma-ray spectroscopy experimental studies of ^{31}S involve production of the ^{31}S nucleus in an excited state, which then emits a gamma-ray in de-excitation. The production target is surrounded by one or more gamma-ray detectors, which measure the de-excitation of the ^{31}S and allow for the creation of a gamma spectrum, from which resonance energies can be determined. These may be used to create a gamma-decay scheme with gamma *branches* for each excited state – the scheme can be compared with, for example, the nuclear shell model, facilitating the inference of parameters like the spins and parities of states potentially relevant to the ^{30}P$(p,\gamma)^{31}$S reaction.

4.1.3   Charge-Exchange Reactions

The execution of charge-exchange reaction experiments is somewhat similar to that for single-nulceon transfer: impinge a light, fast projectile onto a stable target, produce the desired compound nucleus and measure the energy of the ejectile to learn about the energy and/or spin of the resonance state populated in the exchange. However, the interaction mechanism is different: the projectile nucleus approaches close enough to the target nucleus such that it falls within the potential well of the nuclear force. The two nuclei interact, resulting in a single nucleon in each nucleus flipping its isospin projection T_z: the result is that a proton in the projectile transforms into a neutron while a neutron in the target transforms into a proton, or vice versa.

The mass number A of both nuclei remains the same while their proton numbers Z

increase or decrease by one such that the total Z of both nuclei remains constant. The change in T_z may also be accompanied by a change in isosopin $\Delta T = 0, \pm 1$, as well as a nuclear spin change $\Delta S = 0, \pm 1$, and any transfer of orbital angular momentum Δl (in this case the parity of the state may also change according to the rule: $\pi = (-1)^l$). In the case where no orbital angular momentum is transfered, total angular momentum J changes only by 0 or 1; charge-exchange reactions can here be seen to obey the selection rules mentioned in Section 3.5.1 for Fermi ($\Delta T = 0$) and Gamow-Teller ($\Delta T = 1$) transitions. Along with these selection rules, the angular distribution of the ejectile may be used to constrain the spin and possibly parity of the resonance states populated in the exchange.

4.1.4 Beta Decay

As mentioned in 1, beta decay involves the transformation of a single nucleon within the nucleus: either a neutron to a proton (β^-), or vice-versa (β^+). Similar to charge exchange, beta decay changes the mass and proton numbers (A, Z) of a nucleus to $(A, Z \pm 1)$. Unlike charge-exchange interactions, however, only a single nucleus is involved and the transition is mediated by the weak interaction. The electron/positron emission conserves the charge of the decay, while the simultaneous emission of an electron antineutrino/neutrino conserves the lepton number. As mentioned in Section 3.5.1, beta decay also follows the selection rules for Fermi and Gamow-Teller transitions.

The emission of the two spin-1/2 particles means that, as with charge-exchange reactions, spin may change between the parent and daughter nucleus, $\Delta S = 0, \pm 1$; however, transitions with greater total momentum change ΔJ than this are strongly suppressed ("forbidden," a term denoting that they are not allowed within the usual mathematical formalism used to describe the transition – although they are obviously not forbidden in reality) since there

is no incoming nucleus that may transfer orbital angular momentum. This means that the parity of the final state is, for "allowed" transitions, identical to that of the initial state. Thus, beta-decay experiments are useful in cases where strong constraints on the spins and parities are desired.

4.2 Previous Studies of ^{30}P$(p, \gamma)^{31}$S

It should be noted that no single method mentioned above has been exclusively used to obtain information about the ^{30}P$(p, \gamma)^{31}$S reaction. In many cases, due to the natures of the experimental methods, constraints on the resonance states are not perfectly unambiguous. The Gamow window for ^{30}P$(p, \gamma)^{31}$S at nova temperatures extends about 600 keV above the ^{31}S proton threshold at 6130 keV, so the number of resonance states in that region, as well as their properties, is of key importance for constraining the ^{30}P$(p, \gamma)^{31}$S rate. Presented here is a brief overview of the history of ^{30}P$(p, \gamma)^{31}$S studies which have been used to piece together the current understanding of the ^{31}S resonances in the energy region of interest.

In 1999, Vernotte *et al.* [53] published work on their use of the single-proton and single-neutron transfer reactions on ^{32}S, ^{32}S$(^3$He,$\alpha)^{31}$S and ^{32}S$(d,^3$He$)^{31}$P, to populate levels with excitation energy $E_x \leq 8$ MeV in both ^{31}S and its mirror nucleus ^{31}P. 31 ^{31}S levels and 41 ^{31}P levels were observed. The measured excitation energies and l values were compared not only with shell model calculations but with each other, with the goal to produce an identification of positive-parity states in ^{31}S using both the mirror nucleus and the *sd* shell model. While this experiment was not motivated by astrophysics, it provided a model for two future transfer reactions intended to probe the ^{30}P$(p, \gamma)^{31}$S reaction for nova studies [54, 55].

It was not until seven years after the publication of Vernotte *et al.* that work was published following up on the astrophysical motivations for study of ^{31}S. Kankainen *et al.* published the results of a beta-decay study of ^{31}Cl [56], which populates ^{31}S resonances in its decay. The experiment measured both the beta-delayed proton emission and beta-delayed gamma decay of states above the proton threshold. Multiple useful results were obtained, including the discovery of a state then evaluated at 6921(15) keV through measurement of proton emissions, gamma rays corresponding to de-excitation of the first two excited ^{31}S states, and the first definitive identification of the ^{31}S isobaric analog state through measurement of its gamma decay.

Jenkins *et al.* performed a measurement of both the ^{12}C(^{20}Ne,$n\gamma$)^{31}S and ^{12}C(^{20}Ne,$p\gamma$)^{31}P reactions, motivated both by considerations of the structural differences between the two mirror nuclei [57] and by considerations of the ^{30}P(p, γ)^{31}S rate [58]. The authors observed several proton-unbound states in ^{31}S and, through analysis of gamma-ray angular distributions and comparison with mirror states in ^{31}P, inferred their spins and parities. Although this method preferentially populated high-spin states, which are less important for the ^{30}P(p, γ)^{31}S reaction due to the heightened centrifugal barrier, the study used this fact to constrain which other resonances were actually important for the reaction rate and concluded that two specific resonances at $E_x = 6257$ keV and 6350 keV dominate the ^{30}P(p, γ)^{31}S rate at temperatures below $T = 0.2$ GK and that an additional two resonances at $E_x = 6543$ and 6593 keV dominate the rate at peak nova temperatures above 0.2 GK – despite not even observing these states.

Ma *et al.* published in 2007 results of a measurement of the ^{32}S(p, d)^{31}S transfer reaction [54], which obtained angular and energy distributions of deuterons and used comparisons to theory to deduce spectroscopic information for ^{31}S levels within 1 MeV of the proton emission

threshold. Because the initial nucleus ^{32}S has a spin and parity $J^\pi = 0^+$, the authors were able to use $l = 0$ transfers to unambiguously confirm the existence of the ^{31}S $J^\pi = 1/2^+$ state then evaluated at 6263 keV (6257 keV in Ref. [57], which they concluded dominated the ^{30}P$(p,\gamma)^{31}$S rate at lower temperatures, $T < 0.2$ GK. A rate was calculated using the experimental parameters obtained in this study and earlier studies, but the authors found that the experimental rate only agreed with the Hauser-Feshbach rate above 0.3 GK; below that temperature, the rate differed up to several orders of magnitude.

Two charge-exchange interaction studies have been performed. The first was a study by Wrede *et al.* published in 2007 [59] which measured the momenta of outgoing tritons from ^{31}P(^{3}He,t)^{31}S. Multiple resonances were either confirmed from tentative assignments in earlier works or discovered for the first time. Included in the latter group was a state at 6400 keV, for which evidence was found. Parikh *et al.* also performed a measurement of ^{31}P(^{3}He,t)^{31}S, again observing evidence for the state at 6402 keV and assigning it a spin and parity of $7/2^+$. The latter also used the angular distributions of the outgoing tritons to help constrain spins and parities of a number of states. Wrede *et al.* also measured ^{32}S$(d,t)^{31}$S, finding more evidence for the peak at 6400 keV.

Multiple in-beam gamma-ray experiments built upon the work by Jenkins *et al.* In 2007 Della-Vedova *et al.* published results of a study of ^{24}Mg(^{16}O,$\alpha\alpha n\gamma$)^{31}S where the authors observed several transitions from high-spin states [60, 61], confirming the observations of Jenkins *et al.*. Doherty *et al.* used the ^{28}S($\alpha, n\gamma\gamma$)^{31}S to populate resonances, including low-spin states, in the region of interest and used γ-γ and γ-γ-γ coincidences to determine the energies of resonance states in the region of interest with very high precision [62, 63]. Using comparisons to the mirror nucleus ^{31}P, the authors determined the spins and parities of the resonances, including a newly-discovered resonance at 6393 keV, which they labeled as a

$J^\pi = 5/2^+$ state. The authors claimed that their comparisons to ^{31}P had positively identified all relevant states in the energy region, but implied that the 6402-keV state observed in Refs. [59, 64] was identical to the state at 6393 keV and not distinct.

Most recently, Irvine *et al.* published in 2013 a study of the ^{32}S$(d, t)^{31}$S reaction, measuring outgoing tritons with excitation energies $6.3 \lesssim E_x \lesssim 7.1$ MeV. The major result of the study was additional evidence for the level at 6402 keV seen by Parikh *et al.*, contributing to the debate on whether the level was distinct from the 6393-keV level mentioned in Ref. [62]. The study also produced new mirror assignments for the ^{31}S-^{31}P mirror pair and used the assignments to conclude that the 6402-keV state's spin and parity were $7/2^+$.

4.2.1 Current State of ^{31}S Experimental Understanding

Although these numerous studies have helped build large, complementary understandings of the energy region above the ^{31}S proton emission threshold, and in some cases have also provided tight constraints on the properties of resonances in the region, there are still ambiguities preventing a complete, precise experimental understanding of these states. As mentioned explicitly above, there is currently no consensus on the number of states in the energy region around $E_x = 6400$ keV. The results from Doherty *et al.* [62, 63] imply that there are only two states in the region, at 6393 and 6394 keV. The results from Refs. [59, 64, 55] taken together, however, imply the existence of a distinct state at 6402 keV, the spin and parity of which is not identical to either of the states mentioned in Refs. [62, 63]. Both interpretations have complications, and an accurate reaction rate determination using indirect study requires unambiguous energies, spins, and parities of the resonance states involved in the reaction.

In fact, several additional states in the Gamow window also have ambiguous spins and

parities at present. Depending on the methods used to study the states, the constraints on their parameters can in cases be at odds. Thus, experiments that strongly constrain spins and parities, such as study via beta-decay, can be very useful toward helping to solve the conundrum.

4.3   NSCL Experiment 12028

Experiment 12028 (E12028) was carried out at the National Superconducting Cyclotron Laboratory (NSCL) using the Coupled Cyclotron Facility (CCF). It ran from 24 February to 4 Mar, 2014 and included collaborators from Michigan State University, Notre Dame University, Oak Ridge National Laboratory, the University of Tennessee, and the University of Southern Indiana. Broadly, the experiment produced two fast beams for two purposes: (1) a beam of ^{32}Cl ions for calibration purposes and (2) a beam of ^{31}Cl ions for the experimental measurement itself. Both of these beams were delivered to an experimental setup where they were implanted into a detector used to measure the beta decay to ^{31,32}S. Surrounding the central detector was an array of gamma-ray detectors used to measure the gamma de-excitation of the ^{31,32}S excited states populated in the decay. The ^{32}Cl beam was produced first, in order to calibrate these detectors.

The purpose of E12028 was to measure these gamma-rays and determine both the relative gamma branchings for the excited states and the beta feedings of the states themselves, using this information to construct a *decay scheme* for the beta decay. This beta decay scheme, including precise information on the beta feedings and gamma branchings of the $1/2^+, 3/2^+$, and $5/2^+$ states in the region, could then be compared with a theoretical decay scheme produced via shell model calculations. By comparing the experimentally-determined

parameters (such as excitation energy) of the states to those of the theoretical states, it would be possible to associate observed states with shell model states, which include spin and parity assignments. Then, theoretically-calculated parameters for the states, such as Γ_p, could be combined with experimentally-derived parameters to produce resonance strengths and, subsequently, a calculation of the reaction rate whose uncertainty was tied to the uncertainty of the theoretical parameters used in the calculation – about a factor of two.

4.3.1   Beam Production at the Coupled Cyclotron Facility

The principle behind the Coupled Cyclotron Facility at NSCL is simple: stable ions from an ECR ion source [3] are injected into a transverse magnetic field, causing circular motion according to the Lorentz force. While the ions are circling the cyclotron, they are affected by an oscillating electric field in the direction of motion, causing the ions to accelerate as they move. When the ions have been accelerated to the proper speed and energy, they exit the cyclotron and are impinged upon a fragmentation target, producing a cocktail beam which includes the desired radioactive isotope for study. The CCF uses two cyclotrons, the K500 and the K1200, to accelerate stable ions up to an energy of 50-180 MeV/u, at an intensity of anywhere from 0.1 pnA [4] (for uranium beams) to 175 pnA (for oxygen).

In the case of E12028, a stable "primary beam" of ^{36}Ar was produced and accelerated up to an energy of 150 MeV/u in the CCF, at a beam current of 75 pnA. The ^{36}Ar was then impinged upon a ^{9}Be target of thickness 1627 mg/cm^2 [5] and fragmented to produce a

---

[3] ECR stands for "electron cyclotron resonance." The ECR technique involves using electromagnetic radiation in conjunction with a magnetic field to move free electrons in a gas according to the electron cyclotron resonance frequency. The free electrons collide with gas molecules in the source, ionizing them for extraction and acceleration.

[4] pnA, "particle nano-Ampere," is a unit of beam current. The transformation from charge current (e.g. nA) to beam current requires dividing by the charge state of the ion.

[5] ≈ 0.88 cm. The unit mg/cm^2 is a more easily-understood measure of the target mass (likelihood of interaction) per unit area (of, e.g., the beam). To convert between the two, simply divide by the density of

cocktail beam that included both ^{32}Cl and ^{32}Cl as constituents. The thickness of the target was chosen to maximize production of both of these isotopes without having to switch out the target.

In order to isolate the desired isotope, in this case either ^{32}Cl (for the calibration) or ^{31}Cl (for the experiment itself), it is possible to separate the beam constituents by their *rigidity*, the ratio of momentum to charge, again using the Lorentz force: $mv/q = Br$. The cocktail beam is sent though one or more transverse magnetic fields and the various constituents experience varying magnitudes of force, causing circular motion with radius dependent upon the rigidity of the particular isotope. Species with higher rigidity have a higher radius of curvature in a constant magnetic field, while those with lower rigidity bend more sharply. Thus, differences in rigidity between the beam constituents result in a spatial distribution of species. Collimating slits may then be used to select isotopes according to spatial position. In order to purify the beam further, an energy degrading "wedge" may be used: ions with a shared rigidity Br but different atomic numbers lose different amounts of momentum in the wedge, further dispersing them and allowing for additional purification in magnetic fields.

The NSCL uses the A1900 fragment separator [65] to purify the fragmented beam. The A1900 fragment separation is accomplished through the use of four dipole magnets, two before and two after the dispersive wedge. The magnetic fields of the dipoles may be tuned to a specific rigidity, such that, after fragmentation, the desired isotope is centered on the beam line, while lighter and heavier beam constituents are bent to off-center paths and blocked. The CCF and the A1900 are shown schematically in Figure 4.1.

For E12028, the dipoles of the A1900 were rigidity-tuned to center ^{32}Cl and ^{31}Cl sequentially on the focal plane at the end of the fragment separator. The magnetic separation

the target material (Be: $\rho = 1848$ mg/cm^3)
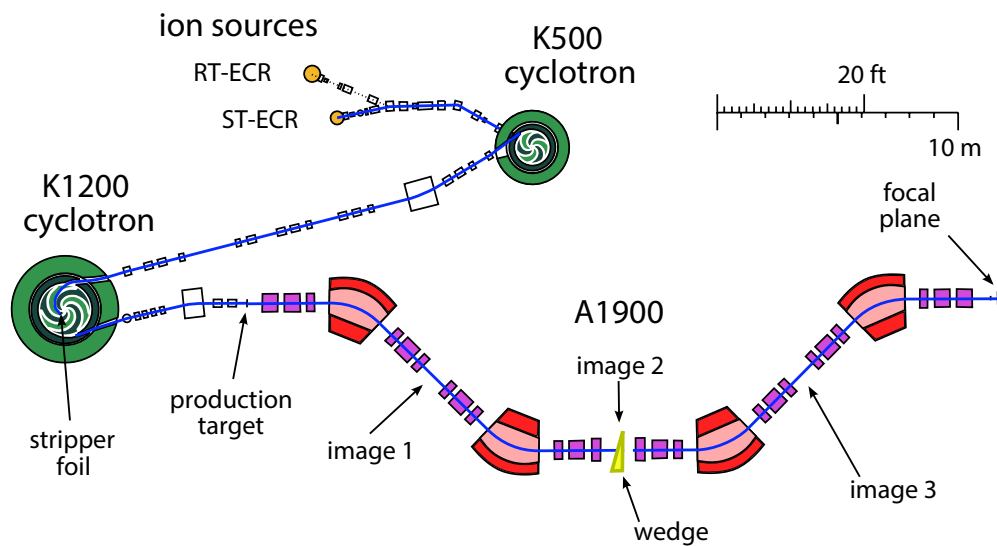
Figure 4.1: A schematic of the coupled cyclotron facility and the A1900 fragment separator. The ion source releases stable ions to the K500, which accelerates the ions to ≈ 13 km/s. Between the K500 and K1200 the ions pass through a gold foil stripper which removes more electrons, then the K1200 accelerates the particles to approximately half the speed of light before impinging them upon the production target. The four dipole magnets of the A1900 are illustrated in red, with the separator wedge in between dipoles 2 and 3 in yellow. The focal plane of the A1900 houses a scintillator which is used to count the beam current after purification. After the focal plane, the beam can be directed into one of several experimental vaults.

was assisted by the inclusion of a wedge of 145 mg/cm^2 Al. The magnets required retuning between the production of the ^{32}Cl beam and the ^{31}Cl beam; this tuning was on the order of 5% rigidity difference. At the focal plane of the A1900, the beam current and purity of the ^{32}Cl beam were roughly 635,000 particles per second (pps) and 11%, respectively, with expected contaminants ^{26}Mg (stable), ^{27}Al (stable), ^{29}Si (stable), ^{30}P (($T_{1/2} = 2.5$ m), ^{31}Si ($T_{1/2} = 157.3$ m), and ^{33}Ar ($T_{1/2} = 173.0$ ms). For the ^{31}Cl beam, the beam current and purity were roughly 13,000 pps and 3%, respectively, with contaminants ^{24}Na ($T_{1/2} = 15$ h), ^{25}Mg (stable), ^{26}Al [6] , ^{28}Si (stable), ^{29}P ($T_{1/2} = 4.1$ s), ^{30}S ($T_{1/2} = 1.2$ s), and ^{32}Ar ($T_{1/2} = 100.5$ ms).

4.3.2 Beam Purification Using the RFFS

The experiment was conducted in the S2 vault of the NSCL experimental area. This location allowed for further purification of the beam using the Radio-Frequency Fragment Separator (RFFS) [66]. The concept behind the RFFS allows for separation of isotopes according to the varying speeds at which they exit the target: produce a transverse time-oscillating RF electric field, whose frequency is synchronized with the accelerator RF. Because the beam constituents have differing speeds coming out of the target, they reach the RFFS chamber at phase differences ϕ with respect to the oscillating field. As the particle traverses the field, it experiences a deflection commensurate with the fraction of the oscillation period it spends while the field is pointed in one direction. As noted in Ref. [66], the deflection angle

---

[6]Ground-state ^{26}Al has a beta-decay half-life of 7.2e^5 y, making it effectively stable. However, the fragmentation process may produce isotopes in excited states; in the case of ^{26}Al, the first excited state is an isomer with beta-decay half-life of 6.3 s, meaning that some of the ^{26}Al produced was radioactive. None of the produced radioactive ^{26}Al resulted in gamma-ray detection, due to purification procedures discussed in Section 4.3.2.

difference before and after application of the RF field is

$$\delta b = \frac{1}{Br}\frac{V}{g\omega}(cos(\phi) - cos(\omega T + \phi)) \tag{4.1}$$

where V is the RF voltage, ω is the RF frequency, which itself is coupled to the operating frequency of the CCF (≈ 25 MHz), ϕ is the phase difference between the particle and the cavity, g is the gap across the electrode creating the field, and T is the time taken by the particle to travel across the electrode. From this equation, it can be seen that maximum deflection occurs when the particle enters the separator chamber in phase with the field (that is, $\phi = 0$), so that the field deflection increases monotonically during the particle's traversal of the chamber. Conversely, minimum deflection occurs when the field varies such that it deflects the particle equally in both transverse directions, leaving it in the center of the beamline when it exits the chamber. As with the A1900, collimating slits may be used to select beam constituents of a certain deflection angle. To select the deflection for the desired isotope, the phase of the oscillating field in the RFFS may be set to a desired value.

For E12028, the field production voltage of the RFFS was set to 100 kV. In order to guard against the possibility of RFFS failure, which would result in the entirety of the beam passing through undeflected, the phase of the RFFS was set such that the desired isotope (^{32}Cl and ^{31}Cl, sequentially) was deflected to the maximum angle, and the other constituents were deflected less sharply. The collimating slits were then used to block the transit of the contaminant ions, allowing the desired isotope through. The nominal phase angle was ≈ 60 degrees; the purity of the beam was monitored during periodic beam diagnostic checks throughout the experiment (see Section 4.3.3), and the angle was adjusted slightly to maximize the purity and transmission of the desired isotope. The purity of the beam after

filtering in the RFFS was assessed at the experimental setup. An image and a schematic of the RFFS are shown in Figure 4.2.

4.3.3 Experimental Setup

After passing through the RFFS, the beam continued to the experimental setup, which included a scintillator into which the beam was implanted, a suite of high-purity germanium detectors to measure the beta-delayed gamma-rays from the decay of ^{31}Cl, and the NSCL digital data acquisition system (DDAS). About one meter upstream of the experimental area, a pair of silicon PIN detectors were used to measure the purity and composition of the beam.

PIN (*positive-intrinsic-negative*) detectors are semiconducting detectors with an undoped intrinsic semiconductor sandwiched between a section of p-type semiconductor (that is, a semiconductor doped with an impurity resulting in fewer electrons and a greater concentration of holes) and a section of n-type semiconductor (doped with an impurity resulting in a higher concentration of electrons). If a voltage is applied in the n-to-p direction (that is, electrons flow in the p-to-n direction, a so-called *reverse bias*), an electric field extends into the intrinsic semiconductor region, creating a region where holes [7] and electrons are quickly swept to opposite sides of the detector and making the detector useful for measuring ionization in the region, such as that caused by an incoming beam particle. The amount of charge detected, and thus the amplitude of the voltage pulse the amplifier sends to the data acquisition system, is dependent upon the energy deposited in the detector.

To measure the purity and composition of the beam exiting the RFFS, the silicon PIN detectors were inserted into the beamline. The beam passed through a collimator to make

---

[7]That is, an *electron hole*, a position in the valence band where an electron is expected to be but is absent.
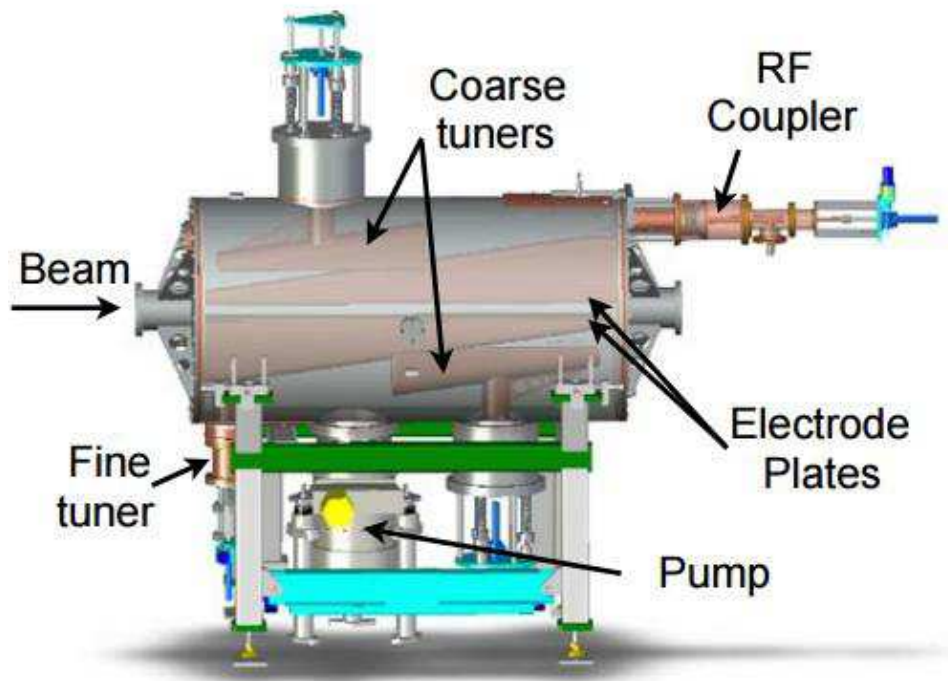
Figure 4.2: A schematic and photograph of the RFFS. The beam enters the chamber at left, experiences deflection according to the electric field throughout its flight between the two electrode plates, and exits to the right. The RF coupler at top is used to couple the oscillation frequency of the RFFS to that of the cyclotron. This figure is reproduced from the original RFFS paper, Ref. [66].

sure it only impinged upon the active detector area of the detectors, then deposited energy in the detectors as it passed through, with different beam constituents depositing varying amounts of energy according to their mass. Both PIN detectors measured energy deposition, but one of the detectors was also used to measure the time of flight (TOF) of the ions between the PINs and both the cyclotron and a scintillator at the focal plane at the end of the A1900. The detector was connected to a TC 241s fast timing amplifier and a Canberra 454 constant fraction discriminator [8], then split into two separate signals and connected as the "start" signal for two separate time-to-amplitude converters (TACs), which used the CCF RF signal and the signal from a scintillator at the A1900 focal plane, respectively, as "stop" signals [9].

With these energy and TOF measurements, a two-dimensional spectrum was created which separated incoming beam ions by their mass and charge (Figure 4.3). From this 2D spectrum, it was a simple matter to integrate various clusters of incoming ions to determine the purity of the beam as well as which contaminants were present. The ^{32}Cl beam was found to be 99% pure ^{32}Cl, with only trace amounts of other contaminants. The ^{31}Cl beam was found to be $\approx$85% pure; however, the strongest contaminant was the stable isotope ^{28}Si, so the radio-purity of the beam was found to be 95%, with ^{24}Na ($\sim$2%) and ^{29}P ($\sim$1.5%) the strongest radioactive contaminants. In principle, the PINs could be inserted into the beam indefinitely, so that particle identification (PID) and purity diagnostics could be performed continuously throughout the experiment. However, both the ^{32}Cl and ^{31}Cl beams had a

---

[8]A constant fraction discriminator measures the timing of a voltage pulse from a detector by splitting the incoming signal, inverting part of it, and delaying the inverted signal such that the sum of the two split signals always crosses the zero voltage mark at the same fraction of the original pulse's rise time. It allows for precise timing measurements of pulses with nonzero rise times.

[9]Although this method of time-of-flight measurement may appear backward, it is important to use the downstream detector as the "start" signal, since not every particle creating a signal at the A1900 upstream will reach the experimental setup. This method prevents the measurement of TOF "starts" without their according "stops." In order to receive the signals in the proper order, a cable delay box was used with lengths of wire designed simply to delay the signal from the A1900 reaching the TAC.
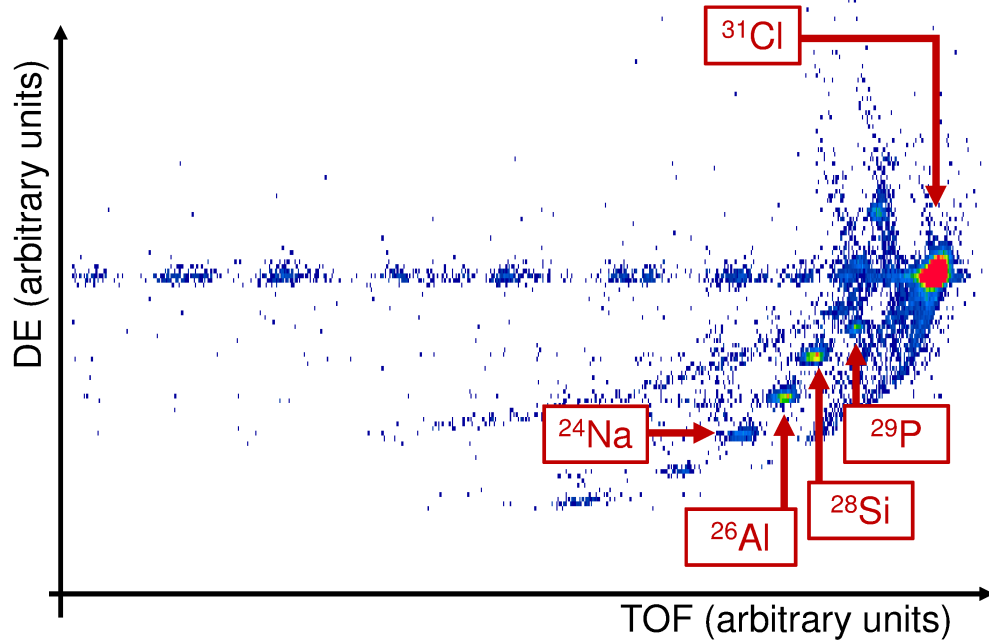
Figure 4.3: A particle identification plot for ^{31}Cl showing ^{31}Cl and strongest likely contaminants. As described above, the beam constituents are separated both by time of flight, in this case between the A1900 focal plane scintillator and the PIN detector at the experimental setup, and by energy loss in the PIN detector. It is customary to plot time of flight on the horizontal axis and energy loss on the vertical axis. The large blob near the right edge of the plot is the ^{31}Cl, while the additional blobs are beam contaminants, which have been identified either by their presence in the gamma spectrum or inferred from the expected beam composition at the A1900 provided by the NSCL beam group. The horizontally repeating structure is likely an artifact caused by reflection within the electronics, creating a false signal with the appropriate energy but inflated time of flight.

very high intensity, even after purification in the RFFS. To prevent the destruction of the PIN detectors via radiation damage, they were attached to a hydraulic drive which could be raised and lowered into the beamline. At various points throughout the experiment, the beam intensity was reduced by a factor of ten at the cyclotron, at which point the PINs were inserted into the beam for diagnostics purposes. In practice, this procedure was performed once per 8-hour experimenter shift.

The experimental setup, as mentioned, consisted of a central scintillator composed of BC408 plastic surrounded by high-purity germanium detectors. The scintillator ($51 \times 51 \times$

25 mm) was mounted in alumninum square housing with an entrance window of aluminized mylar at a much lower density and thickness to prevent interactions before implantation. It was attached on a 51 × 21 mm side to a Hamamatsu R1924A photomultiplier tube (PMT) [10] which was connected directly to the NSCL DDAS. The PMT needed to be biased in order to produce the electron cascade and subsequent voltage pulse, and was kept at an operating voltage of 1 kV throughout the experiment. Incoming ions were implanted into the scintillator, deposited energy, and decayed after a time. Both the implants and decays produced energy in the scintillator, which was not able to differentiate between the two except for broad energy distribution shape in spectral analysis. The scintillator's main purpose in the experiment was simply to record when each implant or decay happened, so that coincidence sorting could be performed during analysis (see discussion in Chapter 5). No timing information from the scintillator beyond the arrival time of the pulses was required, so it was sufficient to connect the PMT output to the DDAS input.

Surrounding the central scintillator was an array of 9 high-purity germanium "clover" detectors – the Yale Clovershare Array. Clover detectors consist of four semiconducting germanium crystals, packed in a square clover-like formation within the detector. Similar to the silicon PIN detectors, the germanium crystals in the clover have a positive-intrinsic-negative structure which allows for rapid detection of ionizing radiation such as gamma-rays. Germanium is used for the gamma detectors instead of silicon because the depleted intrinsic semiconductor region can be manufactured to be more than a few millimeters thick, allowing for a significant probability of complete absorption of incoming photons.

Like the PIN detectors, the clover detectors needed to be biased: the operating voltage of

---

[10]A PMT operates according to the photo-electric effect: incoming photons release electrons on a *photocathode*. These electrons then cascade through a series of dynodes, multiplying the total charge. The electrons are then detected at an anode, with the resulting pulse amplitude being proportional to the initial photoelectron flux generated at the photocathode.
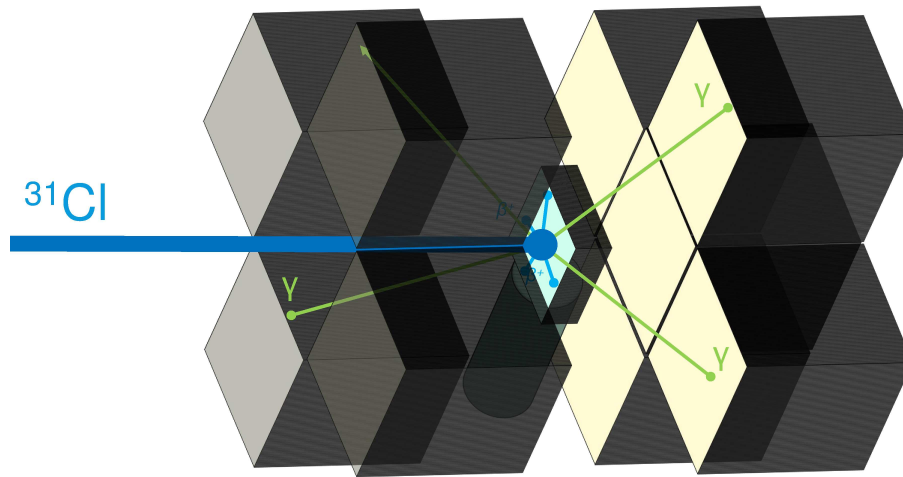
Figure 4.4: A simple schematic showing the central scintillator and the germanium clover detectors. The nine clovers surround the scintillator as shown. The ^{31}Cl beam implants in the scintillator, which detects the beta decays (blue). The subsequent gamma decay of the daughter ^{31}S nucleus creates gamma-rays (green) which are detected by the clover array.

the detectors was around 5kV. Because the band gap of germanium is low, thermal generation of charge carriers in the detectors can cause "leakage current," which compromises the energy resolution of the detectors (manifesting as a broadening of the energy peak in a spectrum and a decrease in the precision of measurement of the peak's centroid) and can even destroy the detector. To prevent this, the clovers are kept in a vacuum chamber which is attached to a dewar of liquid nitrogen. The liquid nitrogen cools the detectors to ≈75K, cold enough to prevent thermally-created noise from being a problem. The dewars for the clover detectors were filled twice a day throughout the entire experiment to replenish evaporated nitrogen.

The 9 clover detectors were arranged in two "rings" of four detectors each, with one ring upstream of the scintillator and one ring downstream of the scintillator such that the germanium crystals were centered on the scintillator and as close to it as possible. The ninth clover was centered on the beam axis behind the scintillator, inserted into the "ring" made by the back four germanium crystals. The clovers and the scintillator were all held in
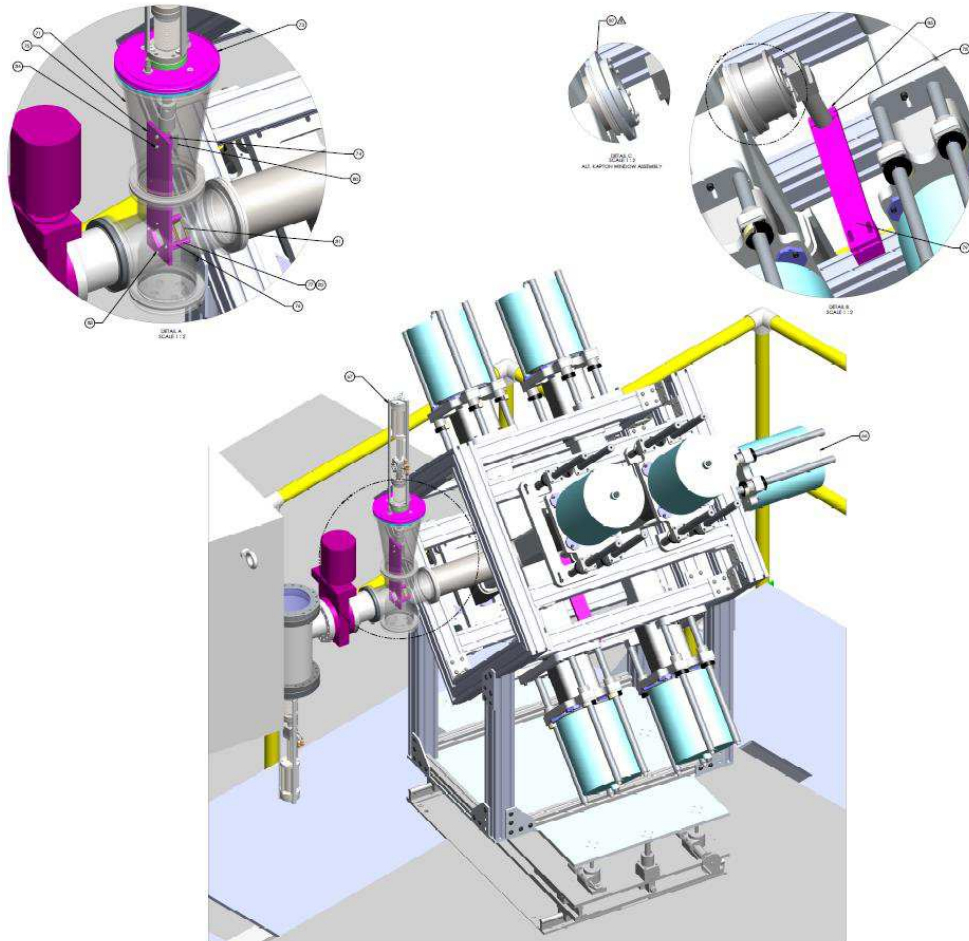
Figure 4.5: A full CAD drawing of the experimental setup, including the pneumatic drive attached to the PIN detectors (left insert), the central scintillator which was attached to the clover frame by a metal arm (right insert), and the full clover frame with all nine clover detectors (bottom). The liquid nitrogen dewars for the clovers are shown in light blue, and the clover detectors themselves can be seen as the light gray extensions into the center of the array.

place by an aluminum frame designed and fabricated at the NSCL. Schematics of the clovers and scintillator are shown in Figures 4.4 and 4.5. No timing information from the clovers was needed other than the arrival time of the pulses generated by energy deposition of the gamma-rays, so it was sufficient to connect the energy output for all 36 crystals to the DDAS without further modification.

4.3.4   Brief Discussion of Detector Mechanisms

The detectors mentioned in Section 4.3.3 utilize a number of different techniques to produce a signal for processing. It is useful for interpreting the spectra produced by the detectors to engage in a brief discussion detailing the interaction mechanisms occurring within the detector that ultimately result in the signal output from the detector and sent for processing.

For **high-purity germanium detectors** such as the clovers, an incoming gamma-ray may interact in multiple ways: it may undergo *photoelectric absorption*, where the photon is absorbed by the atom and the electron is freed; it may *Compton scatter*, transfering some of its energy to an atomic electron in the germanium; or, it may undergo *pair production* in the presence of the strong electric field of the protons in the nuclei of the atoms that make up the detector [67]. In the first case, the incident photon disappears in an interaction with an atom in the detector. An electron is freed, via the photoelectric effect, from one of the atomic shells; this electron has total kinetic energy equal to the photon's energy minus the binding energy of the electron in its shell. To fill in the gap left by the electron, the atom rearranges its electron configuration, releasing the binding energy of the vacated shell in the form of an X-ray or Auger electron. The X-ray quickly undergoes its own photoelectric absorption and is re-absorbed by the atom with the result of the emission of electron such that the sum of the energies of all electrons produced this way is equal to the original photon

energy. The electrons are collected at the edge of the semiconductor and a voltage pulse corresponding to the full photopeak energy is produced. The corresponding observable in the spectrum is a sharp peak at the original gamma-ray energy. This is of course the ideal situation for gamma-ray spectroscopy.

In the second case, the photon deposits only some of its energy, causing the electron to recoil and leaving at some outgoing angle with new energy according to the standard Compton formula:

$$E'_\gamma = \frac{E_\gamma}{1 + E_\gamma/m_e c^2 (1 - \cos\theta)} \tag{4.2}$$

where m_e is simply the electron mass, 511 keV/c^2. In this case the recoiling electron therefore has energy $E_e = E'_\gamma - E_\gamma$. The two extreme cases of Compton scattering are a minimally grazing collision, where $\theta \approx 0$ and the electron leaves with very little energy, and $\theta = \pi$, a head-on collision where the electron leaves with maximal energy $E_{e_{max}} = E_\gamma/(1 + 2E_\gamma/m_e c^2)$. The distribution of recoiling electron energies in the detector produces a *Compton spectrum*, demarcated by the *Compton edge*, corresponding to the maximum electron energy $E_{e_{max}}$. The specific shape of the Compton spectrum is somewhat dependent on the binding energy of the electron prior to the scattering process.

In pair production, a gamma of energy $E_\gamma > 2m_e c^2$ ($m_e c^2 = 511$ keV) may, as a result of interaction with the intense electric field near protons in the nuclei of the detector material, disappear completely and produce in place of the gamma-ray an electron positron pair with total shared kinetic energy equal to $E_\gamma - 2m_e c^2$. Both the electron and positron will typically travel less than a few millimeters before depositing the entirety of their kinetic energy (the original photopeak energy minus 1022 keV) into the detector. The positron will

then annihilate with an electron already in the detector, producing two gamma rays of 511 keV, which may or may not deposit their energy in the detector. If both 511-keV gammas deposit their full energy, the full photopeak energy is recovered in the detector. If one or both of the gammas escape from the detector without depositing any of their energy, a *first escape peak* or *second escape peak*, respectively, is produced instead, with peak energies lower than the full photopeak energy by 511 keV and 1022 keV, respectively. These escape peaks are a very consistent feature of gamma-ray spectra and in some cases can be used to infer the existence of a photopeak if the detector's energy range does not extend to high enough photopeak energies.

For **plastic scintillator detectors**, the above gamma-ray effects may occur as they do for germanium detectors. However, since the atoms making up the plastic have much lower Z values than germanium, the photoelectric cross section is much lower. A vast majority of gamma interactions in plastic scintillators are simple Compton scattering events, making production of a gamma-ray photopeak almost impossible. Organic scintillators such as the plastic scintillator used in E12028 are, on the other hand, often favored for beta-decay spectroscopy due to their hydrogen content [67].

Light production in scintillators begins when the incoming particles (beta particles, nuclei, etc) excite valence electrons in the molecules composing the scintillator material from a "ground state" singlet state (S_0) to an excited singlet state (S_n). The excited singlet state immediately decays without emitting a photon to the S_1 singlet state, which can then quickly emit a photon with energy equal to the difference between the electron singlet states S_1 and S_0 [11], producing prompt radiation known as *fluorescence*. However, the excited

---

[11] In principle the excitation or de-excitation can occur to any of the vibrational states associated with the state; however, the energy spacing between these vibrational states is small compared to the spacing between electron states, so they do not factor heavily into the light production.

singlet states can also decay to excited triplet states T_n, which will decay, similarly to the S_n states, to the lowest triplet state T_1. This state decays, with a long lifetime, via photon emission to the ground state S_0. The prolonged de-excitation of the T_1 state is known as *phosphorescence*, or after-glow.

The amount of light produced via fluroescence is thus seen to be a function of the beta or charged particle energy, as higher-energy particles can excite greater numbers of molecules. However, for high-energy particles, an effect known as *quenching* can occur, resulting in a reduced light output as the high-energy particles heavily ionize the scintillator material in a compact region. The light output for a proton in a plastic scintillator is typically $\approx 1/10$ that for electrons [67]. This means that, for E12028, the effective "gain" in the plastic scintillator for the incoming ≈ 50 MeV/u ^{31}Cl beam particles was lower than that of the $\lesssim 12$ MeV electrons. While the charged particles stop quickly in the scintillator, however, beta particles can undergo a process known as *backscattering*. Similar to the situation with Compton scattering for gamma rays, this scattering changes the direction of the traveling electrons and creates the possibility that they may escape the detector without depositing their entire energy. This consequently leads to a beta detection efficiency that is less than unity.

4.3.5 The NSCL Digital Data Acquistion System

This simple setup – central scintillator surrounded by germanium gamma-ray detectors – was nonetheless sufficient for measuring all of the observables we intended to study. However, performing the measurement is not as simple as taking voltage pulses from detectors. Traditionally, detectors have been connected to a series of analog nuclear instrumentation modules (NIM) designed to properly shape the incoming voltage pulse, align in time any

signals which are meant to be detected in coincidence (that is, account for the timing differences created by the electronics differences between detectors that might receive signals simultaneously), and then digitize the analog voltage pulse so that it can be read into a data acquisition computer.

The NSCL Digital Data Acquisition System is a computerized system designed to replace many of the hardware modules used in between the detector and the data collection computer. One or more 16-channel Pixie-16 signal processing PXI cards are connected to an operating computer crate [68]. Each channel from the Pixie-16 card can accept signals from a variety of detectors. The signal is digitized in the system, and pulse shaping and timing correction is accomplished by using the module software. The system uses the software parameters to obtain the pulse area, and sends the processed pulse information to the data acquisition computer. A number of parameters can be set in the DDAS, including the trigger threshold (the voltage level below which an event in the detector will not register in the electronics) and the rise and decay time of the pulse. A thorough discussion of the DDAS implementation at the NSCL is beyond the scope of this work, but there are a number of excellent treatments of the topic [69, 70, 68].

In the case of the clover detectors, the most critical pulse-shaping parameter to set in the DDAS is the decay constant τ of the pulse shape. Since the signals coming from these detectors have a very fast rise time and an exponential decay time, it is important to set the decay constant τ properly for each detector in order to accurately integrate the output energy signal. For the NSCL DDAS, this is accomplished by recording the waveform of an incoming pulse using a digitized spectrum generator attached to the Pixie crate. The waveform typically has a very fast rise time followed by an exponential decay, so the decay constant τ may be set simply by fitting the waveform for a given detector with an exponential

of the form $e^{t/\tau}$. In the case of E12028, precise energy determination was not strictly necessary for the scintillator, as the scintillator's main purpose was simply to the timing of implants and decays; however, precise energy determination for the clover detectors was critical to obtaining a narrow energy resolution of the incoming gamma-rays. Thus, it was necessary to individually set τ for each of the 36 clover detectors in DDAS. The τ value for each crystal was set to a value between 41.5 μs and 57.4 μs, with most of the crystals having a τ value of around 44 μs.

The electronics used in E12028 are relatively simple; a brief description of each component is given here.

- **TC 241s Amp:** a pre-amplifier used to shape the signal from the PIN detector for timing. The signal was patched out to the user area at the NSCL, the Data-U.

- **QCFD:** a constant fraction discriminator with four inputs, used for precise timing. Operates by splitting the incoming signal into two identical pulses, inverting and delaying one of the two, then summing the two pulses back together. The zero-point crossover of the mixed pulse is the pulse time.

- **TAC:** time-to-amplitude converter. Records a start and stop signal, then produces a voltage pulse with height proportional to the time difference between the two.

- **2mm / LEMO Converter** Converts between the DDAS cable standard (LEMO) and the standard for the patch panel electronics (2mm cable).

- **Fast Trigger:** A logic module that fires when it receives a signal indicating that the DDAS has received a pulse from a detector that surpasses the threshold for measurement.

- **FIFO:** Fan-in, fan-out. Takes data from a number of sources, combines it into a single channel, and can output to several sources.

- **Delay:** A length of wire measured to impede the delivery of an electronic signal by the desired time. Typically comes in a delay box with several lengths of wire.

The energy signals from all of the detectors as well as the TOF signals from the PIN detector setup were fed into DDAS, which processed the signals and sent them to the data acquisition computer, which was running the NSCL Readout software. Further description of the user-side analysis procedure is the focus of Chapter 5. In order to quickly assess the operation of each of the detectors, the processed detector signals from DDAS were exported through a number of logic modules designed to isolate specific components of the signals or combine signals from multiple sources. The relevant signals were then patched out of the S2 vault in the NSCL and into a patch panel in the NSCL Data-U counting room area. An electronics diagram, including the diagnostic patches, is shown in Figure 4.6.
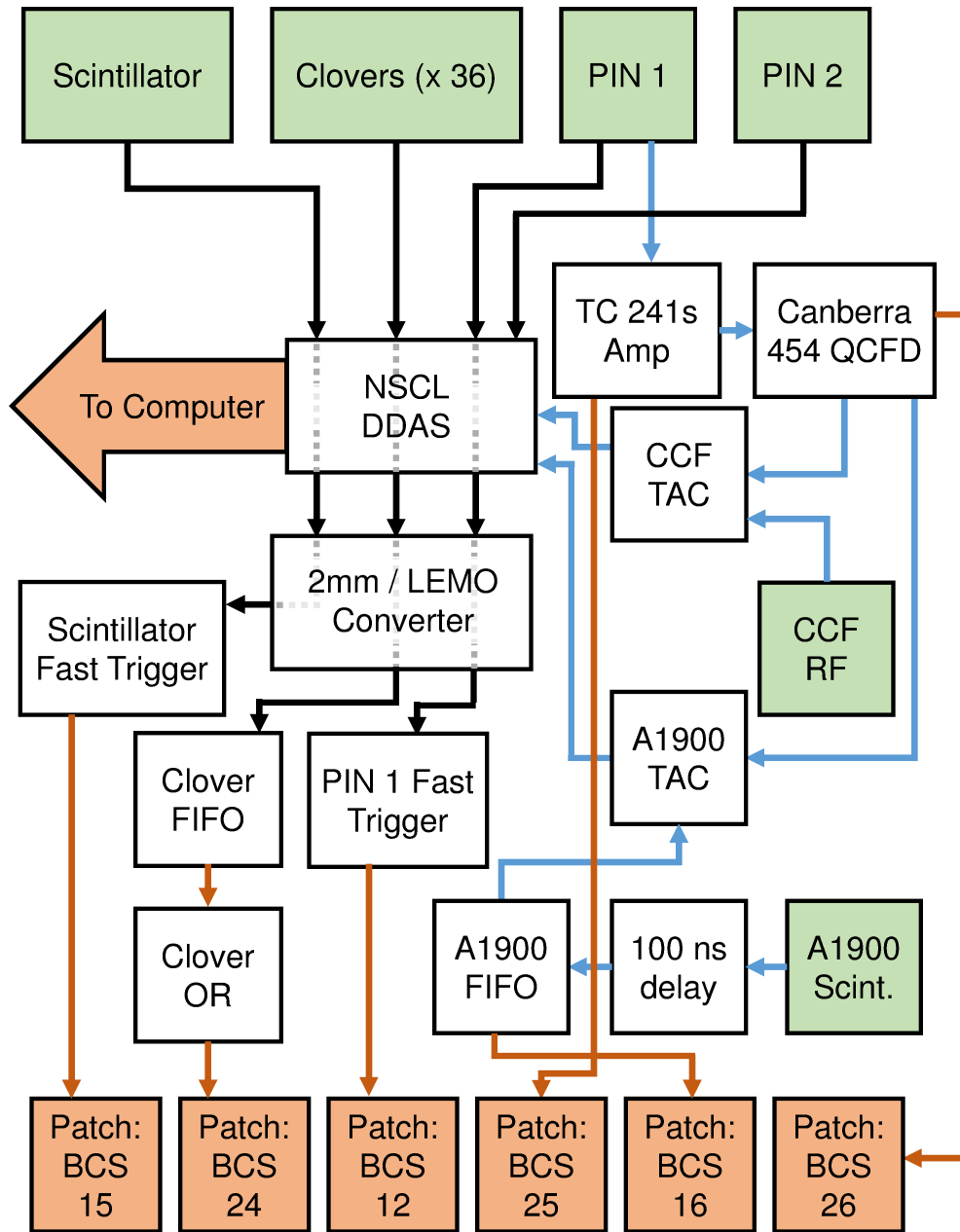
Figure 4.6: A simplified electronics diagram of E12028. Data sources (both detectors and NSCL apparati) are marked as green boxes. Intermediate modules and the NSCL DDAS are marked as white boxes. Destinations for data (both the data acquisition computer and the patch panels to the Data-U) are marked as orange boxes, and connections to exterior patches are marked as orange arrows. Energy information was passed from the sources and into the DDAS according to the black arrows, and timing information for time-of-flight measurements was passed from the sources and into the DDAS according to the blue arrows. Brief descriptions of the various components are given in the text.

Chapter 5

E12028 Analysis Procedure and Results

Although the electronic equipment used to acquire data for a nuclear experiment is a critical component in answering the research question, the equipment by itself is worthless without an analysis suite to record, sort, and make sense of the data. For example, the NSCL Digital Data Acquisition System (DDAS) receives as input the voltage pulses from various detectors that signify the energy deposited in the detector from various physical sources: incoming beam particles, implantations, beta decays, gamma-rays, etc. These incoming signals (referred from here on as *events*) must be time-stamped and sent from the DDAS to a computer used for processing, monitoring, and storing the data in a meaningful way for future offline analysis.

In practice, no two experiments will use exactly the same data processing procedure, even if they have similar goals and observables. This is due to several factors including differences in instrumentation needs and analysis goals. In this chapter we will discuss the specific analysis procedures used in E12028, including software parameters, data reduction procedures, particle identification, data calibration, and procedures for the calculations required to produce the ^{31}Cl beta decay scheme. We will also present the results of analysis, including the decay scheme itself, the data used to build it, and the gamma-ray spectra used

for analysis and results.

5.1 Data Processing

Each event received by the DDAS is time-stamped and sent to a data buffer that is attached to the NSCL Readout program. Readout receives the time-stamped event from DDAS and groups them within an *event window* according to a timing parameter set by the experimenter, thus creating small groups of data with the same top-level event window time-stamp in addition to the second-level time-stamps of the individual events (see Fig. 5.1). In this way, voltage pulses that occur within a set event window are labeled by the system as being *coincident* with one another, allowing for more specific gating procedures later on in analysis. The optimal event window for the experiment is dependent upon the rate of incoming experimental data and the specific processes that produce it. For example, *gamma-gamma coincidence* gates are designed to filter out of a spectrum all gamma-rays that are not part of a cascade with the gated gamma, but they only do so within the event window. Making the event window too large thus increases the risk of *accidental coincidences* from other beta-delayed gamma-rays, which increase the background in the coincidence spectrum.

In the case of E12028, our total rate of beam implantation was high, up to 9000 particles per second. However, for every ^{31}Cl implantation and decay to ^{31}S recorded in the scintillator, there is a subsequent additional decay of the ^{31}S nucleus to ^{31}P, which produces its own beta-delayed gamma rays that can be in coincidence with gammas from the beta decays of different nuclei including ^{31}Cl. This also does not take into account the risk of accidental coincidences from radioactive beam contaminants or room background radiation. To limit the probability of accidental coincidences at this high rate, we set the Readout event window
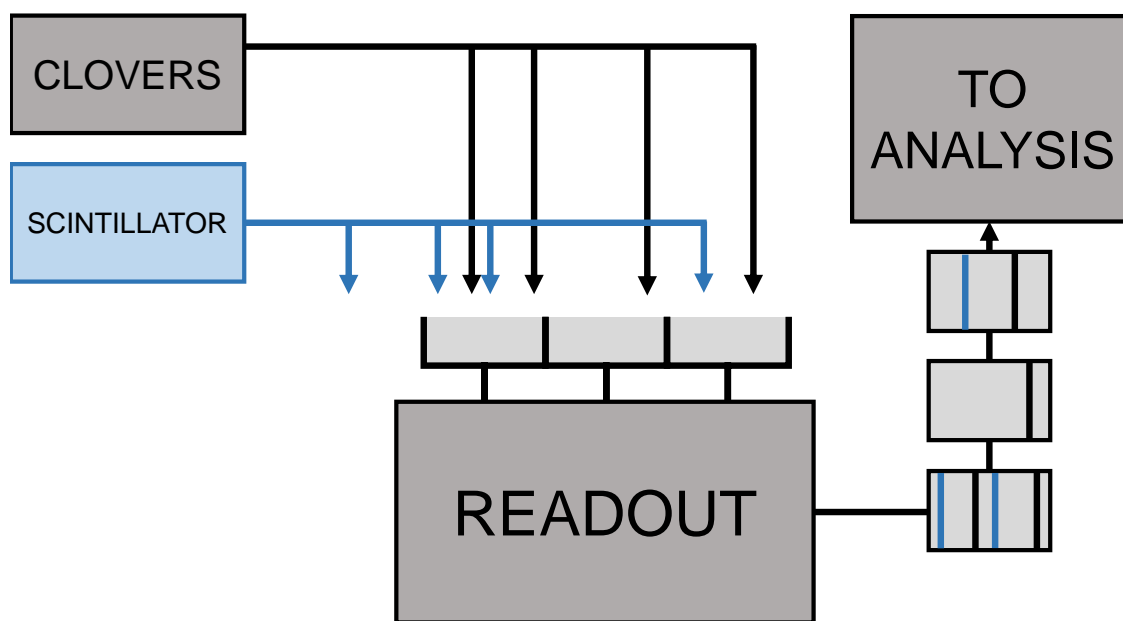
Figure 5.1: A simplified diagram showing the processing that the Readout program does to allow coincidence sorting for incoming data. Events from (in the case of E12028) the clover detectors (black arrow) and the scintillator detector (blue arrows) are buffered into the Readout program, which segregates them according to the event window (grey boxes) and pushes them into an event file for analysis.

to be 1μs wide. Data from the ring buffer was thus segmented into 1-μs event windows and stored in an *event file*, a file format that stores data in "words" denoting the time of an incoming event, the channel on which the event arrived, and the size of the event (that is, the pulse height), all organized by event windows. The Readout program is capable of creating multiple event files as needed according to the amount of incoming data, but it is common practice to organize data into "runs" of a few event files each so that, if the buffered data becomes corrupted, data loss is kept to a minimum. For E12028 our procedure was to stop and restart data acquisition roughly every hour, typically resulting in a "run" of three to five event files depending upon the implantation rate throughout the hour.

5.1.1 Online Analysis

Because beam time is at a premium, it is important to analyze the incoming data as soon as it has been processed into an event file. This allows experimenters to determine whether the experiment is likely to meet its research goals at the current experimental settings, or whether changes must be made. In addition, it allows experimenters to diagnose whether changes in the experimental electronics are needed, e.g. whether the delay cables used in particle identification (PID) time-of-flight measurements are an appropriate length to leave the "stop" signal from the upstream A1900 scintillator later than the "start" signal from the downstream PIN detectors at the experimental setup.

Typically, experimenters at the NSCL will use a program called SpecTcl for their online analysis. SpecTcl can be attached to either the incoming online data or to stored evt files, so the procedure for E12028 was to run two instances of SpecTcl on different computers, one attached to online data that allowed for quick analysis changes (new gates, calibrations, etc.) and one attached sequentially to stored data to produce a comprehensive accumulation of

data for the purpose of assessing the experiment's status. Fig. 5.2 shows a typical SpecTcl

display.
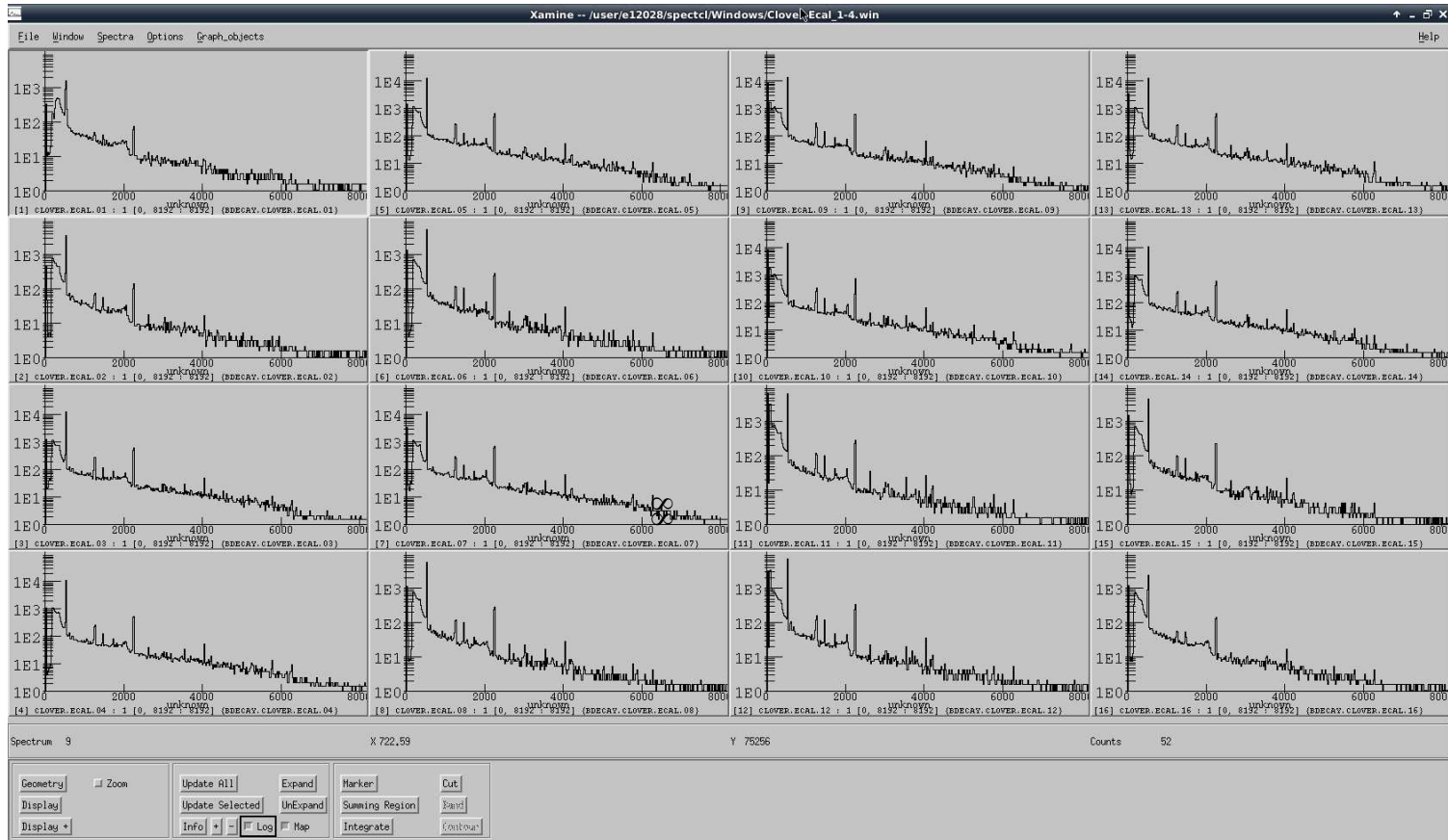
Figure 5.2: A screenshot of the SpecTcl analysis program spectrum window showing gamma-ray spectra for each crystal in the first four clover detectors (that is, the detectors in the ring upstream of the scintillator). These spectra have had a preliminary energy calibration (see Section 5.2.1) applied to them, and they demonstrate the slight differences that each detector crystal sees as it records information (for example, compare the relative heights of the peak at 2234 keV).

5.2 Calibration Procedure

In order to meaningfully understand and interpret the incoming data, it must be calibrated – the DDAS only forwards to Readout the time-stamped voltage pulses from the detectors, each of which has been amplified according to its unique electronic gain. This means that at the analog-to-digital conversion (ADC) step in the DDAS, gamma rays of the same energy detected in different detectors will likely result in voltage pulses of different heights and consequently be sorted into different digitized "ADC channel" histogram bins. Thus, plotting the uncalibrated gamma-ray spectrum combining multiple detectors results in a nonsensical histogram. In order to even make sense of the data at all, the first calibration applied to the data must be an *energy scale calibration.*

Further, once the calibrated spectra have been produced, any analysis procedure whose goal is to derive intensities of gamma-rays must take into account the fact that no detector is perfectly efficient for detection. Not only is it possible that a gamma-ray of a given energy will not deposit its full energy into the detector, or even fail to interact at all, the detectors simply do not cover the full 4π solid angle surrounding the gamma-ray source. To produce accurate intensities of gamma-rays, an *efficiency calibration* must also be performed. Here we will discuss both of these procedures for E12028.

5.2.1 Energy Calibrations

The general technique used in an energy scale calibration is to fix the ADC scale at several places where the energy is well-known. This is typically done by selecting several precisely-measured gamma-ray photopeaks in the uncalibrated gamma spectrum, plotting them as a series of ordered pairs of ADC channel and known energy, and fitting the points with an

analytical function that can translate ADC channel into energy at all points along the axis. Then, the data can be sorted again using this analytic function to produce a calibrated spectrum whose horizontal axis is an accurate energy scale.

This procedure can be performed in a number of ways when multiple detectors are involved. Each individual clover crystal can be individually calibrated, or the crystals as a group can be *gain matched* so that their ADC scales align with one another, and the aggregate spectrum then calibrated as one. Further, the choice of peaks to use for calibration is at the discretion of the experimenter and the needs of the analysis. In the case of E12028, several options existed: we could for example use photopeaks from ^{31}S beta-delayed gamma rays themselves, or use peaks from contaminants or room background radiation.

Each option presents its own set of concerns for producing an accurate calibration function. In the first case, the necessary assumption is that previous studies of ^{31}S gamma-rays have produced accurate values for the photopeak energies. This assumption may not be warranted however, given that the in-beam gamma-ray spectroscopy experiments mentioned in Chapter 4 have produced excitation energies for various ^{31}S states that are systematically higher than the ^{31}Cl beta-decay experiments done to-date by a few keV [59, 71, 56, 72]. In both cases, the issue of energy scale extrapolation is also a concern, since if the curve is fixed only at lower energies and extrapolated to higher energies, the error on the calibration increases monotonically with energy. This experiment aimed to precisely measure gamma-rays up to energies of 7100 keV, and the highest-energy known photopeak in ^{31}S that is not in the energy region we wished to study is the deexcitation to the ground state from the 6280 keV IAS – an almost 1 MeV extrapolation. A calibration based on room background peaks would have introduced even more of a problem, since the highest-energy commonly-used background peak is at only 2614 keV.

As mentioned in Chapter 4, we produced a ^{32}Cl beam for the purpose of calibration, and opted to use it for both energy and efficiency calibration. A detailed gamma-ray spectroscopy study of ^{32}Cl was published in 2012 [73] which produced ^{32}S gamma-ray energies up to 7189 keV. We fit the ^{32}Cl peaks up to 7189 keV, obtained ADC channel maxima (we used the peak maximum instead of the centroid, as discussed more fully in Section 5.2.2), and fit the obtained points to obtain a calibration curve for each clover crystal for the ^{32}Cl data. We used a quadratic function for the calibration to account for small nonlinearities in the gain of the detectors, which may happen over such a large energy range as ours. Typical quadratic coefficients for the ^{32}Cl energy scale calibration were on the order of 10^{-9} keV, indicating that the nonlinearity in the detector was very small.

The calibration curves we produced for the clover crystals were used to calibrate the ^{32}Cl data, which was taken over only a few hours. However, because the gains in detectors can drift over time, it is not feasible to apply a single calibration to a detector over an entire experiment, which may last for hundreds of hours. This *gain drift* has the effect of spreading out the photopeak, creating a peak with a lower amplitude and a wider peakshape. This can result in less precise measurements of the peak, and can even prevent peaks from low-intensity transitions from being visible at all. We found that five of the 36 clover crystals exhibited impractically large gain drift over time as well as changes in resolution, which produced odd peak shapes; data from these crystals was discarded entirely, as they would not have contributed productively to producing an accurate and precise calibration.

In order to counter the potential effects of gain drift in the ^{31}Cl data, which was taken over the course of many days, we grouped runs into small sets that were obtained close to one another and did not exhibit appreciable gain drift. We then applied the ^{32}Cl calibration to the set of runs that was taken closest in time to the ^{32}Cl calibration runs (only about

four hours difference) to produce a calibrated ^{31}Cl spectrum based on the independent ^{32}Cl calibration. We fit several ^{31}S photopeaks in this calibrated ^{31}Cl spectrum to produce our own set of ^{31}Cl calibration values, to which the remainder of the ^{31}Cl data was gain-matched, producing a ^{31}Cl calibration that did not require extrapolation or reliance on external ^{31}Cl values.

In order to check this calibration, we performed a second, completely separate calibration on the first segment of ^{31}Cl data to be calibrated with the ^{32}Cl calibration curve using the *cascade crossover method.* This method utilizes well-known low-energy room background peaks to perform a precise linear calibration in a known energy region (e.g., the well-known ^{40}K and ^{208}Tl lines at 1460.8 and 2614.5 keV, respectively). Within that region, it is then assumed that photopeak energies are precisely determined. In the event that two gamma-rays within that region are part of a cascade, their *transition energies* (which are related to the gamma-ray energies by a simple reference-frame transformation) may be added to get the transition energy of the gamma-ray that de-excites the level to which the two cascading gammas sum. This new gamma-ray, which ostensibly lies outside of the calibration, may then be used to extend the calibration, extending the region in which the cascade crossover method may be applied. This technique is time-consuming and arduous, but it does produce a calibration that, except for the two peaks used to begin the calibration, relies only on internally-obtained energies. We used this method to verify the accuracy of the ^{32}Cl calibration method, but the two methods were found to give consistent results, so the ^{32}Cl method was used on the rest of the ^{31}Cl data exclusively.
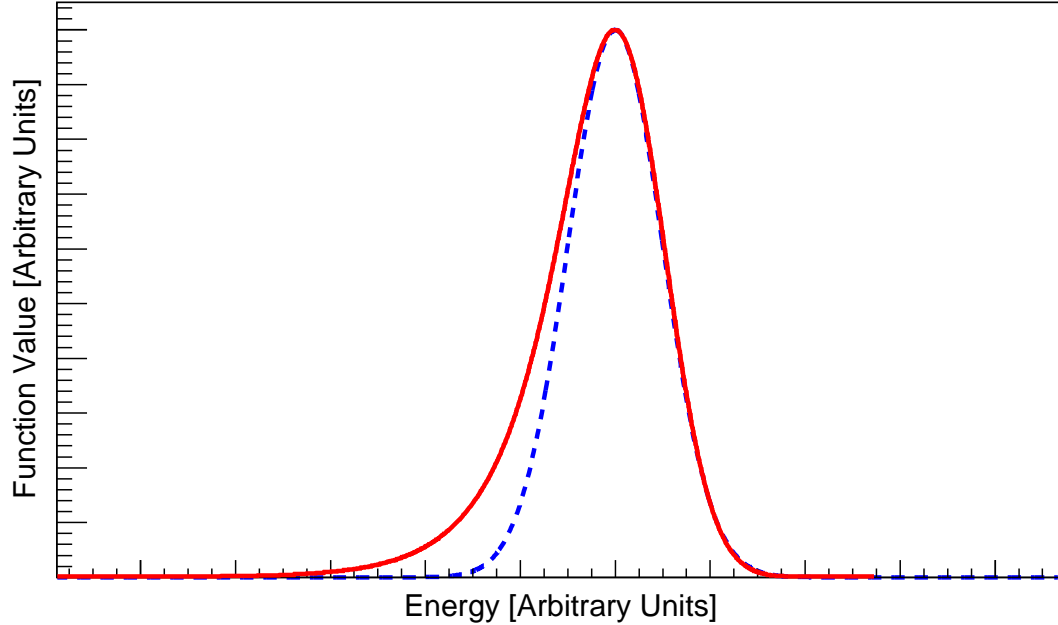
Figure 5.3: A comparison between the peak shape function used in the analysis of E12028 (red solid line) and the standard Gaussian peak shape (blue dashed line). The two functions have been normalized to have the same maximum value, centroid, and standard deviation parameter, σ. The large low-energy tail is the result of the convolution with the exponential.

5.2.2   The Peak Shape

Ideally, gamma-rays of a given energy would deposit the entirety of their energy into the Ge detector and produce a peak that follows the Gaussian distribution, with a centroid and maximum at the energy of the gamma-ray and a standard deviation based on the resolution of the detector. However, because of a number of physical effects in the detector, the actual photopeak shape is skewed as shown in Figure 5.3. The most prominent feature of this shape is the low-energy tail. This is due to incomplete charge collection in the detector of electron-hole pairs [74]. In principle, pile-up effects in the ADC could also change the shape of the peak; however, the charge-collection tail is a much stronger effect and the latter can usually be safely ignored.

For fitting photopeaks in the gamma-ray data, we used the following function, created

through the convolution of a Gaussian with an exponential, the complementary error function:

$$\frac{N}{2\tau} \cdot \exp\left[\frac{\sigma^2}{2\tau^2} + \frac{x-\mu}{\tau}\right] \cdot \left(1 - \mathrm{erf}\left[\sigma^2 + \tau \cdot \frac{x-\mu}{\sqrt{2}\sigma\tau}\right]\right) \tag{5.1}$$

where N is the peak integral (*not* simply the amplitude; the peak shape function relates the integral N to the amplitude A by the factor 2τ), μ is the centroid, σ is the Gaussian standard deviation, and τ is the "decay constant" of the exponential. Note that this τ is not related to the lifetime τ of the nuclear state whose deexcitation may create the photopeak being fit, nor the waveform decay constant τ used in setting the DDAS pulse-shaping parmeters. The function shown in Equation 5.1 represents a single peak with no background; throughout analysis we combined multiple peak-shape functions as needed to model doublets or series of peaks, and we found a simple linear background $A + Bx$ to be sufficient for our background modeling.

This modified Gaussian peakshape is also appropriate to model the systematic widening of the photopeaks due to the energy absorption effects in the detector as the gamma-ray energy increases. At low energies, the peak shape generally looks more Gaussian, whereas at higher energies the deviation becomes more pronounced. In practice, both σ and τ affect the width of the photopeak; thus, least-squares minimizations of the fit will produce unreliable fits with correlated uncertainties if these parameters are not constrained somehow. To increase the reliability of the peak-shape, we fit a number of strong, isolated peaks from a ^{152}Eu calibration source at a number of lower energies. When we were assured that the fit was good (that is, a χ^2/ν value close to 1 and a fit result where the minimization function did not have correlated errors) for each of these peaks, we plotted the σ and τ values as functions of

energy and fit them with parametrization function: $\sigma = \sqrt{A + B \cdot E})$, $\tau = A + B \cdot E + C \cdot E^2$.

In this way, we were able to systematically vary both σ and τ across the entire energy spectrum, allowing the peak shape to widen monotonically with increasing energy and eliminating the potential for correlated errors involving σ and τ. We also opted to use for the recorded energy value of the photopeak the maximum of the peak shape [1] instead of the centroid as described above. We chose to use the maximum instead of the function centroid because, for multiple fits of the same peak with slightly different fit boundaries, the maximum was found to vary less than the centroid. We used the centroid parameter's statistical uncertainty from the fit for the uncertainty in the maximum.

5.2.3   Energy Calibration Systematics

For our energy calibration, we obtained both the energies and the statistical uncertainties of the energies from the peak shape used to fit the photopeaks. However, a calibration cannot be more precise than the data used to perform it, so we needed to take into consideration the systematic error as a result of the calibration. To assess the accuracy of the calibration and assign systematic uncertainties at low energies, we measured the peak-shape maximum of a number of room background peaks known to a very high precision, and assigned a 0.2-keV blanket systematic uncertainty up to 2.7 MeV based on the variance of the peak centroids around their literature values [75]. Above 2.7 MeV, we measured the excitation energy of various levels using the cascade-crossover method with multiple cascades of the same level and compared the spread in the excitation energy derived from the cascades. We were able, using this method, to produce a widening uncertainty envelope to high energies: 0.2 keV for

---

[1] To find the energy corresponding to the maximum of the fit function peak, we used a computer function that iteratively steps through the function over the fit range and searches for the maximum value of the function. It then finds the energy value at that maximum function value.

$E_\gamma < 2.7$ MeV, 0.3 keV for 2.7 MeV $< E_\gamma < 4.8$ MeV, and 0.6 keV for $E_\gamma > 4.8$ MeV.

5.2.4 Efficiency Calibration

As mentioned above, the detector array was not capable of measuring every single gamma-ray emitted by the ^{31}Cl decay. In order to properly deduce accurate absolute intensities for the gammas emitted as a result of ^{31}Cl beta decay, it was necessary to perform an *efficiency calibration*, providing a scale factor for the integral of the peak as a function of energy: $N(E_{peak}) = \epsilon(E_{peak}) \cdot I(E_{peak})$ where N is the number of gamma-rays detected (the peak integral), I is the actual intensity of the peak (effectively, the number of gamma-rays emitted at the source), and the efficiency ϵ is simply the ratio between the two – all of these are evaluated at each peak energy E_{peak}.

In practice, when experimenters discuss "efficiency," they typically refer to the *absolute efficiency*, which is the efficiency as defined here: simply the ratio of the number of gammas measured by the detector array during the measurement time interval to the number gammas emitted from the source during that time. However, the absolute efficiency of a detector has itself two factors, the *geometrical efficiency* and the *intrinsic efficiency* of the detector: $\epsilon_A(E) = \epsilon_G \cdot \epsilon_I(E)$. The geometrical efficiency E_G is essentially a measure of how the detectors are arrayed, how much of the solid angle surrounding the source is covered by material that may detect the gamma-ray. The intrinsic efficiency $E_I(E)$ is a measure of how likely the detector material is to absorb the incoming gamma-ray, which depends upon the energy of the photon. While these factors may in principle be determined independently, it is usually easier to measure the combined absolute efficiency directly.

Typically, the procedure to determine absolute efficiency is to use an "absolutely calibrated" source, whose activity at a specific point in time was precisely known, and determine

its current activity over a span of time by applying the known half life. Then, it is possible to count the number of gamma-rays in a given photopeak detected during the interval and compare it to the expected yield of gamma-rays for that photopeak using the radiation law: $N_{peak}(t) = I_{peak} \cdot R_o e^{-\ln(2)t/T_{1/2}}$, where R_o is the activity measured at the point at which the source was absolutely calibrated, t is the time since that point, $T_{1/2}$ is the half-life of the source, I_{peak} is the branching intensity of the photopeak being measured (that is, the absolute intensity of that gamma-ray per decay of the source), and N_{peak} is thus the expected number of counts in that peak. The absolute efficiency then is simply determined as $N_{counted}/N_{expected}$. This process can be performed for a number of peaks and an analytic *efficiency curve* may be produced from a fit of the data, allowing for determination of absolute efficiency anywhere on the curve.

In cases where an absolutely calibrated source is not available, it is not possible to produce an absolute efficiency curve. However, the *relative efficiency* of the detector array as a function of energy may still be determined, since the ratios of efficiencies at any two energies is constant. In this case, the experimenter can simply measure the photopeak integral at an anchor-point energy and use the absolute intensity of that gamma-ray to produce a floating "anchor" for the rest of the curve. For example, the efficiency could be set to unity; then the relative efficiency of lower-energy peaks would be comparably higher and the relative efficiency of higher-energy peaks would be lower, with the curve overall retaining the same shape as an absolute efficiency curve.

As with the energy calibration case, standard calibration sources typically do not produce gamma-rays of sufficient energy for precision determination of an efficiency calibration curve over a large range of energies. In the case of E12028, we had ^{32}Cl data up to 7189 keV and the ^{152}Eu calibration source data below 1400 keV. We produced a relative efficiency curve

for our data using these two datasets. The ^{152}Eu was used to produce a curve up to 1400 keV. This curve was then extrapolated by extending the function up to 1547 keV, where the first ^{32}Cl photopeak was anchored to the ^{152}Eu curve. The relative intensities of the ^{32}Cl photopeaks [73, 76] were then used to extend the curve from 1547 keV to 7189 keV, producing a relative efficiency curve over the entire energy range of our data. The specific shape of this curve was an exponential of the form $\epsilon(E) = \exp[\Sigma_i A_i ln(E)^i]$, where $\epsilon(E)$ is the efficiency at a given energy E and the exponential contains a polynomial of order i with argument $ln(E)$, the natural log of the energy. The energy curve and uncertainty envelope is shown in Fig. 5.4.

5.2.5 Efficiency/Intensity Systematics

Although the ^{152}Eu source was absolutely calibrated, our procedure for determining the absolute intensities of the gamma-rays only required relative efficiencies, so we did not propagate the error due to the calibrated activity of the source. However, our derived intensities still relied on data from Ref. [73] and our own calibration procedure, so it was necessary to propagate uncertainties in the efficiency through the intensity calculation. To do this, we included a flat efficiency uncertainty of 0.7% across all energies based on variations in the photopeak integral as a result of variations in the peak fitting procedure, an uncertainty of 0.2% for $E_\gamma < 1547$ keV from spread between the data points used for calibration and the calibration curve itself in the ^{152}Eu data, a flat 1.4% uncertainty for $E_\gamma > 1400$ keV from the extrapolation of the ^{152}Eu data to 1547 keV, and the energy-dependent uncertainty envelope values above $E_\gamma = 1547$ keV taken from Ref. [73]: 0.4% for $1.5\text{MeV} < E_\gamma < 3.5$ MeV, 1% for $3.5\text{MeV} < E_\gamma < 5$ MeV, and 5% for $E_\gamma > 5$ MeV. The envelope from these combined uncertainties is shown along with the efficiency curve in Fig. 5.4.

χ^2 / ndf	4.562 / 9
Prob	0.8707
p0	8.399 ± 0.01096
p1	-0.7796 ± 0.001724
p2	-0.1023 ± 0.0002485
p3	$-0.0003201 \pm 3.486e\text{-}05$
p4	$0.001498 \pm 4.699e\text{-}06$
p5	$0.0001753 \pm 6.184e\text{-}07$
p6	$-2.632e\text{-}05 \pm 7.636e\text{-}08$
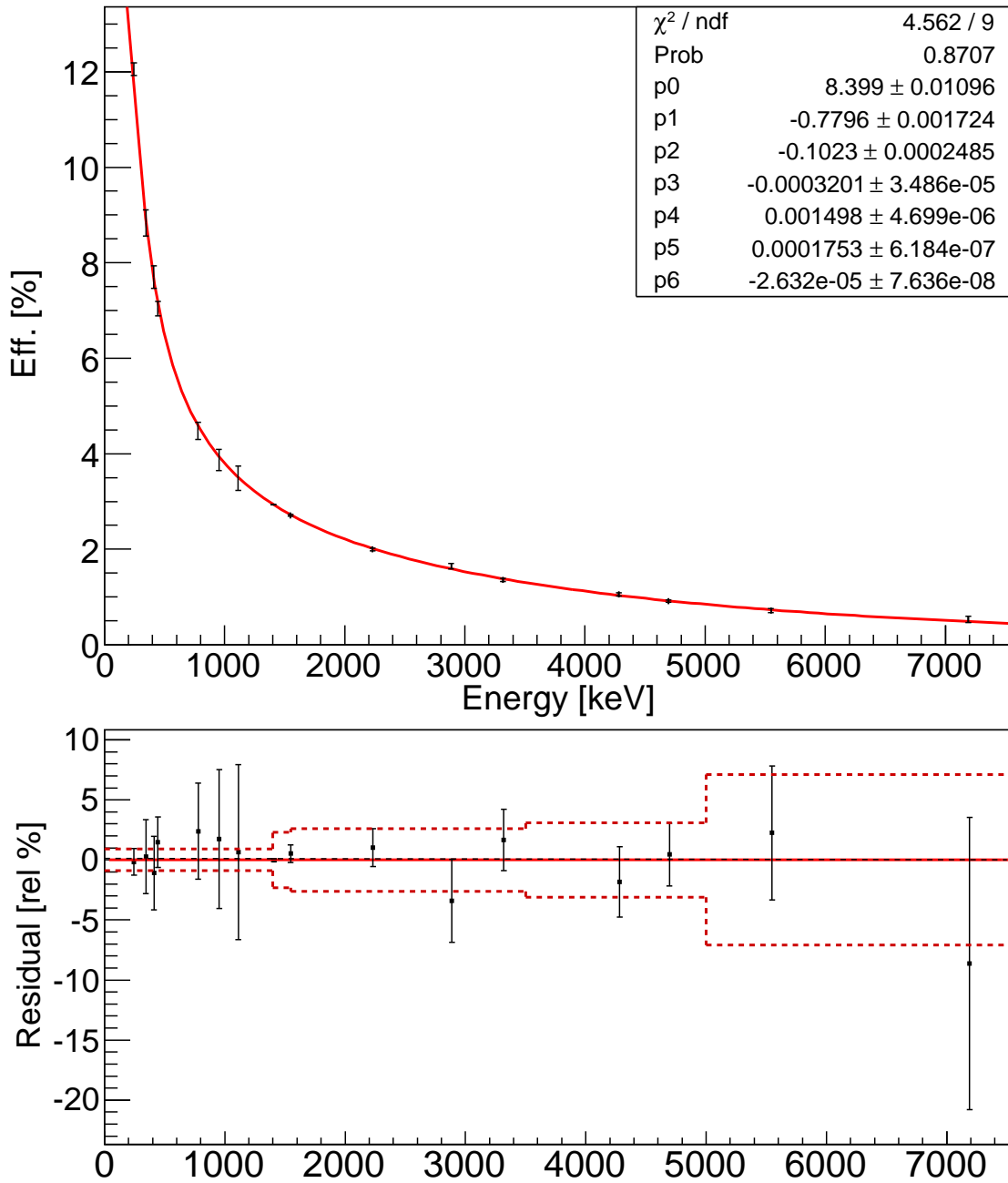
Figure 5.4: Upper panel: the efficiency curve generated from fitting the relative efficiencies of the ^{152}Eu and ^{32}Cl data. The polynomial required six terms, listed in the box at top-right along with the reduced chi-squared value and the p-value for the fit. Lower panel: the uncertainty envelope adopted across the energy region, based on the envelope in Ref. [73] and the other considerations detailed in the text.

In addition to the systematic uncertainty derived from our efficiency calibration proce-
dures, we also included a uniform 1% uncertainty in the efficiencies at all energies due to
summing. In the event that multiple gamma-rays enter a detector simultaneously, they may
be detected simultaneously, resulting in a recorded energy that is higher than the actual
energy of either gamma ray. Even if one of the two gamma rays only deposits some of
its energy, scattering out of the detector afterward, it will cause the apparent photopeak
intensity of the other gamma to decrease, as an event of the particular photopeak energy
will no longer be recorded. To arrive at the 1% uncertainty, we simulated the interaction of
gamma-rays in the clover detector over a range of energies and recorded the total efficiency
of the gamma in the detector (that is, we integrated the entire simulated spectrum, not just
the photopeak). This 1% uncertainty was factored into the photopeak intensities used to
determine the branching ratios and absolute efficiencies for each transition.

5.3   Data Reduction and Final Results Spectra

We obtained cumulative spectra for both the central scintillator and the surrounding 36
clover crystals. The cumulative scintillator spectrum is shown and described in Figure 5.5.
Because the purpose of the scintillator was only to gate out room background, we did not
need to calibrate its energy scale. The software gate, as described above, loops over all events
within the event window and determines whether they meet the gate criteria. If an event
meets the gate criteria (for example, "the event occurs within a certain detector" or "the
event occurs within a certain amount of time after or before another event"), the software
continues to process the other events in the event window according to the rules of the gate.
Typically, gates such as this are used to eliminate unwanted events while keeping good events
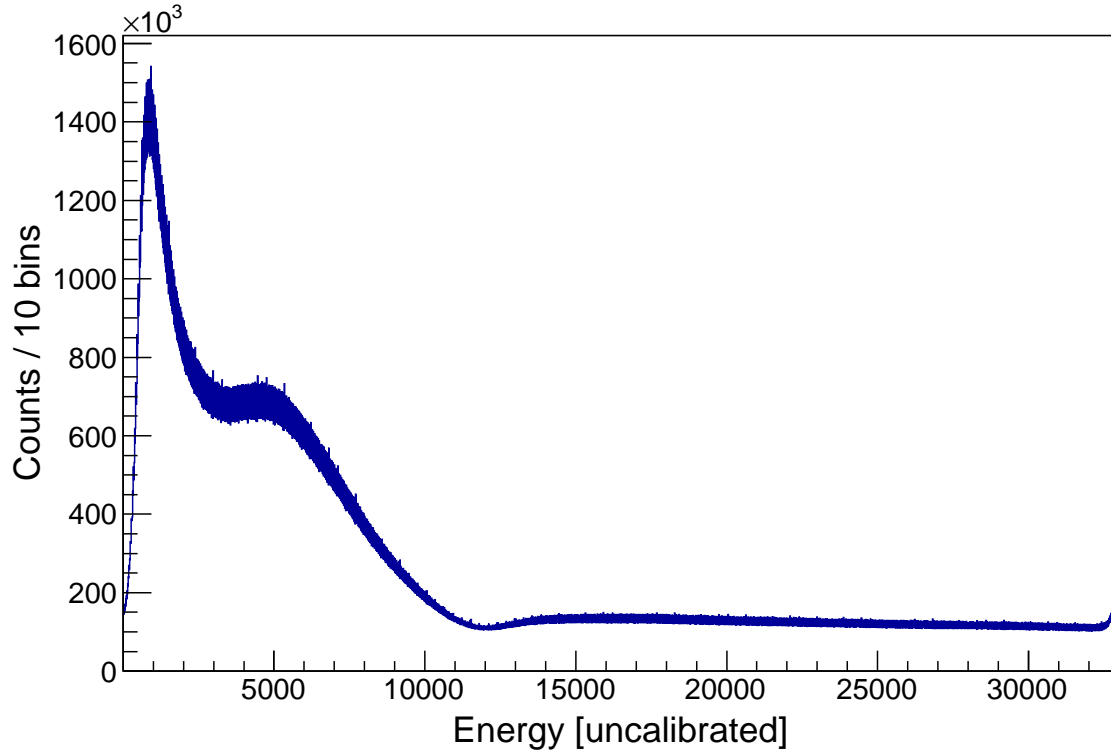
Figure 5.5: A histogram showing the uncalibrated scintillator energy spectrum. Because the central scintillator was only used to count the number of implants and decays and allow for gating of clover events, a calibration was not needed, although since the Q-value of the ^{31}Cl beta decay is approximately 12 MeV, it is likely that the uncalibrated spectrum, which appears to show a distribution of events similar to that expected for a 12-MeV beta endpoint energy, is close to any actual calibration that would be applied.

for processing – this procedure is known as *data reduction.*

In the case of the scintillator gate, we produced a spectrum plotting the time-stamp difference between events in the same window recorded in the scintillator and in any of the clover detectors, shown in Fig. 5.6. The vast majority of clover events related to ^{31}Cl decay occur very quickly after the decay itself, whereas clover events originating from other sources, such as room background, occur randomly throughout the event window. As shown in Fig. 5.6, this manifests as a broad plateau of *accidental coincidence* timing values, with a central *true coincidence* timing value peak. We gated on the central peak, a window of approximately 1μs as compared to the broad 10-μs plateau.
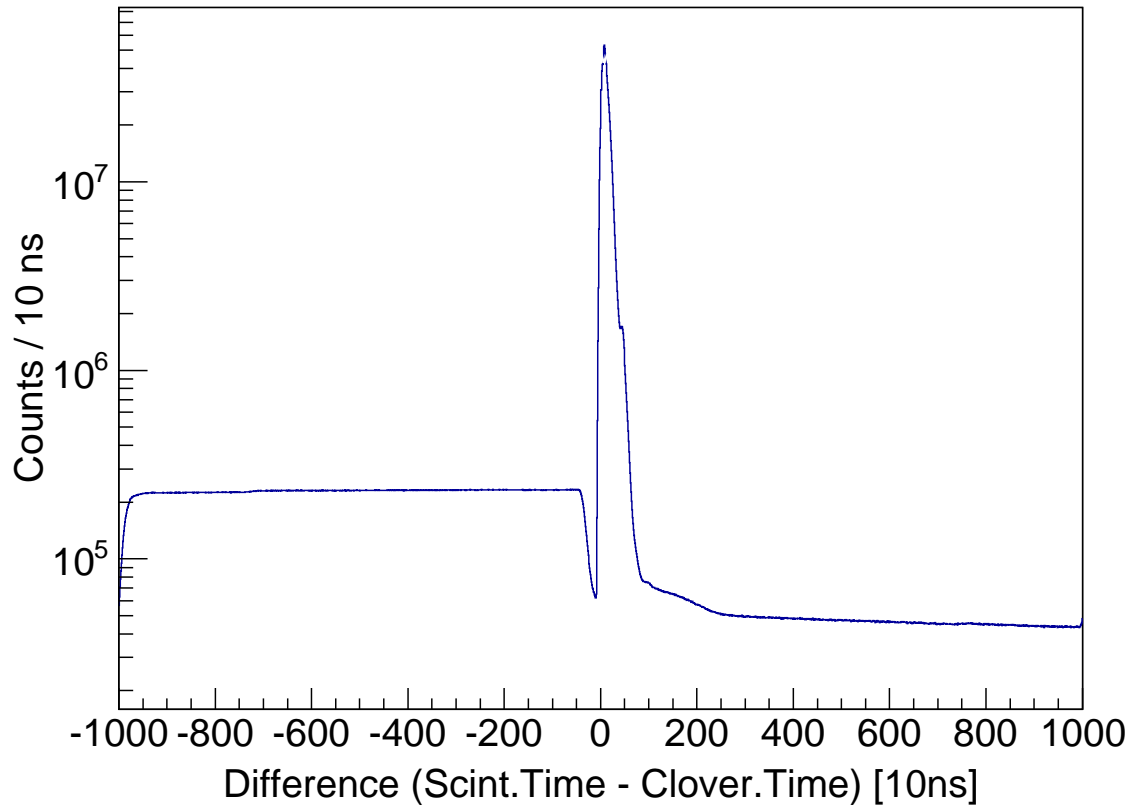
Figure 5.6: A histogram populated by calculating the time difference between an event in the scintillator and an event in any clover crystal. Most of the ^{31}Cl events occur in the large peak near the center of the plateau while the rest of the plateau events are likely caused by accidental coincidences. The trough to the left of the central peak and the higher plateau background to the left of the central peak are likely caused by reflections in the data connections between the detector and the DDAS.

As mentioned above, five clover crystals were found to be inappropriate for analysis and were not included in the calibration procedure. The remaining clover crystals were calibrated and gain-matched to produce the cumulative spectrum shown in Fig. 5.7. This spectrum represents the highest-statistics gamma-ray spectrum resulting from ^{31}Cl spectrum produced to-date by over two orders of magnitude. It has not been processed beyond the energy scale calibration (that is, there is no coincidence gate applied). Gating on the scintillator/clover timing peak produced a gamma spectrum with significantly reduced room background peaks and only very slightly reduced ^{31}S peaks. A comparison of the ungated and scintillator/timing gated spectrum (referred from this point forward as the "timing-gated spectrum," for the time difference), including an insert of a region with greatly-reduced background peaks, is shown in Fig. 5.8. The determination of gamma-ray energies and intensities for E12028 was carried out on this gated spectrum.
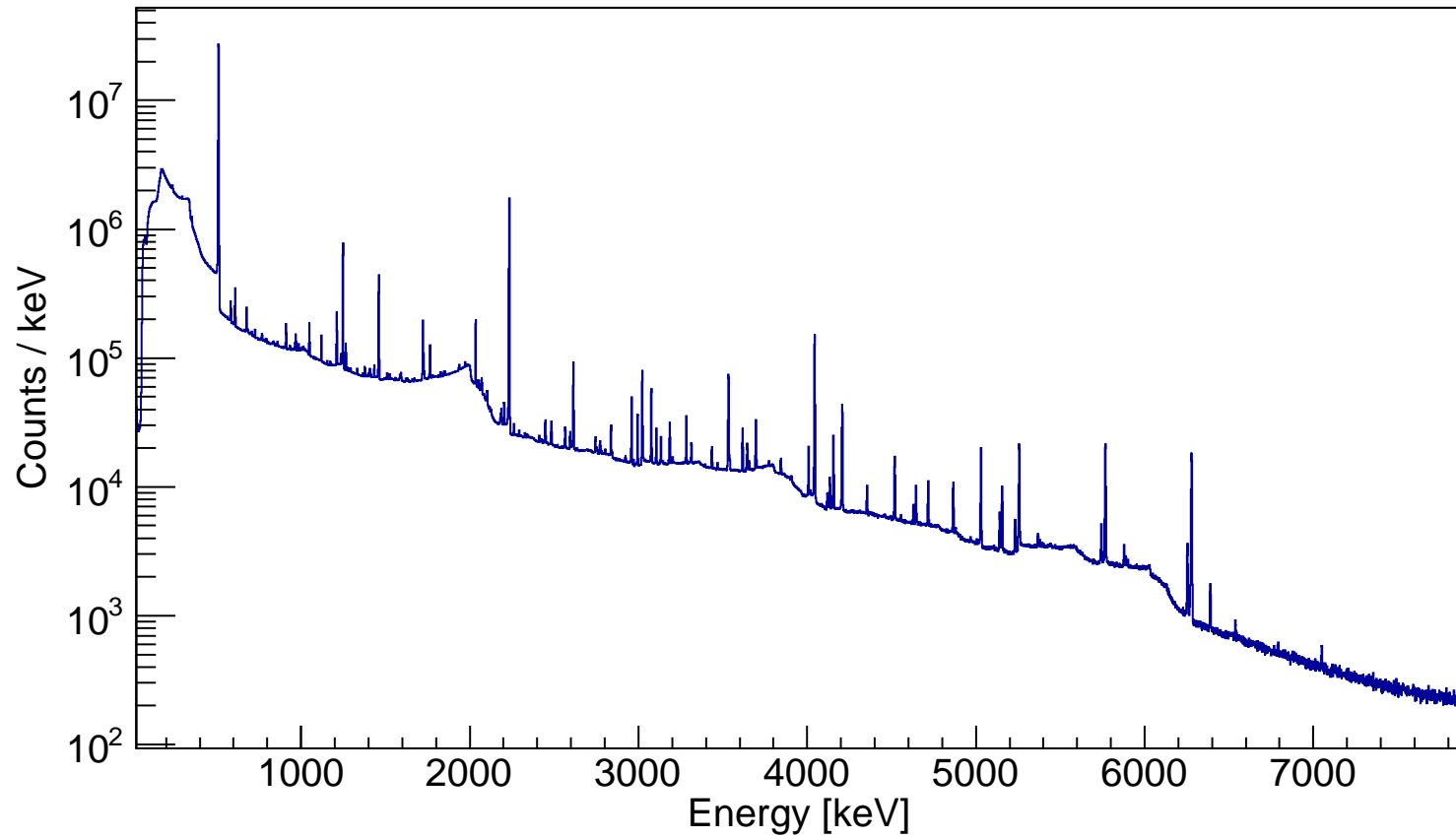
Figure 5.7: A histogram showing an energy-scale calibrated clover spectrum, including all 31 clovers used for analysis. This spectrum represents, by over two magnitudes, the highest-statistics ^{31}Cl beta-delayed gamma ray spectrum to date.
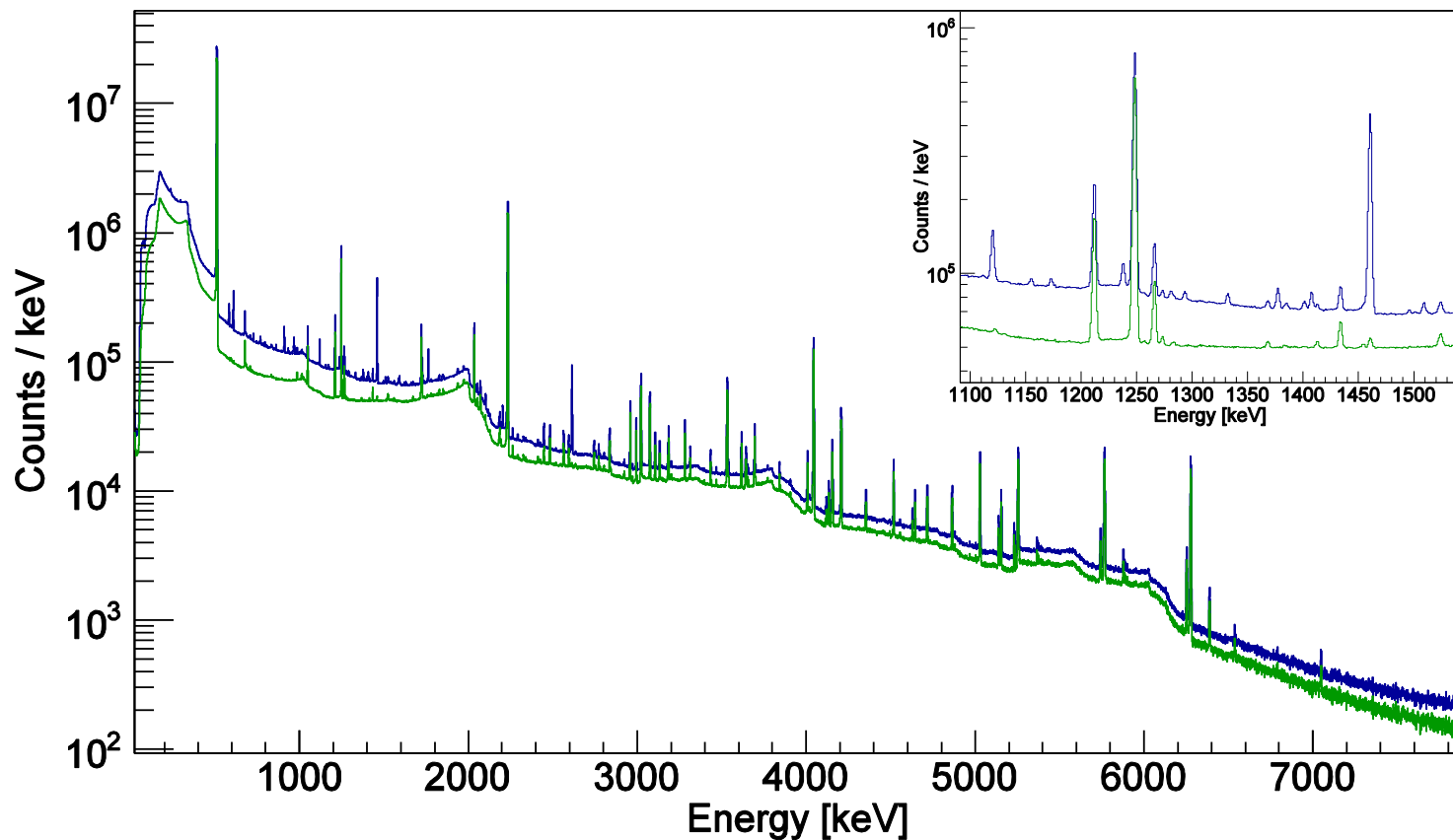
Figure 5.8: **Main figure:** A comparison of the scintillator-gated (blue) and timing-gated (green) clover spectra. As illustrated here, the background is reduced considerably, especially at lower energies, while the photopeak integral for ^{31}Cl events is only slightly reduced according to the efficiency of the scintillator to detect beta particles. **Inset:** A zoomed-in region between 1100 keV and ≈1600 keV, demonstrating the effects of the scintillator-timing gate compared to the scintillator-only gate. As illustrated here, several photopeaks caused by room background, including the very prominent 1460-keV peak, are almost completely eliminated.

5.3.1 Gamma Decay Selection Rules

While the beta decay selection rules discussed in Section 3.5.2 narrow the range of states which are likely to be populated in ^{31}Cl beta decay, they do not in principle affect how those states undergo gamma decay. The electromagnetic transition does not change the mass number of nucleonic composition of the nucleus, so it does not require specific isospin values between levels. However, there are a few gamma decay selection rules which affect the observed gamma branching of excited states; these will be discussed briefly here.

As with the Gamow-Teller beta decay transitions, the electromagnetic transition operator couples to nuclear spin J and prohibits $J = 0 \rightarrow J = 0$ transitions. Electromagnetic "allowed" transitions similarly have $\Delta J = 0, \pm 1$. However, unlike allowed beta decays, allowed gamma decays require a parity change, $\pi_f = -\pi_i$. To determine where this additional rule comes from, we can write out the transition probability for gamma decay [77]:

$$T_{fi}^{(\sigma \lambda \mu)} = \frac{2}{\epsilon_0 \hbar} \frac{\lambda + 1}{\lambda [(2\lambda + 1)!!]^2} \left(\frac{E_\gamma}{\hbar c} \right)^{2\lambda+1} |\langle \xi_f J_f m_f | \mathcal{M}_{\sigma \lambda \mu} | \xi_i J_i m_i \rangle|^2 \tag{5.2}$$

where E_γ is the gamma-ray energy and $\mathcal{M}_{\sigma \lambda \mu}$ is the matrix element associated with the transition. The indices σ, λ, and μ are the multipole radiation field numbers: σ delineates the electric field ($\sigma = $ E) or the magnetic field ($\sigma = $ M), and λ and μ are the l and m multipole numbers of the electromagnetic field spherical harmonics. It is possible to rewrite $\mathcal{M}$ in terms of the separate electric and magnetic components:

$$\mathcal{M}_{E\lambda\mu} = Q_{\lambda\mu}, \quad \mathcal{M}_{M\lambda} = M_{\lambda\mu} \tag{5.3}$$

where

$$Q_{\lambda\mu} = \zeta^{E\lambda} \sum_{j=1}^{A} e(j) r_j^{\lambda} Y_{\lambda\mu}(\Omega_j),$$

$$M_{\lambda\mu} = \frac{\mu_N}{\hbar c} \zeta^{M\lambda} \sum_{j=1}^{A} \left[\frac{2}{\lambda+1} g_l^{(j)} l(j) + g_s^{(j)} s(j) \right] \cdot \nabla_j [f_j^{\lambda} Y_{\lambda\mu}(\Omega_j)], \quad (5.4)$$

$e(j)$ the electric charge, r_j is the radius of the nucleon j, $Y_{\lambda\mu}(\Omega_j)$ is the spherical harmonic of order $\lambda\mu$, μ_N is the nuclear magneton $\frac{e\hbar}{2m_p}$, $l(j)$ and $s(j)$ are the orbital and spin angular momenta of nucleon j, g_l and g_s are the orbital and spin gyromagnetic ratios, $g_l = 1$ for protons and 0 for neutrons, $g_s = 5.586$ for protons and -3.826 for neutrons. $\zeta^{E\lambda}$ and $\zeta^{M\lambda}$ are phase factors, $\zeta^{E\lambda} = i^{\lambda}$ and $\zeta^{M\lambda} = i^{\lambda-1}$ [77].

From the above equations it can be seen that the electric and magnetic operators for the electromagnetic require different parity constraints: the parity of $Y_{\lambda\mu}$ is $(-1)^{\lambda}$, and the parity of r^{λ} is $+1$, so the parity of $r_j^{\lambda} Y_{\lambda\mu}$ and hence the electric transition of order λ, $E\lambda$, is $\pi = (-1)^{\lambda}$, where λ is the order of the transition. Similarly, since the parity of ∇ is -1 and the parity of $r_j^{\lambda} Y_{\lambda\mu}$ is $(-1)^{\lambda}$, the parity of the magnetic transition $M\lambda$ is $(-1)^{\lambda-1}$. These constraints are the origin of the parity selection rule and also help to infer the probability of transitions between different states.

Transition probability decreases by about approximately one order of magnitude per increasing order of multipolarity – thus, the most likely transitions are electric and magnetic *dipole* transitions, $E1$ and $M1$. Less likely than their respective dipole transitions by an order of magnitude are the *quadrupole* transitions $E2$ and $M2$ – however, the strengths of magnetic transitions are typically an order of magnitude weaker than the comparable electric transitions, meaning that $E2$ transitions compete not with $M2$ transitions but with $M1$. The "allowed" electromagnetic transitions referenced above can therefore be seen to correspond

to $E1$ transitions, while $M\lambda$ and $E\lambda$ ($\lambda \geq 2$) transitions can be thought of as the various orders of "forbidden" transitions.

In this way, experimenters can estimate the probability of transitions to a given lower energy state using the rule-of-thumb selection rules. In addition, the Q-value of the transition (in this case, the difference in energy between the two nuclear states) affects the probability of decay: a higher energy difference between the two states increases the probability that the photon will be created with the requisite angular momentum, and transitions between states with a large ΔJ but low Q-value proceed more slowly than transitions between states with the same difference in angular momentum but a greater difference in energy [2] In fact, a set of rule-of-thumb equations known as "Weisskopf estimates" [78] can be used to give a ballpark number for the expected number of gamma decays per second for electric and magnetic transitions of order l:

$$\lambda^{El} = C_{El}A^{2l/3}Q^{2l+1} \qquad \lambda^{Ml} = C_{Ml}A^{(2l-2)/3}Q^{2l+1} \qquad (5.5)$$

with coefficients [78]:

l	1	2	3	4	5
C_{El}:	$1.0 \cdot 10^{14}$	$7.3 \cdot 10^7$	$3.4 \cdot 10^2$	$1.1 \cdot 10^{-5}$	$2.4 \cdot 10^{-12}$
C_{Ml}:	$3.1 \cdot 10^{13}$	$2.2 \cdot 10^7$	$1.0 \cdot 10^1$	$3.3 \cdot 10^{-6}$	$1.0 \cdot 10^{-13}$.

These estimates include a number of simplifying assumptions, including that only one single proton changes states in the transition and that the final state of that proton has angular momentum 1/2. The methods used for estimating the transition strength matrix

---

[2] A notable example is the isomeric state of tantalum-180, ^{180m}Ta. The ground state of ^{180}Ta has spin and parity $J^{\pi} = 1+$, while the isomeric second excited state has $J^{\pi} = 9-$ but an excitation energy of only 77.2(12) keV. With only the ground state and the $J^{\pi} = 2+$ first excited state to which to decay, ^{180m}Ta is expected to have a half life no less than 10^{15} years.

element $\mathcal{M}$ in sophisticated computational tools such as the USD shell-model calculations performed for the analysis in the present work are much more complex, but have the same basic goal: provide probabilities for electromagnetic transitions between states in a given nucleus, which can be normalized in the form of gamma decay *branching ratios*, relative probabilities for a given state to decay to a given lower-energy state in a nucleus. These theoretical branching ratios may then be compared to those calculated from observed gamma transitions in an experiment.

5.3.2   Photopeak Identification – Building the Decay Scheme

As mentioned, E12028 produced a beta-delayed gamma-ray spectrum with statistics over two orders of magnitude higher than the two ^{31}Cl beta-decay studies to-date [56, 72]. The wealth of data proved invaluable to the construction of a new, more comprehensive and precise beta-decay scheme. However, the process of building the decay scheme was not without its challenges. Even though the ^{31}Cl beam was very pure (95%), the high intensity meant that even the small contaminant activity could produce detectable peaks in the gamma-ray spectrum. Even peaks that could not be positively identified as a product of contaminant processes were not assumed to come from ^{31}Cl decay. And even among those peaks that could be shown to be ^{31}Cl($\beta\gamma$) peaks, it was not known *a priori* where in the decay scheme to place them.

We utilized two methods of filtering out contaminant peaks and identifying and placing peaks corresponding to transitions from ^{31}Cl beta decay. First, we found that, when we applied the timing gate and compared the integrals of the gated peaks to the ungated peaks, the timing gate reduced known ^{31}Cl peaks by a constant factor, yielding a ratio of timing-gated intensity to ungated intensity of 0.806(7)%, a number ostensibly related to the beta

detection efficiency of the scintillator. This ratio was observed for a number of ^{31}Cl peaks over the entire energy range and is shown in Fig. 5.9. In comparison, peaks known to come from beam contaminants were found to have ratios that were different from this value, typically lower by $\approx$0.2%, ostensibly due to implantation depth (simulations performed prior to the experiment predicted that the ^{31}Cl would implant the farthest into the scintillator and that the contaminants, having lower energy, would implant at shallower depths). In this way, we were able to use the timing gate to infer that any given photopeak did or did not in fact come from ^{31}Cl decay, with a few notable exceptions that will be discussed in Section 5.4. A comprehensive beta-delayed gamma-ray spectrum with peak labels is shown in Fig. 5.10.

Second, because of both the high statistics and the large number of detectors, we were able to make great use of *gamma-gamma* coincidences. Similar to the beta-gamma coincidences, it is possible to gate on a range of specific gamma-ray energies (e.g., on a specific peak) and, when one clover crystal event within the event window falls inside that energy gate, process only those events that occur in different crystals of the detector, or even in different whole detectors. This gate can then be combined in the software with other gates, for example the scintillator timing gate, to reduce background even further. The benefit of gamma-gamma coincidence gates is in the identification of cascades: since cascading gamma-rays are emitted essentially simultaneously compared to the implantation and beta-decay rate, gating on one gamma-ray in a cascade will allow for the production of a spectrum with greatly reduced background, but with a strong enhancement of other gammas in the cascade. In the event that multiple cascades include de-excitation from a particular level, a gamma-gamma coincidence spectrum produced from gating on that de-excitation can yield much information about transitions from higher states. This kind of gate is particularly effective when applied
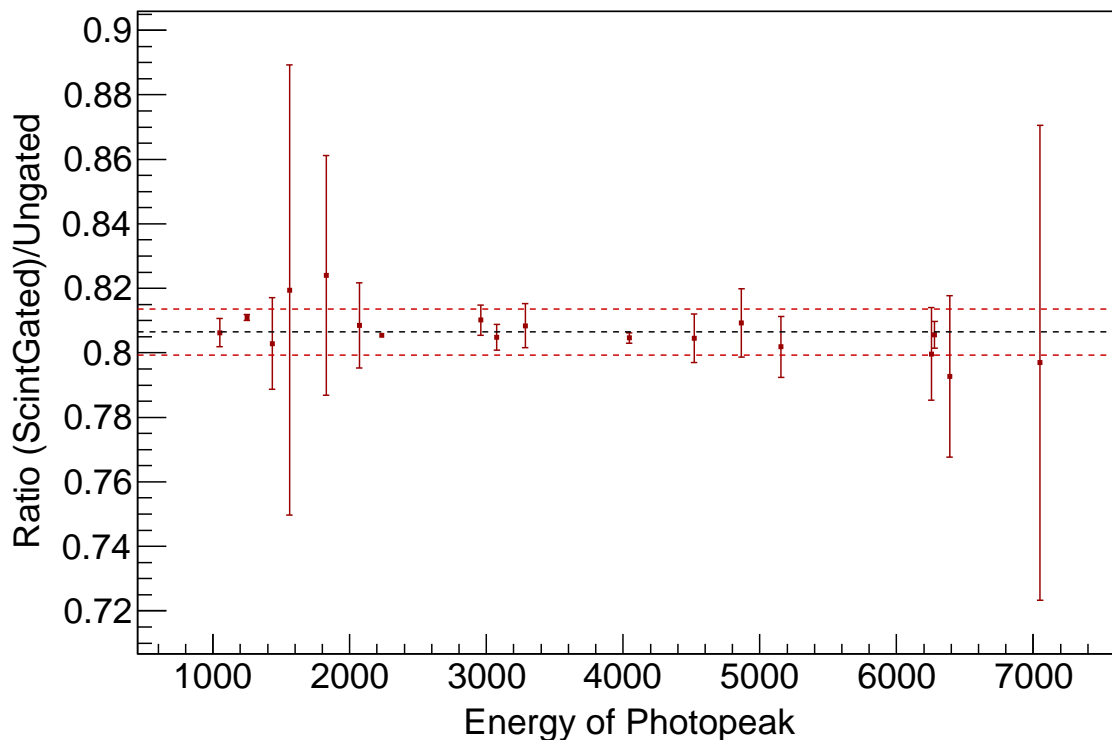
Figure 5.9: For photopeaks of several energies between 1 MeV and 7 MeV, the ratio of the measured photopeak intensity in the timing spectrum to the measured intensity in the ungated spectrum, the mean of the measurements (black dashed line, 80.6%) and the one-sigma envelope denoting the standard deviation of the points about that mean (red dashed lines, 0.7%). This figure illustrates that the scintillator efficiency was essentially constant over its entire energy range, regardless of the beta endpoint energy of any particular ^{31}Cl transition.
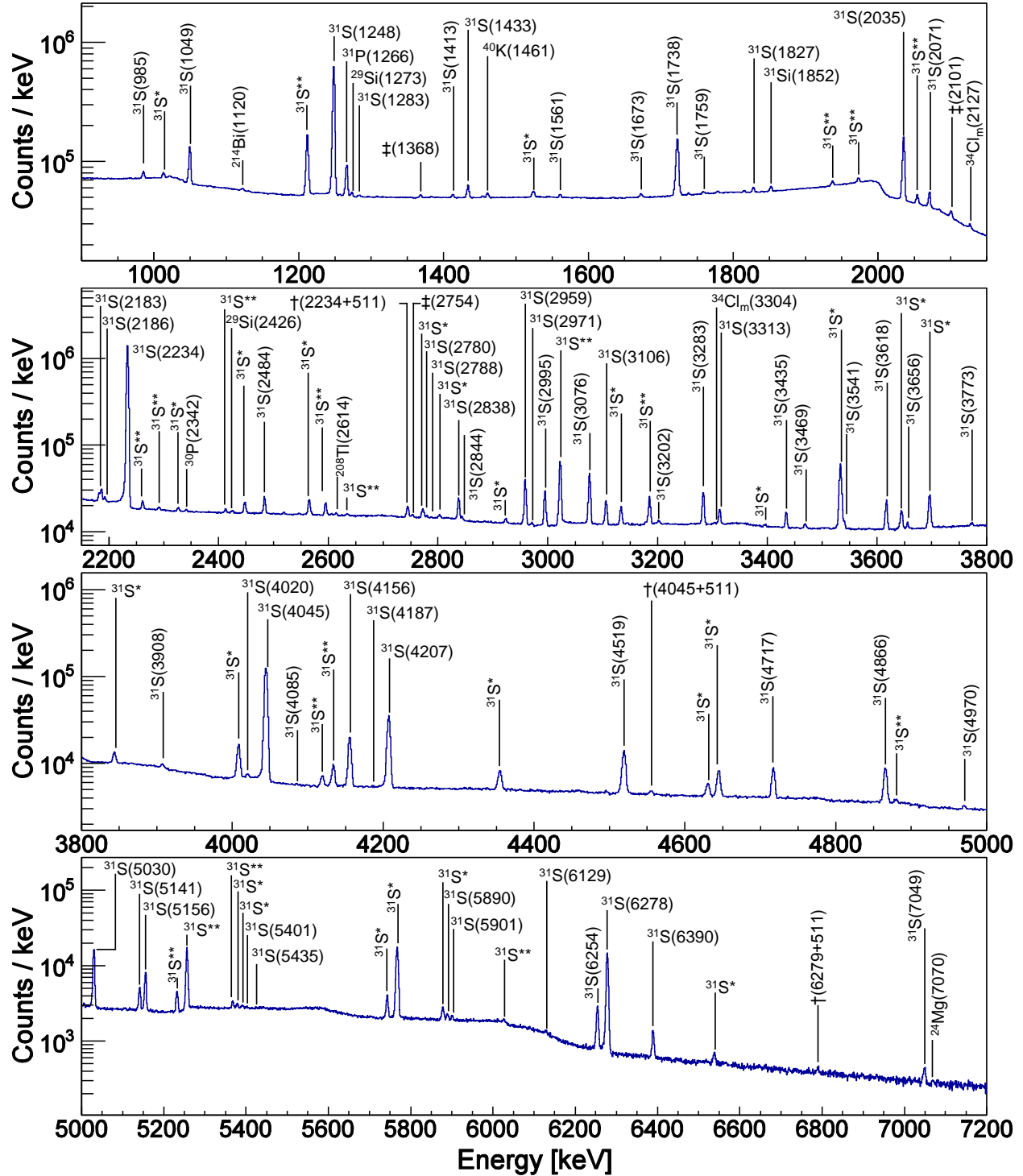
Figure 5.10: A comprehensive spectrum showing the assignments for the photopeaks used in analysis as well as those of identified beam contaminants. Each photopeak is labeled by the emitting nucleus and its energy. Peaks labeled with one or two asterisks correspond to single and double escape peaks, respectively. Peaks marked with a single dagger are sum peaks and the summation is noted, and peaks marked with a double dagger have multiple contributions and are discussed in detail in Section 5.4.

to lower excited states – the $\beta\gamma$ spectrum and a $\beta\gamma\gamma$ spectrum gated on the transition from the first excited state at 1248 keV is shown in Fig. 5.11.
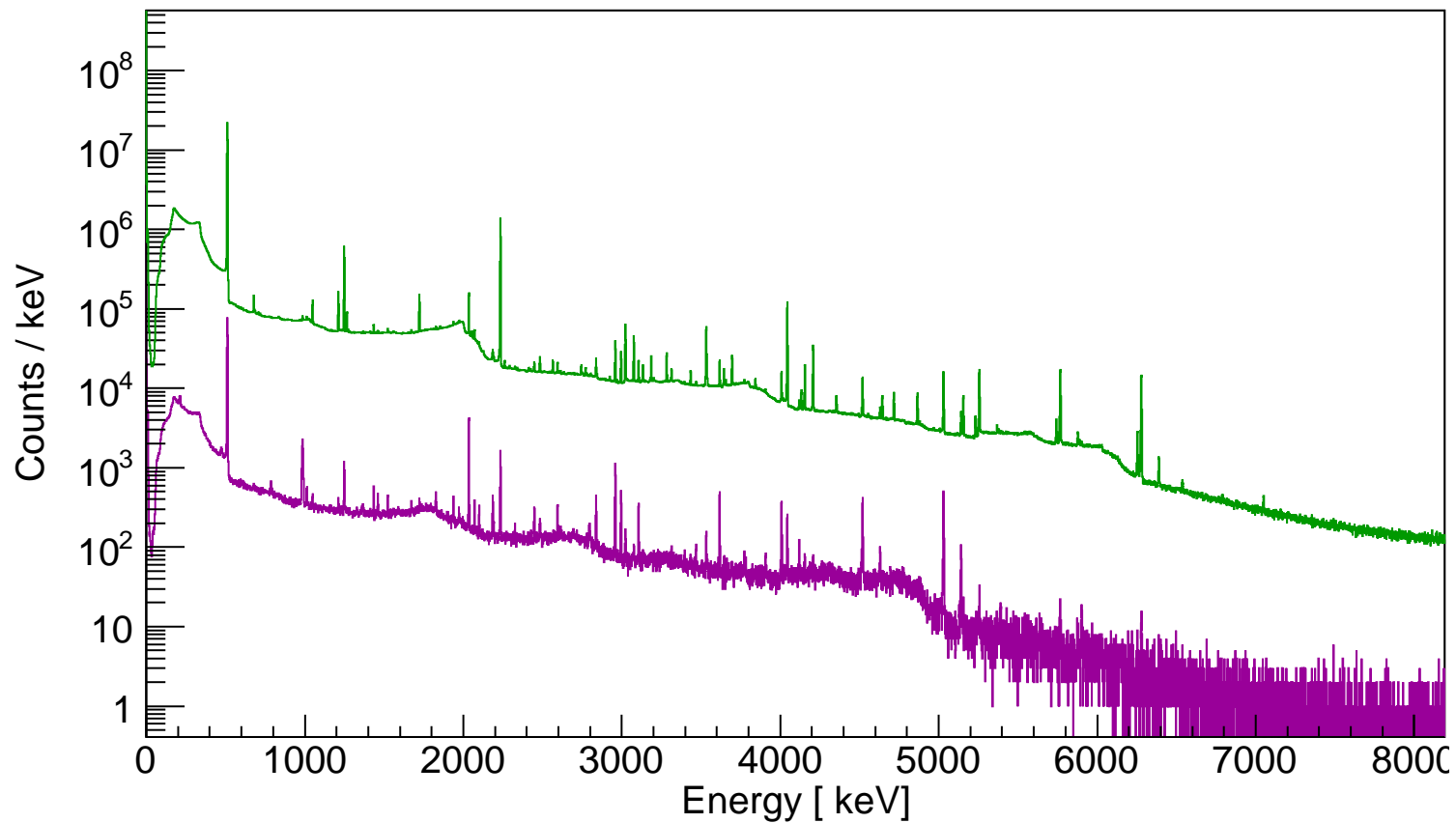
Figure 5.11: The timing-gated spectrum (green) and the timing-gated spectrum additionally gated on transitions from the first excited ^{31}S state, at $E_x = 1248$ keV, to the ground state. The overall statistics of the spectrum are reduced by several orders of magnitude, but several features are nonetheless visible, including enhanced peaks at energies corresponding to transitions to the 1248-keV state, such as the peaks at 985 keV ($2234 \rightarrow 1248$), 2035 ($3283 \rightarrow 1248$), and 5031 ($6279 \rightarrow 1248$). Many other peaks can be seen to be enhanced as well; these enhancements were used to help confirm the placement of several of the transitions shown in Fig. 5.12 and reported in Table 5.1.

5.3.3 Spin and Parity Assignments:

As mentioned in Chapter 4, ^{31}Cl beta decay selectively populates states with $J^\pi = 1/2^+, 3/2^+, 5/2^+$. This reduces the number of options for assigning spin and parity, but does not provide immediately unambiguous constraints. Typically, experimenters will use the results of complementary experiments to populate nuclear states and make spin and parity constraints. However, as discussed in Chapter 4, despite the relative wealth of experimental data on the resonances involved in the ^{30}P$(p,\gamma)^{31}$S, unambiguous constraints for the resonances are still elusive. In part this is due to conflicting spin and parity constraints from different experiments, so in order to approach the experimental study of these states free from the concerns of previous experiments, we utilized a partially theoretical method of assigning spin and parity.

Prior to the analysis of E12028, we performed shell-model calculations using the USDB interaction [38] to predict both the beta feedings of the various ^{31}S states populated in allowed ^{31}Cl beta-decay transitions and the gamma branchings for a number of positive-parity ^{31}S states, including those addressed in the beta-decay calculation. The results of these calculations are reported in Appendix A. During analysis, we then assigned spin and parity based on comparison between observed beta feedings and gamma branchings for each state (calculated according to the procedure in the following section) and those predicted by both the USDB calculations and by new USD calculations performed following the experiment (see discussion in Section 6.1).

Many of the ^{31}S states below the proton threshold that are populated by ^{31}Cl decay already have unambiguous J^π values, so they were used to confirm that the USD calculations were correct. Then, for the states with uncertain spin and parity, including states never seen

before in ^{31}Cl beta decay, we applied the USD results to make the spin and parity assignment. In some cases this allowed for a more definite assignment than is reported in the $A = 31$ Nuclear Data Sheets [79] (for example, the state at 3283 keV), and in one case, the state at 4867 keV, our assignment based on the shell-model calculations disagreed with the spin and parity reported in NDS ($J^\pi = 1/2^+$ in our analysis compared to $(1/2, 3/2)^-$ in NDS). For most states, the observed quantities and predicted quantities were in very good agreement; where the agreement was not very good, we have indicated a tentative assignment in the conventional way: (J^π) in parentheses. Again: no single reaction or decay experiment can absolutely determine the spins and parities of the important states, but relying on our shell-model calculations rather than the previous experimental work at the least allowed us the freedom to make complementary assignments independently of any precedents set by those experiments – which may or may not be accurate.

5.3.4   Beta Feedings and Gamma-ray Absolute Intensities

Constructing a beta decay scheme requires two things: beta feedings for each level and gamma intensities for each observed transition. The latter is often presented both in terms of relative gamma branchings for each level, denoting the relative intensity of all gamma-rays that de-excite a level, and in terms of absolute gamma-ray intensity per unit beta decay, denoting the number of times per single decay (or 100, for example), that a gamma-ray of that energy will be detected.

The typical procedure for determining absolute intensity of a given gamma-ray per beta decay is simply to count the number of gamma-rays observed, use the detector efficiency to determine an absolute photopeak intensity, and then divide by the number beta decays observed. One common method for determining the number of implants and thus the number

of ^{31}Cl decays is simply to count the number of ^{31}Cl ions that pass through the PIN detector in the PID spectrum, giving the number of implanted ^{31}Cl ions. Then, the beta-detection efficiency of the central detector (in this case the scintillator) can be used to scale this number to arrive at the number of decays that result in detected gamma-rays in the beta-gamma spectrum.

Determination of beta feedings is a slightly more involved process because a given energy level can be populated both by beta feeding and by gamma de-excitation from higher levels. Since it is not known *a priori* which of the two processes a de-exciting gamma ray originates from, the absolute photopeak intensity cannot be used by itself to determine the beta feeding of the level. Instead, the procedure for a given level is to sum the intensities of all gammas de-exciting the level, then subtract the sum of all gammas feeding the level. The assumption here is that every gamma feeding the level will result in a gamma de-exciting the level as well, which is a valid assumption for levels below the proton threshold, where gamma decay is the only energetically allowed channel. The resulting quantity is the number of gamma-rays de-exciting the level *not* from gamma feeding; each of these gammas must therefore come from a beta decay which feeds the level. So, the beta branch for the state is typically calculated by dividing this value, which represents the number of beta decays feeding the level, by the total number of beta decays.

In the case of E12028, both of these processes were complicated by the fact that the PIN detectors had to be extracted from the beamline for the majority of the experiment. Thus, any normalization to the estimated number of implanted ^{31}Cl ions would be approximate and potentially inaccurate. In addition, since we only used a relative efficiency curve, we did not have absolute photopeak efficiencies for the observed gamma-ray transitions, making determination of the absolute number of gamma rays in any given photopeak difficult.

Instead, we circumvented calculations using the number of beta decays and performed a normalization for the beta feedings and absolute gamma-ray intensities per beta decay entirely from the measured gamma-ray photopeak intensities.

To calculate the beta feeding for each level, we first adopted branches for the beta decay to the ground state (which cannot be determined from ^{31}S gamma de-excitations as there are none to measure), beta-alpha and beta-proton emission (since a number of decays are above the emissions threshold for these two particles), and estimated unseen beta-gamma branches. Following Ref. [56] we adopted a 7(2)% beta feeding for the ground state; this value is based on the ^{31}Si beta decay branch to the ^{31}P ground state, the mirror process for ^{31}Cl beta feeding of the ^{31}S ground state. This value was corroborated by a 7.9% ground-state beta feeding in the USD shell-model calculation we performed to help interpret the data we generated (Section 5.3.3). The beta-alpha and beta-proton branch we adopted, 1.4(6)%, was based on improvements to the value used in Ref. [56] by Ref. [72] and our shell model calculations. We estimated a conservative 0.5(5)% branch for unseen gamma rays based on comparisons between the gamma branches we expected our from shell model calculations and what we actually observed.

We summed these branches to a total 8.9(22)% for unobserved beta feeding and, reasoning that the remaining beta feeding was split between the levels from which gamma decay was observed, used the remaining 91.1(22)% of the beta feeding as the total feeding for all observed levels. Then, we subtracted the relative intensity of the gamma-ray transitions feeding the level from the relative intensity of the gamma-ray transitions de-exciting the level. These adjusted relative intensities for each level were then all summed together to give the total relative number of beta decays, and the beta branchings were determined by taking the ratio of each level's subtracted relative gamma feedings to the total sum of all

subtracted relative gamma feedings.

The absolute gamma-ray intensities per decay were then determined according to the formula:

$$I_{\gamma,abs,i} = I_{\gamma,rel,i} \cdot \frac{100 - (I_{\beta p} + I_{\beta \alpha} + I_{\beta,g.s.} + I_{\gamma,unsn})}{(\Sigma_n I_{\gamma n,all} - I_{\gamma m,all}) + \Sigma_j I_{\gamma,rel,j}} \tag{5.6}$$

where $I_{\gamma,abs,i}$ is the absolute intensity of transition i per unit beta decay, $I_{\gamma,rel,i}$ is the relative intensity of the transition, determined from the integral and the efficiency curve, $I_{\beta p}$ and $I_{\beta \alpha}$ are the beta-proton and beta-alpha branches, respectively, $I_{\beta,g.s.}$ is the ground-state beta branch, $I_{\gamma,unsn}$ is the adopted unseen gamma branch, $\Sigma_n I_{\gamma n,all}$ is the sum of all adjusted relative intensities for each level n (the total relative number of beta decays), $I_{\gamma m,all}$ is the adjusted relative intensity of the level m which transition i de-excites, and $\Sigma_j I_{\gamma,rel,j}$ is the sum of all transitions j de-exciting level m. The uncertainty on this value factored in the uncertainty in the adopted non-observed-gamma branches (essentially a purely systematic uncertainty), the statistical and systematic uncertainties of the relative gamma-ray intensities, and the uncertainties propagated through the derivation of the adjusted relative gamma intensities for each level.

With these quantities, and using the analysis tools mentioned above, we were able to produce a beta decay scheme with 62 total gamma-ray transitions – over twice as many as the number of transitions reported in the 2012 $A = 31$ Nuclear Data Sheets [79], which reported 29 transitions, and in the most recent ^{31}Cl beta-decay study [72], which reported 27. In addition, we observed beta-decay transitions to ten levels previously unobserved in ^{31}Cl beta decay. A full decay scheme with beta intensities and gamma-ray energies and relative branching ratios is shown in Fig. 5.12, and lists of all ^{31}S gamma-ray transitions observed

in the decay, including their energies and absolute intensities, are reported in Tables 5.1 and 5.2. These results, including the effect on the $^{30}\text{P}(p, \gamma)^{31}\text{S}$ reaction rate, will be discussed in-depth in Chapter 6.

5.4 Analysis Anomalies

In any analysis procedure, cases requiring special attention will often crop up. In building the ^{31}Cl decay scheme and determining the absolute gamma-ray intensities and beta feedings, for example, several cases occurred which required modification of the general analysis technique described above. Here we discuss the analysis procedures used to determine the quantities reported in Fig. 5.12 and Table 5.1. First, we will discuss the observation of so-called "forbidden transitions," gamma-ray transitions corresponding to beta decays populating states forbidden by the Fermi and Gamow-Teller selection rules (Section 3.5.2). We will also discuss the amended analysis procedures used when gamma-ray photopeaks from multiple sources overlap in the energy spectrum. The significance of these findings is discussed in Chapter 6.

5.4.1 Forbidden Transitions: The Levels at 3349 keV and 4970 keV

A cursory analysis of the ^{31}Cl beta decay scheme (Fig. 5.12) shows that while most of the spin and parity assignments of ^{31}S states observed enable them to be populated by the beta-decay selection rules for allowed transitions, two states, the states at 3349 keV and 4970 keV, were assigned spins and parities of $J^{\pi} = 7/2^{+}$ and $3/2^{-}$, respectively. Only $1/2^{+}, 3/2^{+}$, and $5/2^{+}$ states are allowed by the selection rules of beta decay from the $3/2^{+}$ ^{31}Cl ground state;
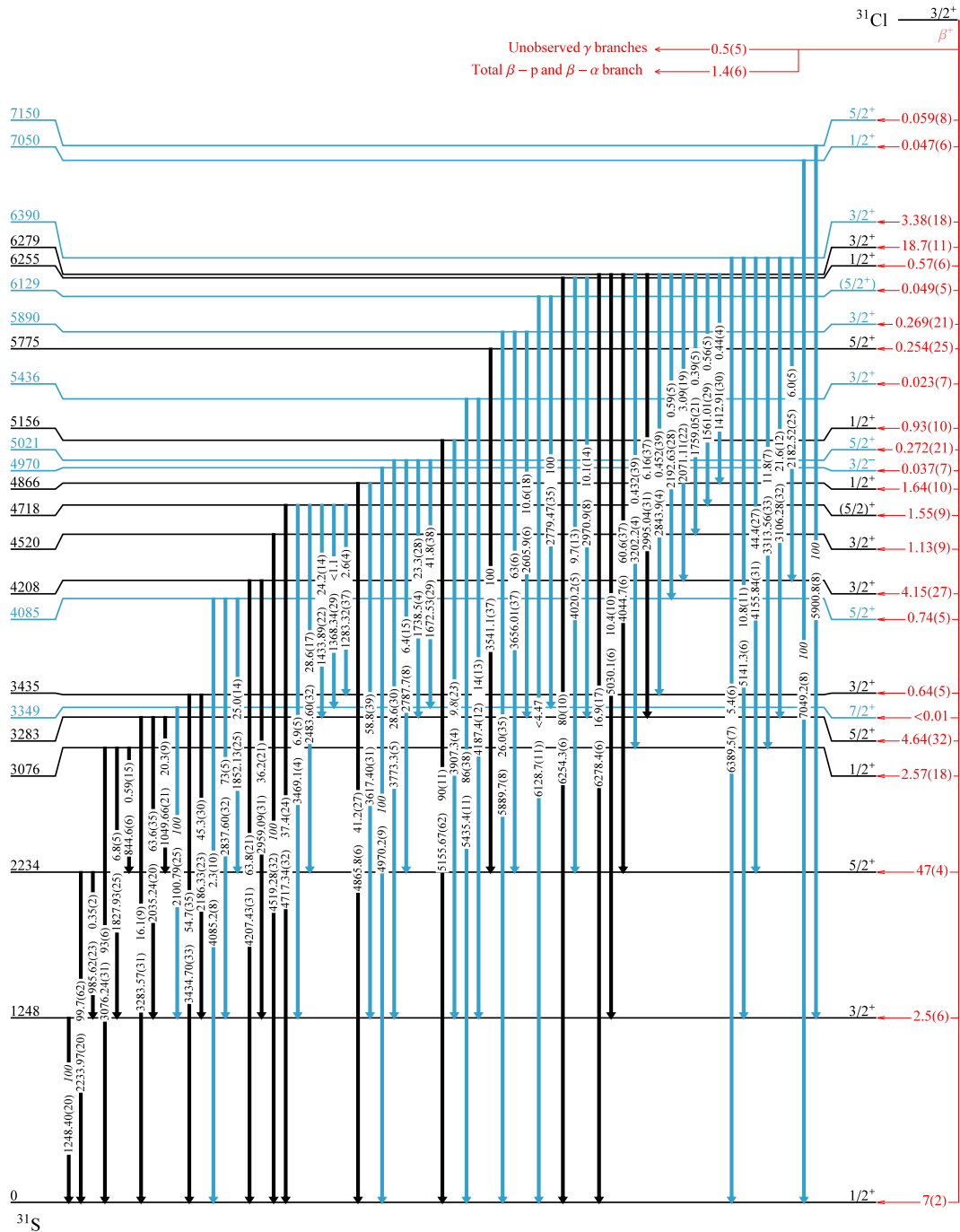
Figure 5.12: The final, comprehensive ^{31}Cl decay scheme produced from the analysis of E12028. For each level, the level's energy rounded to the nearest keV is reported on the left wing of the level and its spin and parity J^π are reported on the right wing. The precise excitation energies E_x of each level are reported in Table. 5.1. Each beta decay transition is depicted by a red arrow on the right side and includes its beta feeding I_β, also reported in Table 5.1. Blue coloring for a level indicates that the level has never been observed in ^{31}Cl beta decay before.

Fig. 5.12 (cont'd) Gamma-ray transitions between ^{31}S levels are also denoted in the table by the vertical arrows. Each transition includes the gamma-ray energy E_γ and branching ratio (B.R.), which are both reported in Table 5.1. As with the populated levels, gamma transitions which have never been observed in ^{31}Cl beta decay before are colored blue. The scheme also reports the adopted branches for beta-proton and beta-alpha and unobserved gamma-rays.

transitions to these two states are known as *forbidden* transitions because they violate the selection rules discussed in Section 3.5.2: in the case of the $3/2^+$ state, the parity selection rule is violated, $\pi+ \to \pi-$ (a *first forbidden* transition), and in the case of the $7/2^+$ state, $\Delta J = 2$ instead of 0 or 1 (a *second forbidden* transition). As mentioned in Section 3.5.2, however, the *forbidden* appelation does not mean impossible, simply proceeding at a greatly reduced rate. The high statistics of E12028 therefore potentially allow for observation of these transitions. We will discuss here the analysis procedure for, and interpretation of, both of these levels.

5.4.1.1 4970-keV Level

We observed a gamma ray at a photopeak energy of $E_\gamma = 4970.2(9)$ keV (reported in Table 5.1). It was not observed to be in coincidence with any other gamma ray, and the ratio of its gated intensity to its ungated intensity was found to be consistent with the average ratio of 0.806(7), indicating a likely origin from ^{31}Cl beta decay. The $A = 31$ Nuclear Data Sheets [79] report a state at $E_x = 4971(3)$ based on a number of nuclear reaction experiments, some of which were discussed in Chapter 4 [80, 81, 82, 83, 84, 85] with a spin and parity assignment $J^\pi = 3/2^-$; none of these experiments, however, measured gamma-ray transitions. We calculated a beta feeding for this level of 0.037(7), which yields, using the same procedure as for the 6279-keV and 6390-keV states, a $\log(ft_{1/2})$ value of 6.61, which is consistent with the interpretation that this level was fed via the first-forbidden beta

Table 5.1: ^{31}S level excitation energies E_x, beta-decay intensities I_β and corresponding $\log(ft)$ values, and transitions from each level observed to be populated in the beta decay of ^{31}Cl (the designation J_n^π denotes the nth state of a given spin and parity). Also included for each transition are the gamma-ray energies E_γ, relative gamma-ray branching ratios (B.R.), and absolute gamma-ray intensity per 100 beta decays, I_γ.

E_x	I_β	$\log(ft)$	Transition	E_γ	B.R.	I_γ
1248.43(20)	2.5(6)	5.8	$3/2_1^+ \to 1/2_1^+$	1248.40(20)	100	12.3(5)
2234.06(20)	47(4)	4.3	$5/2_1^+ \to 1/2_1^+$	2233.97(20)	99.7(62)	53.2(27)
			$5/2_1^+ \to 3/2_1^+$	985.62(23)	0.35(2)	0.187(9)
3076.40(31)	2.58(18)	5.3	$1/2_2^+ \to 1/2_1^+$	3076.24(20)	93(6)	2.82(14)
			$1/2_2^+ \to 3/2_1^+$	1827.93(25)	6.8(5)	0.205(14)
3283.76(31)	4.64(32)	5.0	$5/2_2^+ \to 1/2_1^+$	3283.57(31)	16.1(9)	1.11(6)
			$5/2_2^+ \to 3/2_1^+$	2035.24(20)	63.6(35)	4.38(22)
			$5/2_2^+ \to 5/2_1^+$	1049.66(21)	20.3(9)	1.40(5)
3349.30(32)	< 0.01	¿7.7	$7/2_1^+ \to 3/2_1^+$	2100.79(25)	100	0.076(14)
3434.90(33)	0.64(5)	5.8	$3/2_2^+ \to 1/2_1^+$	3434.70(32)	54.7(35)	0.420(24)
			$3/2_2^+ \to 3/2_1^+$	2186.33(33)	45.3(30)	0.348(21)
4085.4(8)	0.74(5)	5.6	$5/2_3^+ \to 1/2_1^+$	4085.2(8)	2.3(10)	0.019(8)
			$5/2_3^+ \to 3/2_1^+$	2837.60(32)	73(5)	0.614(34)
			$5/2_3^+ \to 5/2_1^+$	1852.19(25)	25.0(14)	0.211(14)
4207.7(31)	4.15(27)	4.8	$3/2_3^+ \to 1/2_1^+$	4207.43(31)	63.8(21)	3.12(18)
			$3/2_3^+ \to 3/2_1^+$	2959.09(31)	36.2(21)	1.77(9)
4519.63(32)	1.13(9)	5.3	$3/2_4^+ \to 1/2_1^+$	4519.28(32)	100	1.20(7)

Table 5.1 (cont'd)

4717.72(32)	1.55(9)	5.1	$5/2_4^+ \to 1/2_1^+$	4717.34(32)	37.5(24)	0.618(37)
			$5/2_4^+ \to 3/2_1^+$	3469.13(31)	6.9(5)	0.113(8)
			$5/2_4^+ \to 5/2_1^+$	2483.60(22)	28.7(17)	0.472(26)
			$5/2_4^+ \to 5/2_2^+$	1433.89(22)	24.3(14)	0.399(22)
			$5/2_4^+ \to 7/2_1^+$	1368.34(29)	≤ 1.1	≤ 0.018
			$5/2_4^+ \to 3/2_2^+$	1283.32(37)	2.6(4)	0.043(7)
4866.2(6)	1.64(10)	5.0	$1/2_3^+ \to 1/2_1^+$	4865.8(6)	41.2(27)	0.71(4)
			$1/2_3^+ \to 3/2_1^+$	3617.40(31)	58.8(39)	1.01(6)
4970.7(9)	0.037(7)	6.6	$3/2_1^- \to 1/2_1^+$	4970.2(9)	100	0.037(7)
5021.9(5)	0.273(21)	5.7	$5/2_5^+ \to 3/2_1^+$	3773.2(5)	28.6(30)	0.078(7)
			$5/2_5^+ \to 5/2_1^+$	2787.7(8)	6.4(15)	0.0173(39)
			$5/2_5^+ \to 5/2_2^+$	1738.52(36)	23.3(28)	0.063(7)
			$5/2_5^+ \to 7/2_1^+$	1672.53(29)	41.8(38)	0.114(9)
5156.1(6)	0.93(10)	5.2	$3/2_3^+ \to 1/2_1^+$	5155.7(62)	90(11)	0.84(8)
			$3/2_3^+ \to 3/2_1^+$	3907.3(4)	9.8(23)	0.091(8)
5435.9(9)	0.023(7)	6.6	$3/2_5^+ \to 1/2_1^+$	5435.4(9)	86(38)	0.020(7)
			$3/2_5^+ \to 3/2_1^+$	4187.4(15)	14(5)	0.0034(7)
5775.4(4)	0.254(25)	5.5	$5/2_6^+ \to 5/2_1^+$	3541.10(27)	100	0.254(21)
5890.3(8)	0.269(21)	5.4	$3/2_6^+ \to 1/2_1^+$	5889.7(8)	26.0(35)	0.070(9)
			$3/2_6^+ \to 5/2_1^+$	3656.01(37)	63(6)	0.170(12)
			$3/2_6^+ \to 5/2_2^+$	2605.9(5)	10.6(18)	0.029(5)
6129.3(10)	0.0253(31)	6.3	$5/2_7^+ \to 1/2_1^+$	6128.7(10)	≤ 4.47	≤ 0.0012
			$5/2_7^+ \to 7/2_1^+$	2779.5(6)	100	0.0253(18)

Table 5.1 (cont'd)

6255.0(6)	0.57(6)	4.9	$1/2_5^+ \to 1/2_1^+$	6254.3(6)	80(10)	0.46(4)
			$1/2_5^+ \to 5/2_1^+$	4020.2(5)	9.7(13)	0.055(6)
			$1/2_5^+ \to 5/2_2^+$	2970.9(4)	10.1(14)	0.058(6)
6279.0(6)	18.7(11)	3.4	$3/2_7^+ \to 1/2_1^+$	6278.4(6)	16.9(17)	3.15(30)
			$3/2_7^+ \to 3/2_1^+$	5030.1(6)	10.4(10)	1.94(18)
			$3/2_7^+ \to 5/2_1^+$	4044.7(30)	60.6(37)	11.3(6)
			$3/2_7^+ \to 1/2_2^+$	3202.2(4)	0.432(39)	0.081(7)
			$3/2_7^+ \to 5/2_2^+$	2995.04(31)	6.16(37)	1.15(6)
			$3/2_7^+ \to 3/2_2^+$	2843.9(4)	0.452(39)	0.084(7)
			$3/2_7^+ \to 5/2_3^+$	2192.63(28)	0.59(5)	0.110(9)
			$3/2_7^+ \to 3/2_3^+$	2071.11(22)	3.09(19)	0.577(32)
			$3/2_7^+ \to 3/2_4^+$	1759.05(34)	0.39(5)	0.072(8)
			$3/2_7^+ \to (5/2_4^+)$	1561.01(29)	0.56(5)	0.104(8)
			$3/2_7^+ \to 1/2_3^+$	1412.91(30)	0.44(4)	0.082(7)
6390.2(7)	3.38(18)	4.1	$3/2_8^+ \to 1/2_1^+$	6389.5(7)	5.4(6)	0.181(18)
			$3/2_8^+ \to 3/2_1^+$	5141.3(6)	10.8(11)	0.368(36)
			$3/2_8^+ \to 5/2_1^+$	4155.84(31)	44.4(27)	1.51(9)
			$3/2_8^+ \to 1/2_2^+$	3313.56(33)	11.8(7)	0.401(22)
			$3/2_8^+ \to 5/2_2^+$	3106.28(31)	21.6(12)	0.734(39)
			$3/2_8^+ \to 3/2_2^+$	2182.52(25)	6.0(5)	0.210(16)
7050.0(8)	0.047(6)	5.7	$1/2_6^+ \to 1/2_1^+$	7049.2(8)	100	0.047(5)
7149.8(9)	0.059(8)	5.5	$5/2_8^+ \to 3/2_1^+$	5900.8(8)	100	0.059(7)

Table 5.2: All gamma-rays observed in E12028 assigned to the beta decay of ^{31}Cl. For each gamma-ray, the transition energy E_t and gamma energy E_γ are given in keV. The transition and the absolute intensity per 100 beta decays I_γ are also listed for each transition.

E_{trans}	E_γ	Transition	I_γ
985.63(23)	985.62(23)	$5/2_1^+ \to 3/2_1^+$	0.187(9)
1049.68(21)	1049.66(21)	$5/2_2^+ \to 5/2_1^+$	1.40(5)
1248.43(20)	1248.40(20)	$3/2_1^+ \to 1/2_1^+$	12.3(5)
1283.35(37)	1283.32(37)	$5/2_4^+ \to 3/2_2^+$	0.043(7)
1368.37(29)	1368.34(29)	$5/2_4^+ \to 7/2_1^+$	$\leq$0.018
1412.94(30)	1412.91(30)	$3/2_7^+ \to 1/2_3^+$	0.082(7)
1433.93(22)	1433.89(22)	$5/2_4^+ \to 5/2_2^+$	0.399(22)
1561.05(29)	1561.01(29)	$3/2_7^+ \to (5/2_4^+)$	0.104(8)
1672.58(29)	1672.53(29)	$5/2_5^+ \to 7/2_1^+$	0.114(9)
1738.57(36)	1738.52(36)	$5/2_5^+ \to 5/2_2^+$	0.063(7)
1759.10(34)	1759.05(34)	$3/2_7^+ \to 3/2_4^+$	0.072(8)
1827.99(25)	1827.93(25)	$1/2_2^+ \to 3/2_1^+$	0.205(14)
1852.19(25)	1852.19(25)	$5/2_3^+ \to 5/2_1^+$	0.211(14)
2035.31(20)	2035.24(20)	$5/2_2^+ \to 3/2_1^+$	4.38(22)
2071.18(22)	2071.11(22)	$3/2_7^+ \to 3/2_3^+$	0.577(32)
2100.87(25)	2100.79(25)	$7/2_1^+ \to 3/2_1^+$	0.076(14)
2182.60(25)	2182.52(25)	$3/2_8^+ \to 3/2_2^+$	0.210(16)
2186.41(33)	2186.33(33)	$3/2_2^+ \to 3/2_1^+$	0.348(21)
2192.71(28)	2192.63(28)	$3/2_7^+ \to 5/2_3^+$	0.110(9)
2234.06(20)	2233.97(20)	$5/2_1^+ \to 1/2_1^+$	53.2(27)
2483.71(22)	2483.60(22)	$5/2_4^+ \to 5/2_1^+$	0.472(26)
2606.0(5)	2605.9(5)	$3/2_6^+ \to 5/2_2^+$	0.029(5)
2779.6(6)	2779.5(6)	$5/2_7^+ \to 7/2_1^+$	0.0253(18)
2787.8(8)	2787.7(8)	$5/2_5^+ \to 5/2_1^+$	0.0173(39)
2837.74(32)	2837.60(32)	$5/2_3^+ \to 3/2_1^+$	0.614(34)
2844.0(4)	2843.9(4)	$3/2_7^+ \to 3/2_2^+$	0.084(7)
2959.24(31)	2959.09(31)	$3/2_3^+ \to 3/2_1^+$	1.77(9)
2971.1(4)	2970.9(4)	$1/2_5^+ \to 5/2_2^+$	0.058(6)
2995.19(31)	2995.04(31)	$3/2_7^+ \to 5/2_2^+$	1.15(6)
3076.40(31)	3076.24(20)	$1/2_2^+ \to 1/2_1^+$	2.82(14)
3106.45(31)	3106.28(31)	$3/2_8^+ \to 5/2_2^+$	0.734(39)
3202.4(4)	3202.2(4)	$3/2_7^+ \to 1/2_2^+$	0.081(7)

Table 5.2 (cont'd)

3283.76(31)	3283.57(31)	$5/2_2^+ \to 1/2_1^+$	1.11(6)
3313.75(33)	3313.56(33)	$3/2_8^+ \to 1/2_2^+$	0.401(22)
3434.90(33)	3434.70(32)	$3/2_2^+ \to 1/2_1^+$	0.420(24)
3469.34(31)	3469.13(31)	$5/2_4^+ \to 3/2_1^+$	0.113(8)
3541.32(27)	3541.10(27)	$5/2_6^+ \to 5/2_1^+$	0.254(21)
3617.63(31)	3617.40(31)	$1/2_3^+ \to 3/2_1^+$	1.01(6)
3656.24(37)	3656.01(37)	$3/2_6^+ \to 5/2_1^+$	0.170(12)
3773.5(5)	3773.2(5)	$5/2_5^+ \to 3/2_1^+$	0.078(7)
3907.5(4)	3907.3(4)	$3/2_3^+ \to 3/2_1^+$	0.091(8)
4020.4(5)	4020.2(5)	$1/2_5^+ \to 5/2_1^+$	0.055(6)
4044.94(30)	4044.7(30)	$3/2_7^+ \to 5/2_1^+$	11.3(6)
4085.4(8)	4085.2(8)	$5/2_3^+ \to 1/2_1^+$	0.019(8)
4156.14(31)	4155.84(31)	$3/2_8^+ \to 5/2_1^+$	1.51(9)
4187.71(15)	4187.4(15)	$3/2_5^+ \to 3/2_1^+$	0.0034(7)
4207.7(31)	4207.43(31)	$3/2_3^+ \to 1/2_1^+$	3.12(18)
4519.63(32)	4519.28(32)	$3/2_4^+ \to 1/2_1^+$	1.20(7)
4717.72(32)	4717.34(32)	$5/2_4^+ \to 1/2_1^+$	0.618(37)
4866.2(6)	4865.8(6)	$1/2_3^+ \to 1/2_1^+$	0.71(4)
4970.7(9)	4970.2(9)	$3/2_1^- \to 1/2_1^+$	0.037(7)
5030.6(6)	5030.1(6)	$3/2_7^+ \to 3/2_1^+$	1.94(18)
5141.7(6)	5141.3(6)	$3/2_8^+ \to 3/2_1^+$	0.368(36)
5156.1(6)	5155.7(62)	$3/2_3^+ \to 1/2_1^+$	0.84(8)
5435.9(9)	5435.4(9)	$3/2_5^+ \to 1/2_1^+$	0.020(7)
5890.3(8)	5889.7(8)	$3/2_6^+ \to 1/2_1^+$	0.070(9)
6129.3(10)	6128.7(10)	$5/2_7^+ \to 1/2_1^+$	≤ 0.0012
6255.0(6)	6254.3(6)	$1/2_5^+ \to 1/2_1^+$	0.46(4)
6279.0(6)	6278.4(6)	$3/2_7^+ \to 1/2_1^+$	3.15(30)
6390.2(7)	6389.5(7)	$3/2_8^+ \to 1/2_1^+$	0.181(18)
7050.0(8)	7049.2(8)	$1/2_6^+ \to 1/2_1^+$	0.047(5)
7149.8(9)	5900.8(8)	$5/2_8^+ \to 3/2_1^+$	0.059(7)

decay from ^{31}Cl. We have therefore labeled the state as $J^\pi = 3/2^-$ in the decay scheme; the de-exciting gamma ray is the first measured gamma de-excitation of the state and the calculated excitation energy of 4970.7(9) keV is more precise than the NDS reported value.

5.4.1.2 3349-keV Level

We observed a gamma-ray of 3773 keV, which was observed to be in coincidence with the de-excitation of the first excited state at 1248-keV. Initially, the simplest interpretation of this gamma-ray seemed to be that it was the de-excitation of a known level at 5021 keV to the first excited state. However, we also observed two gamma-rays, energies 2100 and 1673 keV, which were observed to be in coincidence with one another and together sum to 3773 keV. The 2100-keV peak was also observed to be in coincidence with the 1248-keV gamma ray. It was not immediately clear whether these peaks corresponded to a cascade adding up to some new level at 3773 keV, or whether they corresponded to a cascade de-excitation of the 5021-keV state. After further analysis, including consideration of our shell-model calculations, we found that the 5021-keV state is expected to have four primary gamma branches: to the 1248-keV state, to the 2234-keV state, to the 3283-keV state, and to a $J^\pi = 7/2^+$ state at a theoretical energy of 3477 keV.

The $A = 31$ Nuclear Data Sheets [79] report a $7/2^+$ level at 3351.30(19) keV, which is expected to decay primarily via a 2102.4(2)-keV gamma ray. Given the agreement with the NDS and with the shell-model calculations (which are only accurate to within a few hundred keV), we considered it likely that the 2100-keV gamma ray was the de-excitation of a state at an excitation energy $E_x = 3349.30(32)$ keV, and the 1672-keV gamma ray was feeding this state via the de-excitation of the 5021-keV state. We also observed two other relevant gamma rays whose energies correspond to de-excitations of known ^{31}S states: a 1368-keV

gamma ray de-exciting the state at 4717 keV, and a 2779-keV gamma ray de-exciting a state we observed to be at 6129 keV. These transitions are all reported in Table 5.1.

The ^{31}Cl beta-decay transition to the state at 3349 keV would be a first forbidden transition. We calculated a beta feeding upper limit for this state of < 0.01. As described in Section 5.3.4, the procedure for calculating the beta feedings of the ^{31}S states involved subtracting the sum of the intensities of the gamma rays feeding the level (in this case, the 1368, 1672, and 2779-keV gammas) from the sum of the intensities of the gamma rays de-exciting it (in this case, the 2100-keV gamma). However, the procedure for determining the beta feeding of this state deviated significantly from the standard procedure, as both the photopeak of the 2100-keV gamma de-exciting this state and the photopeak of the 1368-keV gamma feeding it overlapped with photopeaks from other processes. This atypical procedure, including the calculation of the beta feeding upper limit, is detailed in the following section.

5.4.2 Overlapping Photopeaks: the 1368-keV, 2100-keV, and 6129-keV Gamma Rays

Ideally, the analysis procedure for high-resolution gamma-ray spectroscopy is simple: for each photopeak in the spectrum, identify the peak's origin and measure its intensity. This data may then be used to produce, for example, a beta decay scheme and absolute gamma intensities. However, occasionally it is the case that various factors prevent the simple identification and analysis of a photopeak. As discussed in Chapter 5, peaks corresponding to background processes (e.g., room background peaks) are often present in the spectrum. Although room background peaks can be gated out of the spectrum, photopeaks corresponding to transitions from beam contaminants will also show up in the spectrum, even if it is

gated on beta decays. Statistically, some number of peaks from disparate processes will have energies similar enough that they overlap in the energy spectrum histogram. This means that simply integrating such a photopeak without careful consideration will give an inaccurate, unphysically high intensity; special care must therefore be taken to disentangle the two contributing sources of the photopeak.

In our analysis of the ^{31}Cl beta-gamma spectrum, we occasionally encountered photopeaks with contributions from multiple sources. Two of these have already been mentioned: the 1368-keV gamma ray feeding the 3349-keV level, and the 2100-keV gamma ray de-exciting it. We also observed two photopeaks corresponding to transitions de-exciting a state at 6129 keV: a 2779-keV transition to the state at 3349 keV and a photopeak at 6129 keV we assigned to a transition to the ground state. The 2779-keV gamma was greatly enhanced in the 2100-keV coincidence spectrum, lending credence to the hypothesis of a state at 6129 keV. However, 6129 keV is also the energy of a known gamma ray ($E_\gamma = 6129.89(4)$) corresponding to a transition from the second excited state of ^{16}O, allowing for the possibility of contributions from two sources in the intensity of this peak. This and the two cases surrounding the 3349-keV state will be discussed here.

5.4.2.1   The 2100-keV Peak

The 2100-keV gamma ray de-exciting the 3349-keV state was measured at a peak energy of $E_\gamma = 2100.79(25)$ keV. This energy is unfortunately only 3 keV lower than the energy of the first escape peak of a well-known strong room background peak at $E_\gamma = 2614.511(10)$ keV from the decay of ^{208}Tl. Although the timing gate on the gamma-ray spectrum greatly reduces room background contributions, particularly intense peaks such as the 2614-keV peak may not be supressed entirely, and although the contribution from the escape peak

is likely very small and relegated to the upper tail of the peak, it could still result in an erroneously high intensity of the 2100-keV peak.

To account for the possible contribution to the peak from the room background escape peak, we fit the 2614-keV peak and its first escape peak in a room background run, a run where no beam was impingent upon the target. From these fits, we obtained the ratio of the escape peak to the photopeak. We then fit 2614-keV peak in the timing-gated spectrum to obtain an intensity and used this ratio to obtain the likely intensity of its first escape peak in the mixed 2100-keV peak. We subtracted this contribution from the measured photopeak intensity of the 2100-keV peak to obtain the contribution of the de-excitation of the state at 3349 keV to the 2100-keV peak.

5.4.2.2 The 1368-keV Peak

Our shell-model calculations predict a small but not-insignificant gamma ray branch de-exciting the 4717-keV state and feeding the 3349-keV state. We did in fact observe a gamma-ray at energy $E_\gamma = 1368.34(29)$ keV, which was enhanced in coincidence with the 2100-keV gamma de-exciting the 3349-keV state. In analyzing the intensity of this peak, however, it became clear that multiple sources were contributing to the peak. The gamma branch from the 4717-keV state was much higher than expected, and the ratio of the timing-gated peak to the ungated peak was 0.61(5), lower than and inconsistent with the average ratio of 0.806(7). A zoomed-in view of the 1368-keV peak and nearby peaks is shown in Fig. 5.13.

^{24}Mg is a stable isotope with a first excited state energy of $E_x = 1368.626(5)$ keV, so if our beam contaminants produced ^{24}Mg through decay, gammas from the decay process could contribute to the photopeak at 1368 keV. Unfortunately, both the beta-plus decay of ^{24}Al and the beta-minus decay of ^{24}Na produce ^{24}Mg, and both have a high probability of
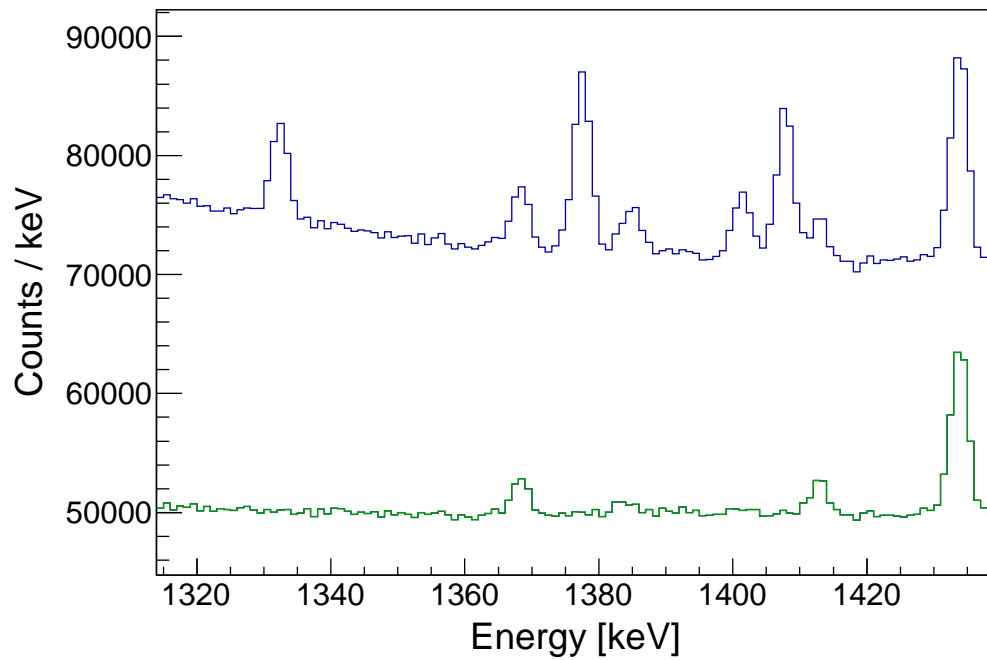
Figure 5.13: A portion of the ^{31}Cl gamma spectra in the region around 1368 keV. The blue histogram is the ungated gamma-ray spectrum while the green spectrum is the timing-gated spectrum. As shown, the room background lines are eliminated while the decay-related peaks at 1368 keV, 1412 keV, and 1433 keV remain. Note however that the 1368-keV peak is reduced more substantially than the other two peaks, which are known to originate from ^{31}Cl beta decay. This implies that the 1368-keV peak does not originate solely from ^{31}Cl beta decay.

producing a 1368-keV gamma ray, and the yield of the various ^{24}Mg beta-delayed gammas is different between these two processes; consequently, if both of these nuclides were produced, it would not even be straightforward to use other ^{24}Mg peaks to separate the components of the 1368-keV peak.

Ground-state ^{24}Na has a half-life of 14.997(12) h, meaning that a room background run taken shortly after removal of beam from the experimental setup should show photopeaks corresponding to ^{24}Na beta-delayed gamma rays in a timing-gated gamma-ray spectrum. In fact, we observed both the 1368-keV photopeak and the 2754-keV photopeak, corresponding to the transition from the ^{24}Mg first excited state to the ground state and the transition from the second excited state to the first, respectively. We also observed, in the timing-gated ^{31}S spectrum, a photopeak with energy $E_\gamma = 7070.9(16)$ ($\sigma = 3.4$). The only gamma with which this value is consistent corresponds to a transition from the ^{24}Mg level at $E_x = 8439.36(4)$ keV to the 1368-keV state. Consequently, it appeared as though both ^{24}Na, which was observed in the PID spectrum, and ^{24}Al, which was not clearly identified in the PID spectrum but of which trace amounts could be included in the beam or produced through interactions between the beam and the scintillator, contributed to the 1368-keV photopeak.

In order to accurately determine the contribution to the peak from beam contaminants, it was therefore necessary to separate the ^{24}Al contribution from the ^{24}Na contribution and separate both contributions from the 1368-keV photopeak. Ordinarily, experimenters try to reduce the contribution to the spectrum from beam contaminants as much as possible; in this case however, our pure beam actually made it more difficult to investigate the nature of the ^{24}Al and ^{24}Na contribution, since very few peaks were available to determine the ratio of the timing-gated contaminant photopeaks to the ungated peaks. The most pronounced peak we found was the peak at 2754 keV, but it is produced in different amounts between ^{24}Al decay

and ^{24}Na decay, requiring further disentanglement. The peak at 7070 keV, however, has an energy higher than the Q-value of the ^{24}Na beta-minus decay (5513.6(6) keV), meaning that only ^{24}Al contributed to the peak integral in our spectrum. We measured the integral of this peak in both gated and ungated spectra and used the relative yields per beta decay of the 2754-keV and 7070-keV ^{24}Al beta-delayed gammas to determine the expected contribution to the integral of the photopeak at 2754 keV from ^{24}Al (14(1)%). The remaining integral of the photopeak (87(6)%) was then taken as the expected contribution from ^{24}Na.

To disentangle the various sources of the 1368-keV gamma ray, we then used the relative yields per beta decay of the 1368-keV gamma branches for both ^{24}Al and ^{24}Na compared to the 7070-keV peak and 2754-keV peak, respectively, to determine the expected contribution of those two contaminants to the 1368-keV photopeak: 25(2)% expected contribution from ^{24}Al and a 67(5)% expected contribution from ^{24}Na. Subtracting these values from the photopeak integral yielded the "leftover" contribution from ^{31}Cl beta decay – only 6(4)% of the total peak integral. Since this value is nearly compatible with zero, we treated the contribution from ^{31}Cl as an upper limit in the calculations for the beta feeding and absolute gamma intensities.

5.4.2.3   The 6129-keV Peak

Although our beam did not contain any ^{16}O as a contaminant, and any ^{16}O produced via fragmentation would be in its ground state by the time it was delivered to the experimental setup, excited ^{16}O could be produced from nuclear reactions between the incoming high-energy beam particles and the atoms in the plastic scintillator. In fact, ^{16}O may be produced via the ^{13}C$(\alpha, n)^{16}$O reaction rate using ^{13}C nuclei present in the plastic scintillator and alpha particles produced via secondary reactions involving the ^{31}Cl and the plastic in the

target. ^{16}O produced this way has a high likelihood of yielding a gamma ray of energy $E_\gamma = 6128.63(4)$ keV, corresponding to a de-excitation of the second excited ^{16}O state [86, 87, 88]. As reported in Table 5.1, we observed a photopeak at $E_\gamma = 6128.7(10)$ keV, which we interpreted as a transition to the ground state from a level at $E_x = 6129.3(10)$ keV and to which we assigned a tentative spin and parity of $J^\pi = (5/2)^+$ based on comparison with our shell-model calculations. The branch to the 3349-keV state was found to agree with the shell-model calculations, and the 2779-keV gamma corresponding to the de-excitation of this state was observed to be strengthened in coincidence spectra gated both on the de-excitation of the 3349-keV state to the first excited state ($E_\gamma = 2100$ keV) and on the 1248-keV de-excitation of the first excited state (both spectra are presented in Fig. 5.14). The 6129-keV state excitation energy derived from adding the transition energies of the cascading gammas ($E_x = 6128.9(5)$ keV) was consistent with the energy derived from the 6129-keV photopeak ($E_x = 6129.3(10)$ keV).

However, the observed gamma branch to the ground state was higher than expected, especially considering that we did not observe two other branches, which, in the shell-model prediction, were predicted to be more intense than the ground-state branch. Thus, it seemed prudent to consider whether reactions in the scintillator were contributing to the 6129-keV line. Using PACE, a fusion-evaporation reaction calculator included in the program LISE++ (see Appendix A), we calculated the rate of production of alpha particles in the scintillator for beam energies up to 50 MeV/u, using the stopping power of the BC408 plastic to model the likely energy the beam at ten different implantation depths, up to the depth at which the beam stopped (approximately 2.5 mm according to LISE++). We found that, for a beam of rate 6000 pps, up to $\approx$1700 alpha particles per second could be produced through fusion-evaporation at the highest interaction probability. These alphas could then interact
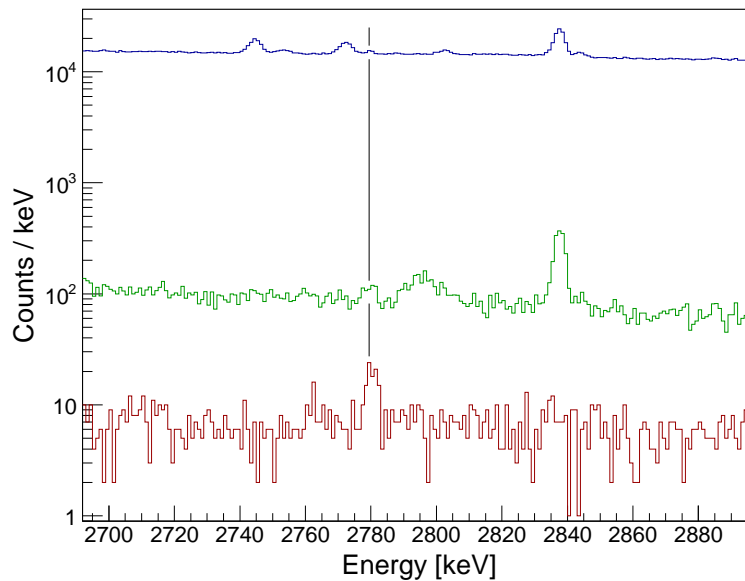
Figure 5.14: Three spectra showing the 2779-keV transition from the 6129-keV state to the 3349-keV state. Blue line: the timing-gated spectrum showing the 2779-keV photopeak without any other coincidence gating applied. Green line: the coincidence spectrum produced by gating on the 1248-keV transition from the first excited state to the ground state. Red line: the coincidence spectrum produced by gating on the 2100-keV transition from the 3349-keV state to the 1248-keV first excited state. The 2779-keV photopeak is enhanced in both coincidence spectra, indicating that the three gammas form a cascade adding up to 6129 keV.

with the ^{13}C that makes up $\approx$1% of the carbon in the BC408.

For alphas with energy between 5 MeV and 10 MeV, the (α, n) cross section for production of the 6129-keV gamma ray has been measured [88]. Using the average alpha energy calculated by PACE, and the cross sections in Ref. [88], we calculated, for the alpha production rates above, 6129-keV gamma production rates of up to 3.9 gammas per second. Factoring in the efficiency of the Clover detectors at 6129 keV (0.63%), we estimated a theoretical count rate of 0.02 ^{13}C$(\alpha, n)^{16}$O 6129-keV gamma rays per second. This value was compared to the theoretical yield of 6129-keV gammas from our shell-model calculations: for a beam of the same rate given the shell model beta branch to the 6129-keV state (0.04%), the gamma branch to the ground state (7.94%), and the efficiency of the detectors at that energy (0.63%), we estimated a detection rate of only 0.001 ^{31}Cl beta-delayed 6129-keV gamma rays per second, approximately 5% the rate of detection for reaction-produced gammas. These theoretical calculations seem to imply that the 6129-keV photopeak is mostly the result of ^{13}C$(\alpha, n)^{16}$O reactions.

To assess the validity of this prediction, we checked the ratio between the timing-gated photopeak integral of the 6129-keV peak and that of the ungated photopeak (the standard procedure for determining a peak's origins, detailed above). We found the ratio to be 0.78(16), consistent with the average value of 0.806(7), but with a much higher uncertainty. It could be however that the slightly lower ratio is evidence, as in the case of the 1368-keV peak, of multiple contributing sources. We also looked at a number of spectra gated on different conditions to try and determine whether the 6129-keV peak's origins could be experimentally determined. We first looked at a gamma-ray spectrum to which the timing-gate was applied, but only for high-energy scintillator events ($E > 15000$ "channels"), ostensibly gating on events above the ^{31}Cl beta decay endpoint energy (Fig. 5.15). This produced

a spectrum with greatly reduced ^{31}Cl beta-delayed gamma-rays, but enhanced room background peaks at low energies. The peak at 6129-keV was also slightly enhanced in this spectrum, indicating that it likely has a large contribution from a prompt process that is not ^{31}Cl decay.

To try and determine the likely contribution to the 6129-keV peak from the non-decay process (in this case the ^{13}C$(\alpha, n)^{16}$O reaction), we obtained, for a number of photopeaks corresponding to room background transitions, the ratio of the photopeak integral in a gamma spectrum gated only on the high-energy scintillator events to the integral in the standard scintillator-gated spectrum (we used the scintillator-only gate instead of the timing gate because almost all of the room background peaks were reduced too much to measure in the timing-gated spectrum). These values were found to be more or less consistent with one another. To determine a reasonable estimate for the ratio, we took a weighted average of the data points and found, with a p-value of 0.48, a ratio of 0.2447(20). That is, the ratio of the photopeak of a non-decay gamma event gated on high-energy (non-decay) scintillator events to the ratio of a non-decay gamma event gated on any energy scintillator event was approximately 25%.

We then compared the ratio of the 6129-keV peak integral in the high-energy scintillator-gated spectrum to the peak integral in the standard scintillator-gated spectrum. The ratio for that peak was found to be 0.27(16) – slightly higher, but still consistent with the average value and with a large uncertainty. If the 6129-keV peak were the result of both ^{31}Cl beta decay and the ^{13}C$(\alpha, n)^{16}$O reaction, this value should actually be lower than 0.2447, since the ^{31}Cl component would be reduced much more strongly than the reaction component. Therefore, it seems unlikely that ^{31}Cl beta decay contributes strongly to this peak in our data. To set an upper limit on the ^{31}Cl contribution, we used the 5% ^{31}Cl contribution from
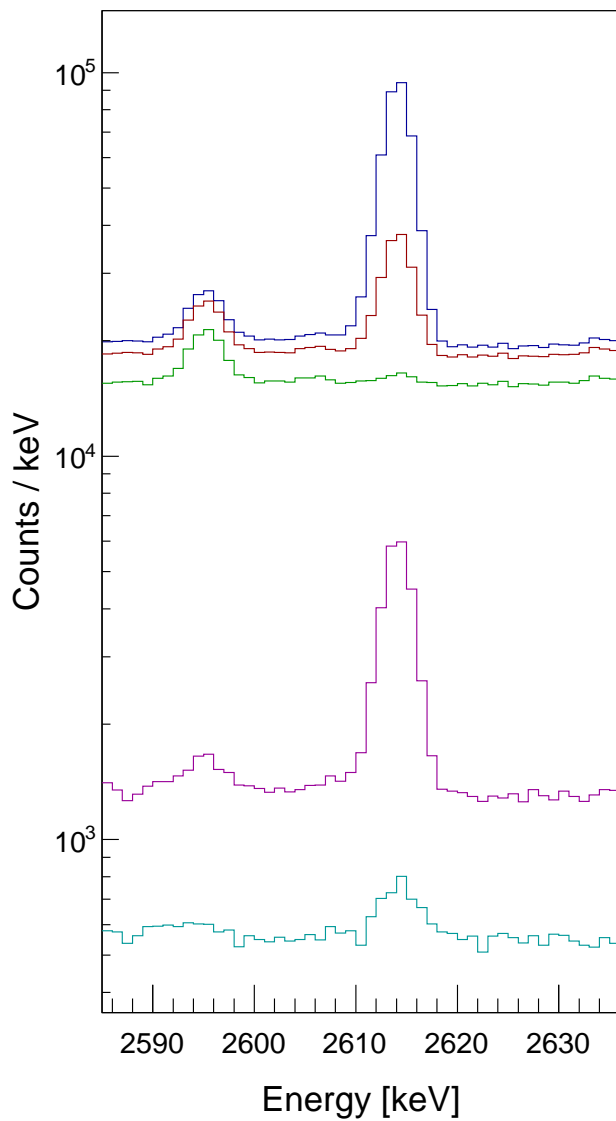
Figure 5.15: A portion of several gamma-ray spectra illustrating the effects of the various scintillator gates on both a ^{31}Cl photopeak (the peak at 2565 keV is the first escape peak of the 3076-keV gamma) and a room background peak (the peak at 2614 keV is from ^{208}Tl). Blue: Ungated gamma spectrum. Red: Scintillator-gated gamma spectrum, showing slight reduction of the 2614-keV peak. Green: Timing-gated gamma spectrum, showing almost complete elimination of the 2614-keV peak and slight enhancement of the 2565-keV peak. Purple: Scintillator-gated spectrum gated ONLY on high-energy scintillator events, showing the enhancement of the 2614-keV peak and reduction of the 2565-keV peak. Turquoise: Timing-gated spectrum gated ONLY on high-energy scintillator events.

the combination of our shell-model calculations and the PACE calculations to estimate that no more than 5% of the photopeak integral is due to ^{31}Cl beta decay. The resulting upper limit is reported in Table 5.1.

Chapter 6

Discussion of E12028 Results

As shown in the preceeding chapter, E12028 successfully produced a new ^{31}Cl beta decay scheme with ten new observed beta transitions and 40 new observed beta-delayed gamma transitions. In fact, the number of new gamma transitions observed is nearly double the number (22) of previously-seen transitions, all of which were observed again in this experiment. This expansion of the decay scheme is useful in general for nuclear structure studies, but as stated in Chapter 2, the motivation for E12028 was the pursuit of constraints on the spins and parities of potentially-important ^{31}S states in the ^{30}P$(p, \gamma)^{31}$S Gamow window, in order to provide experimental constraints on its rate. Here, we present results from E12028 of astrophysical importance, as well as other results from the experiment. The primary result of E12028 was the discovery and unambiguous identification of a new $J^{\pi} = 3/2^{+}$ resonance state (Section 6.1), but analysis also allowed for tests of the isobaric multiplet mass equation (Section 6.2) and comparison with previous experimental spin and parity assignments (Section 6.3).

6.1   Isospin Mixing: A New $J^{\pi} = 3/2^{+}$ Resonance

Note: This section is adapted from a paper previously published by the author and collaborators on this subject, Ref. [89]

As mentioned in Section 3.5.4, Isospin mixing may occur between two states of identical spin and parity but different isospin T, causing each observed state to be a superposition of isospin states, $|\psi_1\rangle = \cos\theta|JT_1\rangle + \sin\theta|JT_2\rangle$ and $|\psi_2\rangle = -\sin\theta|JT_1\rangle + \cos\theta|JT_2\rangle$ (Eqs. 3.17 and 3.18). In this case, the mixed states will, according to the strengths of the mixing, adopt characteristics similar to one another – observing these characteristics, then, can be observational evidence of isospin mixing.

For ^{31}Cl beta decay, the transition to the 6279-keV isobaric analog state (IAS) is greatly strengthened because of the Fermi transition from the $T = 3/2$ ^{31}Cl ground state. In our analysis we found the beta feeding of the state to be $I_\beta = 18.7(11)\%$. *Only* the IAS should have such a high beta feeding at such high excitation energy in ^{31}S. Gamow-Teller transitions to states with similarly high excitation energies are shown in Fig. 5.12 to have beta feedings on the order of half a percent or less, with one notable exception: the state at 6390-keV. This state was found to have a beta feeding of $I_\beta = 3.38(18)\%$.

The beta feeding of this state is abnormally high and did not match the prediction from our USDB shell-model calculations. Further, as reported in Table 5.1, the gamma branching of this state was observed to be qualitatively similar to that for the IAS, especially the highly strengthened branch to the $5/2^+$ second excited state at 2234 keV. In total, we observed six transitions de-exciting this state. A simplified beta decay scheme is depicted in Fig. 6.1, and selected portions of the timing-gated spectrum showing transitions to the first three ^{31}S states, along with gamma-gamma coincidence spectra showing the enhancements of the transitions due to the gates, are shown in Fig. 6.2. Similar to the beta feeding for the level, the gamma branching of this state did not match the prediction from our USDB shell-model calculations; based on these divergences from prediction and similarties with the IAS, we investigated the possibility of isospin mixing between the two states.
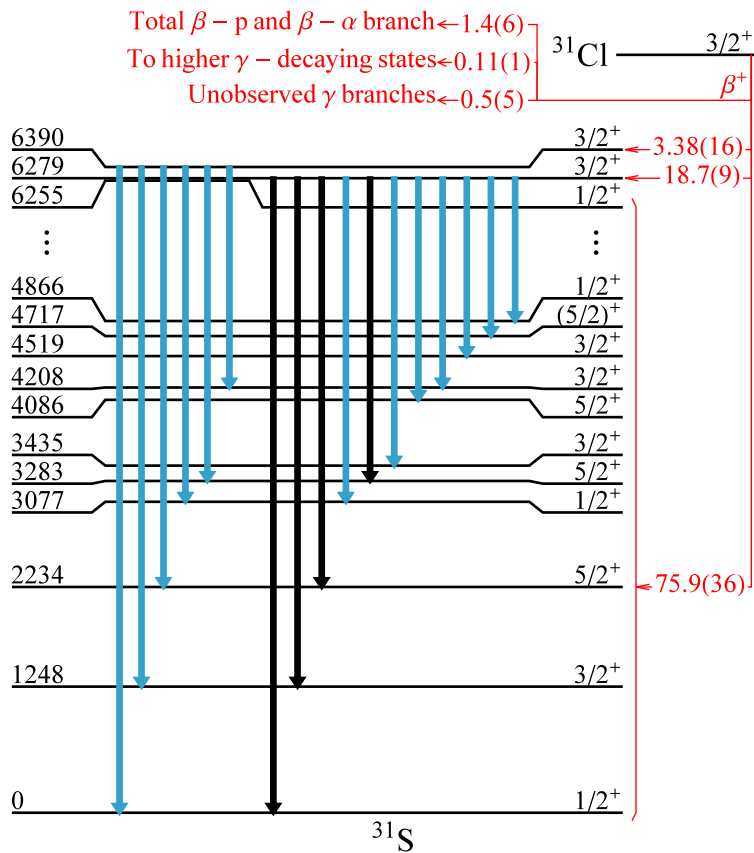
Figure 6.1: A simplified ^{31}Cl decay scheme focusing on the ^{31}S levels at 6279 (IAS) and 6390 keV. The blue vertical arrows indicate previously unobserved transitions. Energies and intensities for these transitions are listed in Table 5.1.
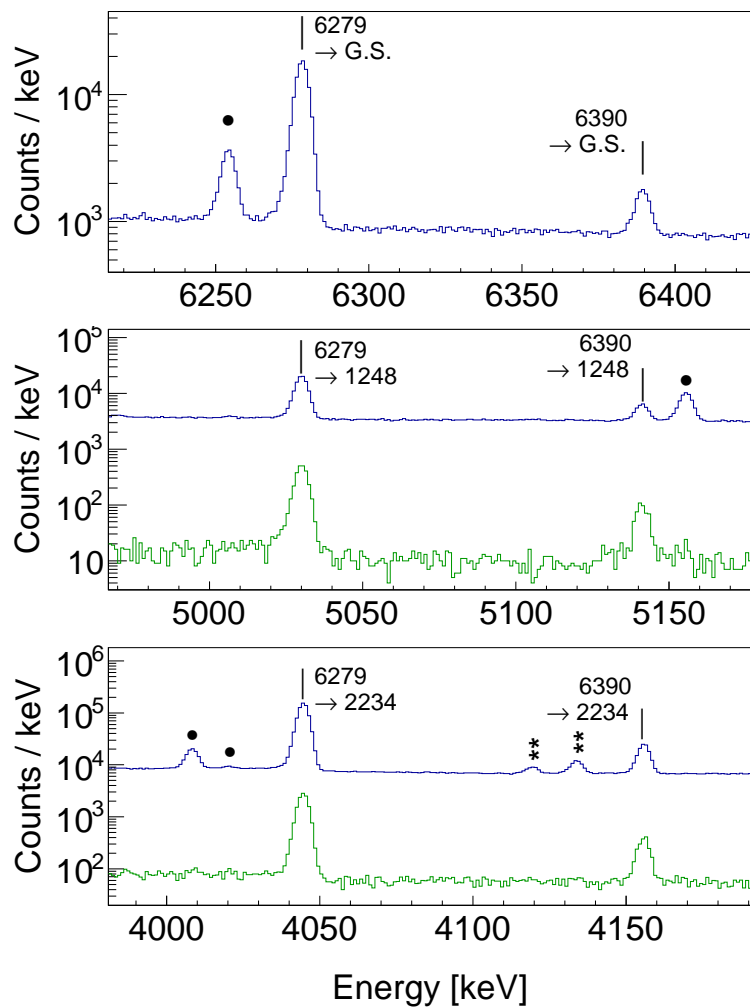
Figure 6.2: Selected portions of the β-coincident γ-ray spectrum (blue) showing transitions from the 6279- and 6390-keV ^{31}S states to the ground state and first two excited states (J^{π} = $1/2^{+}, 3/2^{+}, 5/2^{+}$, respectively). The bottom two panels also show β-γ-γ spectra (green) with additional coincidence conditions on the 1248- and 2234-keV γ rays, respectively. Other photopeaks observed from the β decay of ^{31}Cl are marked with black circles. Double escape peaks are marked with double asterisks.

The expected Fermi strength for the transition to the IAS is easy to calculate according to Eq. 3.15: $B(F) = (T(T+1) - T_{zf}(T_{zf}+1)) = 3/2(3/2+1) - 1/2(1/2+1) = 3$. Using the observed beta feedings of the two states, we were also able to calculate experimental Fermi strengths. By rewriting Eq. 3.13 in terms of the half-life, and combining constants, we can produce the "ft" value, a measure of the transition rate:

$$ft_{1/2} = \frac{C}{[B(F) + (g_A/g_V)^2 B(GT)]} \tag{6.1}$$

where here $C = \ln2 K_o/(g_V)^2 = 6170(4)$, a value determined from several measurements of pure $0^+ \to 0^+$ Fermi transitions [90], and $t_{1/2}$ is the *partial half-life*, the total half-life of beta decay divided by the beta feeding to the level in question. This f value is the result of a number of corrections to an analytic result derived for a nucleus of $Z = 0$, $f_{Z=0}$, which can be calculated using the Q-value of the beta decay and the excitation energy of the level. These corrections account for distortion of the wave function from the electron and the diffuseness of the nuclear charge distribution. They can all be calculated computationally; a derivation is presented in Ref. [90] and coefficients for the calculation of the electron distortion correction can be found in Ref. [91].

If it is assumed that $B(F)$ is much greater than $B(GT)$ (valid for the IAS and any state mixing strongly with it, since the Gamow-Teller transition is fragmented across all states), E. 6.1 can be solved for the Fermi strength: $B(F) = C/f_V \cdot t_1/2$. Here we have rewritten f as f_V to denote the inclusion of the Fermi phase-space factor correction, since the transition is a Fermi decay. For both the IAS and the state at 6390 keV, we calculated f_V and $t_{1/2}$ and subsequently the Fermi strength: the results were a strength of $B(F) = 2.4(1)$ for the IAS and $B(F) = 0.48(3)$ for the state at 6390 keV, which together sum to 2.9(1). The inflated

Fermi transition strength to the state at 6390 keV, the reduced transition strength to the IAS, their sum, and the similarties between their gamma branches are strong evidence that the Fermi transition is split via isospin mixing, primarily between these two states.

To determine the strength of the mixing we adopted the two-level mixing formalism described in Eqs. 3.19, 3.20, 3.21, 3.22, and 3.23 and calculated $R = \tan\theta$ from the Fermi strengths. Using R along with the observed energy spacing between the levels $E = 6390.2(7) - 6279.0(6) = 111.2(9)$ keV, we calculated an empirical mixing matrix element $V = 41(1)$ keV and an unperturbed level spacing $D = 74(2)$ keV. We also used the mixing angle itself to determine the wave functions for the two states: $|\psi_{IAS}\rangle = 0.408|T = 1/2\rangle + 0.913|T = 3/2\rangle$ and $|\psi_{6390}\rangle = 0.913|T = 1/2\rangle - 0.408|T = 3/2\rangle$.

Because the beta feeding and gamma branching of the 6390-keV state was not correctly predicted by our USDB shell-model calculation, B.A. Brown repeated the USD fit for the calculation with the Hamiltonian from Ref. [38], but this time using only excitation energies of levels (that is, excluding the binding energies of the nuclei). This new USD fit, termed by B.A. Brown as "USDE," gives a similar root-mean-square deviation from the experimentally-observed energy levels in the region (126 keV, compared to 122 keV RMS deviation for USDB), but gives a strengthened beta feeding to the 6390-keV level and more quantitatively similar gamma branching. B.A. Brown performed an isospin-mixing calculation with both USDB and USDE and found that both interactions yielded a triplet of $3/2^+$ levels involved in isospin mixing. The excitation energies of the three states and the calculated mixing matrix elements for the two $T = 1/2$ states for both the USDB and USDE calculations are reported in Table 6.1.

Based on the values of excitation energy and matrix elements predicted by these shell-model calculations, as well as the theoretical uncertainties implied by the differences between

Table 6.1: Calculated excitation energies E_x and mixing matrix elements V of the triplet of isospin-mixed states, including the $T = 3/2$ IAS, in ^{31}S for both USDB and USDE interactions. The matrix elements listed are between the listed $T = 1/2$ state and the $T = 3/2$ state. All values are in units of keV.

	J^π	USDB E_x	USDB V	USDE E_x	USDE V
$E_1(T = 1/2)$	$3/2^+$	6205	35	6095	30
$E_2(T = 3/2)$	$3/2^+$	6520	$--$	6184	$--$
$E_3(T = 1/2)$	$3/2^+$	6382	12	6375	27

the USDB calculation and the USDE, theory is consistent with the present experimental result. The experimental results show that the isospin mixing of the IAS is dominated by the nearby 6390-keV state. The best experimental candidate for the other $T = 1/2, J^\pi = 3/2^+$ state in the USDB and USDE triplets is at 5890 keV [62, 63] and has an observed beta feeding of just 0.269(21)%. The relatively large energy difference between this level and the IAS is consistent with the shell model calculations, and both the large spacing and the relatively small beta feeding render the isospin mixing negligible when compared to the mixing with the 6390-keV state – and therefore negligible for the purposes of the present work.

6.1.1 Astrophysical Relevance and Implications

The present work constitutes the first clear observation of isospin mixing between a $T = 3/2$ state and a $T = 1/2$ in the sd shell, with the possible exception of a controversial case for $A = 23$ [92, 93, 94]. As described in Section 3.5.4, the mixed 6390-keV state must have the same spin and parity as the IAS, $J^\pi = 3/2^+$. No experimental study has identified this level before, making this result the first completely unambiguous identification of this state. Furthermore, the $3/2^+$ spin and parity of the state make it an important $l = 0$ resonance state for proton capture, located directly in the heart of the Gamow window where it is likely to greatly impact the ^{30}P$(p, \gamma)^{31}$S rate. Using the formalism described

in Sections 3.2 and 3.3, we attempted to calculate the thermonuclear reaction rate using Eq. 3.10 with our experimentally-determined spin for ω, the experimental resonance energy ($E_r = E_x - S_p$, 259.3(8) keV) and a proton partial with Γ_p calculated according to Eq. 3.12.

For the proton partial width, we calculated a spectroscopic factor C^2S (which included the Clebsh-Gordan coefficient) of 0.0087 using the USDB interaction. We scaled this value by the square of the $T = 1/2$ component of the 6390-keV state ($0.913^2 = 0.83$) to account for the mixing with the IAS. Using the values for F_l and G_l generated by the code described in Ref. [95], we calculated a penetration length $P_l = 2.369 \cdot 10^{-9}$. Along with a single-particle reduced width $\theta_{s.p}^2 = 0.553$ calculated using the tables in Ref. [96], we calculated a value of the proton partial width $\Gamma_p = 36\mu$eV. This value, when combined with the spin of the resonance and a gamma-ray partial width of 0.97 eV as taken from Table III of Ref. [97], leads to a ^{30}P$(p, \gamma)^{31}$S resonance strength of $\omega\gamma = 24\mu$eV. Using this resonance strength and the resonance energy, we calculated the thermonuclear reaction rate for the $3/2^+$ state at 6390 keV. This rate is tabulated in Table 6.2 for peak nova temperatures.

In order to determine the effect of our calculated resonant capture rate on the overall determination of the ^{30}P$(p, \gamma)^{31}$S rate, we compared our rate to the rate calculated using the Hauser-Feshbach statistical model (Section 3.3.1). We chose to compare to the Hauser-Feshbach rate because, as discussed in Sections 4.2 and 4.2.1, the uncertainty surrounding both the number of resonances in the Gamow window and their spins and parities makes calculating the rate through those resonances a specious pursuit at best. Plotted in Fig. 6.3 is the ratio of the reaction rate calculated through the 6390-keV resonance to the Hauser-Feshbach rate. As discussed in Section 3.5.2, only $T = 1/2$ ^{31}S states are allowed by isospin selection rules to be populated via proton capture on ^{30}P. However, because the isospin mixing of the IAS and the 6390-keV state results in a small $T = 1/2$ component for the

Table 6.2: Thermonuclear ^{30}P$(p, \gamma)^{31}$S reaction rate $N_A\langle\sigma v\rangle$ in units of cm^3 mol^{-1} s^{-1} as a function of temperature (reported in GK, commonly notated T_9, as here), for commonly-attained nova temperatures. Here "RC" denotes the resonant capture through the $3/2^+$ state at 6390 keV. N_A is the Avogadro number. The rate is presented here without uncertainty limits because the only experimental uncertainty used in the calculation was that for the resonance energy E_r; this uncertainty affected the resonance strength by less than 0.2%.

T_9	$3/2^+$ RC	T_9	$3/2^+$ RC
0.01	8.002E-128	0.23	7.246E-05
0.015	1.583E-84	0.24	1.173E-04
0.02	6.199E-63	0.25	1.821E-04
0.03	2.034E-41	0.26	2.728E-04
0.04	1.026E-30	0.27	3.957E-04
0.05	2.511E-24	0.28	5.579E-04
0.06	4.336E-20	0.29	7.667E-04
0.07	4.447E-17	0.3	1.030E-03
0.08	7.847E-15	0.31	1.355E-03
0.09	4.295E-13	0.32	1.750E-03
0.1	1.038E-11	0.33	2.222E-03
0.11	1.388E-10	0.34	2.778E-03
0.12	1.190E-09	0.35	3.425E-03
0.13	7.264E-09	0.36	4.169E-03
0.14	3.396E-08	0.37	5.015E-03
0.15	1.283E-07	0.38	5.969E-03
0.16	4.081E-07	0.39	7.032E-03
0.17	1.126E-06	0.4	8.211E-03
0.18	2.764E-06	0.42	1.092E-02
0.19	6.143E-06	0.44	1.410E-02
0.2	1.256E-05	0.46	1.776E-02
0.21	2.389E-05	0.48	2.188E-02
0.22	4.274E-05	0.5	2.645E-02
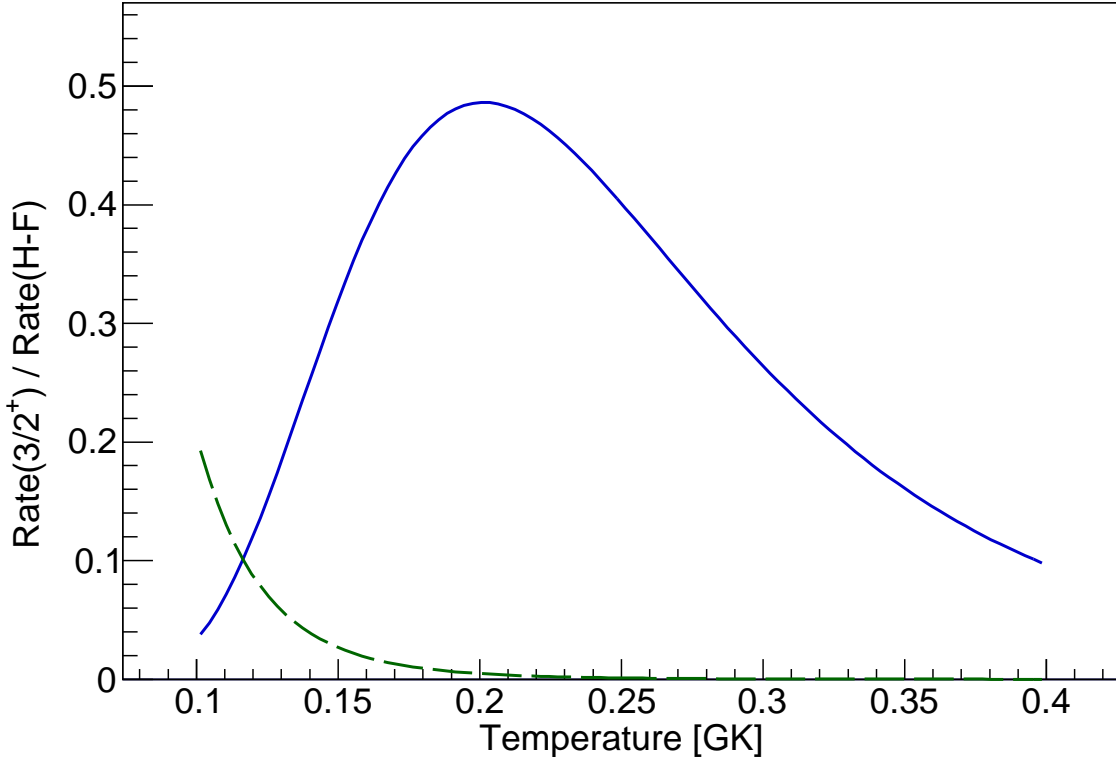
Figure 6.3: Ratios of the ^{30}P$(p, \gamma)^{31}$S thermonuclear reaction rates calculated for both the new $3/2^+$ state at 6390-keV [solid blue line] and the 6280-keV IAS [dashed green line] to the overall Hauser-Feshbach rate [98].

$T = 3/2$ IAS, there is a small contribution to the reaction rate through that level as well, plotted as a ratio to the Hauser-Feshbach rate alongside that of the 6390-keV state.

As shown in Fig. 6.3, the resonant capture reaction rate for this single resonance approaches 50% of the Hauser-Feshbach rate. This is a substantial contribution for a single resonance, considering that the Hauser-Feshbach rate is meant to estimate the total reaction rate through all levels. Despite the experimental progress made by the studies discussed in Section 4.2, the Hauser-Feshbach may remain the best estimate of the reaction rate because of the numerous ambiguities surrounding the resonances in the Gamow window. The fact that this single resonance approaches half of the theoretical estimate at peak nova temperatures means that it is the most important resonance with an unambiguous spin and parity assignment and, hence, a meaningful estimate of the reaction rate.

Given that the ^{30}P$(p,\gamma)^{31}$S rate for this single resonance produces an estimate that is a sizable portion of the Hauser-Feshbach rate, it is possible that the overall reaction rate is higher than previous studies have estimated. In addition to the positive-parity states observed in this study and modeled using the USDB and USDE interactions, the ^{30}P$(p,\gamma)^{31}$S rate is likely affected by the presence of a number of negative-parity states in the 6-7 MeV energy region. A recent study [97, 99] concluded that these negative-parity states, some of which have not yet been observed experimentally, are most important for determination of the ^{30}P$(p,\gamma)^{31}$S rate. The present work calculated a rate through only one single positive parity resonance and found a contribution of up to 50% of the Hauser-Feshbach rate; if the resonant capture rates through the negative parity states mentioned in Ref. [97] are as large as or larger than that for the 6390-keV state, the overall ^{30}P$(p,\gamma)^{31}$S rate could be several times higher than the Hauser-Feshbach rate.

A higher ^{30}P$(p,\gamma)^{31}$S rate could help to address the discrepancy between observed ^{30}Si/^{28}Si ratios from presolar nova grains and predicted ratios from nova models. If the actual ^{30}P$(p,\gamma)^{31}$S rate were much higher than the current estimates, it would be the case that much less ^{30}Si was produced from the beta decay of ^{30}P, since much more ^{30}P would be destroyed via proton capture. Thus, nova nucleosynthesis would produce a more modest excess of ^{30}Si, potentially bringing theoretical predictions of Si isotopic abundances more in line with the observed abundances in grains.

6.2 Isobaric Multiplet Mass Equation Studies and the Second ^{31}Cl $T = 3/2$ State

Note: This section is adapted from a paper previously published by the author and collaborators on this subject, Ref. [100]

6.2.1 Lowest $A = 31, T = 3/2$ Quartet

The isospin mixing of the IAS means that the observed excitation energy of $E_x = 6279.0(6)$ is perturbed from the value of the excitation energy that would be predicted by the isobaric multiple mass equation (Section 3.5.3). Fitting the IMME with the observed excitation energy of this state and its $T = 3/2$ analogs in ^{31}Cl, ^{31}P, and ^{31}Si could therefore result in a breakdown of the IMME, likely requiring a cubic term. It has historically been difficult, however, to test the IMME for the lowest $A = 31, T = 3/2$ quartet because of imprecision in the experimental mass excess value Δ of ^{31}Cl. Until recently, the value used in IMME tests was from a 1977 experimental measurement of the ^{36}Ar(^{3}He,^{8}Li)^{31}Cl Q-value: $\Delta = -7070 \pm 50$ keV [101]. A much more precise Penning trap mass measurement of ^{31}Cl, published in 2016, obtained a value for the ground state mass excess that was 15 times more precise than this value [102]. This observation did in fact lead to an observed breakdown of the IMME, requiring a large cubic term of $d = -3.5(11)$ keV.

Given the observation of strong isospin mixing in ^{31}S, it is interesting to consider whether or not this mixing plays an appreciable role in the breakdown of the IMME for the lowest $A = 31, T = 3/2$ quartet. Ref. [102] used the value of the ^{31}Cl ground-state mass excess obtained in that study along with the literature values for the other ground-state mass excesses of the quartet members and the excitation energies. To confirm the results of that

Table 6.3: Ground-state mass excess Δ and excitation energy E_x values used as input for the IMME fits of the lowest $A = 31, T = 3/2$ quartet. Except for the observed excitation energy of the ^{31}S IAS, which is from Ref. [89], all values are the same as in Ref. [102].

Nucleus	T_z	Δ [keV]	E_x [keV]
^{31}Cl	$-3/2$	$-7034.7(34)$	0
^{31}S	$-1/2$	$-19042.52(23)$	6279.0(6)
^{31}P	$+1/2$	$-24440.5411(7)$	6380.8(17)
^{31}Si	$+3/2$	$-22949.04(4)$	0

Table 6.4: Output coefficients for the quadratic and cubic IMME fits for the lowest $A = 31, T = 3/2$ quartet using input data from Table 6.3. All coefficient values are in units of keV. The cubic fit did not contain any degrees of freedom, so the χ^2/ν value is undefined and hence ommitted.

	Quadratic	Cubic
a	$-15466.3(9)$	$-15464.1(10)$
b	$-5302.4(10)$	$-5295.2(20)$
c	$209.2(9)$	$209.9(10)$
d	$--$	$-4.3(11)$
χ^2/ν	$16.0/1$	$--$

study as a starting point, we have replicated that fit with the only difference being the use of our experimentally-determined excitation value for the IAS, $E_x = 6279.0(6)$. We used this value rather than the literature value, which is based on a fit of gamma-ray energies from a previous ^{31}Cl beta-decay measurement [72] that is currently unpublished and has greater uncertainty on the value ($\approx$2 keV; the two excitation energies are thus consistent). The result of using our excitation energy value is, however, similar to Ref. [102]: the IMME fails, requiring an even larger cubic term $d = -4.3(11)$ keV, and the reduced chi-squared value of the purely quadratic fit increases from $\chi^2/\nu = 11.6$ in Ref. [102] to 16.0. The inputs and outputs for this IMME fit are reported in Tables 6.3 and 6.4, respectively.

It could be the case that the IMME fit would work if, instead of using the observed excitation energy of the ^{31}S IAS, the fit were performed using the unperturbed excitation

Table 6.5: Ground-state mass excess Δ and excitation energy E_x values used as input for the IMME fits of the lowest $A = 31, T = 3/2$ quartet. Except for the unperturbed excitation energy of the ^{31}S IAS, which is from the present work [89], all values are the same as in [102].

Nucleus	T_z	Δ [keV]	E_x [keV]
^{31}Cl	$-3/2$	$-7034.7(34)$	0
^{31}S	$-1/2$	$-19042.52(23)$	$6297.6(13)$
^{31}P	$+1/2$	$-24440.5411(7)$	$6380.8(17)$
^{31}Si	$+3/2$	$-22949.04(4)$	0

Table 6.6: Output coefficients for the quadratic and cubic IMME fits for the lowest $A = 31, T = 3/2$ quartet using input data from Table 6.5. All coefficient values are in units of keV.

	Quadratic	Cubic
a	$-15453.0(12)$	$-15454.6(12)$
b	$-5307.0(10)$	$-5316.1(24)$
c	$206.4(10)$	$205.2(10)$
d	$--$	$5.0(12)$
χ^2/ν	$17.0/1$	$--$

energy of that state. To test whether isospin mixing in ^{31}S could account entirely for the IMME breakdown, we performed an IMME fit including the unperturbed ^{31}S IAS energy, keeping the other inputs constant from Ref. [102]. However, far from solving the IMME breakdown, using the unperturbed ^{31}S IAS energy actually exacerbates the problem: the result is a reduced chi-squared value of $\chi^2/\nu = 17.0$ in the quadratic fit, increased from both the fit in Ref. [102] and our own fit using the observed IAS energy, and a cubic term even larger in magnitude, $+5.0(12)$ keV. Input and output parameters for this fit are reported in Tables 6.5 and 6.6, respectively, and residuals for the quadratic fit are shown in Fig. 6.4.

Clearly, isospin mixing in ^{31}S alone cannot account for the IMME breakdown. However, given the mirror nature of ^{31}S and ^{31}P, it is likely that there is similar isospin mixing present in the latter's isobaric analog state, which has not yet been directly observed. We attempted
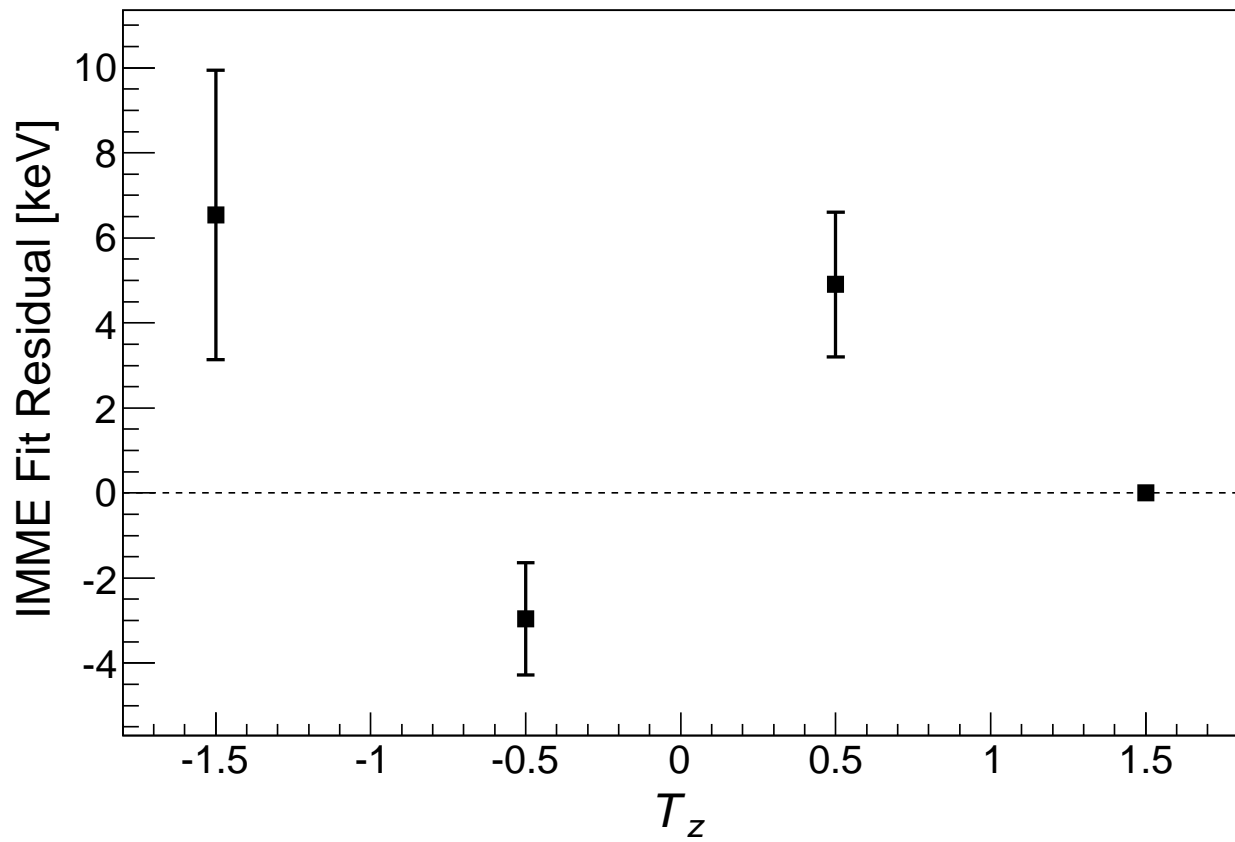
Figure 6.4: Residuals for the quadratic IMME fit of the lowest $A = 31, T = 3/2$ quartet (Tables 6.5 and 6.6) after accounting for the observed isospin mixing in ^{31}S.

to use our unperturbed ^{31}S IAS energy and the results from Ref. [102] to predict the "unperturbed" energy for the ^{31}P IAS, the lowest $T = 3/2$ state in that nucleus. The result of the prediction using the quadratic IMME is a ^{31}P state at $E_x = 6390.8(24)$ keV, only 10 keV above the current observed excitation energy value of 6380.8(17) keV. In the event that the observed excitation energy is the result of a perturbation due to isospin mixing with a nearby higher-energy $T = 3/2$ state or fragment, its actual energy could be high enough to revalidate the IMME after accounting for said mixing.

A cursory glance at the 2013 $A = 31$ Nuclear Data Sheets [79], however, seems to imply that no such state is known to exist. No nearby states in the evaluation have spin and parity required for mixing with the ^{31}P ($J^\pi = 3/2^+$) state. It is possible, using the two-level mixing scheme from Section 3.5.4 to derive combinations of mixing matrix element V and unperturbed excitation energy D for such a state, such that the IMME is revalidated. Using the two-level mixing equations and the observed and predicted energies of the ^{31}P IAS, the curve shown in Fig. 6.5 is the result for $E_x > 6401$ keV. The solution at 6401 keV corresponds to the limiting case of two degenerate states at $E_x \approx 6391$ keV, both pertrubed by 10 keV (that is, $D = 0$ and $E = 2V$).

Using this curve, it is possible to make a naive empirical prediction of the energy of the ^{31}P state involved in mixing with the ^{31}P IAS, assuming that the unperturbed energy spacing is the same (74(2) keV). This value yields a second state at $E_x = 6454.8(35)$ keV, with an associated mixing matrix element of 27.2(35) keV. Coincidentally, this predicted state is near a known ^{31}P state at $E_x = 6460.8(16)$ keV. The $A = 31$ Nuclear Data Sheets [79] list this level as having spin and parity $J^\pi = 5/2^+$. Although this assignment is based on experimental work evaluated previously as leading to an unambiguous spin and parity [103], multiple experimental studies [104, 105, 106, 107, 53], while potentially favoring the

156
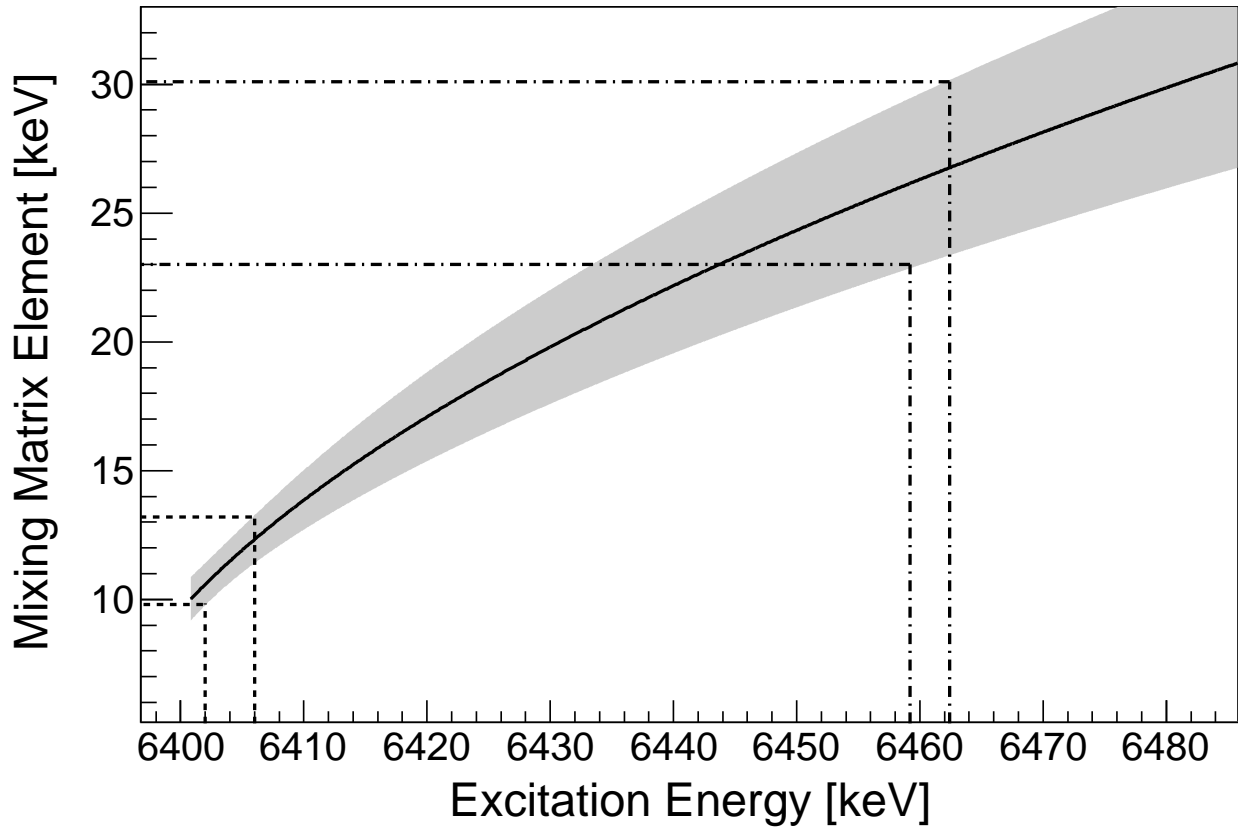
Figure 6.5: Isospin mixing matrix element, including 1σ confidence band, of a hypothetical state engaged in isospin mixing with the ^{31}P IAS at 6381 keV as a function of the observed excitation energy of the second state. The band is derived under the assumption that the IMME provides a good fit of the data after accounting for isospin mixing. The dotted (left) and dot-dashed (right) lines show the 1σ bounds obtained using this prediction when the USD mixing matrix element and 6461-keV state energy, respectively, are used as inputs.

Table 6.7: Calculated excitation energies E_x and mixing matrix elements V of the triplet of isospin-mixed states including the lowest $T = 3/2$ state in ^{31}P for both USDB and USDE interactions. The matrix elements listed are between the listed $T = 1/2$ state and the $T = 3/2$ state. All values are in units of keV.

	J^π	USDB E_x	USDB V	USDE E_x	USDE V
$E_1(T = 1/2)$	$3/2^+$	6258	8.3	6118	4.2
$E_2(T = 3/2)$	$3/2^+$	6364	$--$	6236	$--$
$E_3(T = 1/2)$	$3/2^+$	6579	10.9	6383	12.7

$5/2^+$ assignment, have not excluded the $3/2^+$ assignment. Furthermore, as noted in Ref. [79], one study [108] has even labeled the state as $J^\pi = 1/2^+$, further complicating the matter. If the state did in fact have spin and parity $J^\pi = 3/2^+$, it could mix with the ^{31}P IAS at 6381 keV.

To complement this rudimentary empirical approach and facilitate the search for the hypothetical ^{31}P mixing with the ^{31}P IAS, B.A. Brown performed shell-model calculations using both the USDB and USDE interactions to predict mixing matrix elements and excitation energies for the ^{31}P and nearby states. As with the ^{31}S case described in Section 6.1, the results of the calculations are a triplet of $J^\pi = 3/2^+$, including the IAS, all involved in isospin mixing. The results of these calculations are reported in Table 6.7. As shown in the table, the mixing matrix elements for the ^{31}P case are much smaller than for the ^{31}S case (Table 6.1). While tentative experimental candidates for the lower mixed state in the triplet exist at 6233 keV and 6158 keV [79], no higher candidate is apparent, with the exception of the state at 6461 keV. This state, however, requires a significantly higher mixing matrix element than the calculations using USD predict; as such, it should be regarded as a tentative solution at best. The shell-model matrix elements for the mixed states and the functional form in Fig. 6.5 can be used to derive theoretical upper and lower bounds for the excitation energy of the mixed ^{31}P state of $E_x = 6406$ keV and $E_x = 6402$ keV, respectively.

Experimental searches are therefore needed to uncover potential ^{31}P states in the energy region slightly above $E_x = 6400$ keV which could fulfill the role of the $J^\pi = 3/2^+$ state mixing with the IAS, as well as to determine with certainy the spin and parity of the 6461-keV state. As an interesting astrophysical aside, the spin and parity assignments of Refs. [62, 63] used the $5/2^+$ assignment for this state, additionally using the mirror state assignment to infer the same spin and parity for an observed ^{31}S level at 6393 keV. If this 6461-keV state is in fact a $3/2^+$ state, it would mean that it is the mirror of the 6390-keV ^{31}S level discovered in the present work, rather than the mirror of the 6393-keV ^{31}S level described in Refs. [62, 63]. If another nearby ^{31}P state is discovered to be $J^\pi = 3/2^+$ state instead, it could inversely imply that the two ^{31}S states at 6390 keV and 6393 keV are distinct.

6.2.2   Second $A = 31, T = 3/2$ Quartet

The lowest $A = 31, T = 3/2$ quartet includes the ^{31}Cl and ^{31}Si ground states and the lowest $T = 3/2$ excited states in ^{31}S and ^{31}P. However, as illustrated for $A = 13$ in Fig. 3.6, there is also a $T = 3/2$ quartet for each excited state in ^{31}Cl and ^{31}Si, which also includes $T = 3/2$ states in ^{31}S and ^{31}P with excitation energies greater than the excitation energies of the ground-state isobaric analogs. As with the lower quartet, it has been historically difficult to test the IMME in the second quartet, largely due to uncertainties associated with both the excitation energy of the first excited state in ^{31}Cl and ambiguity in the identity of the second $T = 3/2$ state in ^{31}S.

In fact, a tentative measurement of the first ^{31}Cl excited state via ^{31}Ar β decay [109] was the only evidence for the observation of that state [83] until a recent Coulomb-breakup experiment was performed to confirm the existence of the state [110]. In this study [110], the excitation energy was found to be $E_x = 782(32)$ keV, leaving the identity of the second

^{31}S $T = 3/2$ state as the primary ambiguity in the quartet. Various sources have reported excitation energies for the ^{31}S state ranging from a definite $T = 3/2$ assignment for a state at $E_x = 7006(25)$ keV using the ^{29}Si(^{3}He,n)^{31}S reaction [81] with somewhat low precision to a relatively precise, but tentative, assignment for a state at $E_x = 7036(2)$ keV [111], with alternative candidates at 6975(3) [97, 111] and 7053(2) keV [111].

Although this $J^\pi = 1/2^+$ ^{31}S state is expected to be nearly 1 MeV above the proton threshold, the proton emission is isospin forbidden and, therefore, it should have a substantial gamma-decay branch unlike the other low-spin levels in the region [112]. Precise observation of a high energy γ-ray transition from a low-spin state in this region would be a signature of the second $T = 3/2$ state, allowing for a precise determination of its energy. The shell model predicts that the state decays predominantly to the ground state, and shell model calculations using both USDB [113] and the recently-developed USDE [89] models predict a ^{31}S state 745(50) keV above the ^{31}S IAS energy of $E_x = 6279$ keV. In the shell model, this state has a ^{31}Cl β feeding of 0.03(2)% and a ground-state γ-decay branch of $\Gamma_\gamma^{g.s.}/\Gamma_\gamma = 0.95(4)$.

Analysis of E12028 resulted in the identification of a number of new ^{31}S states. As discussed in Section 5.3.3, the spins and parities for a majority of new states were inferred by comparing to shell model calculations. Isospin mixing of the state at 6390 keV and the IAS allowed for the deduction of that state's spin and parity with precision. We did not observe any photopeaks between $E_x = 6400$ and $E_x = 7000$ keV. Slightly above this energy region, we observed a photopeak at $E_\gamma = 7049.2(8)$ which does not appear in coincidence with any other peak, indicating that it is likely a transition to the ground state. This state's excitation energy of $E_x = 7050.0(8)$ keV, approximately 770 keV above the 6279-keV ^{31}S IAS, is also consistent with our shell-model calculations, which predict a second $T = 3/2$ level 770 keV above the theoretical IAS. The observed beta feeding of this state, 0.047(5)%, is also

Table 6.8: Ground-state mass excess Δ and excitation energy E_x values [79] used as input for the IMME fits of the second-lowest $A = 31, T = 3/2$ quartet.

Nucleus	T_z	Δ [keV]	E_x [keV]
^{31}Cl	$-3/2$	$-7034.7(34)$	$782(32)$
^{31}S	$-1/2$	$-19042.52(23)$	$7050.0(8)$
^{31}P	$+1/2$	$-24440.5411(7)$	$7141.1(18)$
^{31}Si	$+3/2$	$-22949.04(4)$	$752.23(3)$

Table 6.9: Output coefficients for the quadratic and cubic IMME fits for the second-lowest $A = 31, T = 3/2$ quartet using input data from Table 6.8. All coefficient values are in units of keV.

	Quadratic	Cubic
a	$-14697.3(14)$	$-14698.6(22)$
b	$-5307.2(19)$	$-5306.0(25)$
c	$205.0(18)$	$211(8)$
d	$--$	$-4(5)$
χ^2/ν	$0.51/1$	$--$

consistent with shell model predictions, and no other gamma-ray transitions de-exciting the state were observed. Based on the observed agreement with the shell model predictions, the singular gamma branch to the ground state, and a small, previously observed beta-proton branch [83], we have identified this state as the second ^{31}S $T = 3/2$ state, with $J^\pi = 1/2^+$.

Similarly to the lowest quartet, we fit the second $A = 31, T = 3/2$ quartet, including the new 7050-keV state excitation energy and the excitation energies of the other three quartet members, using the IMME. The input mass excesses and excitation energies are reported in Table 6.8, and the output parameters are reported in Table 6.9. As shown, the quadratic fit yields a reduced chi-squared value of $\chi^2/v = 0.51/1$ and a p-value of 0.48, indicating a good fit. This further confirms that the state at 7050 keV is indeed the ^{31}S member of the second $T = 3/2, A = 31$ quartet. The residuals for this fit are shown in Fig. 6.6.

Although the quadratic IMME fit is very good of the measured mass excesses and ex-
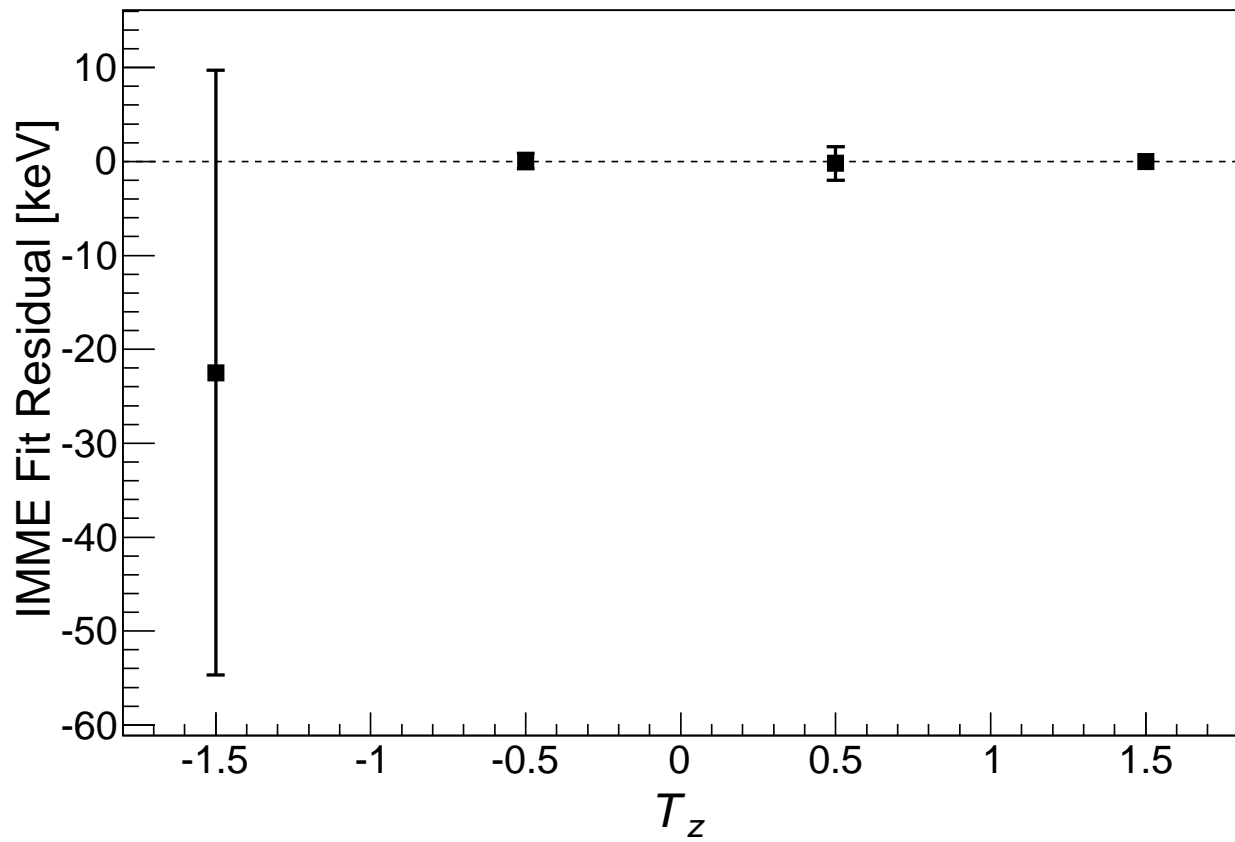
Figure 6.6: Residuals for the quadratic IMME fit of the second-lowest $A = 31, T = 3/2$ quartet (Tables 6.8 and 6.9).

Table 6.10: Calculated excitation energies E_x and mixing matrix elements V of the triplets of states involved in mixing with the second-lowest $T = 3/2$ states in both ^{31}S and ^{31}P, for both USDB and USDE interactions. The matrix elements listed are between the listed $T = 1/2$ state and the $T = 3/2$ state. All values are in units of keV.

^{31}S	J^π	USDB E_x	USDB V	USDE E_x	USDE V
$E_1(T = 1/2)$	$1/2^+$	7234	7.8	6421	6.8
$E_2(T = 3/2)$	$1/2^+$	7271	$--$	6944	$--$
$E_3(T = 1/2)$	$1/2^+$	7814	22	7117	9.4

^{31}P	J^π	USDB E_x	USDB V	USDE E_x	USDE V
$E_1(T = 1/2)$	$1/2^+$	7251	6.5	6417	3.1
$E_2(T = 3/2)$	$1/2^+$	7310	$--$	6982	$--$
$E_3(T = 1/2)$	$1/2^+$	7861	6.1	7127	7.2

citation energies of the quartet members, it is possible that, as with the first quartet, a small amount of isospin mixing perturbs the excitation energies of the ^{31}S or ^{31}P member states. Potential candidate $T = 1/2$ states exist in both nuclei, but no experimental evidence was observed in E12028 to positively identify any such ^{31}S state. As mentioned previously, no ^{31}S gamma-ray transitions were observed corresponding to states between $E_x = 6400$ and $E_x = 7000$. To estimate the potential amount of mixing, B.A. Brown used both the USDE and USDB interactions to predict energy levels and mixing matrix elements for both ^{31}S and ^{31}P, as was done for the lowest quartet (Tables 6.1 and 6.7). The models produce small mixing matrix elements, consistent with the lack of observational evidence from our experimental data. The results of the shell-model calculations are reported in Table 6.10.

Using our high-precision measurement of the excitation energy of the $T = 3/2$ state in ^{31}S, it is possible to test the recent measurement [110] of the ^{31}Cl first excited state using the IMME. By including the new measurement of the second $T = 3/2$ ^{31}S state excitation energy with the excitation energies and ground-state mass excess values for ^{31}P and ^{31}Si to produce

the IMME curve, and accounting for the uncertainty introduced by the possibility of isospin mixing via the d coefficient in the cubic fit, we derive an IMME mass excess for the ^{31}Cl first excited state of $\Delta = -6276(10)$ keV. When combined with the new, precise ground-state mass excess from Ref. [102] and its uncertainty, we calculate an excitation energy $E_x = 759(11)$ keV for the state, a value consistent with the measured value of $E_x = 782(32)$ keV [110].

It is also possible to use the recent value [102] of the ^{31}Cl proton separation energy, $S_p = 265(4)$ keV and the ^{30}S $+p$ resonance energy based on the beta-proton measurement, $E_r = 461(15)$ keV [83, 109]: the result of the calculation is an excitation energy of $E_x = 726(16)$ keV, which is consistent with our prediction to within 1.8 combined standard deviations and with the value from Ref. [110] to within 1.6 combined standard deviations. Given the slight tension between the value based on the beta-proton measurement [109] and the other two values, a new measurement of ^{31}Ar beta decay [114, 115] with high sensitivity to low-energy protons would be an interesting study.

6.3 Discrepancies with the Nuclear Data Sheets and Comparison to Previous Work

E12028 is one of only a few beta decay experiments performed to date, but has nevertheless yielded over two orders of magnitude higher statistics for analysis than the most recent experiment [72], resulting in a decay scheme with double the number of observed gamma-ray transitions and nine new observed beta transitions. The minimum finite beta feeding observed was $I_\beta = 0.023(7)\%$, to the state at 5436 keV. This improvement in sensitivity tells us much about the ^{31}S nucleus, but it also allows for insight into the results of previous

experiments as well.

6.3.1 Unobserved Previously-Reported Transitions

In particular, several states reported in the $A = 31$ Nuclear Data Sheets between $E_x = 5$ MeV and $E_x = 8$ MeV were *not* observed in E12028. The excitation energies of these states reported in the beta decay scheme of the NDS are: 5408.2 keV (J^π unconstrained), 5786.2 keV ($J^\pi = (1/2, 3/2, 5/2)^+$), 6420.7 keV ($J^\pi = (1/2, 3/2, 5/2)^+$), 7280.0 keV ($J^\pi$ unconstrained), 7416.8 keV, (J^π unconstrained), 7631.8 keV ($J^\pi = (1/2, 3/2, 5/2)^+$), and 7644.5 keV ($J^\pi = (1/2, 3/2, 5/2)^+$). The states at 5786, 6421, 7280, 7417, 7632, and 7645 keV are from tentative assignments made in the previous ^{31}Cl decay study [72], but our experiment was much more sensitive and did not observe these peaks. Therefore, we attribute them to contaminants in the experiment of Ref. [72] and have elected to omit them from our normalization and decay scheme.

The $A = 31$ Nuclear Data Sheets also report a transition from the state at 3076 keV to the state at 2234 keV, based on the reports of Refs. [72] and [116], but note in their decay scheme that the transition was not included in the least-squares fit that resulted in the quantities reported in the table. The NDS evaluators note as well that the difference in energy between the two states ostensibly involved in the transition is only 842 keV. Ref. [72] assigned the transition an absolute gamma intensity per 100 beta decays of $I_\gamma = 1.1(1)$, implying that the peak should be stronger than the nearby 985-keV gamma ray marking the transition between the 2234 and 1248-keV states, which is assigned an absolute intensity of only 0.2(1). However, despite observing the 985-keV gamma ray, we did not observe a photopeak at 845 keV in our beta-delayed gamma-ray spectrum or in the 2234-keV coincidence spectrum. After attempting to fit this region, we obtained an upper limit on the intensity of this transition

of $I_\gamma = 0.018(4)$ per 100 beta decays, and have omitted it from the normalization and decay scheme.

6.3.2   Spin and Parity Discrepancies

As discussed in Section 4.2, the spin and parities of several important resonance states in the $^{30}\text{P}(p,\gamma)^{31}\text{S}$ Gamow window are not known unambiguously, due to discrepancies in assignments between different experiments [64, 62, 63]. Since ^{31}Cl preferentially populates $J^\pi = 1/2^+, 3/2^+$, and $5/2^+$ states, we can compare our assignments to any assignments with those spins and parities in previous studies. Refs. [64] and [63] report a number of spin and parity assignments that are at odds with one another; the sensitivity of our experiment allows us to comment on the assignments of Refs. [64] and [63] and the likelihood of these assignments being correct.

Ref. [64], for example, reports two states: one at 6328.6(9) keV and one at 6356.1(9) keV, with $J^\pi = 1/2^+$ and $3/2^+$, respectively. Ref. [63], however, assigns these states spins and parities of $3/2^-$ and $5/2^-$, respectively. Given that these levels were not observed in E12028, we believe it is more likely that the spin and parity assignments of Ref. [63] are correct for these states. Ref. [64] also reports a number of other states that might have been visible in the E12028 data, but are absent: a level at 6719.9(9) keV with $J = 5/2$, a level at 6749.0(9) keV with $J^\pi = 3/2^+$, a level at 6936.7(17) keV with $J^\pi = (1/2 - 5/2)^+$, a level at 6959.6(16) keV with $J^\pi = 1/2^+$, and a level at 7033.5(13) keV with $J^\pi = (1/2 - 5/2)^+$. These states, which are comparatively higher above the proton emission threshold than the low-lying resonances observed in E12028, decay primarily via proton emission, so the lack of observation in E12028 is not a significant cause for concern. The 7033-keV state is interpreted as the state that Ref. [71] tentatively identifies, and E12028 has confirmed as, the second

$T = 3/2$ ^{31}S state.

We also observe a few discrepancies with Ref. [63]. The level reported in Ref. [63] at $E_x = 4527.8(2)$ keV is given a J^π assignment of $3/2^+$. We did not observe any state at this energy; the closest candidate is the state at $E_x = 4519.63(32)$ keV, which we also assigned $J^\pi = 3/2^+$. Ref. [63] also reported a state at $E_x = 4710.1(8)$ with $J^\pi = 5/2^+$. We again did not observe a state at this energy, but instead have identified a $5/2^+$ state at the nearby energy $E_x = 4717.72(32)$ keV. We did not observe the $5/2^+$ state Ref. [63] reports at 5401.5(8) keV or the $5/2^+$ state at 5518.3(3) keV, and the closest state we observed to these energies, at 5435.9(9), was assigned $J^\pi = 3/2^+$. We did observe a state at 5775.4(4) keV, which we have assigned a spin and parity of $5/2^+$, but which Ref. [63] did not observe.

Ref. [63] makes a couple of tentative assignments, which the results of E12028 could help narrow down. Ref. [63] reports a state at 6138.3(21) keV, identified by both the transition to the $7/2^+$ state at 3349 keV and the transition to the $3/2^+$ first excited state at 1248 keV, with spin and parity $J^\pi = (3/2, 7/2)^+$. This state is near in energy to the state we identified at 6129 keV, but we assigned this state a spin and parity of $5/2^+$ based on a comparison to our shell model calculations. The assignment in Ref. [63] is made based on both the angular distributions measured for the transitions and the mirror nucleus assignment to a ^{31}P state at 6233.4(15) keV. Interestingly, however, the two gamma branches observed in Ref. [63] are the two strongest branches reported in our calculations, and the ^{31}P state does not have a certain parity, instead reported in the NDS as $J^\pi = (3/2, 5/2, 7/2)^+$. If these two states are the same, and the shell model calculations are correct, it could imply that the assignment in Ref. [63] is incorrect.

The most interesting potential discrepancy between the present work and Ref. [63] is the state at 6390 keV. Ref. [63] reports a state at the nearby energy of 6392.5(2) keV (this state

was briefly mentioned at the end of Section 6.2.1), but assigns it a spin and parity of $5/2^+$, based on the angular distribution of the transition observed and the mirror assignment with the 6461-keV ^{31}P state. We did not observe this state in our analysis at all and the closest $5/2^+$ state to the 6390-keV state predicted by our shell-model calculations is $\approx$300 keV higher, implying either that its beta feeding is extremely low (in which case its photopeak would likely be entirely overwhelmed by the nearby strong 6390-keV photopeak), or that the assignment in Ref. [63] is incorrect. However, preliminary results from independent work by the authors of Ref. [63] seem to indicate that the gamma branches of the state at 6393 keV are inconsistent with the branches we observed for the 6390-keV state [117], implying that the two states are nonetheless distinct.

Chapter 7

Outlook: The Future of $^{30}\mathrm{P}(p,\gamma)^{31}\mathrm{S}$

7.1 Conclusions

As a result of NSCL experiment 12028, a new $^{30}\mathrm{P}(p,\gamma)^{31}\mathrm{S}$ resonance state was discovered and found unambiguously, via isospin mixing with the nearby isobaric analog state, to have a spin and parity $J^{\pi} = 3/2^{+}$ [89]. This resonance was found to contribute strongly – up to 50% of the theoretical Hauser-Feshbach statistical model rate – to the $^{30}\mathrm{P}(p,\gamma)^{31}\mathrm{S}$ rate, making it the most important unambiguously identified resonance and a meaningful means of estimating the overall $^{30}\mathrm{P}(p,\gamma)^{31}\mathrm{S}$ rate. The revelation of the importance of the 6390-keV state to the $^{30}\mathrm{P}(p,\gamma)^{31}\mathrm{S}$ reaction rate and the implication that the rate may be higher than previously estimated mean that discrepancies between the slight $^{30}\mathrm{Si}$ excess observed in nova grains and the relatively large excess predicted by some nova models may be less at odds than previously thought: if the $^{30}\mathrm{P}(p,\gamma)^{31}\mathrm{S}$ proceeds more quickly than current models suggest, relatively fewer $^{30}\mathrm{S}$ nuclei will ultimately be produced via $^{30}\mathrm{P}$ beta decay, reducing the $^{30}\mathrm{Si}$ yield in models.

The observation of isospin mixing itself is a milestone in its own right: the first clear identification in the *sd* shell of mixing between a $T = 3/2$ state and a $T = 1/2$ state. The new USD interaction "USDE" was created by B. Alex Brown specifically for analysis of the results of isospin mixing in $^{31}\mathrm{S}$ and has already been used to study potential isospin

mixing in another *sd*-shell nucleus, ^{31}P. E12028 allowed for the definite identification of the second $T = 3/2$ state of ^{31}S via the gamma de-excitation of the 7050-keV state to the ground state ^{31}S [100] and, alongside the recent precision measurement of the ^{31}Cl second excited state energy [110], has allowed for the first precision test of the IMME for the second $A = 31, T = 3/2$ quartet. The IMME breakdown observed after the recent ^{31}Cl mass measurement [102] has not yet been solved, but we conclude it is likely that isospin mixing in ^{31}P to match the mixing in ^{31}S likely plays a role. The results of this work will provide an important starting point for the search for the potential mixed ^{31}P state.

The analysis of E12028 has also produced the most complete and detailed ^{31}Cl beta decay scheme to date, with 40 new observed gamma-ray transitions and ten new observed beta feedings, including new observations of forbidden beta decay. This scheme reflects over two orders of magnitude higher statistics acquired compared to previous work and has also allowed for the potential exclusion of several levels tentatively identified in previous work as belonging to ^{31}S. The improved accuracy of level identification in ^{31}S should assist in efforts to assign spins and parities based on, for example, comparisons to ^{31}P mirror states, which itself could help correctly deduce the parameters of the important resonances that contribute to the ^{30}P$(p, \gamma)^{31}$S reaction.

7.2   Outlook and Future Work

The results of E12028 are an important step toward answering the question of whether presolar "nova" grains do indeed originate in classical novae. However, the experiment by itself has not entirely solved the mystery of these ancient stellar messengers. The expected strength of the 6390-keV resonance may indicate that the overall reaction rate is higher than

the previously estimated rate, but unfortunately, constraints on important ^{31}S resonances other than the 6390-keV state remain elusive, and it is still not known with certainty how many ^{31}S states exist between $E_x = 6390$ keV and $E_x = 6410$ keV.

In addition, the rate calculated for the resonant capture through the 6390-keV state, while based on experimental findings, did require theoretical estimates of both the proton partial width Γ_p and the gamma partial width Γ_γ. Conveniently, the isospin mixing of this state with the nearby IAS and its consequently large beta feeding make it ideal for study using ^{31}Cl beta decay. A beta-delayed proton decay measurement of this state could produce an experimental measurement of the proton branching ratio which, alongside a measurement of the lifetime of the state, could yield an entirely experimental resonance strength and the first truly experimental calculation of a lower limit on the ^{30}P$(p,\gamma)^{31}$S rate. With the relatively large resonance strength expected for the 6390-keV state, it is also possible that the resonance could be accesed directly via proton capture on ^{30}P at the next generation of rare isotope beam facilities [118, 119].

Finally, it is probable [97] that a number of negative-parity resonances contribute strongly to the reaction rate at peak nova temperatures; study of these resonances was as a matter of design effectively prohibited in E12028, but future experimental work will also likely need to focus on the effects of these negative-parity states on the ^{30}P$(p,\gamma)^{31}$S rate.

Although the IMME breakdown reported in Ref. [102] has not been solved with the addition of isospin mixing in ^{31}S, a discovery of isospin mixing in ^{31}P could help revalidate the quadratic IMME in the lowest $A = 31, T = 3/2$ quartet. The 6461-keV state is the best candidate for mixing with the ^{31}P IAS, but it is not consistent with USD shell-model predictions and should be investigated further. Future nuclear structure studies could focus on gamma spectroscopy of energy levels in the energy region around the ^{31}P IAS to

complement the numerous charged particle measurements carried out to date and determine whether all levels in the region have been observed.

In the second $A = 31, T = 3/2$ quartet, three out of four members now have mass-excess uncertanties < 2 keV and their masses are well-described by the quadratic form of the IMME, but the extent of isospin mixing, although likely small, is still not known with certainty. Further studies of this multiplet could focus on reducing the uncertainty in the ^{31}Cl first excited state excitation energy. Both the measurement of ^{31}Ar beta-delayed protons and measurement via in-beam gamma ray spectroscopy could provide independent contributions toward reducing this uncertainty: the former could help address the apparent disagreement between Ref. [109] and Refs. [110, 100] and the latter could present a novel approach to measuring the excitation energy of this state.

7.3   Final Thoughts

Ultimately, no one experiment can currently address conclusively the numerous questions surrounding presolar nova grains and the ^{30}P$(p, \gamma)^{31}$S rate. E12028, like the many experimental studies that preceded it, represents only one important step on the journey toward answering whether or not these ancient microscopic grains do indeed come from classical novae. E12028 has also played an important role in helping to motivate future nuclear physics experiments by posing several questions that can be answered using techniques related to the beta-delayed gamma-ray spectroscopy employed for this study. Complementary beta-delayed proton measurements represent a promising pathway toward understanding of the nuclear structure of ^{31}S and other important nuclei. As it happens, a compact beta-delayed proton detector is already under development at the National Superconducting Cyclotron

Laboratory, with designs to answer these and many other interesting questions. With the advent new detectors like this, and the ability to put them to excellent use with next-generation facilities like the Facility for Rare Isotope Beams and the high-intensity exotic beams such facilities promise, the future of experimental study of both the nuclear aspect and the astrophysics aspect of classical novae looks incredibly bright.

APPENDICES

Theoretical Tools

As described in a number of previous chapters, we relied on a number of theoretical and predictive tools both to help plan the experiment and to help interpret the results of analysis. To justify the experiment and receive beam time, experimenters must be able to predict how many hours of beam they will need, and what level of statistics are required to achieve the experimental goals. In addition, experimenters must be able to assess the feasibility of producing the nuclide for study in the first place. For example, as mentioned in Chapter 4, it is not feasible to produce ^{30}P in large quantities for direct study of ^{30}P$(p, \gamma)^{31}$S. It would be costly to learn this fact only after securing dozens of hours of beam time, setting up an experimental setup, and starting an experiment; consequently tools for simulating the production of rare isotopes are required.

In this Appendix, we discuss two simulation tools, LISE++ and GEANT4, which we used both to assess the feasibility of E12028 before its execution and to interpret and check experimental results during its analysis. We will also discuss briefly the USD shell model calculations we performed during analysis and will report the results of those calculations.

Lise++: Exotic Beam Production with Fragment Separators

LISE++ is a freely-available program developed "to calculate the transmission and yields of fragments produced and collected in a spectrometer." [120] LISE++ allows the experimenter

to select a stable projectile and an energy and intensity post-acceleration, simulate the fragmentation of the projectile on a target, and tune the width of the target so as to produce the maximum simulated amount of a desired exotic nuclide "fragment." The experimenter can then build a simulated beamline, including fragment separators such as the A1900 and the RFFS as well as detectors such as silicon PIN detectors or the plastic scintillator used in E12028 (Fig. A.1). LISE++ contains a large list of materials with which experimenters can build "blocks" in the simulation; LISE++ also calculates the time-of-flight, energy loss, position, angular distribution, and other parameters for each of these blocks (Fig. A.2). In this way the experimenter can use LISE++ to simulate things like beam purification and production rate in order to determine the best experimental configuration to meet the experimental needs.

For E12028, we performed a LISE++ simulation that simulated ^{31}Cl fragment production at the NSCL for the ^{36}Ar beam that was ultimately used for the experiment. We were able to use the simulation to determine a baseline for the optimal tuning parameters for the A1900 as well as the thickness of the ^{9}Be target used for production (LISE++ is able to calculate an optimal target thickness (Fig. A.3) to maximize production of the desired fragment) and the optimal settings (voltage, phase angle) of the RFFS upstream of the experimental setup. We were also able to simulate the implantation depth of various beam constituents (Fig. A.4), a quantity subsequently used in our GEANT4 calculations to facilitate predictions of gamma-ray efficiency for the clover detectors.

In addition to the basic beamline simulation components, LISE++ contains a number of useful extras including a calculator to quickly determine energy loss through blocks and tools to simulate the interaction of the beam particles with those blocks. One of these tools, mentioned in Chapter 5, is the fusion-evaporation calculator PACE. PACE is a Monte Carlo
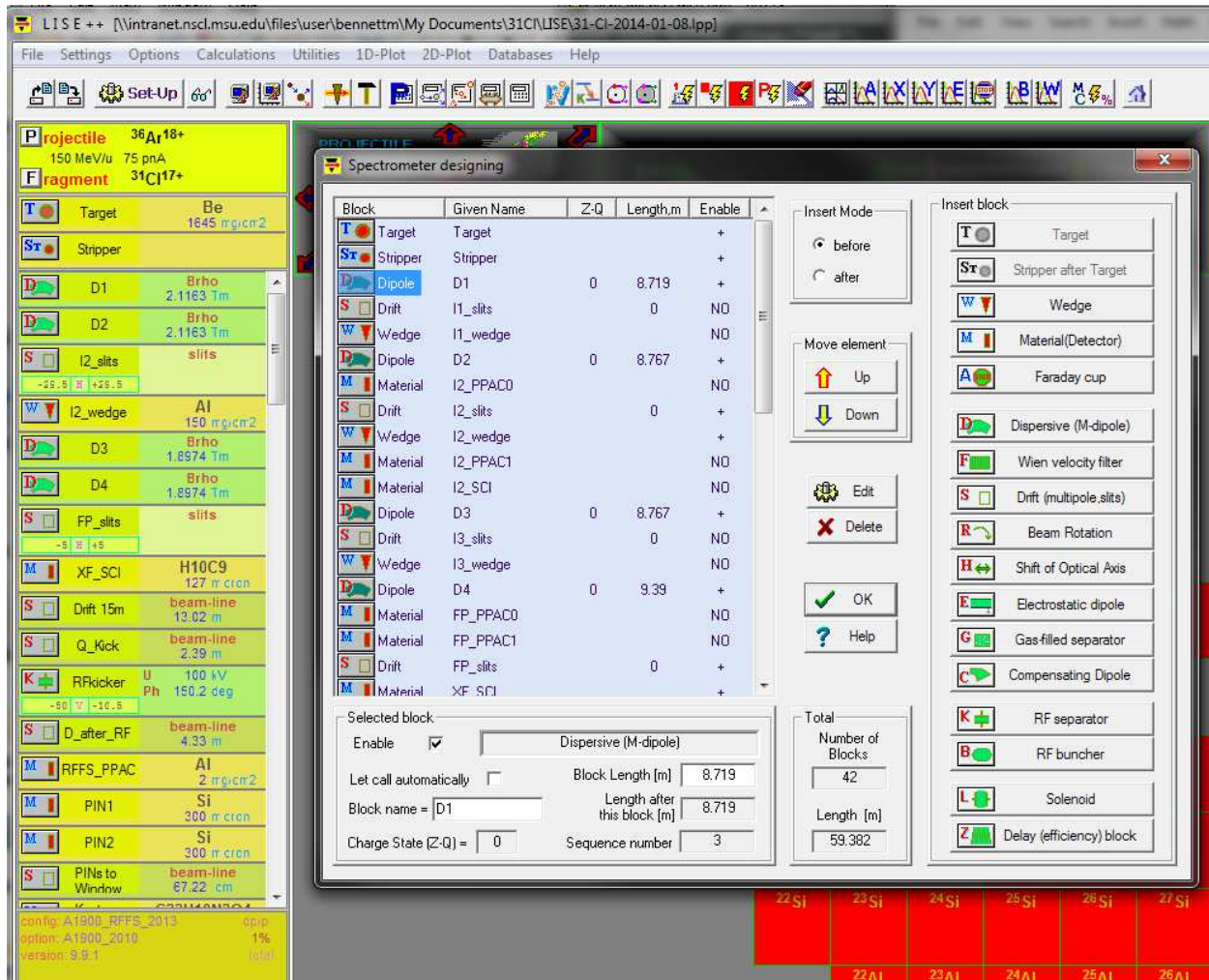
Figure A.1: A screenshot of LISE++, showing the spectrometer setup window in the center of the image and an assembled setup corresponding to the A1900 fragment separator and the RFFS on the left. Each "block" of material is inserted into the beamline using the setup window and has its own set of options, depending upon the type of block used.
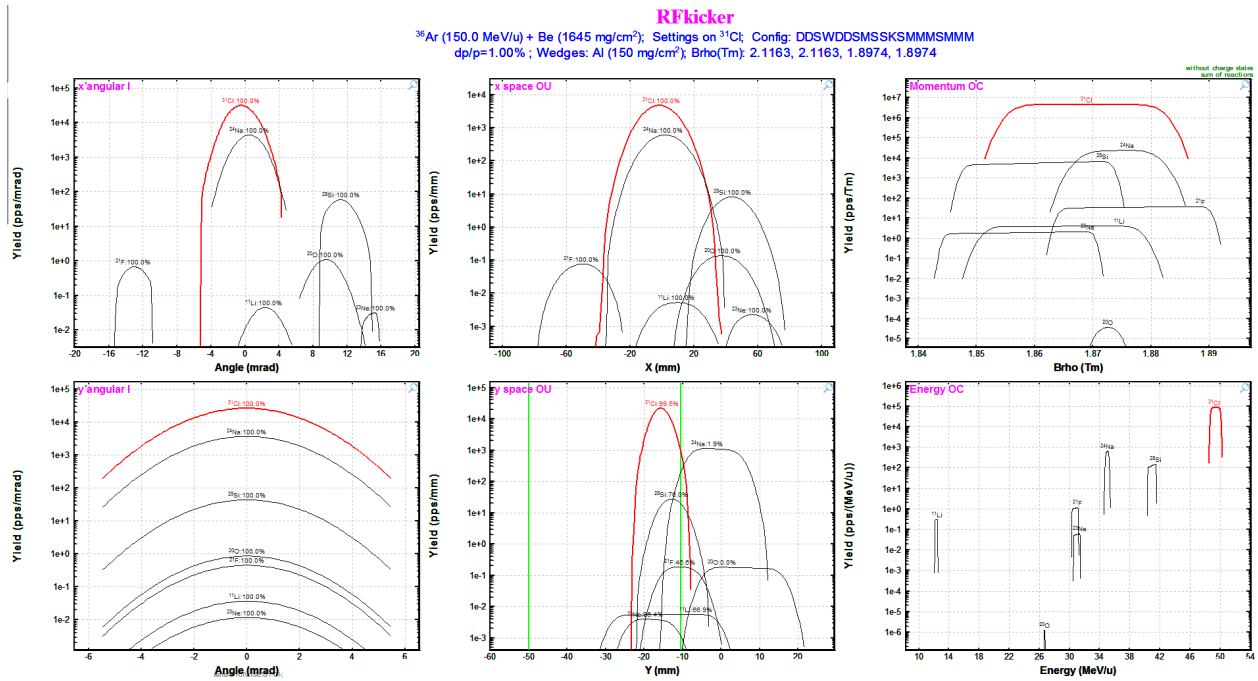
Figure A.2: A series of graphs from LISE++, showing the beam's simulated characteristics at the RFFS. Included calculations are the yield of each isotope, the dispersion angle, and position for both horizontal and vertical transverse directions, the rigidity of the beam constituents, and their energy.
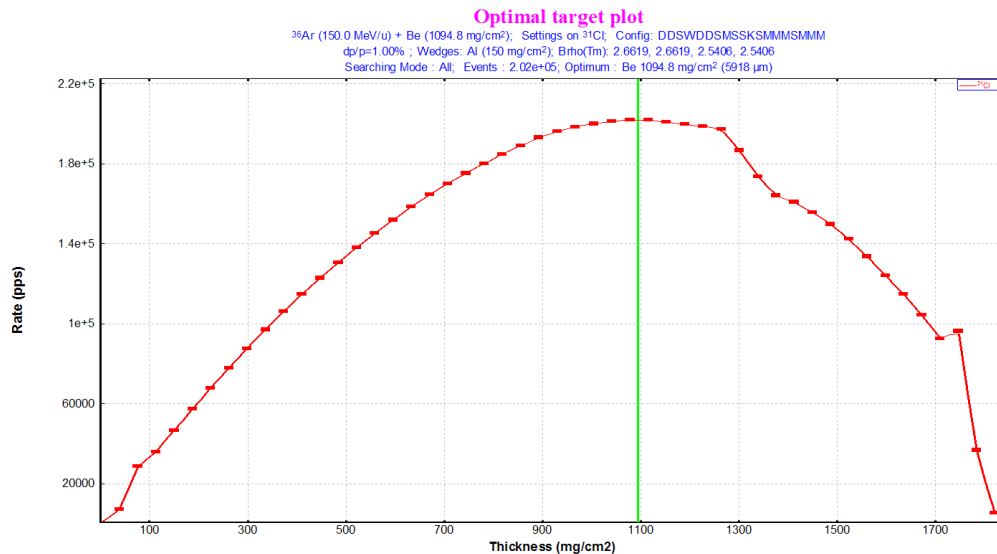
Figure A.3: The result of a LISE++ calculation to find the optimal thickness of the beryllium target for production of ^{31}Cl. Although *Lise++* gives an estimate of the best thickness, experimenters are as always limited by the availability of targets of varying thicknesses.
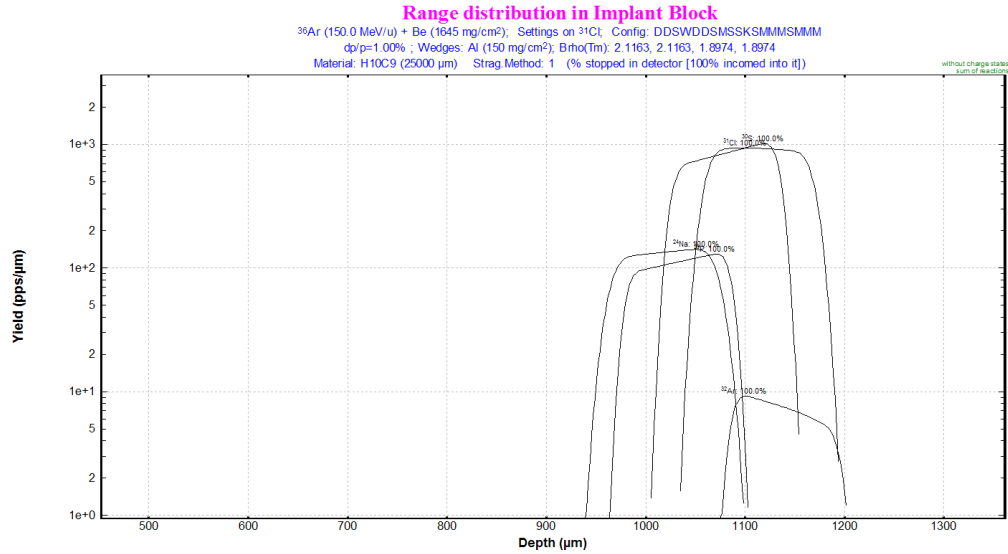
Figure A.4: The result of a LISE++ calculation showing the implantation depth of several beam consituents inside a target block. The calculation shows the yield of each species and its range in the material.

simulation tool that takes as input the masses of two nuclei and the beam energy (Fig. A.5) and produces not only a list of likely fusion-evaporation products but angular and energy distributions for these products as well as for protons, neutrons, and alpha particles produced through the process. PACE produces results in a text file; an output example is produced below in Section A.

Previous page | **CARD 2-1** | **Next page**

Projectile
A = 31   N = 14
Z = 17   Cl
Spin (gs) = 1.5
ME (MeV) = -7.070   DB

Target
A = 12   N = 6
Z = 6   C
Spin (gs) = 0
ME (MeV) = 0.000   DB

Compound
A = 43   N = 20
Z = 23   V
ME (MeV) = -18.020   DB

QCN = 0   Q value of reaction [MeV].
If == 0 it is calculated from mass tables.

Calculation
QCN = 10.950
E_CM = 432.558
Ex = 443.508

Beam Energy (MeV)
Elab = 1550   ☐ Batch Mode

EXPSIG = 0   experimental fusion cross section if known. TL-S from optical model shifted to reproduce this value if inputted, preserving the L-diffuseness. if == 0 Bass model (PRL 1977) fusion cross section being used.

JCMAX = 0   Maximum J to be used during calculations. (if 0 it is taken from optical model routine)

AGRAZ = 2   To bypass input channel optical model routine (TLOM) specify L-diffuseness of fusion cross section. If == 0 diffuseness will be set to 0.5 which is essentially sharp cutoff.

ELOSS = 0   energy loss of beam thru full target width. (total dE) energies will be distributed between Ebeam & Ebeam-Eloss

LMINN = 0   Lowest partial wave L in calculation. Partial waves from L=0 to LMINN excluded, enabling low-L non-fusion window in reaction calculation.

Transmission probabiltiy for a one-dimensional barrier (O.T.)
⦿ Classical (use it above the barrier)
◯ Quantum-mechanical [D.Hill & J.Wheeler, PhysRev 89(1953) 1105]

?

Note: If you are running at high bombarding energies for which the grazing angular momentum is above 75 hbar, it is recomended to input AGRAZ > 0, and to specify an arbitrary value for EXPSIG (or 0 = Bass) which corresponds to a fusion cross section with a limiting L-value around 80. This will give you all the evaporation residue data and the fission probabilities you need. For J>80 all nuclei will fission anyway, and you will run out of dimension if you try.

Figure A.5: The input card for PACE. As shown, the calculation requires the A and Z of both target and projectile as well as the laboratory energy of the beam.

PACE Output

The following code example is the output for a typical PACE fusion-evaporation calculation. The input nuclei in this case are ^{31}Cl and ^{12}C and the beam energy is simulated at 50 MeV/u (1550 MeV total beam energy).

```
\texttt{v.Version 4.20   13:46 30-06-16



                        P A C E    4



                        modified JULIAN



*********** projection angular-momentum coupled evaporation Monte Carlo code  ***********

*********** angular distributions obtained using M-states of angular momentum ***********



                                                MODE=1

 *********** Fusion xsection taken from Bass model

 Bass fusion xsection for E =1550.0 MeV  is 897 mb

 Fusion radius =  5.30 fm. Barrier height is  15.92 MeV
```

Transmission probability for a one-dimens.barrier: Classical

    Starting conditions

                            Z   N   A   Spin

        Projectile   17   14   31   1.5

        Target   6   6   12   0.0

        Compound nucleus   23   20   43

Bombarding energy (MeV)   1550.00

Center of mass energy (MeV)   432.56

Compound nucleus excitation energy (MeV)   443.508

Q-value of reaction (MeV)   10.950

Compound nucleus recoil energy (MeV)   1117.442

Compound nucleus recoil velocity (cm/ns)   7.086e+00

Compound nucleus velocity/c   2.362e-01

Beam velocity (cm/ns)   9.829e+00

Beam velocity/c   3.276e-01

*** Input transmission coefficients determined by input value of TL diffuseness.

*** diffuseness =   2.00

*** Optical model input calculation bypasses. *********

Experimental fusion cross section (mb)   897

Fusion L-grazing   70.907

Fusion L-difusseness   2.000

Yrast spin at maximum excitation energy   82

Compound nucleus formation cross section (mb)   897

                    Partial cross sections (mb)

   J   SIG(J) | J   SIG(J) | J   SIG(J) | J   SIG(J) | J   SIG(J) |

J	SIG(J)	J	SIG(J)	J	SIG(J)	J	SIG(J)	J	SIG(J)
0.5	0.18	17.5	6.3	34.5	12	51.5	18	68.5	18
1.5	0.7	18.5	6.7	35.5	13	52.5	19	69.5	16
2.5	1.1	19.5	7	36.5	13	53.5	19	70.5	14
3.5	1.4	20.5	7.4	37.5	13	54.5	19	71.5	11
4.5	1.8	21.5	7.7	38.5	14	55.5	20	72.5	8.3
5.5	2.1	22.5	8.1	39.5	14	56.5	20	73.5	6
6.5	2.5	23.5	8.4	40.5	14	57.5	20	74.5	4.1

```
7.5      2.8 | 24.5      8.8 | 41.5      15 | 58.5      21 | 75.5      2.7 |

8.5      3.2 | 25.5      9.1 | 42.5      15 | 59.5      21 | 76.5      1.8 |

9.5      3.5 | 26.5      9.5 | 43.5      15 | 60.5      21 | 77.5      1.1 |

10.5      3.9 | 27.5      9.8 | 44.5      16 | 61.5      22 | 78.5      0.7 |

11.5      4.2 | 28.5      10 | 45.5      16 | 62.5      22 | 79.5      0.44 |

12.5      4.6 | 29.5      11 | 46.5      16 | 63.5      22 | 80.5      0.27 |

13.5      4.9 | 30.5      11 | 47.5      17 | 64.5      22 | 81.5      0.17 |

14.5      5.3 | 31.5      11 | 48.5      17 | 65.5      22 | 82.5      0.1 |

15.5      5.6 | 32.5      12 | 49.5      18 | 66.5      21 | 83.5      0.057 |

16.5        6 | 33.5      12 | 50.5      18 | 67.5      20 | 84.5      0.028 |

-------------------------------------------------------------------------------
```

*** Spherical nucleus level density

*** Sierk barrier not found for A =   43 Z= 23

*** Input fission barrier = 39.70 MeV at L=0 taken from Sierk

*** G.S. little A multiplied by factor 1.000 obtain saddle level density

*** No fission calculation for barrier above 30.0 MeV

*** Little-A = MASS / 10.0

```
Energy range for        neutron    proton     alpha      gamma

minimal                  0.01       0.42       0.85       0.00

minimal                 40.00      29.26      51.77      20.00
```

*** Internal probability discriminator of program set to 0.0020   Number of cascades is 1000

Optical model parameters for light emitted particles

V	*E	*E**2	ROR	ARD	ROC	W0	*E	*E**2	RO1	AID	RMCHD	NPD	IMAG	IRAD
47.010	-0.267	-0.002	1.296	0.660	0.000	9.520	-0.053	0.000	1.257	0.480	0.000	250	SURF	1
57.468	-0.550	0.000	1.250	0.650	1.250	13.500	0.000	0.000	1.250	0.470	0.000	250	SURF	1
50.000	0.000	0.000	5.868	0.576	4.098	7.515	0.000	0.000	5.868	0.576	0.000	250	VOL	0

E.M.Transition strengths in Weisskopf units

E1 = 0.000080   M1 = 0.025000   E2 = 4.800000   M2 = 0.019500

*** Gilbert - Cameron spin cutoff parameter used

------   Output results for compound nucleus decay -----

1.Yields of residual nuclei

Z	N	A		events	percent	x-section(mb)
12	14	26	Mg	1	0.1\%	0.897
12	12	24	Mg	2	0.2\%	1.79
11	13	24	Na	1	0.1\%	0.897
12	11	23	Mg	1	0.1\%	0.897
11	12	23	Na	9	0.9\%	8.07
10	13	23	Ne	2	0.2\%	1.79
13	9	22	Al	1	0.1\%	0.897
11	11	22	Na	4	0.4\%	3.59
10	12	22	Ne	12	1.2\%	10.8
11	10	21	Na	7	0.7\%	6.28
10	11	21	Ne	17	1.7\%	15.2
9	12	21	F	2	0.2\%	1.79
10	10	20	Ne	34	3.4\%	30.5
9	11	20	F	8	0.8\%	7.18
10	9	19	Ne	3	0.3\%	2.69
9	10	19	F	12	1.2\%	10.8

8	11	19 O	5	0.5\%	4.48
9	9	18 F	2	0.2\%	1.79
8	10	18 O	13	1.3\%	11.7
9	8	17 F	8	0.8\%	7.18
8	9	17 O	59	5.9\%	52.9
7	10	17 N	3	0.3\%	2.69
9	7	16 F	1	0.1\%	0.897
8	8	16 O	103	10.3\%	92.4
8	7	15 O	28	2.8\%	25.1
7	8	15 N	112	11.2\%	100
6	9	15 C	3	0.3\%	2.69
8	6	14 O	1	0.1\%	0.897
7	7	14 N	17	1.7\%	15.2
6	8	14 C	32	3.2\%	28.7
7	6	13 N	10	1\%	8.97
6	7	13 C	137	13.7\%	123
5	8	13 B	3	0.3\%	2.69
6	6	12 C	105	10.5\%	94.2
6	5	11 C	13	1.3\%	11.7
5	6	11 B	75	7.5\%	67.3
4	7	11 Be	1	0.1\%	0.897

```
  5    5   10 B           1        0.1\%       0.897

  4    6   10 Be          1        0.1\%       0.897

  5    4    9 B          14        1.4\%        12.6

  4    5    9 Be         35        3.5\%        31.4

  3    6    9 Li          1        0.1\%       0.897

  4    4    8 Be         14        1.4\%        12.6

  4    3    7 Be          7        0.7\%        6.28

  3    4    7 Li         31        3.1\%        27.8

  3    2    5 Li          6        0.6\%        5.38

  2    3    5 He          5        0.5\%        4.48

  2    1    3 He          1        0.1\%       0.897

  1    2    3 H           1        0.1\%       0.897

  Total fission         36        3.6\%        32.3

  TOTAL               1000        100\%         897
```

Mode = ALPH   Total number = 113

| 15-30 | 1 | .. | .. | .. | .. | .. | .. | .. | .. | .. | .. | .. | .. | .. | .. | .. | 1 | 2.0 | 0.0 |
| 30-45 | 8 | .. | .. | .. | .. | .. | .. | .. | .. | .. | .. | .. | .. | .. | .. | .. | 8 | 2.0 | 0.0 |

	C1	C2	C3	C4	C5	C6	C7	C8	C9	C10	C11	C12	C13	C14	C15	Total	Mean	SD
45–60	6	4	..	..	..	..	..	..	..	..	..	..	..	..	..	10	4.0	2.4
60–75	8	1	..	..	..	..	..	..	..	..	..	..	..	..	..	9	2.6	1.6
75–90	1	2	..	..	..	..	..	..	..	..	..	..	..	..	..	3	5.3	2.4
90–105	4	2	..	..	..	..	..	..	..	..	..	..	..	..	..	6	3.7	2.4
105–120	1	5	..	..	..	..	..	..	..	..	..	..	..	..	..	6	6.2	1.9
120–135	3	2	..	..	..	..	..	..	..	..	..	..	..	..	..	5	4.0	2.4
135–150	2	1	..	..	..	..	..	..	..	..	..	..	..	..	..	3	3.7	2.4
150–165	2	2	..	..	..	..	..	..	..	..	..	..	..	..	..	4	4.5	2.5
165–180	..	1	..	..	..	..	..	..	..	..	..	..	..	..	..	1	7.0	0.0
180–195	1	1	..	..	..	..	..	..	..	..	..	..	..	..	..	2	4.5	2.5
210–225	..	1	..	..	..	..	..	..	..	..	..	..	..	..	..	1	7.0	0.0
225–240	..	2	..	..	..	..	..	..	..	..	..	..	..	..	..	2	7.0	0.0
240–255	2	..	1	..	..	..	..	..	..	..	..	..	..	..	..	3	5.3	4.7
255–270	..	1	..	..	..	..	..	..	..	..	..	..	..	..	..	1	7.0	0.0
270–285	..	2	..	..	..	..	..	..	..	..	..	..	..	..	..	2	7.0	0.0
285–300	..	2	..	..	..	..	..	..	..	..	..	..	..	..	..	2	7.0	0.0
300–315	..	1	..	..	..	..	..	..	..	..	..	..	..	..	..	1	7.0	0.0
315–330	..	..	3	..	..	..	..	..	..	..	..	..	..	..	..	3	12.0	0.0
330–345	..	1	..	..	..	..	..	..	..	..	..	..	..	..	..	1	7.0	0.0
345–360	..	..	1	1	..	..	..	..	..	..	..	..	..	..	..	2	14.5	2.5
360–375	..	..	1	2	..	..	..	..	..	..	..	..	..	..	..	3	15.3	2.4

Ex / J	-4	-9	-14	-19	-24	-29	-34	-39	-44	-49	-54	-59	-64	-69	-74	-79	sum	avrg	stdv
375-390	..	..	1	..	3	..	..	..	..	..	..	..	..	..	..	..	4	19.5	4.3
390-405	..	1	2	5	1	1	..	..	..	..	..	..	..	..	..	..	10	16.5	5.2
405-420	..	..	..	..	2	..	..	..	..	..	..	..	..	..	..	..	2	22.0	0.0
420-435	..	..	2	1	..	1	..	..	..	..	..	..	..	..	..	..	4	17.0	6.1
435-450	..	..	1	..	5	3	1	3	1	..	..	..	..	..	..	..	14	27.7	8.0
Sum	39	32	12	9	11	5	1	3	1	..	..	..	..	..	..	..			

Geant4: Simulation of Clover Efficiencies

In order to assess the feasibility of an experiment, the amount of statistics required to observe meaningful results must be estimated accurately. Experimenters must therefore take special care to determine not only if the beam production facilities are able to produce the nuclide they want, they must also determine whether the electronics and detectors available to them are capable of recording enough data to make analysis worthwhile. For gamma-ray detectors such as the clover array, this means estimating the efficiency of the detectors at a number of different energies; such an estimation allows the experimenter to make predictions about the probability of observing any given signal for a given number of total events. This in turn allows experimenters to know with greater certainty how much beam time to ask for.

To address this issue, we used a suite of codes called GEANT4. GEANT4 is a freely-available suite of codes "for the simulation of the passage of particles through matter." [121]. At its most basic, GEANT4 creates particles such as protons, electrons, compound particles such as nuclei, photons, or fundamental particles and, using parameters specified by the user and physics interaction routines, simulates the interaction of the particle with a geometrical body made of a user-specified material. This material can be of any makeup and users may define their own material within GEANT4's source code.

We used GEANT4 prior to E12028 in order to assess the feasibility of using the Yale Clovershare array instead of using NSCL's own Segmented Germanium Array (SeGA, a compact germanium array composed of sixteen thirty-two-fold segmented germanium crystals [122]). Preliminary simulations suggested that the Clovershare array would have roughly double the efficiency of SeGA at all energies, so we performed a number of simulations using a simulated Clovershare array to determine the needed statistics for E12028.

To define a geometrical body in GEANT4, the user must define the material out of which the body is created, then place it around an origin point the code's simulation space. We used a set of definitions for the clover array provided by a collaborator, tweaking the position of the nine clover detectors to suit our specific experimental needs (e.g. the use of a small scintillator for implantation as opposed to a larger germanium implantation detector). We also defined a number of central implantation detectors (plastic scintillator, NaI scintillator, LaBr detector) and, using the estimates of the implantation depth from LISE++, performed simulations for a number of different gamma-ray energies to determine both the efficiency of the clover detectors and the attenuation of the gammas in the central detector. These simulations helped fuel both the decision to use a plastic scintillator in the center of the array, and the thickness of the detector.

We also utilized GEANT4 during analysis to help assess the accuracy of our relative efficiency calibration. We performed, for each ^{152}Eu and ^{32}Cl point we used in the calibration, a GEANT4 simulation of the efficiency of the clover detectors where the source was placed in the simulation at the estimated position of the calibration source (^{152}Eu) or the estimated beam implantation depth (^{32}Cl). These simulations were used to produce a theoretical relative efficiency curve as described in Chapter 5, which was then compared to the experimental efficiency curve. We observed the two curves to be very similar, differing less than 10% at all energies and frequently by less than 4%. In situations where experimentally-determined efficiencies are unavailable, theoretically-generated curves such as the curve we produced using GEANT4 may be used instead, but as we did not require extrapolation to higher gamma energies than 7 MeV or extremely low energies, we opted to use only the experimental curve in our analysis.

Geant4 Input Macro Example

Before being able to run, GEANT4 requires the user to input a series of commands defining the parameters of the simulation: which defined geometrical bodies should be "turned on" for the simulation, which particles should the code produce and at what energies, how many iterations of the simulation should be done, etc. We utilized a GEANT4 "macro" file with these commands pre-loaded. Then, at runtime, we were able simply to invoke the macro file and input all the parameters for the simulation at once. Below is an example of a simple macro file designed to produce a simulation of 1e6 1-MeV gamma-rays using the plastic scintillator and the clover detectors. It is worth noting that there are many commands which can be used that do not appear in this simple example; the reader is directed to the GEANT4 documentation for further edification [123].

```
#########################################################################
#                                                                       #
# THIS TEST GENERATES GAMMA RAYS AT THE CENTRE OF THE TARGET            #
# WHICH IS THE ORIGIN.                                  #
#                                                                       #
#########################################################################

#/p26/analysis/dirname
/p26/analysis/filename 1MeVTest


/p26/phys/SelectPhysics LowEnergy_EM


### use the LaBr crystal?
#/p26/det/UseLaBrDetector false


### use the plastic scintillator?
/p26/det/UsePlasticScint true
```

```
/p26/det/UseSega false

/p26/det/UseClover true


/run/initialize

/run/verbose 0

/event/verbose 0

/tracking/verbose 0

/grdm/verbose 0

#/grdm/noVolumes

#/grdm/selectVolume Detector

/grdm/allVolumes


### SOURCE INFO ###


### Gammas ###


/gps/source/intensity 1

/gps/particle gamma

/gps/ang/type iso

/gps/ene/mono 1.000 MeV


###########


# No daughter decays in analogue MC mode

#/grdm/analogueMC 1

/run/setSeed 344

/run/beamOn 1e6


#/vis/enable

#/vis/reviewKeptEvents


######################################################################

######################################################################
```

Shell Model Calculations: USDE Results

As mentioned in Chapters 5 and 6, one set of theoretical tools that was invaluable to the analysis of E12028 were a number of shell-model calculations performed by B. A. Brown using the USD interaction, first mentioned in Chapter 3. Since the nature of shell model calculations has already been mentioned and the results of many of the calculations have already been discussed, we present here simply the results of our USDE calculations for both the beta feedings and gamma branchings of the theoretical states. These calculation results are reprinted with permission from B. A. Brown, and are truncated after the highest energy we used in our experimental analysis (7.455 MeV in the calculations, which we interpreted as the state we observed at 7149 keV).

Beta Feeding Calculations

```
cl310 s_310

 sdpn      f92epn

       input q-value  =        11.972 MeV

 calculated     t1/2  =    0.2154E+00 sec

 experimental   t1/2  =    0.0000E+00 (+/-)   0.0000E+00 sec

 ji,ti =   1.5    1.5

 non gamow-teller br =    0.00%

 ft = 6177/[qf*( 1.260**2.)b(gt)+b(f)] where qf =  0.60 for the quenching factor

 sum     b(gt) b(f)   =    2.75835   2.92792

 centroid            =  7.24777

 sum     b(gt)/3|n-z| =  0.30648 for cl312y

 th  [br*b(gt)/3|n-z|] =  0.01496

 exp [br*b(gt)/3|n-z|] =  0.00000


                                sum                sum
   jf   tf   nf  ex(MeV)   br(%)    br(%)  log(ft) qf*b(gt) qf*b(gt) log(fa)  b(f)

   1/2  1/2   1  0.000    7.9645  92.036   5.569   0.0105   0.0105   5.137  0.0000
```

3/2	1/2	1	1.212	4.9526	87.083	5.532	0.0114	0.0219	4.893	0.0000
3/2	1/2	1	1.212	0.0002	87.083	10.007	0.0000	0.0219	4.893	0.0000
5/2	1/2	1	2.279	41.4741	45.609	4.369	0.1664	0.1884	4.653	0.0000
1/2	1/2	2	3.230	1.7981	43.811	5.493	0.0125	0.2009	4.414	0.0000
5/2	1/2	2	3.304	6.5879	37.223	4.909	0.0480	0.2489	4.394	0.0000
3/2	1/2	2	3.600	0.1889	37.034	6.370	0.0017	0.2505	4.313	0.0000
3/2	1/2	2	3.600	0.0160	37.018	7.442	0.0000	0.2505	4.313	0.0002
5/2	1/2	3	4.230	0.7740	36.244	5.575	0.0104	0.2609	4.130	0.0000
3/2	1/2	3	4.343	3.5158	32.728	4.883	0.0510	0.3119	4.096	0.0000
3/2	1/2	3	4.343	0.0008	32.727	8.542	0.0000	0.3119	4.096	0.0000
3/2	1/2	4	4.607	0.1776	32.550	6.096	0.0031	0.3150	4.012	0.0000
3/2	1/2	4	4.607	0.0457	32.504	6.686	0.0000	0.3150	4.012	0.0013
5/2	1/2	4	4.831	1.4188	31.085	5.121	0.0295	0.3444	3.940	0.0000
1/2	1/2	3	4.911	3.5705	27.515	4.693	0.0788	0.4233	3.913	0.0000
5/2	1/2	5	5.124	0.2884	27.226	5.713	0.0075	0.4308	3.840	0.0000
1/2	1/2	4	5.384	0.0341	27.192	6.549	0.0011	0.4319	3.748	0.0000
3/2	1/2	5	5.710	0.0566	27.136	6.206	0.0024	0.4343	3.626	0.0000
3/2	1/2	5	5.710	0.0863	27.049	6.023	0.0000	0.4343	3.626	0.0059
5/2	1/2	6	5.741	0.1659	26.883	5.727	0.0073	0.4416	3.614	0.0000
3/2	1/2	6	6.102	0.0170	26.866	6.571	0.0010	0.4427	3.470	0.0000
3/2	1/2	6	6.102	0.5812	26.285	5.039	0.0000	0.4427	3.470	0.0565
3/2	1/2	7	6.317	0.4671	25.818	5.043	0.0353	0.4779	3.379	0.0000
3/2	1/2	7	6.317	19.3003	6.518	3.427	0.0000	0.4779	3.379	2.3130
5/2	1/2	7	6.345	0.0435	6.474	6.061	0.0034	0.4813	3.367	0.0000
3/2	1/2	8	6.383	0.1781	6.296	5.433	0.0144	0.4957	3.350	0.0000
3/2	1/2	8	6.383	4.2720	2.024	4.053	0.0000	0.4957	3.350	0.5469
1/2	1/2	5	6.421	0.4239	1.600	5.040	0.0355	0.5312	3.334	0.0000
1/2	1/2	6	7.088	0.0162	1.538	6.140	0.0028	0.5407	3.017	0.0000
5/2	1/2	10	7.455	0.4881	0.475	4.465	0.1333	0.7812	2.820	0.0000

Gamma Branching Calculations

```
--------------------------------------------------------------------------------

gamma decay for s_310y.deo      BR greater than  0.000


! model space = sdpn

! interaction = f9e2pn

! e_p =   1.360    e_n =   0.450    E2

! g_sp =  5.000    g_sn = -3.440  M1 spin

! g_lp =  1.174    g_ln = -0.110  M1 orbital

! g_pp =  0.240    g_pn = -0.160  M1 tensor


     Ei      Ji    ni        tau         T_(1/2)      M1 moment   Q moment        width

    (MeV)                    (psec)       (psec)        (u_N)     (e^2 fm^2)       (eV)


    0.000    1/2+    1      0.000000     0.000000      -0.390        0.00  -----  0.0000E+00


            Ef     Jf   nf   BR      del    B(1)       B(2)          A_p     A_n


    1.212    3/2+    1      3.070748     2.128489       1.177       -8.44  -----  0.2143E-03


            Ef     Jf   nf   BR      del    B(1)       B(2)          A_p     A_n
            0.000  1/2+   1 100.0000    0.79   0.6376E-02  0.3925E+02    -7.093  -6.402


    2.279    5/2+    1      0.295945     0.205134       0.473        2.66  -----  0.2223E-02


            Ef     Jf   nf   BR      del    B(1)       B(2)          A_p     A_n
            0.000  1/2+   1  99.7069  999.00   0.0000E+00  0.4472E+02    -9.040  -9.082
            1.212  3/2+   1   0.2931   -0.21   0.4434E-03  0.2485E+00     0.930  -0.098


    3.230    1/2+    2      0.012390     0.008588       0.150        0.00  -----  0.5311E-01


            Ef     Jf   nf   BR      del    B(1)       B(2)          A_p     A_n
            0.000  1/2+   1  90.3479    0.00   0.1229E+00  0.0000E+00     0.000   0.000
            1.212  3/2+   1   9.6339   -0.31   0.4911E-01  0.1634E+02     3.561   1.941
            2.279  5/2+   1   0.0182  999.00   0.0000E+00  0.1542E+02     3.174   2.750
```

```
3.304    5/2+    2        0.103341      0.071631       0.980         1.28  ----- 0.6367E-02


        Ef     Jf   nf    BR      del    B(1)         B(2)          A_p      A_n

        0.000  1/2+  1  15.3164  999.00  0.0000E+00  0.3072E+01    -3.441    0.857

        1.212  3/2+  1  65.8987   -0.47  0.3231E-01  0.2380E+02     6.634    6.498

        2.279  5/2+  1  18.7849   -0.22  0.9146E-01  0.6036E+02   -10.797   -9.651

        3.230  1/2+  2   0.0000  999.00  0.0000E+00  0.7225E+00     1.066    1.404


3.477    7/2+    1        0.193860      0.134374       2.375        -1.82  ----- 0.3394E-02


        Ef     Jf   nf    BR      del    B(1)         B(2)          A_p      A_n

        1.212  3/2+  1  98.5153  999.00  0.0000E+00  0.6956E+02    13.289   12.252

        2.279  5/2+  1   1.4744   -0.97  0.1298E-02  0.1216E+02     5.470    5.385

        3.304  5/2+  2   0.0103   -0.06  0.5827E-02  0.1150E+02    -5.001   -6.200


3.600    3/2+    2        0.012534      0.008688       0.443         6.35  ----- 0.5250E-01


        Ef     Jf   nf    BR      del    B(1)         B(2)          A_p      A_n

        0.000  1/2+  1  66.3579   -0.51  0.5096E-01  0.1495E+02    -4.154   -4.633

        1.212  3/2+  1  33.5773    0.39  0.9728E-01  0.3642E+02     6.480    7.236

        2.279  5/2+  1   0.0425   -2.35  0.1277E-03  0.5823E+01    -2.219   -4.017

        3.230  1/2+  2   0.0177    0.03  0.1581E-01  0.1463E+01    -1.708   -0.213

        3.304  5/2+  2   0.0047   -0.07  0.8100E-02  0.5688E+01    -2.342   -3.521

        3.477  7/2+  1   0.0000  999.00  0.0000E+00  0.7974E+00     0.987    0.985


4.230    5/2+    3        0.007761      0.005380       0.886         0.70  ----- 0.8478E-01


        Ef     Jf   nf    BR      del    B(1)         B(2)          A_p      A_n

        0.000  1/2+  1   0.0137  999.00  0.0000E+00  0.1061E-01     1.010   -2.492

        1.212  3/2+  1  72.5107    0.26  0.1806E+00  0.1962E+02     5.386    7.843

        2.279  5/2+  1  27.3727   -0.06  0.2688E+00  0.3565E+01     2.437    2.911

        3.230  1/2+  2   0.0003  999.00  0.0000E+00  0.2718E+00    -0.513   -1.288

        3.304  5/2+  2   0.0070    1.12  0.2865E-03  0.6064E+01     3.544    2.693

        3.477  7/2+  1   0.0202    0.74  0.2231E-02  0.3119E+02    -7.439   -7.925

        3.600  3/2+  2   0.0754   -0.28  0.2049E-01  0.5698E+02   -10.311   -9.927
```

```
4.343   3/2+    3       0.022238     0.015414    1.077      8.03  -----  0.2959E-01


        Ef     Jf   nf    BR     del    B(1)       B(2)        A_p     A_n

        0.000  1/2+  1  57.4115  -0.38  0.1565E-01 0.1715E+01  -1.191  -2.222

        1.212  3/2+  1  41.3628  -0.18  0.3331E-01 0.1633E+01   1.171   2.142

        2.279  5/2+  1   0.5977  -1.21  0.7044E-03 0.3480E+01  -2.262  -1.453

        3.230  1/2+  2   0.5929   0.54  0.8473E-02 0.2911E+02   6.418   4.586

        3.304  5/2+  2   0.0096  -5.91  0.6052E-05 0.2816E+01  -2.257  -0.637

        3.477  7/2+  1   0.0003  999.00 0.0000E+00 0.2007E+00   0.830  -0.518

        3.600  3/2+  2   0.0253  -0.24  0.1492E-02 0.2210E+01   1.887   0.902

        4.230  5/2+  3   0.0000  -1.59  0.2095E-05 0.5934E+01  -2.740  -2.547


4.607   3/2+    4       0.023771     0.016477    0.802     -7.92  -----  0.2768E-01


        Ef     Jf   nf    BR     del    B(1)       B(2)        A_p     A_n

        0.000  1/2+  1  14.4199   2.01  0.6980E-03 0.1913E+01   2.184  -0.453

        1.212  3/2+  1  65.4809  -0.22  0.3806E-01 0.2395E+01   2.442  -0.503

        2.279  5/2+  1  16.3837   0.08  0.3082E-01 0.5603E+00  -0.925  -0.532

        3.230  1/2+  2   0.4617   0.42  0.3582E-02 0.4873E+01  -2.415  -2.512

        3.304  5/2+  2   2.9637   0.14  0.3140E-01 0.5171E+01  -2.505  -2.535

        3.477  7/2+  1   0.0129  999.00 0.0000E+00 0.2402E+01  -1.951  -0.994

        3.600  3/2+  2   0.2367   0.13  0.5446E-02 0.1308E+01   1.525   0.473

        4.230  5/2+  3   0.0394   0.06  0.1750E-01 0.6574E+01   2.762   3.047

        4.343  3/2+  3   0.0012   0.13  0.1498E-02 0.4827E+01  -2.675  -1.681


4.831   5/2+    4       0.018640     0.012920    0.128     14.52  -----  0.3530E-01


        Ef     Jf   nf    BR     del    B(1)       B(2)        A_p     A_n

        0.000  1/2+  1  48.2236  999.00 0.0000E+00 0.8023E+01  -3.863  -3.742

        1.212  3/2+  1   2.5966  -5.29  0.5754E-04 0.1768E+01  -2.026  -1.115

        2.279  5/2+  1  22.7086   0.37  0.3674E-01 0.1080E+02   5.064   2.583

        3.230  1/2+  2   0.0282  999.00 0.0000E+00 0.1172E+01   1.598   1.065

        3.304  5/2+  2  22.9195  -0.08  0.1948E+00 0.8566E+01   3.299   5.961

        3.477  7/2+  1   1.1901  -0.06  0.1455E-01 0.4385E+00  -0.528  -2.007

        3.600  3/2+  2   2.1162   0.17  0.3359E-01 0.9335E+01  -4.686  -2.469
```

4.230	5/2+	3	0.1762	-0.13	0.2435E-01	0.1536E+02	-5.408	-4.991
4.343	3/2+	3	0.0393	0.08	0.1023E-01	0.3498E+01	-2.565	-2.428
4.607	3/2+	4	0.0001	-0.05	0.2398E-03	0.1557E+00	-0.653	-0.175
4.738	7/2+	2	0.0016	-0.01	0.6236E-01	0.4783E+01	-2.045	-5.724

4.911	1/2+	3		0.001789	0.001240	-0.184	0.00	-----	0.3679E+00

Ef	Jf	nf	BR	del	B(1)	B(2)	A_p	A_n
0.000	1/2+	1	58.0474	0.00	0.1556E+00	0.0000E+00	0.000	0.000
1.212	3/2+	1	41.0009	0.20	0.2477E+00	0.9986E+01	3.003	0.856
2.279	5/2+	1	0.0280	999.00	0.0000E+00	0.1010E+01	1.012	0.101
3.230	1/2+	2	0.8825	0.00	0.5900E-01	0.0000E+00	0.000	0.000
3.304	5/2+	2	0.0001	999.00	0.0000E+00	0.5317E-01	0.171	0.207
3.600	3/2+	2	0.0195	-0.35	0.2442E-02	0.2536E+01	1.314	1.033
4.230	5/2+	3	0.0000	999.00	0.0000E+00	0.4816E+00	0.610	0.339
4.343	3/2+	3	0.0037	0.09	0.6407E-02	0.2296E+01	-1.461	-0.346
4.607	3/2+	4	0.0179	-0.02	0.2026E+00	0.7231E+01	-1.952	-2.551
4.831	5/2+	4	0.0000	999.00	0.0000E+00	0.4802E+00	0.616	0.315

5.124	5/2+	5		0.046810	0.032446	1.294	0.20	-----	0.1406E-01

Ef	Jf	nf	BR	del	B(1)	B(2)	A_p	A_n
0.000	1/2+	1	0.3076	999.00	0.0000E+00	0.1518E-01	-0.027	0.754
1.212	3/2+	1	23.3452	-0.06	0.4715E-02	0.1546E-01	-0.078	0.911
2.279	5/2+	1	22.7511	-0.24	0.1132E-01	0.1189E+01	0.858	3.343
3.230	1/2+	2	0.0890	999.00	0.0000E+00	0.6364E+00	-0.864	-1.733
3.304	5/2+	2	33.4192	0.09	0.6676E-01	0.2191E+01	2.148	1.567
3.477	7/2+	1	18.7246	-0.14	0.4990E-01	0.5042E+01	-3.831	-0.645
3.600	3/2+	2	0.3078	-0.43	0.8874E-03	0.1037E+01	-1.985	0.458
4.230	5/2+	3	0.3298	-0.01	0.5600E-02	0.4046E-02	0.270	-1.162
4.343	3/2+	3	0.0557	0.68	0.9685E-03	0.1062E+02	-4.298	-4.747
4.607	3/2+	4	0.0419	-0.59	0.2722E-02	0.5163E+02	-10.269	-8.086
4.738	7/2+	2	0.6277	0.01	0.1324E+00	0.4879E+00	-0.725	-1.613
4.831	5/2+	4	0.0005	-0.55	0.1690E-03	0.8518E+01	-4.034	-3.695
4.911	1/2+	3	0.0000	999.00	0.0000E+00	0.2072E+01	-2.716	0.373

```
5.384    1/2+    4        0.002396     0.001661     -0.427         0.00  -----  0.2746E+00


         Ef      Jf    nf    BR        del     B(1)         B(2)           A_p      A_n

         0.000  1/2+   1  93.7399     0.00   0.1424E+00   0.0000E+00      0.000    0.000

         1.212  3/2+   1   3.9300    24.88   0.2069E-04   0.1057E+02     -2.412   -2.928

         2.279  5/2+   1   0.1346   999.00   0.0000E+00   0.1588E+01     -0.728   -1.759

         3.230  1/2+   2   0.6597     0.00   0.1565E-01   0.0000E+00      0.000    0.000

         3.304  5/2+   2   0.0425   999.00   0.0000E+00   0.3721E+01      1.768    0.718

         3.600  3/2+   2   1.2192    -0.09   0.5047E-01   0.1944E+01     -0.901   -1.660

         4.230  5/2+   3   0.0011   999.00   0.0000E+00   0.1878E+01     -1.360   -0.196

         4.343  3/2+   3   0.1760     0.11   0.3653E-01   0.5872E+01      2.223    0.899

         4.607  3/2+   4   0.0701    -0.08   0.3517E-01   0.5872E+01     -1.512   -3.046

         4.831  5/2+   4   0.0000   999.00   0.0000E+00   0.1636E+01     -1.002   -0.994

         4.911  1/2+   3   0.0268     0.00   0.6007E-01   0.0000E+00      0.000    0.000

         5.124  5/2+   5   0.0000   999.00   0.0000E+00   0.3937E+01      1.328    2.222


5.710    3/2+    5        0.003660     0.002537      1.246         6.76  -----  0.1798E+00


         Ef      Jf    nf    BR        del     B(1)         B(2)           A_p      A_n

         0.000  1/2+   1  77.8778    -0.01   0.6490E-01   0.6053E-02     -0.114   -0.002

         1.212  3/2+   1  15.2811    -0.02   0.2605E-01   0.4489E-02     -0.436    1.020

         2.279  5/2+   1   0.0333     0.67   0.8864E-04   0.4814E-01     -0.198    1.575

         3.230  1/2+   2   4.6813    -0.17   0.4633E-01   0.3015E+01      2.148    1.226

         3.304  5/2+   2   0.0533     5.02   0.2268E-04   0.1416E+01     -2.111    1.092

         3.477  7/2+   1   0.0205   999.00   0.0000E+00   0.8236E+00      0.445    2.687

         3.600  3/2+   2   0.5933     0.04   0.9781E-02   0.6228E-01      0.524   -0.473

         4.230  5/2+   3   0.0329    -0.75   0.1007E-02   0.3717E+01     -2.082   -2.276

         4.343  3/2+   3   0.2281    -0.02   0.1385E-01   0.3561E-01      0.130    0.445

         4.607  3/2+   4   0.9022     0.05   0.1040E+00   0.3312E+01     -1.474   -3.636

         4.738  7/2+   2   0.0003   999.00   0.0000E+00   0.6716E+00     -0.516   -2.083

         4.831  5/2+   4   0.1082    -0.05   0.2465E-01   0.1350E+01     -1.169   -1.632

         4.911  1/2+   3   0.0625    -0.12   0.1874E-01   0.6010E+01     -2.511   -3.306

         5.124  5/2+   5   0.1178     0.03   0.9078E-01   0.3122E+01      1.945    1.975

         5.384  1/2+   4   0.0075    -0.07   0.3340E-01   0.2166E+02     -4.901   -5.872

         5.481  7/2+   3   0.0000   999.00   0.0000E+00   0.7320E+01      2.899    3.263
```

```
5.741   5/2+   6       0.016548     0.011470     0.940        11.29  -----  0.3976E-01


        Ef     Jf   nf    BR        del    B(1)        B(2)          A_p     A_n

        0.000  1/2+  1   5.8503    999.00  0.0000E+00  0.4626E+00    -1.734   1.537

        1.212  3/2+  1  12.7606     -0.55  0.3621E-02  0.7661E+00     1.574   0.008

        2.279  5/2+  1  49.2195      0.30  0.3727E-01  0.4128E+01     3.110   1.661

        3.230  1/2+  2   4.3081    999.00  0.0000E+00  0.2128E+02     5.939   7.160

        3.304  5/2+  2   0.6739     -5.51  0.5093E-04  0.3743E+01    -2.982  -1.520

        3.477  7/2+  1   7.8246     -0.02  0.2314E-01  0.1727E-01     0.578  -1.031

        3.600  3/2+  2   8.5576      0.10  0.2961E-01  0.1005E+01    -1.577  -0.689

        4.230  5/2+  3   1.5854     -0.05  0.1573E-01  0.2908E+00    -0.842  -0.392

        4.343  3/2+  3   5.8696     -0.15  0.7218E-01  0.1145E+02    -4.942  -3.479

        4.607  3/2+  4   0.0015      3.85  0.2255E-05  0.3725E+00     0.988   0.335

        4.738  7/2+  2   0.8737     -0.10  0.2944E-01  0.3974E+01     2.542   3.168

        4.831  5/2+  4   2.4278     -0.02  0.1105E+00  0.7877E+00    -0.955  -1.943

        4.911  1/2+  3   0.0022    999.00  0.0000E+00  0.2785E+01     2.185   2.480

        5.124  5/2+  5   0.0383     -0.07  0.5569E-02  0.1087E+01    -1.331  -1.653

        5.323  9/2+  1   0.0000    999.00  0.0000E+00  0.1476E+01    -1.883  -0.921

        5.384  1/2+  4   0.0001    999.00  0.0000E+00  0.5171E+01     3.289   2.436

        5.481  7/2+  3   0.0065     -0.05  0.1267E-01  0.5671E+01    -3.073  -3.675

        5.710  3/2+  5   0.0000      0.00  0.3862E-01  0.5515E-02     0.241  -0.323


6.102   3/2+   6       0.003880     0.002689     1.049        -5.25  -----  0.1696E+00


        Ef     Jf   nf    BR        del    B(1)        B(2)          A_p     A_n

        0.000  1/2+  1  34.3950      0.37  0.1949E-01  0.1031E+01     1.120   1.129

        1.212  3/2+  1   0.8614     -0.20  0.1037E-02  0.2457E-01    -0.771   1.634

        2.279  5/2+  1  42.0900     -0.22  0.1052E+00  0.5018E+01    -2.804  -1.483

        3.230  1/2+  2   0.6473      0.23  0.3795E-02  0.3582E+00     0.255   1.888

        3.304  5/2+  2  14.1417      0.12  0.9321E-01  0.2385E+01     1.599   2.032

        3.477  7/2+  1   0.5454    999.00  0.0000E+00  0.9202E+01     3.520   2.842

        3.600  3/2+  2   5.6506     -0.29  0.4877E-01  0.9269E+01     3.251   3.706

        4.230  5/2+  3   0.0404      0.81  0.5457E-03  0.1456E+01     1.450   0.980

        4.343  3/2+  3   0.7172     -0.14  0.1891E-01  0.1782E+01    -1.610  -1.069

        4.607  3/2+  4   0.0295      0.08  0.1284E-02  0.5818E-01    -0.359   0.013

        4.738  7/2+  2   0.0063    999.00  0.0000E+00  0.2802E+01     1.962   1.512
```

4.831	5/2+	4	0.0176	0.32	0.1137E-02	0.1051E+01	1.363	0.436
4.911	1/2+	3	0.6646	-0.07	0.5726E-01	0.3253E+01	1.768	2.672
5.124	5/2+	5	0.1255	0.02	0.1963E-01	0.1043E+00	-0.039	1.553
5.384	1/2+	4	0.0334	-0.26	0.1239E-01	0.2271E+02	-5.276	-5.237
5.481	7/2+	3	0.0000	999.00	0.0000E+00	0.1313E+00	-0.547	0.043
5.710	3/2+	5	0.0320	0.06	0.7748E-01	0.2254E+02	5.298	5.089
5.741	5/2+	6	0.0023	0.00	0.7048E-02	0.7448E-02	-0.459	1.002
5.785	7/2+	4	0.0000	999.00	0.0000E+00	0.1892E+01	-1.366	-1.984
5.983	7/2+	5	0.0000	999.00	0.0000E+00	0.2404E+00	0.496	0.681

6.317	3/2+	7	0.001219	0.000845	1.029	-8.66	-----	0.5398E+00

Ef	Jf	nf	BR	del	B(1)	B(2)	A_p	A_n
0.000	1/2+	1	11.1342	-0.45	0.1711E-01	0.1250E+01	-2.330	2.072
1.212	3/2+	1	15.0990	-0.17	0.5144E-01	0.7948E+00	-1.800	1.480
2.279	5/2+	1	59.7927	-0.06	0.4219E+00	0.1132E+01	1.257	0.930
3.230	1/2+	2	1.2088	0.02	0.1914E-01	0.7006E-02	-0.416	0.884
3.304	5/2+	2	8.5343	0.08	0.1444E+00	0.1549E+01	-1.344	-1.469
3.477	7/2+	1	0.0035	999.00	0.0000E+00	0.1258E+00	-0.286	-0.712
3.600	3/2+	2	0.0868	-0.22	0.1923E-02	0.1802E+00	-0.496	-0.387
4.230	5/2+	3	0.1625	-0.04	0.8317E-02	0.4435E-01	0.184	-1.492
4.343	3/2+	3	2.6742	0.03	0.1618E+00	0.5307E+00	-0.695	-1.137
4.607	3/2+	4	0.0088	0.52	0.6431E-03	0.8519E+00	-1.502	0.437
4.738	7/2+	2	0.0010	999.00	0.0000E+00	0.6488E+00	-0.158	-3.102
4.831	5/2+	4	0.2920	-0.04	0.4139E-01	0.4796E+00	-0.558	-1.391
4.911	1/2+	3	0.8478	0.02	0.1421E+00	0.5446E+00	0.817	0.812
5.124	5/2+	5	0.1193	0.01	0.3272E-01	0.1480E-01	-0.024	-0.467
5.384	1/2+	4	0.0136	-0.04	0.7806E-02	0.2179E+00	0.737	-0.154
5.481	7/2+	3	0.0001	999.00	0.0000E+00	0.1160E+01	1.817	-0.706
5.710	3/2+	5	0.0098	0.03	0.2045E-01	0.7208E+00	1.542	-0.887
5.741	5/2+	6	0.0113	0.00	0.2767E-01	0.6223E-03	0.212	-0.753
5.785	7/2+	4	0.0000	999.00	0.0000E+00	0.2006E+00	-0.831	0.522
5.983	7/2+	5	0.0000	999.00	0.0000E+00	0.3347E-02	0.199	-0.860
6.102	3/2+	6	0.0002	-0.02	0.8510E-02	0.9254E+00	1.438	-0.070

6.345	5/2+	7	0.004477	0.003103	0.799	-2.79	-----	0.1470E+00

Ef	Jf	nf	BR	del	B(1)	B(2)	A_p	A_n
0.000	1/2+	1	7.9359	999.00	0.0000E+00	0.1407E+01	-1.848	-0.870
1.212	3/2+	1	23.0814	0.09	0.2148E-01	0.9398E-01	0.633	-0.244
2.279	5/2+	1	18.0718	-0.12	0.3363E-01	0.4155E+00	-1.029	-0.399
3.230	1/2+	2	0.0575	999.00	0.0000E+00	0.3572E+00	-0.162	-2.764
3.304	5/2+	2	0.9538	0.64	0.3060E-02	0.1931E+01	-2.178	-0.983
3.477	7/2+	1	41.6568	0.09	0.2223E+00	0.2960E+01	2.871	0.689
3.600	3/2+	2	0.2610	-0.20	0.1539E-02	0.1179E+00	-0.801	0.552
4.230	5/2+	3	2.0329	-0.11	0.2693E-01	0.1051E+01	1.428	1.265
4.343	3/2+	3	2.0244	-0.12	0.3157E-01	0.1583E+01	2.584	-0.961
4.607	3/2+	4	0.9477	0.05	0.2284E-01	0.2882E+00	0.902	0.197
4.738	7/2+	2	2.5438	0.03	0.7768E-01	0.4862E+00	-1.088	-0.507
4.831	5/2+	4	0.0159	0.54	0.4527E-03	0.8125E+00	1.430	0.585
4.911	1/2+	3	0.1020	999.00	0.0000E+00	0.3065E+02	7.327	7.994
5.124	5/2+	5	0.0518	0.70	0.2416E-02	0.1153E+02	-4.413	-5.148
5.323	9/2+	1	0.0002	999.00	0.0000E+00	0.3427E+00	-1.182	0.385
5.384	1/2+	4	0.0001	999.00	0.0000E+00	0.2162E+00	0.813	0.075
5.481	7/2+	3	0.0169	-0.08	0.3295E-02	0.3841E+00	0.930	0.563
5.710	3/2+	5	0.0689	0.01	0.3416E-01	0.2031E+00	0.571	0.726
5.741	5/2+	6	0.0494	-0.02	0.2844E-01	0.6481E+00	1.077	1.129
5.785	7/2+	4	0.1178	0.02	0.8511E-01	0.1378E+01	1.888	0.684
5.822	9/2+	2	0.0000	999.00	0.0000E+00	0.4423E+00	1.215	-0.052
5.983	7/2+	5	0.0098	0.01	0.2632E-01	0.5551E+00	1.377	-0.106
6.033	9/2+	3	0.0000	999.00	0.0000E+00	0.1961E-01	0.069	0.553
6.102	3/2+	6	0.0001	-0.03	0.7623E-03	0.1554E+00	0.233	1.443
6.317	3/2+	7	0.0000	0.00	0.7526E-02	0.3309E-01	0.297	0.092
6.383	3/2+	8	0.001879	0.001303	0.722	-7.91 -----	0.3501E+00	

Ef	Jf	nf	BR	del	B(1)	B(2)	A_p	A_n
0.000	1/2+	1	15.9169	-0.25	0.1738E-01	0.3931E+00	1.342	-1.268
1.212	3/2+	1	6.2754	-0.10	0.1357E-01	0.7829E-01	0.901	-1.479
2.279	5/2+	1	50.2996	0.09	0.2182E+00	0.1504E+01	1.145	1.991
3.230	1/2+	2	7.5002	0.05	0.7217E-01	0.2159E+00	0.323	1.090
3.304	5/2+	2	13.5578	-0.18	0.1362E+00	0.6350E+01	-3.270	-1.319

3.477	7/2+	1	0.0212	999.00	0.0000E+00	0.4436E+00	1.609	-1.904
3.600	3/2+	2	0.4143	-0.23	0.5513E-02	0.5498E+00	1.504	-1.250
4.230	5/2+	3	0.4627	0.12	0.1382E-01	0.6076E+00	-0.968	-0.538
4.343	3/2+	3	3.3777	-0.09	0.1192E+00	0.3656E+01	-1.899	-2.757
4.607	3/2+	4	0.3841	-0.09	0.2056E-01	0.7285E+00	-0.840	-1.253
4.738	7/2+	2	0.0324	999.00	0.0000E+00	0.1167E+02	-4.786	-0.716
4.831	5/2+	4	0.3200	0.14	0.2541E-01	0.2776E+01	-2.008	-1.335
4.911	1/2+	3	1.3862	-0.08	0.1305E+00	0.5691E+01	2.458	3.172
5.124	5/2+	5	0.0146	-0.16	0.2153E-02	0.5256E+00	-0.910	-0.472
5.384	1/2+	4	0.0127	-0.13	0.3788E-02	0.9063E+00	-1.643	0.734
5.481	7/2+	3	0.0000	999.00	0.0000E+00	0.1172E-01	-0.562	2.179
5.710	3/2+	5	0.0233	0.03	0.2307E-01	0.5768E+00	0.447	2.025
5.741	5/2+	6	0.0005	-0.13	0.5525E-03	0.3469E+00	-0.661	-0.620
5.785	7/2+	4	0.0000	999.00	0.0000E+00	0.8658E-02	0.340	-1.441
5.983	7/2+	5	0.0000	999.00	0.0000E+00	0.2836E+00	-0.558	-0.681
6.102	3/2+	6	0.0005	0.04	0.7379E-02	0.2104E+01	1.331	2.425
6.317	3/2+	7	0.0000	0.00	0.7683E-02	0.4167E+00	1.075	-0.380
6.345	5/2+	7	0.0000	0.00	0.2678E-01	0.5134E-02	-0.886	2.360

6.421	1/2+	5		0.004032	0.002795	-0.993	0.00 -----	0.1632E+00

Ef	Jf	nf	BR	del	B(1)	B(2)	A_p	A_n
0.000	1/2+	1	87.6292	0.00	0.4663E-01	0.0000E+00	0.000	0.000
1.212	3/2+	1	0.5384	-0.86	0.3078E-03	0.1212E+00	-0.927	1.707
2.279	5/2+	1	5.1445	999.00	0.0000E+00	0.8541E+01	2.703	1.016
3.230	1/2+	2	1.8775	0.00	0.8141E-02	0.0000E+00	0.000	0.000
3.304	5/2+	2	2.3516	999.00	0.0000E+00	0.1618E+02	-3.183	-3.022
3.600	3/2+	2	1.8544	-0.23	0.1106E-01	0.1050E+01	0.718	1.051
4.230	5/2+	3	0.1542	999.00	0.0000E+00	0.6181E+01	1.583	3.030
4.343	3/2+	3	0.1744	-0.38	0.2387E-02	0.1167E+01	0.807	0.958
4.607	3/2+	4	0.1086	-0.10	0.2537E-02	0.1135E+00	-0.175	-0.531
4.831	5/2+	4	0.0332	999.00	0.0000E+00	0.6610E+01	-2.460	-0.646
4.911	1/2+	3	0.0000	0.00	0.1356E-05	0.0000E+00	0.000	0.000
5.124	5/2+	5	0.0039	999.00	0.0000E+00	0.2167E+01	1.041	1.481
5.384	1/2+	4	0.0313	0.00	0.3949E-02	0.0000E+00	0.000	0.000
5.710	3/2+	5	0.0788	-0.13	0.3041E-01	0.1417E+02	-2.726	-3.594

```
        5.741  5/2+   6    0.0002   999.00   0.0000E+00  0.2782E+01      1.313    1.274

        6.102  3/2+   6    0.0193    -0.03   0.8352E-01  0.8765E+01      2.224    2.582

        6.317  3/2+   7    0.0005     0.01   0.5756E-01  0.7924E+01     -1.678   -3.774

        6.345  5/2+   7    0.0000   999.00   0.0000E+00  0.5638E-03      0.172   -0.595

        6.383  3/2+   8    0.0001     0.00   0.2476E+00  0.3479E+02     -4.595   -4.649


 7.088   1/2+   6        0.000307      0.000212      0.979      0.00   -----  0.2147E+01


        Ef     Jf    nf     BR       del      B(1)        B(2)           A_p      A_n

        0.000  1/2+   1   96.6628     0.00   0.5030E+00  0.0000E+00      0.000    0.000

        1.212  3/2+   1    0.2146     0.75   0.1256E-02  0.2929E+00     -0.777    0.649

        2.279  5/2+   1    0.2448   999.00   0.0000E+00  0.2533E+01      2.147   -1.486

        3.230  1/2+   2    0.5121     0.00   0.1653E-01  0.0000E+00      0.000    0.000

        3.304  5/2+   2    0.0036   999.00   0.0000E+00  0.1231E+00      0.867   -1.519

        3.600  3/2+   2    0.9135    -0.15   0.3900E-01  0.1048E+01      1.143   -0.235

        4.230  5/2+   3    0.0017   999.00   0.0000E+00  0.2317E+00     -0.643    0.430

        4.343  3/2+   3    0.1280     0.25   0.1079E-01  0.1291E+01      0.757    1.284

        4.607  3/2+   4    0.1666    -0.18   0.1958E-01  0.1477E+01     -1.567    0.918

        4.831  5/2+   4    0.0030   999.00   0.0000E+00  0.1384E+01      0.655    1.717

        4.911  1/2+   3    0.7835     0.00   0.1407E+00  0.0000E+00      0.000    0.000

        5.124  5/2+   5    0.0000   999.00   0.0000E+00  0.3903E-01     -0.078   -0.387

        5.384  1/2+   4    0.0306     0.00   0.1148E-01  0.0000E+00      0.000    0.000

        5.710  3/2+   5    0.2488     0.02   0.1762E+00  0.3128E+00      0.736   -0.466

        5.741  5/2+   6    0.0006   999.00   0.0000E+00  0.3548E+01      1.862    0.292

        6.102  3/2+   6    0.0332     0.02   0.6408E-01  0.2864E+00      0.124    1.306

        6.317  3/2+   7    0.0266     0.04   0.1075E+00  0.3798E+01      1.405    1.877

        6.345  5/2+   7    0.0000   999.00   0.0000E+00  0.1738E+00      0.560   -0.382

        6.383  3/2+   8    0.0145    -0.05   0.7644E-01  0.4873E+01     -2.463    0.505

        6.421  1/2+   5    0.0114     0.00   0.7110E-01  0.0000E+00      0.000    0.000

        6.702  5/2+   8    0.0000   999.00   0.0000E+00  0.1762E-01      0.062    0.229

        7.010  5/2+   9    0.0000   999.00   0.0000E+00  0.1157E+01      0.885    0.704


 7.455   5/2+  10        0.004728      0.003277      1.533     -2.61   -----  0.1392E+00


        Ef     Jf    nf     BR       del      B(1)        B(2)           A_p      A_n

        0.000  1/2+   1    0.4127   999.00   0.0000E+00  0.3093E-01      0.515   -0.599
```

```
1.212  3/2+   1  33.1050     0.17   0.1586E-01  0.1778E+00     0.792   -0.096

2.279  5/2+   1   0.5511    -0.31   0.4344E-03  0.2310E-01     0.217    0.172

3.230  1/2+   2   0.3433   999.00   0.0000E+00  0.4401E+00     0.935    0.786

3.304  5/2+   2  12.2493    -0.13   0.2021E-01  0.3056E+00    -0.768   -0.688

3.477  7/2+   1   0.3102     3.40   0.4704E-04  0.4948E+00    -1.753    1.469

3.600  3/2+   2   1.2961    -0.81   0.1644E-02  0.1038E+01    -1.692   -0.433

4.230  5/2+   3   6.1183    -0.07   0.2180E-01  0.1499E+00     0.397    0.909

4.343  3/2+   3   0.0528    -0.05   0.2099E-03  0.6801E-03    -0.091    0.133

4.607  3/2+   4  29.1054    -0.20   0.1453E+00  0.1068E+02    -3.974   -5.778

4.738  7/2+   2   0.5800    -1.16   0.1485E-02  0.3870E+01    -2.870   -2.035

4.831  5/2+   4   2.2139    -0.02   0.1471E-01  0.1889E-01    -0.001    0.752

4.911  1/2+   3   0.2467   999.00   0.0000E+00  0.3995E+01     3.046    1.675

5.124  5/2+   5   0.2387     3.66   0.1574E-03  0.5570E+01     3.174    3.255

5.323  9/2+   1   0.0002   999.00   0.0000E+00  0.9584E-02     0.027    0.452

5.384  1/2+   4   0.0048   999.00   0.0000E+00  0.2162E+00     0.261    1.744

5.481  7/2+   3   5.9569     0.10   0.9213E-01  0.3320E+01     2.042    3.749

5.710  3/2+   5   1.8912    -0.12   0.4212E-01  0.3020E+01    -2.477   -1.975

5.741  5/2+   6   0.2458    -0.15   0.5741E-02  0.6010E+00     1.675   -0.841

5.785  7/2+   4   0.0209     0.61   0.3929E-03  0.7590E+00    -0.995   -1.736

5.822  9/2+   2   0.0029   999.00   0.0000E+00  0.4283E+00     1.032    0.445

5.983  7/2+   5   1.0836    -0.04   0.4074E-01  0.4982E+00     1.225    0.141

6.033  9/2+   3   0.0095   999.00   0.0000E+00  0.2821E+01     2.424    1.817

6.102  3/2+   6   0.1141     0.69   0.3760E-02  0.1394E+02     4.974    5.289

6.317  3/2+   7   3.1906    -0.02   0.2600E+00  0.8348E+00    -1.485   -0.486

6.345  5/2+   7   0.2738     0.21   0.2305E-01  0.1162E+02     4.549    4.805

6.383  3/2+   8   0.2339    -0.03   0.2278E-01  0.3146E+00    -0.694   -0.957

6.421  1/2+   5   0.0088   999.00   0.0000E+00  0.1287E+02     4.722    5.262

6.487  7/2+   6   0.0543    -0.05   0.7176E-02  0.2360E+00    -0.558   -0.959

6.702  5/2+   8   0.0555     0.03   0.1562E-01  0.2489E+00    -0.689   -0.633

7.010  5/2+   9   0.0009    -0.02   0.1267E-02  0.4298E-01     0.338    0.106

7.045  9/2+   4   0.0000   999.00   0.0000E+00  0.1170E+01    -1.487   -1.394

7.088  1/2+   6   0.0000   999.00   0.0000E+00  0.9744E-01     0.423    0.419

7.120  1/2+   7   0.0000   999.00   0.0000E+00  0.4755E+00     1.032    0.634

7.157  3/2+   9   0.0257     0.02   0.1166E+00  0.1078E+02    -4.061   -5.595

7.166  7/2+   7   0.0000     0.48   0.1354E-04  0.5257E+00    -0.817   -1.479

7.319  3/2+  10   0.0031     0.01   0.1474E+00  0.1191E+02     4.305    5.778
```
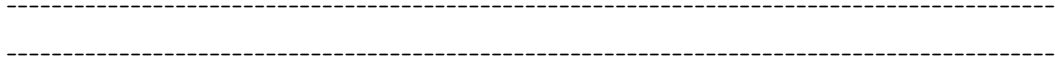
APPENDIX B

Detector Data Sheets

In order to facilitte use of this thesis as a reference tool, we have included here the data sheets for a number of detectors specific to our experimental setup. While we refer the reader to the appropriate literature for devices like the A1900 [65] and the RFFS [66], we have here included data sheets for the silicon PIN detectors used in the experiment, the plastic scintillator, and its attached photomultiplier tube.
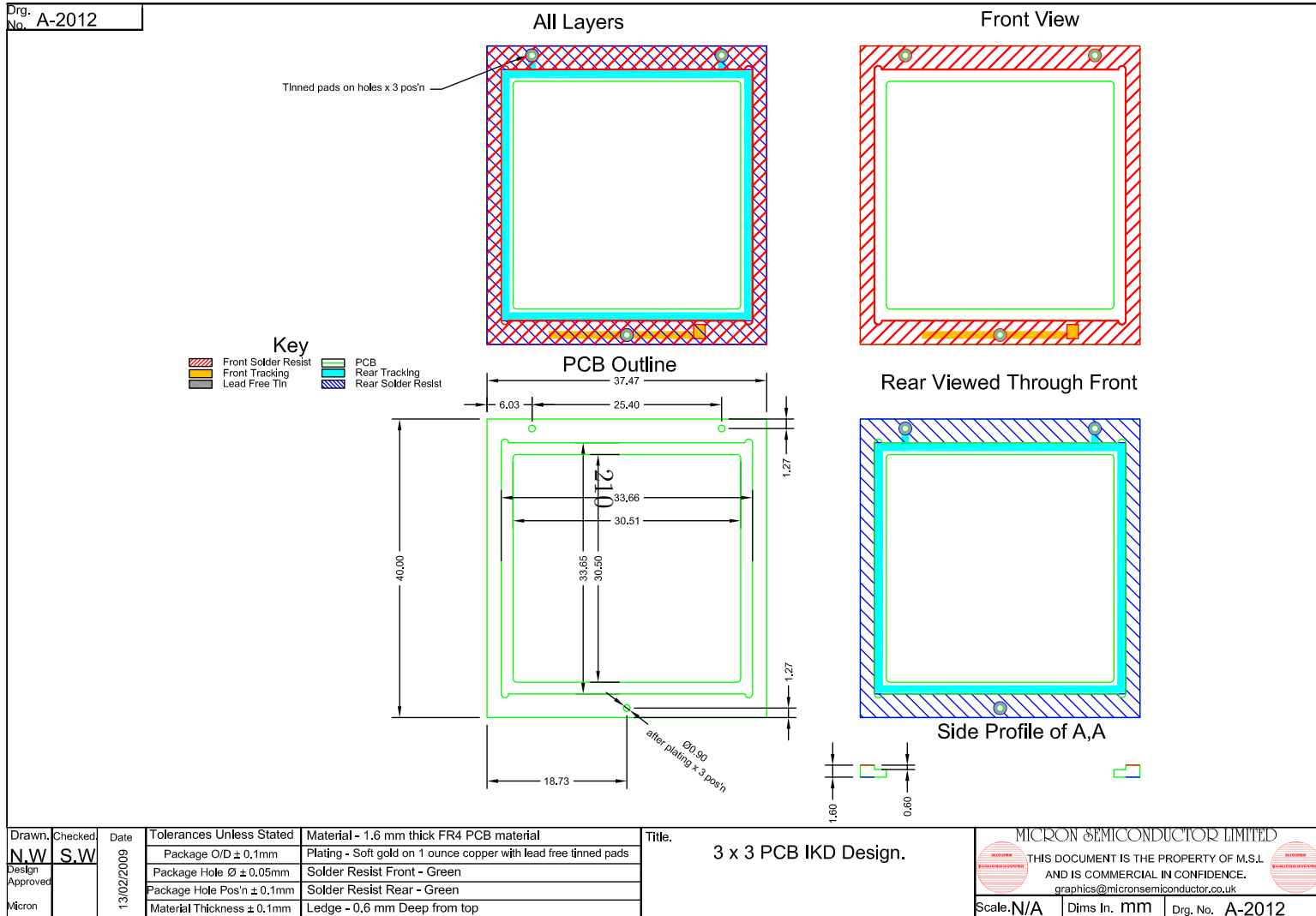
Figure B.1: A schematic of the silicon PIN detectors used for E12028.

EJ-200 PLASTIC SCINTILLATOR

This plastic scintillator combines the two important properties of long optical attenuation length and fast timing and is therefore particularly useful for time-of-flight systems using scintillators greater than one meter long. Typical measurements of 4 meter optical attenuation length are achieved in strips of cast sheet in which a representative size is 2 cm x 20 cm x 300 cm.

The combination of long attenuation length, high light output and an emission spectrum well matched to the common photomultipliers recommends EJ-200 as the detector of choice for many industrial applications such as gauging and environmental protection where high sensitivity of signal uniformity are critical operating requirements.
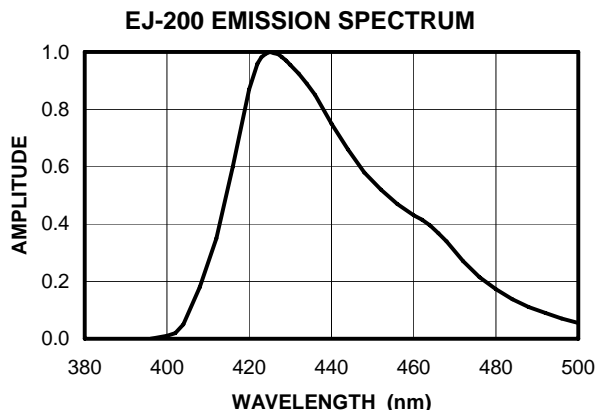
Physical and Scintillation Constants:

Light Output, % Anthracene	64
Scintillation Efficiency, photons/1 MeV e^-	10,000
Wavelength of Max. Emission, nm	425
Rise Time, ns	0.9
Decay Time, ns	2.1
Pulse Width, FWHM, ns	~2.5
No. of H Atoms per cm^3, x 10^{22}	5.17
No. of C Atoms per cm^3, x 10^{22}	4.69
No. of Electrons per cm^3, x 10^{23}	3.33
Density, g/cc:	1.023

Polymer Base: …………. Polyvinyltoluene
Refractive Index: ……….1.58
Vapor Pressure: ……….. Is vacuum-compatible
Coefficient of Linear
Expansion: ……………… 7.8 x 10^{-5} below +67°C

Light Output vs. Temperature:
At +60°C, L.O. = 95% of that at +20°C
No change from +20°C to -60°C

Chemical Compatibility: Is attacked by aromatic solvents, chlorinated solvents, ketones, solvent bonding cements, etc. It is stable in water, dilute acids and alkalis, lower alcohols and silicone greases. It is safe to use most epoxies and "super glues" with EJ-200.

EJ-200 EMISSION SPECTRUM

ELJEN TECHNOLOGY
PO Box 870, 300 Crane Street
Sweetwater TX 79556 USA

Tel: (325) 235-4276 or (888) 800-8771
Fax: (325) 235-0701
Website: www.eljentechnology.com

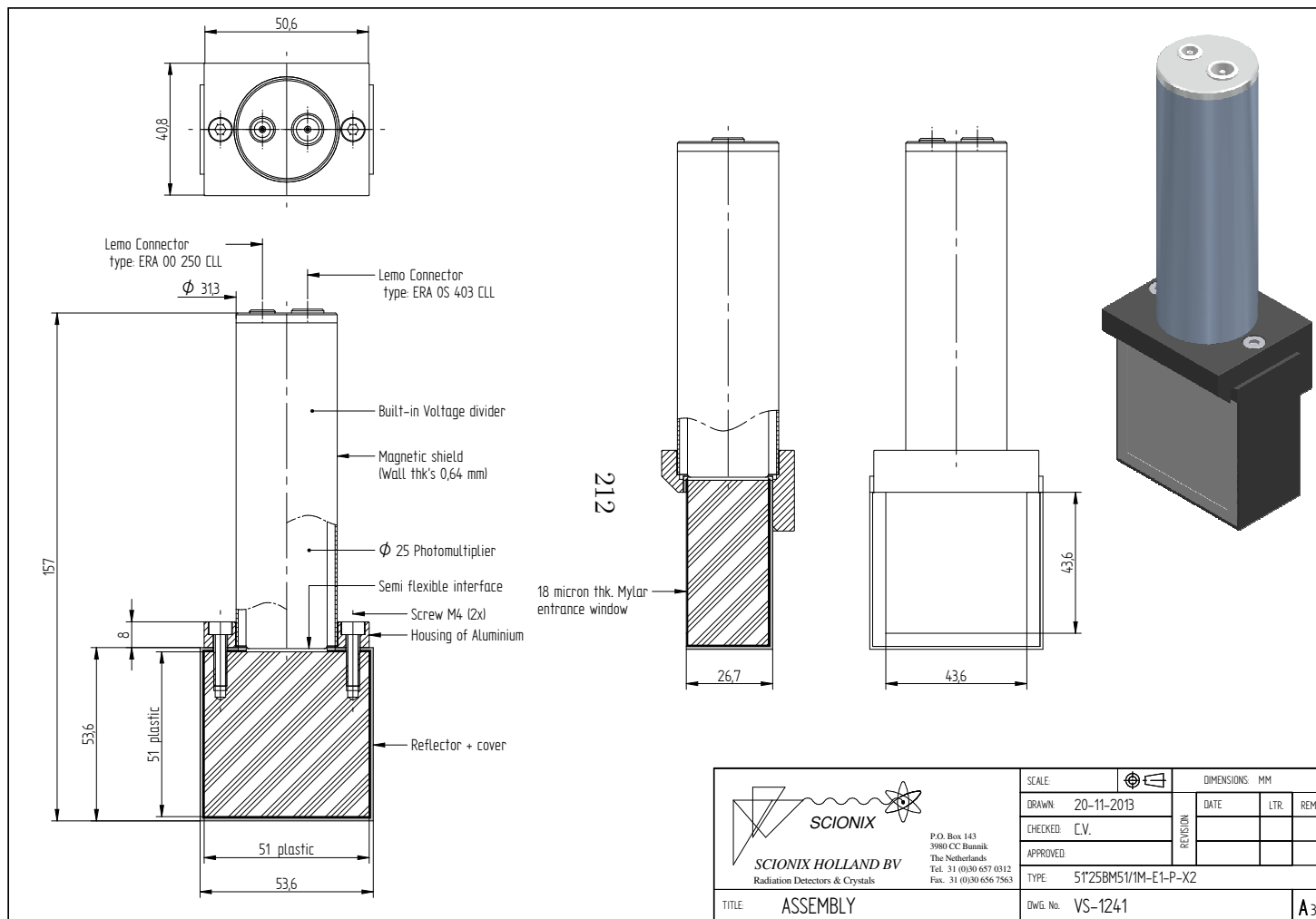Figure B.2: The Hammamatsu EJ200 Plastic Scintillator Data Sheet.

Figure B.3: A schematic of the plastic scintillator used in the experiment.

BIBLIOGRAPHY

BIBLIOGRAPHY

[1] E. M. Burbidge, G. Ronald Burbidge, W. A. Fowler, and F. Hoyle. Synthesis of the elements in stars. *Reviews of modern physics*, 29(4):547, 1957.

[2] A. G. W. Cameron. Stellar evolution, nuclear astrophysics, and nucleogenesis. Technical report, Atomic Energy of Canada Ltd. Chalk River Project, Chalk River, Ontario (Canada), 1957.

[3] C. Iliadis. *Nuclear physics of stars*. John Wiley & Sons, 2015.

[4] C. E. Rolfs and W. S. Rodney. *Cauldrons in the cosmos: Nuclear astrophysics*. University of Chicago press, 1988.

[5] M. Politano, S. Starrfield, J. W. Truran, A. Weiss, and W. M. Sparks. Hydrodynamic studies of accretion onto massive white dwarfs: ONeMg-enriched nova outbursts. I. dependence on white dwarf mass. *Astrophys. Journal*, 448:807, 1995.

[6] C. J. Lada. Stellar multiplicity and the initial mass function: Most stars are single. *Astrophys. Journal Lett.*, 640(1):L63, 2006.

[7] D. M. Townsley and L. Bildsten. Theoretical modeling of the thermal state of accreting white dwarfs undergoing classical nova cycles. *Astrophys. Journal*, 600(1):390, 2004.

[8] A. Kovetz and D. Prialnik. CNO abundances resulting from diffusion in accreting nova progenitors. *Astrophys. Journal*, 291:812–821, 1985.

[9] D. Prialnik. The evolution of a classical nova model through a complete cycle. *Astrophys. Journal*, 310:222–237, 1986.

[10] J. José, M. Hernanz, and C. Iliadis. Nucleosynthesis in classical novae. *Nucl. Phys. A*, 777:550 – 578, 2006. Special Issue on Nuclear Astrophysics.

[11] J. S. Gallagher and S. Starrfield. On the total energy output of the nova outburst. *Monthly Notices of the Royal Astronomical Society*, 176(1):53–61, 1976.

[12] J. José. Classical nova explosions–hydrodynamics and nucleosynthesis. *Bull. Astr. Soc. India*, 40:443–456, 2012.

[13] A. W. Shafter. The galactic nova rate. In *CLASSICAL NOVA EXPLOSIONS: International Conference on Classical Nova Explosions*, volume 637, pages 462–471. AIP Publishing, 2002.

[14] G. A Tammann, W. Loeffler, and A. Schroeder. The galactic supernova rate. *The Astrophysical Journal Supplement Series*, 92:487–493, 1994.

[15] O. Yaron, D. Prialnik, M. M. Shara, and A. Kovetz. An extended grid of nova models. II. the parameter space of nova outbursts. *Astrophys. Journal*, 623(1):398, 2005.

[16] K. Lodders. Solar system abundances of the elements. In *Principles and perspectives in cosmochemistry*, pages 379–417. Springer, 2010.

[17] G. W. Kallemeyn and J. T. Wasson. The compositional classification of chondritesI. the carbonaceous chondrite groups. *Geochimica et Cosmochimica Acta*, 45(7):1217 – 1230, 1981.

[18] M. Zolensky, R. Barrett, and L. Browning. Mineralogy and composition of matrix and chondrule rims in carbonaceous chondrites. *Geochimica et Cosmochimica Acta*, 57(13):3123 – 3148, 1993.

[19] J. T. Wasson and G. W. Kallemeyn. Compositions of chondrites. *Philosophical Transactions of the Royal Society of London A: Mathematical, Physical and Engineering Sciences*, 325(1587):535–544, 1988.

[20] J. José. Classical novae theory and observations. *Proc. Sci.*, 2010.

[21] J. José and A. Coc. Nucleosynthesis in classical nova explosions: Modeling and nuclear uncertainties. *Nucl. Phys. News*, 15(4):17–22, 2005.

[22] M. B. Bennett, C. Wrede, K. A. Chipps, J. José, S. N. Liddick, M. Santia, A. Bowe, A. A. Chen, N. Cooper, D. Irvine, et al. Classical-nova contribution to the Milky Ways ^{26}Al abundance: Exit channel of the key ^{25}Al$(p, \gamma)^{26}$Si resonance. *Phys. Rev. Lett.*, 111(23):232503, 2013.

[23] D. Pérez-Loureiro, C. Wrede, M. B. Bennett, S. N. Liddick, A. Bowe, B. A. Brown, A. A. Chen, K. A. Chipps, N. Cooper, D. Irvine, E. McNeice, F. Montes, F. Naqvi, R. Ortez, S. D. Pain, J. Pereira, C. J. Prokop, J. Quaglia, S. J. Quinn, J. Sakstrup, M. Santia, S. B. Schwartz, S. Shanab, A. Simon, A. Spyrou, and E. Thiagalingam. β-delayed γ decay of ^{26}P: Possible evidence of a proton halo. *Phys. Rev. C*, 93:064320, Jun 2016.

[24] C. Iliadis, R. Longland, A. E. Champagne, A. Coc, and R. Fitzgerald. Charged-particle thermonuclear reaction rates: II. tables and graphs of reaction rates and probability density functions. *Nucl. Phys. A*, 841(1):31–250, 2010.

[25] L. N. Downen, C. Iliadis, J. José, and S. Starrfield. Nuclear thermometers for classical novae. *Astrophys. J.*, 762(2):105, 2013.

[26] A. L. Sallaska, C. Iliadis, A. E. Champange, S. Goriely, S. Starrfield, and F. X. Timmes. STARLIB: a next-generation reaction-rate library for nuclear astrophysics. *The Astrophysical Journal Supplement Series*, 207(1):18, 2013.

[27] T. Rauscher and F-K. Thielemann. Tables of nuclear cross sections and reaction rates: an addendum to the paper astrophysical reaction rates from statistical model calculations. *At. Data Nucl. Data Tables*, 79(1):47–64, 2001.

[28] G. Boato. The isotopic composition of hydrogen and carbon in the carbonaceous chondrites. *Geochimica et Cosmochimica Acta*, 6(56):209 – 220, 1954.

[29] J. H. Reynolds and G. Turner. Rare gases in the chondrite renazzo. *Journal of Geophysical Research*, 69(15):3263–3281, 1964.

[30] P. Hoppe and E. Zinner. Presolar dust grains from meteorites and their stellar sources. *Journal of Geophysical Research: Space Physics*, 105(A5):10371–10385, 2000.

[31] Milton Blander and Louis H. Fuchs. Calcium-aluminum-rich inclusions in the allende meteorite: evidence for a liquid origin. *Geochimica et Cosmochimica Acta*, 39(12):1605 – 1619, 1975.

[32] P. Williams. Secondary ion mass spectrometry. *Annual Review of Materials Science*, 15(1):517–548, 1985.

[33] J. P. Young, R. W. Shaw, and D. H. Smith. Resonance ionization mass spectrometry. *Analytical Chemistry*, 61(22):1271A–1279A, 1989.

[34] G. K. Nicolussi, A. M. Davis, M. J. Pellin, R. S. Lewis, R. N. Clayton, and S. Amari. s-process zirconium in presolar silicon carbide grains. *Science*, 277(5330):1281–1284, 1997.

[35] J. José, M. Hernanz, S. Amari, K. Lodders, and E. Zinner. The imprint of nova nucleosynthesis in presolar grains. *Astrophys. J.*, 612(1):414, 2004.

[36] S. Amari. Presolar grains from novae: their isotopic ratios and radioactivities. *New Astronomy Reviews*, 46(810):519 – 524, 2002. Proceedings of the International Workshop Astronomy with radioactivities {III}.

[37] A. R. Barnett. COULFG: Coulomb and Bessel functions and their derivatives, for real arguments, by Steed's method. *Computer Phys. Comm.*, 27(2):147 – 166, 1982.

[38] B. A. Brown and W. A. Richter. New "USD" Hamiltonians for the sd shell. *Phys. Rev. C*, 74:034315, Sep 2006.

[39] W. Heisenberg. On the structure of atomic nuclei. *Z. Phys*, 77:1–11, 1932.

[40] E. P. Wigner. Proceedings of the robert a. welch foundation conferences on chemical research, houston, texas, 1957. *Conf. on Chem. Res., Houston, edited by W.O. Millikan*, Robert A. Welch Foundation, Houston, Texas, 1957.

[41] S. Weinberg and S. B. Treiman. Electromagnetic corrections to isotopic spin conservation. *Phys. Rev.*, 116:465–468, Oct 1959.

[42] J Britz, A Pape, and M.S Antony. Coefficients of the isobaric mass equation and their correlations with various nuclear parameters. *At. Data Nucl. Data Tables*, 69(1):125 – 159, 1998.

[43] Y. H. Lam, B. Blank, N. A. Smirnova, J. B. Bueb, and M. S. Antony. The isobaric multiplet mass equation for $a \leq 71$ revisited. *At. Data Nucl. Data Tables*, 99(6):680–703, 2013.

[44] M. Brodeur, T. Brunner, S. Ettenauer, A. Lapierre, R. Ringle, B. A. Brown, D. Lunney, and J. Dilling. Elucidation of the anomalous $a = 9$ isospin quartet behavior. *Phys. Rev. Lett.*, 108(21):212501, 2012.

[45] C. Yazidjian, G. Audi, D. Beck, K. Blaum, S. George, C. Guénaut, F. Herfurth, A. Herlert, A. Kellerbauer, H.-J. Kluge, D. Lunney, and L. Schweikhard. Evidence for a breakdown of the isobaric multiplet mass equation: A study of the $a = 35, t = 3/2$ isospin quartet. *Phys. Rev. C*, 76:024308, Aug 2007.

[46] J. Jänecke. The quartic isobaric multiplet mass equation. *Nucl. Phys. A*, 128(2):632 – 640, 1969.

[47] A. Signoracci and B. A. Brown. Effects of isospin mixing in the $a = 32$ quintet. *Phys. Rev. C*, 84:031301, Sep 2011.

[48] Samuel S. M. Wong. *Introductory nuclear physics*. John Wiley & Sons, 2008.

[49] N. Bohr. Neutron capture and nuclear constitution. *Nature*, 137(3461):344–348, 1936.

[50] S. N. Ghoshal. An experimental verification of the theory of compound nucleus. *Phys. Rev. C*, 80:939–942, Dec 1950.

[51] M. J. Fluss, J. M. Miller, J. M. D'Auria, N. Dudey, B. M. Foreman, L. Kowalski, and R. C. Reedy. Investigation of the bohr-independence hypothesis for nuclear reactions in the continuum: α+co^{59}, p+ni^{62} and α+fe^{56}, p+cl^{59}. *Phys. Rev. C*, 187:1449–1465, Nov 1969.

[52] Louis C. Vaz, C. C. Lu, and J. R. Huizenga. Isospin and the bohr independence hypothesis. *Phys. Rev. C*, 5:463–476, Feb 1972.

[53] J. Vernotte, G. Berrier-Ronsin, S. Fortier, E. Hourani, A. Khendriche, J. M. Maison, L.-H. Rosier, G. Rotbard, E. Caurier, and F. Nowacki. One-nucleon pickup reactions on ^{32}S: Experimental results and shell-model calculations. *Nucl. Phys. A*, 655(34):415 – 439, 1999.

[54] Z. Ma, D. W. Bardayan, J. C. Blackmon, R. P. Fitzgerald, M. W. Guidry, W. R. Hix, K. L. Jones, R. L. Kozub, R. J. Livesay, M. S. Smith, et al. Astrophysically important ^{31}S states studied with the ^{321}S$(p, d)^{31}$S reaction. *Phys. Rev. C*, 76(1):015803, 2007.

[55] D. Irvine, A. A. Chen, A. Parikh, K. Setoodehnia, T. Faestermann, R. Hertenberger, H-F. Wirth, V. Bildstein, S. Bishop, J. A. Clark, et al. Evidence for the existence of the astrophysically important 6.40-mev state of ^{31}S. *Phys. Rev. C*, 88(5):055803, 2013.

[56] A. Kankainen, T. Eronen, S. P. Fox, H. O. U. Fynbo, U. Hager, J. Hakala, J. Huikari, D. G. Jenkins, A. Jokinen, S. Kopecky, et al. Excited states in ^{31}S studied via beta decay of ^{31}Cl. *Eur. Phys. J. A*, 27(1):67–75, 2006.

[57] D. G. Jenkins, C. J. Lister, M. P. Carpenter, P. Chowdhury, N. J. Hammond, R. V. F. Janssens, T. L. Khoo, T. Lauritsen, D. Seweryniak, T. Davinson, et al. Mirror energy differences in the $a = 31$ mirror nuclei, ^{31}S and ^{31}P, and their significance in electromagnetic spin-orbit splitting. *Phys. Rev. C*, 72(3):031303(R), 2005.

[58] D. G. Jenkins, A. Meadowcroft, C. J. Lister, M. P. Carpenter, P. Chowdhury, N. J. Hammond, R. V. F. Janssens, T. L. Khoo, T. Lauritsen, D. Seweryniak, et al. Reevaluation of the ^{30}P$(p, \gamma)^{31}$S astrophysical reaction rate from a study of the $t = 1/2$ mirror nuclei, ^{31}S and ^{31}P. *Phys. Rev. C*, 73(6):065802, 2006.

[59] C. Wrede, J. A. Caggiano, J. A. Clark, C. Deibel, A. Parikh, and P. D. Parker. New ^{30}P$(p, \gamma)^{31}$S resonances and oxygen-neon nova nucleosynthesis. *Phys. Rev. C*, 76(5):052802(R), 2007.

[60] F. Della Vedova. *Isospin Symmetry in the sd shell: The $A = 31$ and $A = 35$ Mirror Nuclei*. PhD thesis, Universita Degli Studi di Padova, December 2004.

[61] F. Della Vedova, S. M. Lenzi, M. Ionescu-Bujor, N. Mărginean, M. Axiotis, D. Bazzacco, A. M. Bizzeti-Sona, P.G. Bizzeti, A. Bracco, F. Brandolini, et al. Isospin symmetry breaking at high spin in the mirror nuclei ^{35}Ar and ^{35}Cl. *Phys. Rev. C*, 75(3):034317, 2007.

[62] D. T. Doherty, G. Lotay, P. J. Woods, D. Seweryniak, M. P. Carpenter, C. J. Chiara, H. M. David, R. V. F. Janssens, L. Trache, and S. Zhu. Key resonances in the ^{30}P$(p, \gamma)^{31}$S gateway reaction for the production of heavy elements in ONe novae. *Phys. Rev. Lett.*, 108(26):262502, 2012.

[63] D. T. Doherty, P. J. Woods, G. Lotay, D. Seweryniak, M. P. Carpenter, C. J. Chiara, H. M. David, R. V. F. Janssens, L. Trache, and S. Zhu. Level structure of ^{31}S: From low excitation energies to the region of interest for hydrogen burning in novae through the ^{30}P$(p, \gamma)^{31}$S reaction. *Phys. Rev. C*, 89(4):045804, 2014.

[64] A. Parikh, K. Wimmer, T. Faestermann, R. Hertenberger, J. José, R. Longland, H-F. Wirth, V. Bildstein, S. Bishop, A. A. Chen, et al. Improving the ^{30}P$(p, \gamma)^{31}$S rate in oxygen-neon novae: Constraints on j^{π} values for proton-threshold states in ^{31}S. *Phys. Rev. C*, 83(4):045806, 2011.

[65] D. J. Morrissey, B. M. Sherrill, M. Steiner, A. Stolz, and I. Wiedenhoever. Commissioning the A1900 projectile fragment separator. *Nucl. Instrum. Methods Phys. Res., Sect. B*, 204:90–96, 2003.

[66] D. Bazin, V. Andreev, A. Becerril, M. Doléans, P. F. Mantica, J. Ottarson, H. Schatz, J. B. Stoker, and J. Vincent. Radio frequency fragment separator at nscl. *Nucl. Instrum. Methods Phys. Res., Sect. A*, 606(3):314–319, 2009.

[67] Glenn F. Knoll. *Radiation Detection and Measurement*. John Wiley & Sons, 2010.

[68] USA XIA LLC, CA. *Digital Gamma Finder (DGF) Pixie-16 Manuals, 1.4 edition*. 2009.

[69] K. Starosta, C. Vaman, D. Miller, P. Voss, D. Bazin, T. Glasmacher, H. Crawford, P. Mantica, H. Tan, W. Hennig, et al. Digital data acquisition system for experiments with segmented detectors at national superconducting cyclotron laboratory. *Nucl. Instrum. Methods Phys. Res., Sect. A*, 610(3):700–709, 2009.

[70] C. J. Prokop, S. N. Liddick, B. L. Abromeit, A. T. Chemey, N. R. Larson, S. Suchyta, and J. R. Tompkins. Digital data acquisition system implementation at the national superconducting cyclotron laboratory. *Nucl. Instrum. Methods Phys. Res., Sect. A*, 741:163 – 168, 2014.

[71] C. Wrede, J. A. Caggiano, J. A. Clark, C. M. Deibel, A. Parikh, and P. D. Parker. Measurements of ^{31}S energy levels and reevaluation of the thermonuclear resonant ^{30}P$(p,\gamma)^{31}$S reaction rate. *Phys. Rev. C*, 79:045803, Apr 2009.

[72] A. Saastamoinen. *Studies of $T_z = -3/2$ Nuclei of Astrophysical Interest*. PhD thesis, University of Jyväskylä, September 2011.

[73] D. Melconian, S. Triambak, C. Bordeanu, A. Garcia, J. C. Hardy, V. E. Iacob, N. Nica, H. I. Park, G. Tabacaru, L. Trache, et al. β decay of ^{32}Cl: Precision γ-ray spectroscopy and a measurement of isospin-symmetry breaking. *Phys. Rev. C*, 85(2):025501, 2012.

[74] L. Varnell and J. Trischuk. A peak-fitting and calibration program for ge(li) detectors. *Nucl. Instrum. Methods*, 76(1):109–114, 1969.

[75] M. M. Be, B. Duchemin, J. Lame, C. Morillon, F. Piton, E. Browne, V. Chechev, R. Helmer, and E. Schonfeld. Table of radionuclides. Technical Report CEA-ISBN 2-7272-0200-8, 1999.

[76] C. Ouellet and B. Singh. Nuclear data sheets for A = 32. *Nuclear Data Sheets*, 112(9):2199–2355, 2011.

[77] J. Suhonen. *Electromagnetic Multipole Moments and Transitions*. Springer Berlin Heidelberg, Berlin, Heidelberg, 2007.

[78] Leon van Dommelen. Quantum Mechanics for Engineers, 2013.

[79] C. Ouellet and B. Singh. Nuclear data sheets for A = 31. *Nucl. Data Sheets*, 114(2):209–396, 2013.

[80] F. Ajzenberg-Selove and J. L. Wiza. Energy levels of s^{31}. *Phys. Rev.*, 143:853–855, Mar 1966.

[81] J. M. Davidson, D. A. Hutcheon, D. R. Gill, T. Taylor, D. M. Sheppard, and W. C. Olsen. Energy levels of ^{31}S. *Nucl. Phys. A*, 240(2):253–262, 1975.

[82] W. P. Alford, R. N. Boyd, and D. Elmore. Structure of ^{29}P and ^{31}S studied in the $(^{3}$He, $n)$ reaction. *Phys. Rev. C*, 26:789–796, Sep 1982.

[83] C. Wrede, J. A. Caggiano, J. A. Clark, C. M. Deibel, A. Parikh, and P. D. Parker. Thermonuclear ^{30}S$(p,\gamma)^{31}$Cl reaction in type I x-ray bursts. *Phys. Rev. C*, 79:045808, Apr 2009.

[84] C. E. Moss. Nuclear energy levels of ^{31}S and ^{33}C1. *Nucl. Phys. A*, 145(2):423 – 448, 1970.

[85] T. S. Bhatia, W. W. Daehnick, and G. J. Wagner. Search for $1p$ neutron strength in ^{31}S by the reaction ^{32}S$(^{3}$He,$\alpha)^{31}$S. *Phys. Rev. C*, 5:111–117, Jan 1972.

[86] J. P. Mason. A 6130-kev gamma-ray source using the ^{13}C$(\alpha,n)^{16}$O reaction. *Nucl. Instrum. Methods Phys. Res., Sect. A*, 241(1):207 – 209, 1985.

[87] J. K. Dickens and R. D. Baybarz. A monoenergetic 6130-kev gamma-ray source for detector calibration. *Nucl. Instrum. Methods*, 85(1):143 – 145, 1970.

[88] R. H. Spear, J. D. Larson, and J. D. Pearson. Excitation function for the reaction ^{13}C$(\alpha,n\gamma)^{16}$O. *Nucl. Phys.*, 41:353 – 363, 1963.

[89] M. B. Bennett, C. Wrede, B. A. Brown, S. N. Liddick, D. Pérez-Loureiro, D. W. Bardayan, A. A. Chen, K. A. Chipps, C. Fry, B. E. Glassman, C. Langer, N. R. Larson, E. I. McNeice, Z. Meisel, W. Ong, P. D. O'Malley, S. D. Pain, C. J. Prokop, H. Schatz, S. B. Schwartz, S. Suchyta, P. Thompson, M. Walters, and X. Xu. Isospin mixing reveals ^{30}P$(p,\gamma)^{31}$S resonance influencing nova nucleosynthesis. *Phys. Rev. Lett.*, 116:102502, Mar 2016.

[90] B. A. Brown. *Lecture Notes in Nuclear Structure*. NSCL Document Server, 2004.

[91] D.H. Wilkinson and B.E.F. Macefield. A parametrization of the phase space factor for allowed β-decay. *Nucl. Phys. A*, 232(1):58 – 92, 1974.

[92] V. Tripathi, S. L. Tabor, A. Volya, S. N. Liddick, P. C. Bender, N. Larson, C. Prokop, S. Suchyta, P-L. Tai, and J. M. VonMoss. Split isobaric analog state in ^{55}Ni: Case of strong isospin mixing. *Phys. Rev. Lett.*, 111(26):262501, 2013.

[93] V. E. Iacob, Y. Zhai, T. Al-Abdullah, C. Fu, J. C. Hardy, N. Nica, H. I. Park, G. Tabacaru, L. Trache, and R. E. Tribble. β decay of proton-rich nucleus ^{23}Al and astrophysical consequences. *Phys. Rev. C*, 74:045810, Oct 2006.

[94] R. J. Tighe, J. C. Batchelder, D. M. Moltz, T. J. Ognibene, M. W. Rowe, J. Cerny, and B. A. Brown. Observation of strong isospin mixing in proton emission from the astrophysically interesting isobaric analog state in ^{23}Mg. *Phys. Rev. C*, 52:R2298–R2301, Nov 1995.

[95] A. R. Barnett, D. H. Feng, J. W. Steed, and L. J. B. Goldfarb. Coulomb wave functions for all real η and ρ. *Computer Physics Communications*, 8(5):377 – 395, 1974.

[96] C. Iliadis. Proton single-particle reduced widths for unbound states. *Nucl. Phys. A*, 618(1):166 – 175, 1997.

[97] B. A. Brown, W. A. Richter, and C. Wrede. Shell-model studies of the astrophysical rapid-proton-capture reaction ^{30}P$(p, \gamma)^{31}$S. *Phys. Rev. C*, 89(6):062801(R), 2014.

[98] T. Rauscher and F. K. Thielemann. Astrophysical reaction rates from statistical model calculations. *At. Data Nucl. Data Tables*, 75:1, 2000.

[99] B. A. Brown, W. A. Richter, and C. Wrede. Erratum: Shell-model studies of the astrophysical rapid-proton-capture reaction ^{30}P$(p, \gamma)^{31}$S [phys. rev. c **89** , 062801(r) (2014)]. *Phys. Rev. C*, 92:069901, Dec 2015.

[100] M. B. Bennett, C. Wrede, B. A. Brown, S. N. Liddick, D. Pérez-Loureiro, D. W. Bardayan, A. A. Chen, K. A. Chipps, C. Fry, B. E. Glassman, C. Langer, N. R. Larson, E. I. McNeice, Z. Meisel, W. Ong, P. D. O'Malley, S. D. Pain, C. J. Prokop, S. B. Schwartz, S. Suchyta, P. Thompson, M. Walters, and X. Xu. Isobaric multiplet mass equation in the $a = 31$, $t = 3/2$ quartets. *Phys. Rev. C*, 93:064310, Jun 2016.

[101] W. Benenson, D. Mueller, E. Kashy, H. Nann, and L. W. Robinson. Mass of ^{27}P and ^{31}Cl. *Phys. Rev. C*, 15(4):1187, 1977.

[102] A. Kankainen, L. Canete, T. Eronen, J. Hakala, A. Jokinen, J. Koponen, I. D. Moore, D. Nesterenko, J. Reinikainen, S. Rinta-Antila, A. Voss, and J. Äystö. Mass of astrophysically relevant ^{31}Cl and the breakdown of the isobaric multiplet mass equation. *Phys. Rev. C*, 93:041304(R), Apr 2016.

[103] P. M. Endt. Energy levels of $a = 21 - 44$ nuclei (VII). *Nucl. Phys. A*, 521:1–400, 1990.

[104] A. C. Wolff and H. G. Leighton. High-resolution investigation of the ^{30}Si$(\tau, d)^{31}$P reaction. *Nucl. Phys. A*, 140(2):319 – 332, 1970.

[105] M. N. I. Al-Jadir, H. T. Fortune, and D. J. Pullen. States of high e_x in ^{31}P. *J. Phys. G*, 6(6):731, 1980.

[106] R.A. McCulloch, N.M. Clarke, R.J. Griffiths, J.S. Hanspal, S. Roman, and J.M. Barnwell. The interaction of 33 Mev polarised helions with ^{30}Si. *Nucl. Phys. A*, 431(2):344 – 366, 1984.

[107] J. Vernotte, A. Khendriche, G. Berrier-Ronsin, S. Grafeuille, J. Kalifa, G. Rotbard, R. Tamisier, and B. H. Wildenthal. ^{30}Si$(^{3}$he, d $)^{31}$p reaction at 25 mev. *Phys. Rev. C*, 41:1956–1974, May 1990.

[108] G. Th. Kaschl, G. Mairle, U. Schmidt-Rohr, G. J. Wagner, and P. Turek. Proton pick-up from the $2s - 1d$ and $1p$ shells of ^{32}S. *Nucl. Phys. A*, 136(2):286 – 300, 1969.

[109] L. Axelsson, J. Äystö, M. J. G. Borge, L. M. Fraile, H. O. U. Fynbo, A. Honkanen, P. Hornshj, A. Jokinen, B. Jonson, P. O. Lipas, I. Martel, I. Mukha, T. Nilsson, G. Nyman, B. Petersen, K. Riisager, M. H. Smedberg, and O. Tengblad. Beta decay of ^{31}Ar. *Nucl. Phys. A*, 634(4):475 – 496, 1998.

[110] C. Langer, O. Lepyoshkina, Y. Aksyutina, T. Aumann, S. Beceiro Novo, J. Benlliure, K. Boretzky, M. Chartier, D. Cortina, U. Datta Pramanik, O. Ershova, H. Geissel, R. Gernhäuser, M. Heil, G. Ickert, H. T. Johansson, B. Jonson, A. Kelić-Heil, A. Klimkiewicz, J. V. Kratz, R. Krücken, R. Kulessa, K. Larsson, T. Le Bleis, R. Lemmon, K. Mahata, J. Marganiec, T. Nilsson, V. Panin, R. Plag, W. Prokopowicz, R. Reifarth, V. Ricciardi, D. M. Rossi, S. Schwertel, H. Simon, K. Sümmerer, B. Streicher, J. Taylor, J. R. Vignote, F. Wamers, C. Wimmer, and P. Z. Wu. Thermonuclear reaction ^{30}S$(p,\gamma)^{31}$Cl studied via coulomb breakup of ^{31}Cl. *Phys. Rev. C*, 89:035806, Mar 2014.

[111] C. Wrede, J. A. Caggiano, J. A. Clark, C. M. Deibel, A. Parikh, and P. D. Parker. Measurements of ^{31}S energy levels and reevaluation of the thermonuclear resonant ^{30}P$(p,\gamma)^{31}$S reaction rate. *Phys. Rev. C*, 79(4):045803, 2009.

[112] B. E. Glassman, D. Pérez-Loureiro, C. Wrede, J. Allen, D. W. Bardayan, M. B. Bennett, B. A. Brown, K. A. Chipps, M. Febbraro, C. Fry, et al. Revalidation of the isobaric multiplet mass equation for the $a = 20$ quintet. *Phys. Rev. C*, 92(4):042501, 2015.

[113] W. A. Richter, S. Mkhize, and B. A. Brown. *sd*-shell observables for the usda and usdb hamiltonians. *Phys. Rev. C*, 78:064302, Dec 2008.

[114] G. T. Koldste, B. Blank, M. J. G. Borge, J. A. Briz, M. Carmona-Gallardo, L. M. Fraile, H. O. U. Fynbo, J. Giovinazzo, J. G. Johansen, A. Jokinen, B. Jonson, T. Kurturkian-Nieto, J. H. Kusk, T. Nilsson, A. Perea, V. Pesudo, E. Picado, K. Riisager, A. Saastamoinen, O. Tengblad, J.-C. Thomas, and J. Van de Walle. Relative proton and γ widths of astrophysically important states in ^{30}s studied in the β-delayed decay of ^{31}ar. *Phys. Rev. C*, 87:055808, May 2013.

[115] G. T. Koldste, B. Blank, M. J. G. Borge, J. A. Briz, M. Carmona-Gallardo, L. M. Fraile, H. O. U. Fynbo, J. Giovinazzo, B. D. Grann, J. G. Johansen, A. Jokinen, B. Jonson, T. Kurturkian-Nieto, J. H. Kusk, T. Nilsson, A. Perea, V. Pesudo, E. Picado, K. Riisager, A. Saastamoinen, O. Tengblad, J.-C. Thomas, and J. Van de Walle. Multiparticle emission in the decay of ^{31}Ar. *Phys. Rev. C*, 89:064315, Jun 2014.

[116] P. M. Endt. Supplement to energy levels of $a = 2144$ nuclei (VII). *Nucl. Phys. A*, 633(1):1 – 220, 1998.

[117] P.J. Woods. Private communication, 2016.

[118] K. Rehm, A. Spyrou, M. Syphers, M. Wiescher, W. Wittmer, C. Wrede, X. Wu, and A. Zeller. SEparator for CApture reactions (SECAR) pre-conceptual design report. 2014.

[119] G. P. A. Berg, J. C. Blackmon, M. Couder, U. Greife, F. Montes, K. E. Rehm, H. Schatz, M. S. Smith, M. Wiescher, A. Zeller, et al. Design of a new recoil separator for measurements of radiative capture reactions in astrophysics. In *AIP Conference Proceedings*, volume 1269, page 445, 2010.

[120] D. Bazin and O. Tarasov. Exotic beam production with fragment separators, 2016.

[121] CERN. Geant4: A toolkit for the simulation of the passage of particles through matter, 2016.

[122] W. F. Mueller, J. A. Church, T. Glasmacher, D. Gutknecht, G. Hackman, P. G. Hansen, Z. Hu, K. L. Miller, and P. Quirin. Thirty-two-fold segmented germanium detectors to identify γ-rays from intermediate-energy exotic beams. *Nucl. Instrum. Methods Phys. Res., Sect. A*, 466(3):492 – 498, 2001.

[123] CERN. Geant4 documentation, 2016.